I. Surfactant Effects on the Interaction of a Three Dimensional Vortex Pair with a Free Surface
II. Turbulent Flow over a Flexible Body Undergoing Fish-like Swimming Motion

by

Xiang Zhang

B.S., Mechanics, University of Science and Technology of China, 1991

Submitted to the Department of Ocean Engineering
in partial fulfillment of the requirements for the degree of

Doctor of Philosophy

at the

MASSACHUSETTS INSTITUTE OF TECHNOLOGY

June 2001

Author .....
Department of Ocean Engineering
October 24, 2000

Certified by .....
Dick K. P. Yue
Professor of Hydrodynamics and Ocean Engineering
Thesis Supervisor

Accepted by .....
Henrik Schmidt
Professor of Ocean Engineering
Chairman, Department Committee on Graduate Students

I. Surfactant Effects on the Interaction of a Three Dimensional Vortex Pair with a Free Surface

II. Turbulent Flow over a Flexible Body Undergoing Fish-like Swimming Motion

by

Xiang Zhang

B.S., Mechanics, University of Science and Technology of China, 1991

Submitted to the Department of Ocean Engineering
on October 24, 2000, in partial fulfillment of the
requirements for the degree of
Doctor of Philosophy

Abstract

In part I of the thesis, a canonical problem of three dimensional surfactant hydrodynamics, the three-dimensional laminar interaction between a clean or contaminated free surface and a vortical flow underneath is considered. Initially, the vortical flow is in the form of two modulated finite-core vortex tubes parallel to the free surface. The vortex tubes break down via instability and helical vorticity is generated. The most prominent feature at the surface is that associated with the connection of helical vorticity to the free surface. For clean surface, the helical vorticity would interact fully with the free surface and reconnects to it under the influence of the primary vorticity. The presence of surfactant leads to substantial increase in the generation of free-surface secondary vorticity which results from large gradients in the surface surfactant distribution created by induced velocities at the free surface due to the primary vortex tubes. The secondary structure in the bulk interacts with the helical vorticity, which totally alters the vortex pattern and connection process. The presence of contamination considerably weakens the connection in terms of strength, location and duration. The degree of secondary vorticity generation by the surfactant is limited by a closed-loop interaction between the flow field (primary flow and secondary flow) and surfactant transport. The presence of secondary vorticity tends to smooth out the surfactant distribution on the free surface and consequently leads to a reduction in the generation of secondary vorticity itself associated with the surfactant gradient (together with surfactant diffusion). This negative feedback process and the rebounding of the primary vorticity by the secondary vorticity are the key processes underlying effects of insoluble surfactant. For contaminated free surface, the secondary and helical vortical structures interact strongly and new structures are

generated. The split of helical vorticity because of the strong secondary vorticity leads to the new structures. When the surfactant is soluble, the effects are generally diminished due to the sorption kinetics between the surface and the bulk phase. Both vorticity isosurfaces and vortex filaments are used to describe vortex structures and their evolution.

In Part II of the thesis, we investigated the turbulent flow over a smooth wavy wall undergoing traveling wave motion in the mean flow direction. Results are presented from direct numerical simulation with periodic and non-periodic streamwise boundary conditions. The Reynolds number in terms of mean velocity and motion wavelength is in the range of 3000-6500 and wave phase speed c relative to incoming flow velocity U is in the range of -0.5 and 2.0. The flow pattern is a strong function of c/U. For $c = 0$, there are features like separated region, attached boundary layer, and free shear layer. The pressure gradient created on the surface is balanced by viscous force in the momentum equation. For $c/U = -0.2$, the separation point and reattachment point move away from the wall but the separation bubble persists. Secondary flow exists both at the wave crest and wave trough. For $c/U > 0$, the pressure gradient is not balanced by viscous stress only, but also by centrifugal force. Separation and reattachment points move away from the wall but not as far away as $c/U < 0$ case. As c increases, the separation bubble disappears at a certain c value. For $c/U = 2$, there is a secondary reverse flow near the wave crest and local friction velocity becomes very small. For large ka at $c/U = 0$, the flow is not sensitive to ka because separation location does not change much and outer flow cannot feel the difference. Our results show that when the wave speed c is approximately equal to the outer flow velocity U, turbulence is reduced and separation disappears. Kinetic energy and all components of turbulent shear stress are reduced significantly and are distributed non-uniformly for the value of $c/U = 1.2$, compared to smaller c/U cases. The averaged velocity profiles exhibit evidence of laminarization. As c/U increases from zero to a critical value, the separation bubble relocates upstream and finally disappears. However, for $c/U > 1.6$, separation reappears near the wave crest. Both favorable surface curvature and pressure gradient contribute to the stability behavior of turbulence near the surface. Wavy motion not only affects the turbulent properties but also force balance and propulsive efficiency. Pressure thrust can be achieved for about $c > U$, and for even bigger c/U, this thrust is greater than the friction drag, and consequently a net thrust develops. For $c/U < 0$, the pressure drag increases while the friction drag decreases. The friction drag reaches a maximum at a c slightly smaller than U. It is shown that the total power required to propel the wavy plate is minimum at about $c/U = 1.2$.

Thesis Supervisor: Dick K. P. Yue
Title: Professor of Hydrodynamics and Ocean Engineering

Acknowledgments

I would like to express my sincere gratitude to my advisors, Professor Yue and Professor Triantafyllou for their patient guidance and support. They provided me with the opportunity to work on the interesting and challenging problems of fish swimming and free surface flow. My experience here at MIT will keep my interest in the dynamics of fish propulsion will for a very long time. To my regret, my unique personal situation near the end of my degree program made it impossible for me to work full time or even part time on my project and thesis. I know that I owe big to my advisors and hope I will be able to redeem myself one way or the other in the future.

I also owe my gratitude to the system administrators and fellow students in the Vortical Flow Research Laboratory. Thank you all.

Contents

List of Figures

List of Tables

Part I

Surfactant Effects on the Interaction of a Three Dimensional Vortex Pair with a Free Surface

Chapter 1

Introduction

1.1 Background

1.1.1 Ship wakes and ocean surfactants

Free surface phenomena are of great importance to ocean engineering because a thorough, fundamental understanding of the behavior of free surface flow is necessary for the solution of many dynamical problems involving ocean. Almost all the work on ocean wave, ship wake, free surface turbulence and free-surface body juncture concerns only clean free surface. However in reality, ocean surface is never clean and we have to understand how contaminated fluid modifies free surface stress conditions and to what degree available results are affected.

The term "surfactant", a short form of the term surface-active agent, is used in this thesis to describe the materials that contaminate the otherwise clean free surface. This term is primarily used to describe synthetic industrial products and has a connotation implying that the substance is man-made (see Edwards D. A. *et al* 1991). We also include natural surfactant in this term. Surfactants can form monomolecular films by adsorption at an air/water interface. Surfactants exist not only on the surface but can also be dissolved in the bulk flow at various degrees and for the problems which involve strong bulk flow, we identify two kinds of surfactant by its solubility. Insoluble surfactants usually have a molecular structure such that they have both a hydrophilic

end and a hydrophobic, or "water hating" end. On the surface, the molecules tend to arrange themselves in such an order that the hydrophobic ends are out of the water and a monolayer is formed. Because the monolayer is only one molecule thick, it is possible that a very small amount of surfactant within the bulk of the fluid can have a large effects on surface stress. Surfactant reduces the surface tension in a rate proportional to the molecular concentration at the surface. In addition to insoluable surfactant, there is a large collection of surfactants that are soluable in water. The soluability is determined by factors including the size and structure of the molecules, free energy of the surfactant molecues and temperature. Surface-bulk adsorption mechanism and bulk transport must be considered for flows with soluble surfactant.

Surfactants are commonly found in natural waters. Sources of surfactants in the ocean include marine organisms, terrestrial delivered by atmospheric transport, and petroleum sources such as oils seeps or spills. The composition of marine surfactants is of great variety. Several major mechanisms determine the composition and concentration of ocean surfactants. These include local biological productivity, subsurface currents and internal waves, wind stress, wave stress, wave breaking, and aerosol formation.

The degree of surfactant effect is determined by surfactant properties, flow field configuration, and the length scale of the problem. For ship wakes, the role played by surfactant is significant for remote sensing because of the large surface convection and great deviation in surface surfactant concentration. It is well known that features of ship wakes do not decay as rapidly as people might expect. The formation of two large bands of surfactants behind a ship has been observed by satellite imaging. It can be contemplated that two counter-rotating vortex tubes whose axis is parallel to the ship's direction of travel exist underneath the free surface. In the first part of this thesis, we are interested in how the free surface interacts with vortex pair and how free surface turbulence is affected by the surfactant. Of course, the problem of ship wakes is very complicated because of turbulent boundary layer shedding, large Reynolds number, nonlinear surface boundary condition, and complex geometry etc.

1.1.2 Previous study of vortex interaction with a free surface

The understanding of the interactions of a vortex pair with a free surface is much enriched after years of research. This problem has attracted a lot of researchers because knowledge of this subject can help us investigate the coherent structures of free surface turbulence, especially ship wake structures. People have found many turbulent flows are dominated by spatial coherent, temporally evolving vortex structures. Even though there is no generally accepted definition and quantitative criteria for "coherent structures", this concept has definitely provided new insights and approaches in turbulence research. By studying the elements (pairs and rings) of those complex vortex structures, one can collect necessary knowledge for understanding coherent structures in ship wakes.

Because surfactant is ubiquitous in real ocean, one can not get a complete understanding of any surface phenomenon without taking into account of surfactant effects. The importance of surfactants was discovered shortly after people found discrepancy between theory and experiments. Barker & Crow (1977) were among the first to study the surface effects on vortical flows. They observed 'rebounding' of impinging vortex pair from both a wall and a free surface and they claimed that the shape change of tubes from originally circular cores to oval cores was the reason for rebounding in free surface situation. However, the oval shape is an effect of interaction with the surface and not necessarily causes rebounding. The problem remained unsettled until the important role of surface contamination was postulated by Saffman in 1979. He examined the experimental work done by Barker & Crow and found that their explanation of vortex rebounding was not correct for the free surface case. Saffman claimed that if the free surface is clean, the rebounding would not happen. And he made an assumption that the water Barker & Crow used had been contaminated. Later Bernal *et al* (1989) showed that the rebounding effect was much reduced when the surface was cleaned by draining. Now it has been clarified in two dimensional study that the rebounding of impinging vortex tube from the free surface is caused by the secondary vorticity outboard the primary tube created by the surfactant con-

centration gradient. However, when the surface is clean, there is still small amount of secondary vorticity generated, but not large enough to block the horizontal motion of the vortex pair.

As for the numerical simulation of the interaction of vortex pair with a free surface, Ohring & Lugt (1991) performed nonlinear numerical simulation of a two dimensional vortex pair interacting with a free surface. Their Froude numbers were high and Reynolds numbers were low. They showed that the production of secondary vorticity decreases as surface tension increases, which is a reasonable result. The curvature effect is smaller when surface elevation is decreased due to larger surface tension, which leads to decreased secondary vorticity. Tsai & Yue (1995) studied the two dimensional vortex pair-free surface interaction under the influence of surfactant and they presented detailed two dimensional process and mechanisms by numerical simulation. They described the generation of secondary vorticity and the relation between Reynolds ridge and surfactant concentration.

Three dimensional case is much more complicated because of the instability of the vortex tube and therefore more complex vortex structures involved. A lot of the experimental research work concerning the interaction of trailing vortices or vortex pairs with a free surface was performed by Sarpkaya (1983, 1985, 1986, 1991) and Sarpkaya & Henderson (1985). Figure 1-1 reproduces photographs from the experiments of Sarpkaya & Suthon (1991) which show the time evolution of surface features as a function of time. Their experiments showed that the first surface signature is an upwelling region above the center line (a straight line parallel to and in the middle of the two tubes), a two dimensional phenomenon as a result of upward momentum of the vortex pairs. At the same time, two bands of surface depression (trough) form on the outer side of the upwelling region. Later, striations which are normal to the vortex pairs form in the upwelling region. The striations are the transverse undulations in the free surface elevation. After the intensification of striations, dimples or scars form in the trough region which exist at the ends of the striations. In this process, the striationsextend outward slightly, and so do the scars. Dimples on the free surface may indicate generation of normal vorticity on the free surface. Hirsa's

(1990) and Hirsa & Willmarth's (1994) experiments confirmed those features. The relation between these subsequent surface features is not clear for some time. Hirsa & Willmarth claimed that the cross-axis vorticity is the cause of the striations, but they did not reveal the origin of the cross-axis vorticity. Striations become less evident at the same time the dimples appear, signaling that there may exist a relation between the two events. When straight-edged vortex generators (such as towing foil) were used in the earliest experiments, in order to simulate the instability the center velocity must be relatively large to prevent vortex from completely disappearing due to dissipation before connection on the free surface. This leads to high Reynolds number and turbulence. People found that the above features still exist in this case, but highly irregular (Willert, 1992).

Later researchers (including Willert, 1992) used serrated edge to introduce instability and thus performed experiment at lower Reynolds numbers so that features are easier to observe using DPIV in a laminar flow. However because of the medium Reynolds number (about 10^3) in their experiments, it is inevitable that the flow is in its transition to turbulence, especially in the period of whirl generation. This serration of the core of the initial vortex pair is also used in our simulation as well as in other numerical work. So it is possible that our numerical results can be tested by experiments. Our simulation shows that the spatial and temporal relations between the striations and the dimples are observed, and both the instability and helical vorticity are adequately represented.

In order to get a full understanding of the three dimensional vortex free surface interaction, one must be able to explain the mechanisms involved in the vortex reconnection. People already came up with several connection mechanisms, for example, as described by Melander & Hussain (1990). Because the vortex structural configurations in the problems they studied vary, their mechanisms are not the same even though there exist some similarities. Melander & Hussain (1990) studied two anti-parallel vortices with mutually inclined symmetric sinusoidal perturbations. They described three phases involved in the connection and the bridging mechanism. Kida, Takaoka & Hussain (1991) studied interactions between two vortex rings, and

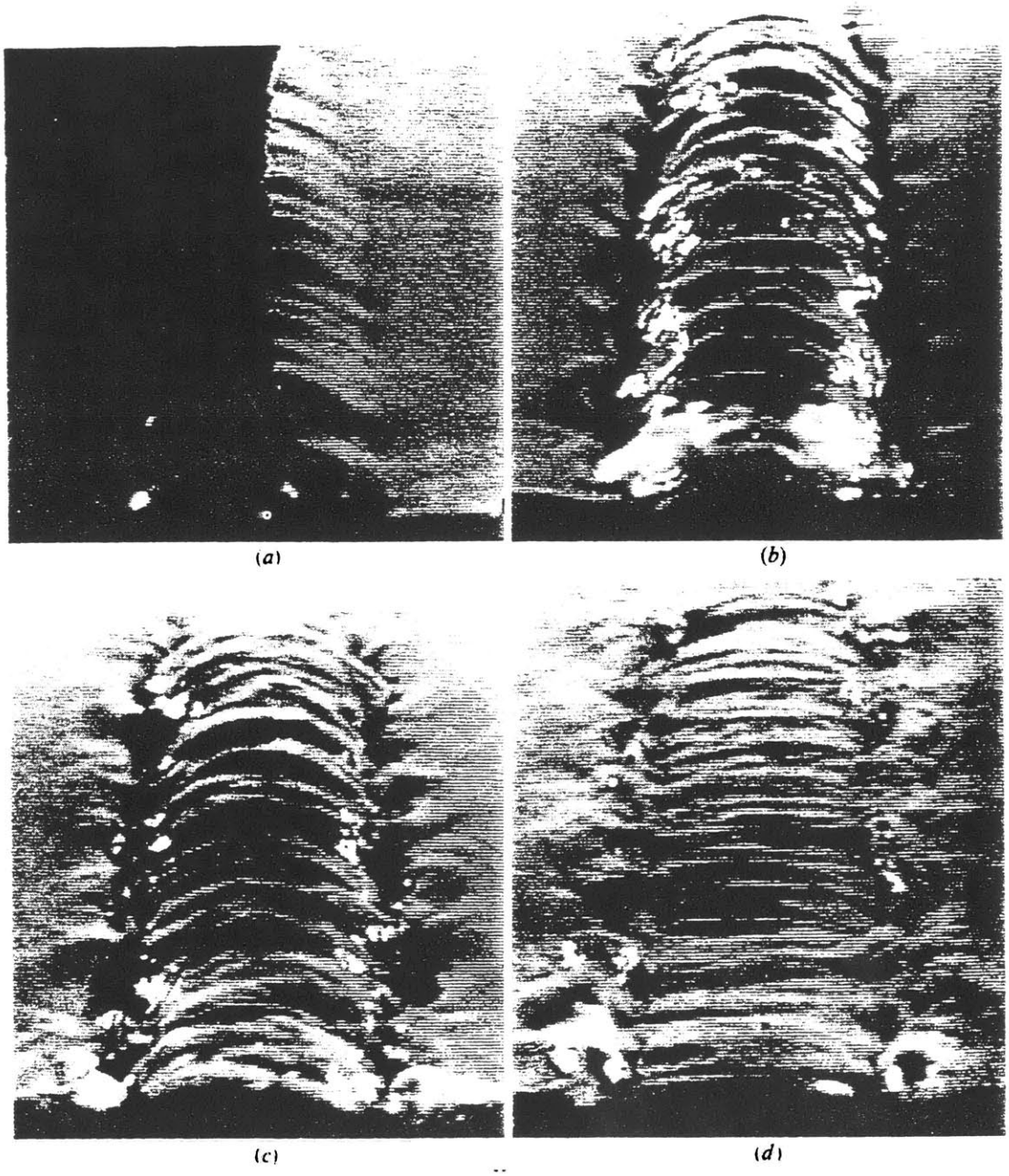

Figure 1-1: Surface signature of a vortex pair interaction with a free surface. (a) Rise of a corrugated vortex dome; (b) formation of scars and dimples; (c) intensification of scars and striations; and (d) late stages of scars and striation formation. (reproduced from Sarpkaya & Suthon, 1991)

they found that the bridging mechanism is still valid even though the location of the bridges is on the front of the dipole close to the position of maximum strain rate. They made use of quantities such as helicity density and enstrophy production to study the topological structures in detail. Dommermuth (1993) briefly mentioned the bridge mechanism in his isosurface plotting of ω_{xz}. Besides Dommermuth's work, Chiong (1997) worked on vortex ring connection on the free surface. She decomposed vorticity equation and introduced stretching, diffusion and turning rates to study the connection process. Our present work not only shows the effects of surfactant but also provides a new prototype of vortex connection on the free surface.

Some experiments have been conducted to investigate the case when there is surfactant present. Hirsa & Willmarth (1994) and Willert (1992) found that even a small amount of surfactant can prevent the connection process. But some important questions remain to be answered, such as why the connection is greatly diminished when surfactant is present. Some researchers offered their answers, but their arguments were either incomplete or wrong. Although experiments are important and useful in studying free surface features, the available data collection methods have limits in producing large amount of volume data in the bulk flow. Numerical simulation can overcome this shortcoming and provide data fine enough to study detailed mechanisms. The surfactant model and computational methods remain the same. Both insoluble and soluble cases are studied. Our simulation revealed the detailed underlying mechanism. The major difference of our connection involving free surface compared to the cases of vortices reconnection among themselves is that the primary vortices break and reconnect in their simulation. In our simulation, the primary vortices keep their strong cores intact during their evolution and the connection on the surface is due to the helical vortices which evolve from the instability of the primary tube. This key difference inevitably leads to modified mechanisms and features.

1.2 Overview of part I of the dissertation

The first part of this thesis is organized as follows. In Chapter 2, a description of the numerical methods and surfactant model are presented as well as the detailed physical problem. In Chapter 3, results on the laminar interaction of vortex pair with a contaminated free surface is presented. How the major structures are extracted from the flow is discussed in this chapter. Chapter 4 investigates the effect of surfactants on free surface turbulence.

Chapter 2

Mathematical Formulation of Surfactant Hydrodynamics

2.1 Free surface hydrodynamics

The interaction of the vortex pair with a free surface is simulated by solving the Navier-Stokes equations governing Newtonian fluid

$$\frac{\partial \boldsymbol{u}}{\partial t} + \boldsymbol{u} \cdot \nabla \boldsymbol{u} = \frac{1}{\mathcal{R}_e} \nabla^2 \boldsymbol{u} - \nabla p, \tag{2.1}$$

together with the continuity equation

$$\nabla \cdot \boldsymbol{u} = 0, \tag{2.2}$$

where $\boldsymbol{u}$ is the velocity vector with components u, v, w in x, y and z directions respectively, p the dynamic pressure, $\mathcal{R}_e = UL/\nu$ the Reynolds number, and ν the kinematic viscosity. The vertical coordinate z is positive upward, and the origin is located at the mean free surface. The axis origin is defined as $(0, 0, 0)$ and is located on the mean free-surface. The equations have been normalized by a characteristic length L (details to be discussed), a velocity scale U, and the density of the bulk fluid ρ.

After the surface dilatational viscosity κ^s and surface shear viscosity μ^s are taken into account, the dynamic boundary conditions are (from Edwards D. A. *et al* 1991 p.111):

$$-\boldsymbol{n}\cdot\|\overline{\boldsymbol{P}}\|\cdot\boldsymbol{n} = 2H\sigma + \mu^s(\boldsymbol{b} - 2H\boldsymbol{I}_s):\nabla_s\boldsymbol{v}^o + 2H(\kappa^s+\mu^s)\nabla_s\cdot\boldsymbol{v}^o, \tag{2.3}$$

$$\begin{aligned}-\boldsymbol{n}\cdot\|\overline{\boldsymbol{P}}\|\cdot\boldsymbol{I}_s &= \nabla_s\sigma + (\kappa^s+\mu^s)\nabla_s\nabla_s\cdot\boldsymbol{v}^o \\ &+\mu^s\{\boldsymbol{n}\times\nabla_s[(\nabla_s\times\boldsymbol{v}^o)\cdot\boldsymbol{n}] + 2(\boldsymbol{b}-2H\boldsymbol{I}_s)\cdot(\nabla_s\boldsymbol{v}^o)\cdot\boldsymbol{n}\},\end{aligned} \tag{2.4}$$

both on $z=\eta$. Here η is the free surface.

(2.3) and (2.4) are the boundary conditions for Newtonian interfaces. Here $\boldsymbol{n}$ denotes unit surface normal. κ^s is the surface dilatational viscosity, and μ^s is the surface shear viscosity. $\|\overline{\boldsymbol{P}}\|$ denotes the jump of the pressure tensor across the singular surface. Detailed discussion and of notations such as surface gradient operator ∇_s and further derivation of these boundary conditions can be found in Appendix A. The definition of surfactant model can be found in section 2.2. Assuming a boundary layer thickness of order δ beneath the free surface and an order of ϵ on the free surface elevation, after normalization one can get

$$\begin{aligned}&-p+\frac{2}{\mathcal{R}_e}[w_z+\eta w_{zz}-\eta_x u_z-\eta_y v_z] \\ &=\frac{\eta}{\mathcal{F}_r^2}+(\eta_{xx}+\eta_{yy})\frac{\sigma}{\mathcal{W}_e}+\frac{\tilde{\mathcal{B}}_o}{\mathcal{R}_e}(-\eta_{yy}u_x+\eta_{xy}u_y+\eta_{xy}v_x-\eta_{xx}v_y) \\ &\quad+\frac{\mathcal{B}_o}{\mathcal{R}_e}(\eta_{xx}+\eta_{yy})(u_x+v_y)+O(\epsilon\delta,\frac{\epsilon^2}{\delta^2}), \quad \text{on } z=0\end{aligned} \tag{2.5}$$

from (2.3), which is the normal boundary condition.

For tangential stress condition (2.4), by resolving it into $x-z$ and $y-z$ planes, one can get

(a) on $x-z$ plane:

$$\frac{1}{\mathcal{R}_e}(w_x+u_z+\eta u_{zz})$$

$$= \frac{\sigma_x}{\mathcal{W}_e} + \frac{\mathcal{B}_o}{\mathcal{R}_e}(u_{xx} + v_{xy}) + \frac{\tilde{\mathcal{B}}_o}{\mathcal{R}_e}(-v_{xy} + u_{yy}) + O(\frac{\epsilon}{\delta}, \frac{\epsilon^2}{\delta^3}), \quad \text{on } z = 0 \qquad (2.6)$$

(b) on $y - z$ plane:

$$\frac{1}{\mathcal{R}_e}(w_y + v_z + \eta v_{zz})$$
$$= \frac{\sigma_y}{\mathcal{W}_e} + \frac{\mathcal{B}_o}{\mathcal{R}_e}(u_{xy} + v_{yy}) + \frac{\tilde{\mathcal{B}}_o}{\mathcal{R}_e}(v_{xx} - u_{xy}) + O(\frac{\epsilon}{\delta}, \frac{\epsilon^2}{\delta^3}), \quad \text{on } z = 0 \qquad (2.7)$$

with σ the surface tension normalized by the equilibrium tension σ_0. The nondimensional parameters in the equations are: Froude number $\mathcal{F}_r = U/(gL)^{\frac{1}{2}}$, Weber number $\mathcal{W}_e = \rho U^2 L/\sigma_0$ and Boussinesq numbers $\mathcal{B}_o = (\kappa^s + \mu^s)/(\mu L)$; $\tilde{\mathcal{B}}_o = \mu^s/(\mu L)$.

The weakly nonlinear kinematic boundary condition can be written as

$$\frac{\partial \eta}{\partial t} + \nabla_2 \cdot (\eta V) - w = 0, \quad \text{on } z = 0. \qquad (2.8)$$

Here $V = (u, v)$ is the velocity components in the x, y directions, and $\nabla_2 \equiv (\partial/\partial x, \partial/\partial y)$.

2.2 Surfactant model and its transportation

There are two transport equations, one for bulk concentration $c(x, y, z, t)$, and one for surface concentration $\gamma(x, y, t)$. The transport equation for γ is

$$\frac{\partial \gamma}{\partial t} + \nabla_s \cdot (\boldsymbol{u}\, \gamma) - \frac{1}{Pe^s}\nabla_s^2 \gamma = F, \qquad (2.9)$$

with F the normal diffusive flux, and Pe^s the surface Peclet number.

The equation for bulk concentration c is

$$\frac{\partial c}{\partial t} + \nabla \cdot (\boldsymbol{u}\, c) - \frac{1}{Pe}\nabla^2 c = 0, \qquad (2.10)$$

with Pe the bulk phase Peclet number.

According to Fick's law of diffusion, F can be expressed as

$$F = -\frac{1}{Pe^s}\frac{1}{\mathcal{K}}\left[-\frac{\eta_x}{\mathcal{N}}\frac{\partial c}{\partial x} - \frac{\eta_y}{\mathcal{N}}\frac{\partial c}{\partial y} + \frac{1}{\mathcal{N}}\frac{\partial c}{\partial z}\right]_{z=\eta}. \tag{2.11}$$

Solution of the surface- and bulk-concentration transport equations (2.9) and (2.10) requires a constitutive equation for the interfacial transport F. This means that a kinetic-rate expression is required for F at the interface in terms of local surface and substrate bulk (bulk concentration at the free surface) concentrations. Such a constitutive expression in general depends on a large number of factors including the physico-chemical properties of the surfactant, equilibrium conditions, and thermodynamic ideality of the interface and bulk phase. In the present study we adopt one classical adsorption isotherms which assume nonionic surfactant, thermodynamically ideal bulk fluid and equilibrium conditions.

The simplest kinetic expression is the linear rate equation:

$$F = \frac{1}{Pe}\frac{1}{\mathcal{K}}\frac{1}{\mathcal{T}}(c - \gamma), \tag{2.12}$$

where $\mathcal{K}=\gamma_0/Lc_0$ is the nondimensional equilibrium ratio between bulk and surface concentrations. Note that $\mathcal{K}$ measures the degree of solubility: for decreasing $\mathcal{K}$, the surfactant becomes more soluble in the substrate; while for large $\mathcal{K}$, the surfactant adsorbs preferentially on the free surface. In (2.12), $\mathcal{T}$ is the interfacial transport rate number. For small $\mathcal{T}$, the kinetics is the so-called diffusion-controlled adsorption. In this limit surfactant transport by diffusion is slow and adsorption can be considered to occur instantaneously relative to the diffusion process. In the limit of large $\mathcal{T}$, the surfactant is transported, the surfactant is transported rapidly to the interface by diffusion and the kinetics is known as adsorption-controlled transport. For insoluble surfactant, there is no diffusive flux of surface from the bulk fluid, i.e. $F = 0$, and the surface-concentration equation (2.9) is solved independently of the bulk-concentration equation (2.10). Note that (2.9) and (2.11) are nonlinear equations applied on $z = \eta$. For the present simulation, a linear form of these equations applied on $z = 0$ is

employed.

In the presence of surfactant contamination, the surface tension variation is related to the surfactant surface concentration γ through a surface equation of state. For insoluble surfactant, quantitative experimental data are well documented (e.g. Gaines 1966). Here we assume a linear variation of the surface tension with the surfactant concentration around their equilibrium points, i.e.

$$\sigma - 1 = \frac{\gamma_0}{\sigma_0}\left(\frac{d\sigma}{d\gamma}\right)_{\gamma=1}(\gamma - 1) = \mathcal{M}a(1-\gamma) \tag{2.13}$$

where $\mathcal{M}a \equiv \frac{\gamma_0}{\sigma_0}\left(\frac{d\sigma}{d\gamma}\right)_{\gamma=1}$ is the Marangoni number for the surfactant.

For soluble surfactant, Gibbs' adsorption equation provides an equilibrium relationship between ther surface tension and the surface concentration:

$$\sigma - 1 = RT\frac{\gamma_0}{\sigma_0}\int_1^{\gamma}\frac{\gamma}{c}\frac{dc}{d\gamma}d\gamma \tag{2.14}$$

where σ_0 is the equilibrium surface tension, R the gas constant, and T the absolute temperature. Such an equilibrium relation is usually assumed to be applicable to non-equilibrium kinetics involving kinetics involving instantaneous surfactant adsorption. For a linear (Henry) isotherm, (2.14) becomes

$$\sigma - 1 = RT\frac{\gamma_0}{\sigma_0}(1-\gamma) = \mathcal{M}a(1-\gamma) \tag{2.15}$$

For a nonlinear (Langmuir) isotherm, the equation of state becomes

$$\sigma - 1 = RT\frac{\gamma_0}{\sigma_0}(1+\beta)\ln\left(\frac{1+\beta-\gamma}{\beta}\right) = \mathcal{M}a(1+\beta)\ln\frac{1+\beta-\gamma}{\beta} \tag{2.16}$$

For nonlinear adsorption kinetics (small β), the surface-tension decreases exponentially as surface concentration increases.

Because of the above model we use, higher contamination affects both the Marangoni number and the Weber number. When there is higher level of overall surfactant contamination, equilibrium values of σ and γ are changed according to the equation of

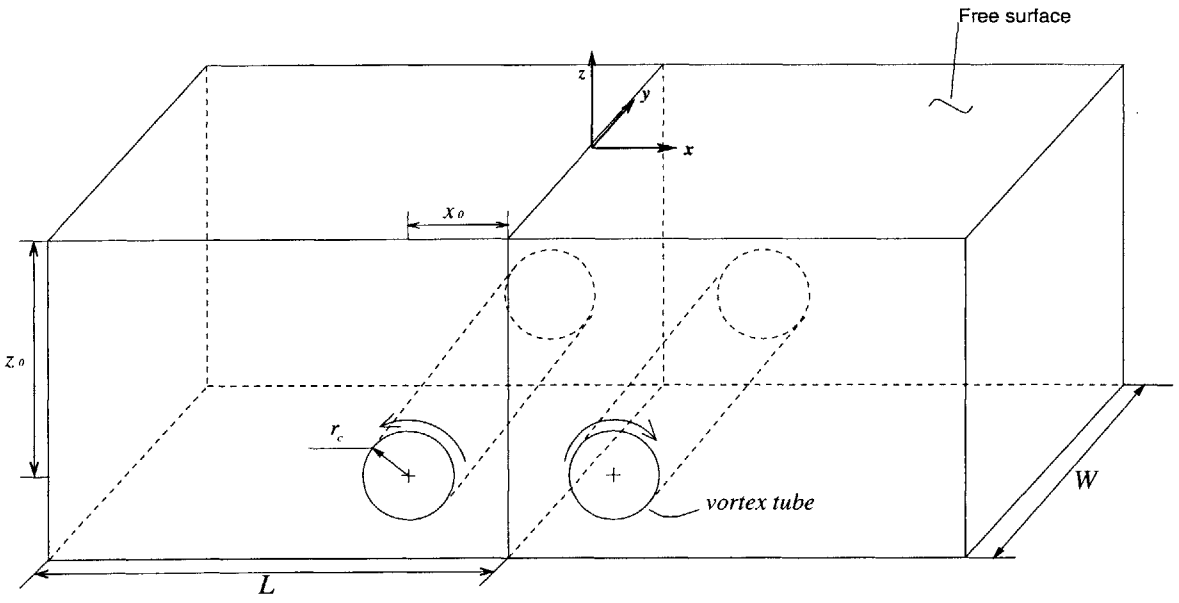

Figure 2-1: The numerical simulation of a vortex pair impinging a free surface. (a) coordinate system and vortex pair location; (b) core position projected to x-y plane; (c) core position projected to x-z plane.

state, thus Weber number alone cannot stay the same. It can be deduced that simulation with the parameters pair ($\mathcal{M}_a$, $\mathcal{W}_e$) should be compared with that of pair ($\alpha\mathcal{M}_a$, $\frac{1+\alpha\mathcal{M}_a}{1+\mathcal{M}_a}\mathcal{W}_e$). For example, pair $(0.5, 15)$ should be compared with $(1, 20)$ if the $\mathcal{M}_a$ number is increased from 0.5 to 1. Of course, this subtle difference is present only for $\mathcal{M}_a \neq 0$ case. For our model, there is surface elasticity which depends on $\mathcal{M}a$ and γ but not on the temporal evolution of the surface elevation. So surface rheology parameters are not function of frequency. In this study, we keep length scale the same and use the same kind of surfactant in all simulations.

2.3 Description of the problem

Three dimensional laminar interactions between a clean or contaminated free surface and a vortical flow underneath are studied. Initially the vortical flow is in the form of two modulated vortex tubes with Gaussian core distribution, and the self-induced velocities cause the deeply submerged vortex tubes to rise up to the free surface. The initial geometric configuration is shown in figure 2-1 (a). We only apply one set of

wavelength and amplitude to the perturbation of the core center. The distribution of ω_y and the core position are specified as follows:

$$(\omega_y)_0 = \omega_c \exp(-[(x - x_{cen})^2 + (z - z_{cen})^2]/r_c^2), \tag{2.17}$$

$$x_{cen} = x_0 + x_{amp}\cos(2\pi y/W), \quad z_{cen} = z_0 + z_{amp}\cos(2\pi y/W), \tag{2.18}$$

where ω_c is the peak vorticity, r_c is the core radius, x_{amp} and z_{amp} are the perturbation amplitudes and W is the wave length of the perturbation and also the length of computational domain along the y axis. The initial core position projected to x-y and x-z plane is shown in figure 2-1 (b), (c). The instability leads to a 45 degree difference in the orientation of the position of the core ω_y relative to the center plane $x = 0$. There are more than one way to implement the initialization of the vorticity field. Any perturbation can be considered a good model if it is capable of revealing the moving away of dimples from the center plane and explaining all the processes involved. In fact, this simple initial condition leads to rather complex vortex structures, all of which have implication on free surface features. As shown in figure 2-2 of the transverse vorticity contours on $y = 0$ plane, there exists negative vorticity (a) in the core region; while further underneath and near the center plane ($x = 0$) there exists certain amount of positive vorticity as shown in (b). Of course, the magnitude of the negative part of the primary tube is much larger than that of the positive part of the primary tube. The positive portion and negative portion are related despite the huge difference in strength. Major portion of the negative vorticity constitutes the primary vortex bundle that stretches along the y axis and there is no positive vorticity that stretch in the y direction more than half wave length. In fact, the negative and positive portions of the primary vortex tube constitute the spanwise component (on $y = 0$) of a small vortex ring near the center plane. This vortex ring is symmetric regarding to $y = 0$ and possesses vorticity component only in the $y = 0$ plane. On $y = -1$ and $y = 1$, the positive portion of ω_y disappears. The spatial and temporal relations between striations and dimples are observed in our simulation. This consistency with experiment shows that the instability and helical vorticity are

adequately represented by the modification of ω_y.

The initial vortex structural topology can be further illustrated by the distribution of ω_x and ω_z on $y = -0.5$, and ω_x on $x = 0$ at the start of simulation shown in figure 2-3. There are vortices connected across the center plane well underneath the free surface because of the instability, and the ω_x is the origin of the cross centerline striations. We propose the new finding that there are vortices connected across the center plane because of the instability which is the origin for the cross centerline surface striations. From figures 2-2 and 2-3, one can see that instability is not triggered for gradual development afterwards. Late stage of instability is presented at the very beginning of the simulation. This perturbation does provide the features of vortex connection moving away from the centerline, which means that the simulation is valid. The problem with this initialization is that we have to justify the selection of the wavelength of the perturbation.

There are two scales that can be used to define the Reynolds number. One is based on vortex strength (U_{cl}) and the other is based on surface tension and bulk viscosity. In our case, the first scale is used because the flow is vortex driven instead of surfactant driven. We choose the velocity at the center of two vortices $U_{cl} = \frac{2\Gamma}{\pi d}$ as the velocity scale and half the vortex pair's span $L = d/2$ as the length scale. Based on these scales and other surfactant properties, the nondimensional parameters are defined in the following,

$$\mathcal{R}_e = \frac{\Gamma}{\pi\nu}, \qquad Fr = \frac{\Gamma}{\pi\sqrt{g(d/2)^3}}, \qquad W_e = \frac{\rho\Gamma^2}{\pi^2\sigma d/2},$$
$$Pe^s = \frac{\Gamma\pi}{D^s}, \qquad \mathcal{M}_a, \qquad B_o = \frac{(\delta^s+\nu^s)}{\nu L}.$$

The following numerical parameters are used in our computation:

$$\mathcal{R}_e = 200, \qquad \mathcal{F}_r = 0.25, \qquad W_e = 20,$$
$$x_0 = 1.0, \qquad z_0 = -2.0, \qquad x_{amp} = -0.125, \qquad z_{amp} = -0.125,$$
$$\omega_c = 16.0, \qquad r_c = 0.25, \qquad \Gamma = \pi\omega_c r_c^2 = \pi.$$

The above parameters are used in our simulation of clean free surface interaction. When there is insoluble surfactant, in addition to those parameters, we choose $\mathcal{M}_a = 0.4$ (linear isotherm), $B_o = 0.5$ and $Pe^s = 200$. Based on these two cases, we further

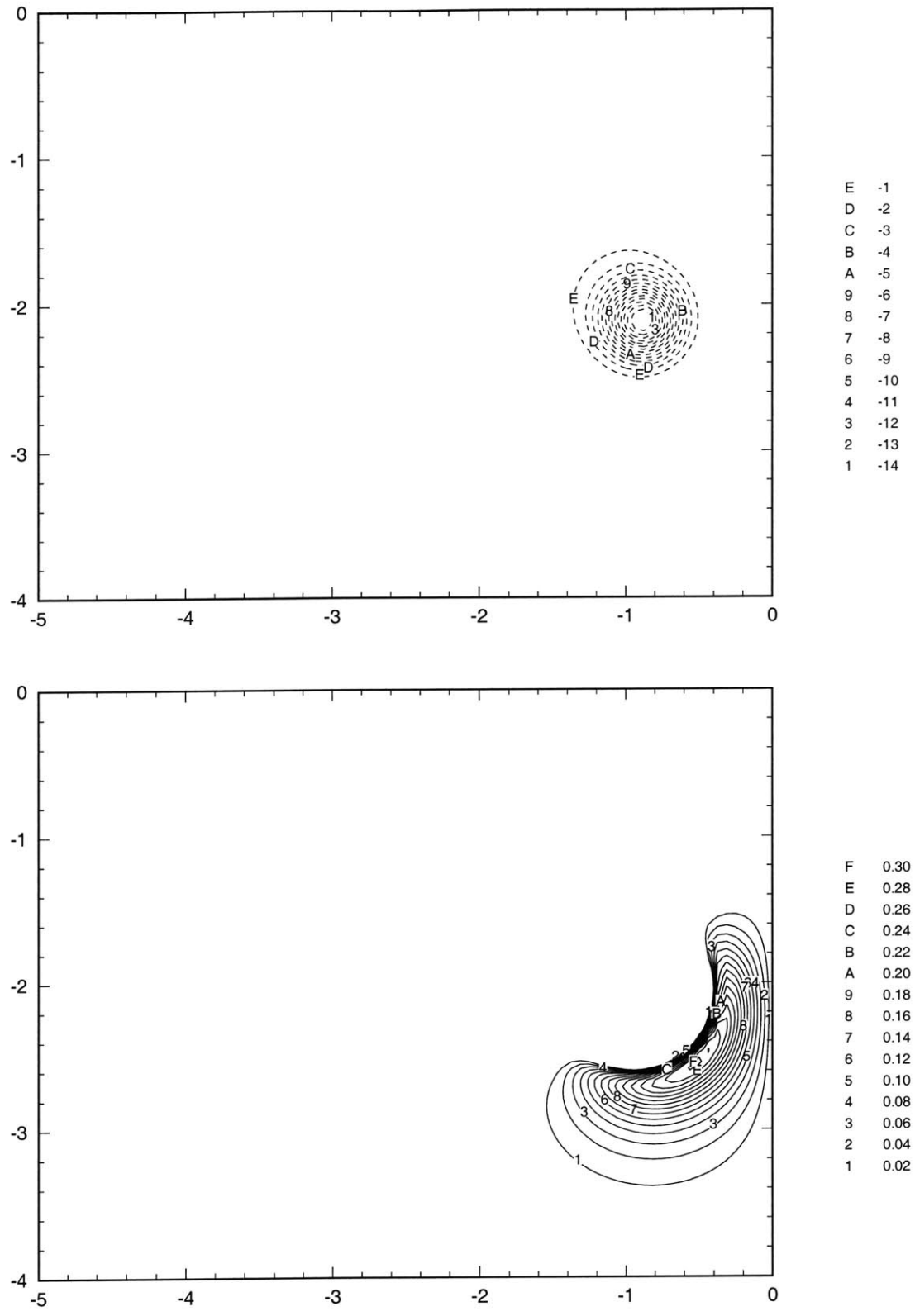

Figure 2-2: Transverse vorticity ω_y distribution on $y = 0$ at $t = 0$: (a) contours of $\omega_y < 0$; (b) contours of $\omega_y > 0$. The horizontal axis is x and the vertical axis is z.

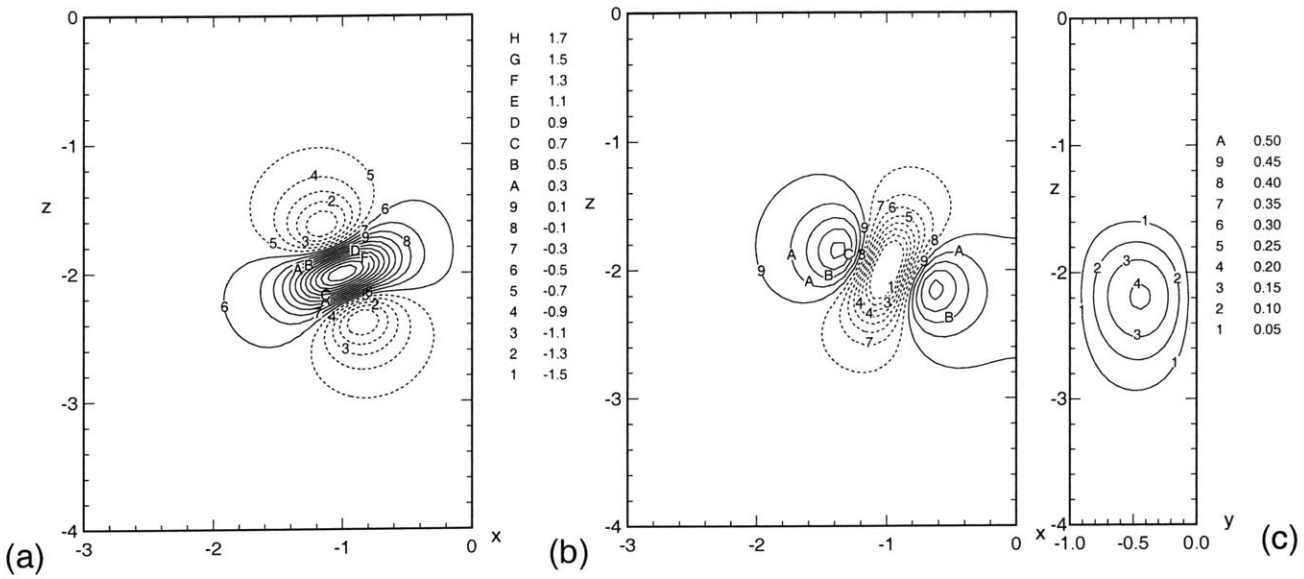

Figure 2-3: Surface normal ω_z and cross-axis vorticity ω_x distribution ($t = 0$): (a) ω_z on $y = -0.5$; (b) ω_x on $y = -0.5$; (c) ω_x on $x = 0$. (a) and (b) use the same contour table between (a) and (b). Dashed lines denote negative contour value.

study the effects of Marangoni number and surface viscosity. For the soluble case, we have three more parameters: R_k, Pe, R_j and Pe of 200 is used. The $\mathcal{M}_a$ number is the most important parameter, while others are of less importance in terms of affecting the whole flow field. The initial surface and bulk concentrations of surfactant are constant.

The continuity and Navier-Stokes equations together with the surfactant-transport equations, subject to the weakly nonlinear free-surface boundary condition on $z = 0$ are solved numerically as an initial-boundary-value problem. The numerical scheme for the free-surface hydrodynamics problem is based on a primitive-variables formulation of the Navier-Stokes equations with spectral and finite-difference discretization in the horizontal and vertical dimensions respectively. Continuity is enforced by solving a pressure Poisson equation in vertical staggered grid system. Third-order Runge-Kutta integration is applied to integrate the Navier-Stokes equations and kinematic free-surface condition. The mass, free surface and energy are all well conserved. With Dirichlet conditions on the free surface and bottom, bulk-concentration transport is

integrated using Runge-kutta scheme as well.

Our objective is to study the effects of surfactant on bulk phase vortical flow and the features related to the free surface. Three dimensional study of the perturbed tube case is performed because the two dimensional simulation is not real, even though it reveals many important features. Even in unbounded flow field, the vortex filament can not remain rectilinear because instability sets in very soon. When there is a free surface, instability still happens and develops slightly faster due to mutual interaction of image tubes above the free surface.

Chapter 3

Numerical Results

The initial stage of vortex tube evolution which happens well underneath the free surface is discussed first in this chapter. In this stage, the primary vortex evolves into two discrete but dynamically related vortex structures. Then the interaction of the near-surface vortices with the clean and contaminated free surface is analyzed. Finally the detailed vortex connection mechanism in the presence of surfactant is presented. For two-dimensional case, the primary vortices first move towards the free surface, and then the interaction of the vortex pair with the free surface causes the two vortex filaments to depart from one another and rebound from the free surface when there is surfactant. The generation of secondary vorticity is the most important character of the two-dimensional surfactant vortical flow. When the flow is three dimensional, the interaction of secondary vorticity with the helical vorticity which is absent in the two dimensional case is crucial in determining the behavior of the vortex connection and free surface features.

3.1 Initial vortex configuration and the formation of helical vorticity

In this section, the early stage of vortex evolution in which the surface contamination does not play a role is studied. The understanding of this stage establishes the basis

for studying evolution at later times since every structure originates from this initial flow configuration. When there is no instability, the flow field is two-dimensional and only one vorticity component $\omega_y(x,z)$ is present. Spatial spanwise perturbation in the core position (2.18) is required to get three dimensional field and maintain the dominance of the spanwise vorticity. If one particular dominant vortical component can be defined as a structure in this case, that is ω_y. So for now, ω_y prescribed in (2.17) is considered to be the primary structure at $t = 0$ as well as afterwards before we switch to vortex line approach. Due to the short-wave instability of vortex filaments, which is triggered here by perturbing the vortex tubes, sheets of helical vorticity are spiraled off. For the time being, we define vorticity components ω_x and ω_z that are not directly related to the primary vortex structure (ω_y) as the helical vorticity or cross-axis vorticity.

When the initial ω_y is available, the stream functions can be obtained by solving the Poisson's equation $\nabla^2\psi_i = \omega_i = (0,\omega_y,0)$, and then velocity components are calculated from the stream function. The resulting velocity field is solenoidal. Note that the resulting vorticity components ω_x and ω_z can not be zero. Because $\frac{\partial\omega_y}{\partial y}$ is non-zero and $\nabla\cdot\vec{\omega} = 0$, it can be deduced that $\frac{\partial\omega_x}{\partial x} + \frac{\partial\omega_z}{\partial z} \neq 0$, therefore there is non-zero distribution of the helical vorticity represented in figure 2-3 by the distributions of ω_x on $y = -0.5$ and ω_z on $y = -0.5$ and $x = 0$. Cut $y = -0.5$ is chosen because on this plane the magnitudes of ω_x and ω_z are largest and helical vorticity show most of their features and the same is true for $y = 0.5$ plane. Because of symmetry only the region of $x < 0$ are plotted and there are no helical vorticity components on $y = -1, 0$ and 1 planes. On $x = 0$, only ω_x can be non-zero.

Here the contours of vorticity components are presented first, later on isosurface plots will be presented to complete the description of the vorticity field. The cross-axis vorticity (ω_x) is almost fully developed at $t = 0$ in magnitude. This is clear when compared with the plot at $t = 1$ in the figure 3-1. The vorticity magnitudes at these two instants are of the same order. So not only is the instability triggered but also a certain amount of magnitude is introduced to the helical vorticity at the very beginning of numerical simulation. It can be assumed that the instability introduced

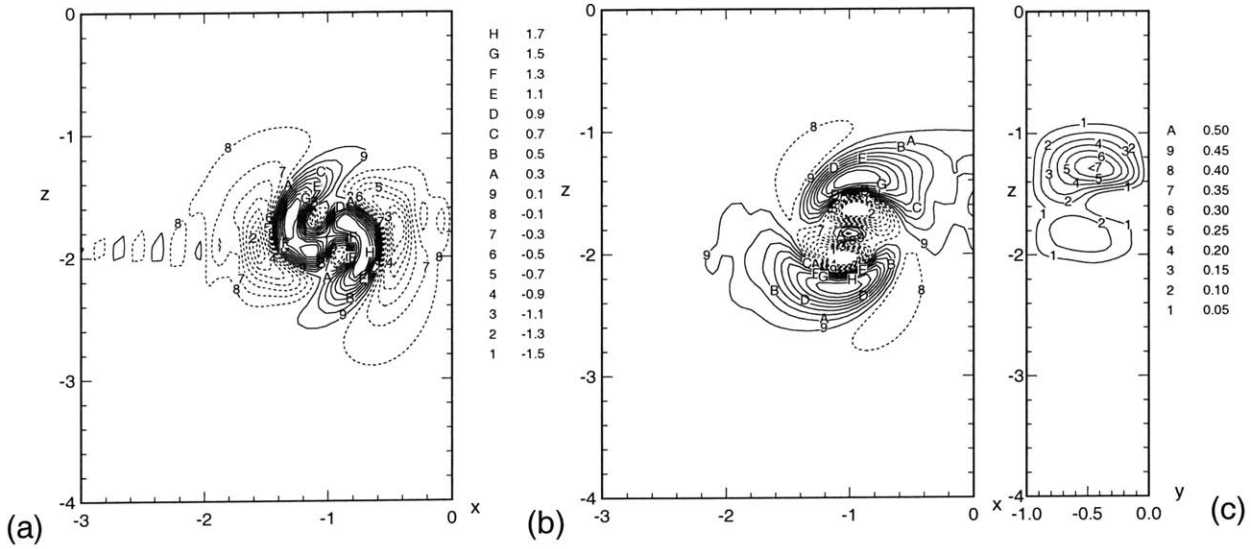

Figure 3-1: Surface normal ω_z and cross-axis vorticity ω_x distribution (t=1): (a) ω_z on $y = -0.5$; (b) ω_x on $y = -0.5$; (c) ω_x on $x = 0$. (a) and (b) use the same contour table between (a) and (b).

is reasonable at all times afterwards and reveals all the instability features. At $t = 0$, the location of maximum connection across $x = 0$ ($z = -2.2$) is slightly below the mean core position $z = -2$.

At $t = 0$, both ω_x and ω_z possess positive and negative components on $y = -0.5$, implying complicated structures involved, which will be discussed later. From the distribution of ω_x, there is already connection over a wide range on $x = 0$ plane. The helical vortices due to the two primary tubes are so strongly related that they have to be regarded as one structure, contrary to previous understandings of the helical vorticity. So for the two individual vortices which form the primary vortex pair, there exists one structure which is induced by the interaction of the two vortex filaments. This kind of helical vortex does not exist for a single vortex tube.

The induced velocity due to the strong primary structure is shown in figure 3-11. The geometrical center of the primary vortex at $y = 0$ is ($x = -0.96$, $z = -2.05$). The induced velocity rotates and twists the helical vorticity distribution which, at a later time $t = 1$, is shown in figure 3-1. The helical vorticity has an effect on the

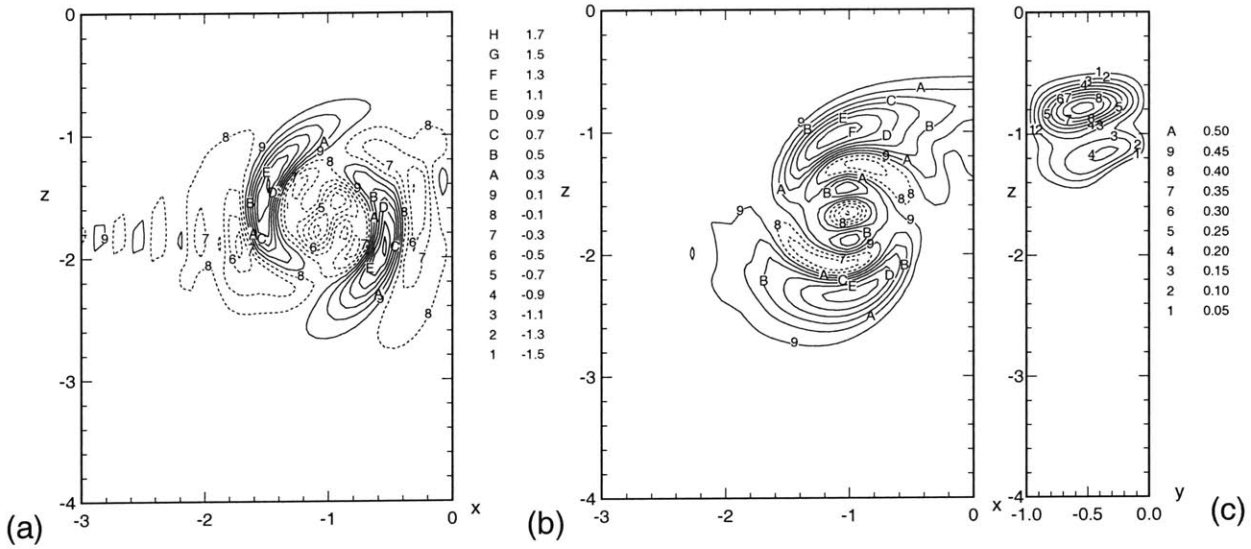

Figure 3-2: Surface normal ω_z and cross-axis vorticity ω_x distribution (t=2): (a) ω_z on $y = -0.5$; (b) ω_x on $y = -0.5$; (c) ω_x on $x = 0$. (a) and (b) use the same contour table between (a) and (b).

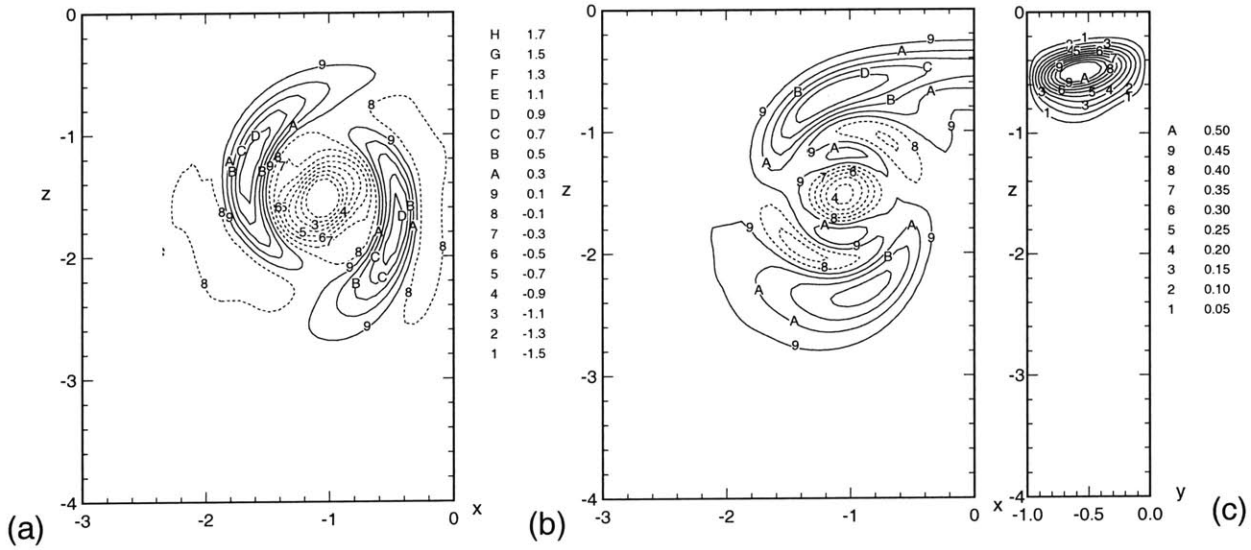

Figure 3-3: Surface normal ω_z and cross-axis vorticity ω_x distribution (t=3): (a) ω_z on $y = -0.5$; (b) ω_x on $y = -0.5$; (c) ω_x on $x = 0$. (a) and (b) use the same contour table between (a) and (b).

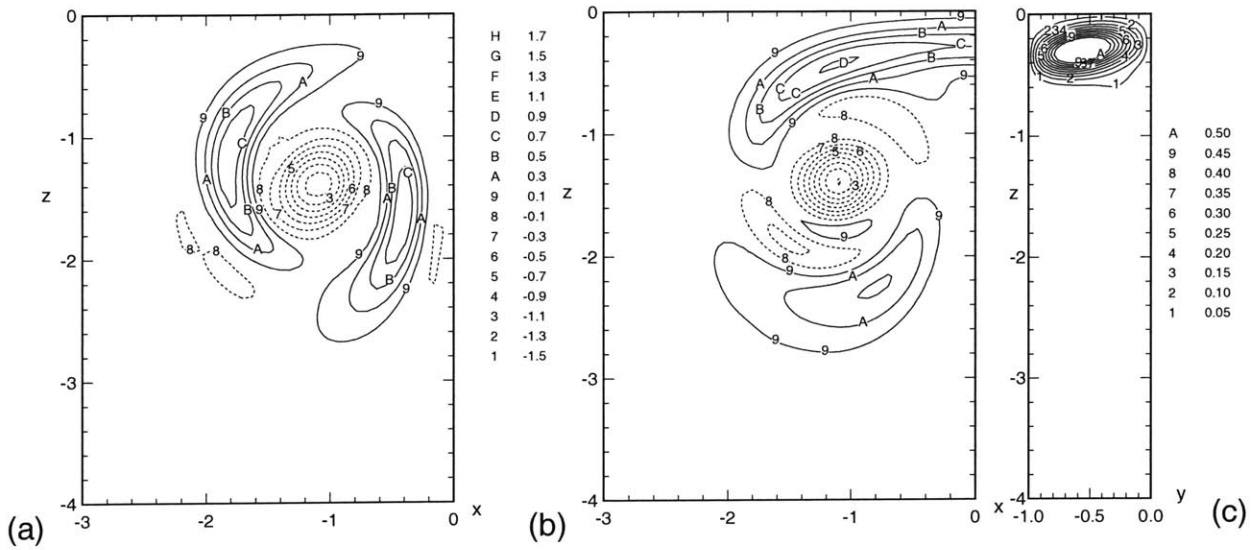

Figure 3-4: Surface normal ω_z and cross-axis vorticity ω_x distribution (t=4): (a) ω_z on $y = -0.5$; (b) ω_x on $y = -0.5$; (c) ω_x on $x = 0$. (a) and (b) use the same contour table between (a) and (b).

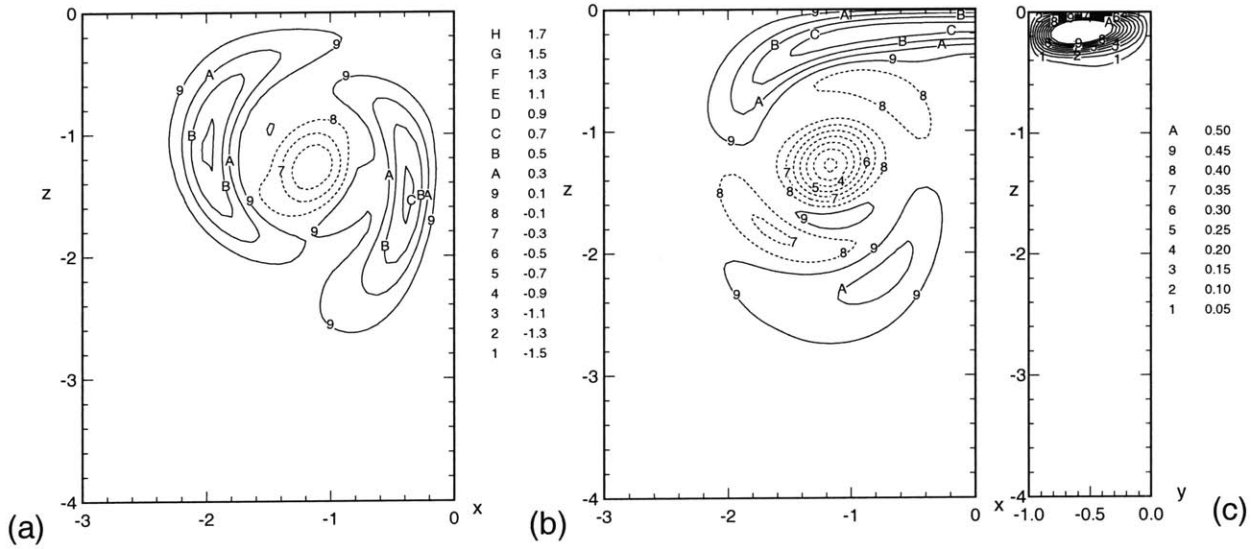

Figure 3-5: Surface normal ω_z and cross-axis vorticity ω_x distribution (t=5): (a) ω_z on $y = -0.5$; (b) ω_x on $y = -0.5$; (c) ω_x on $x = 0$. (a) and (b) use the same contour table between (a) and (b).

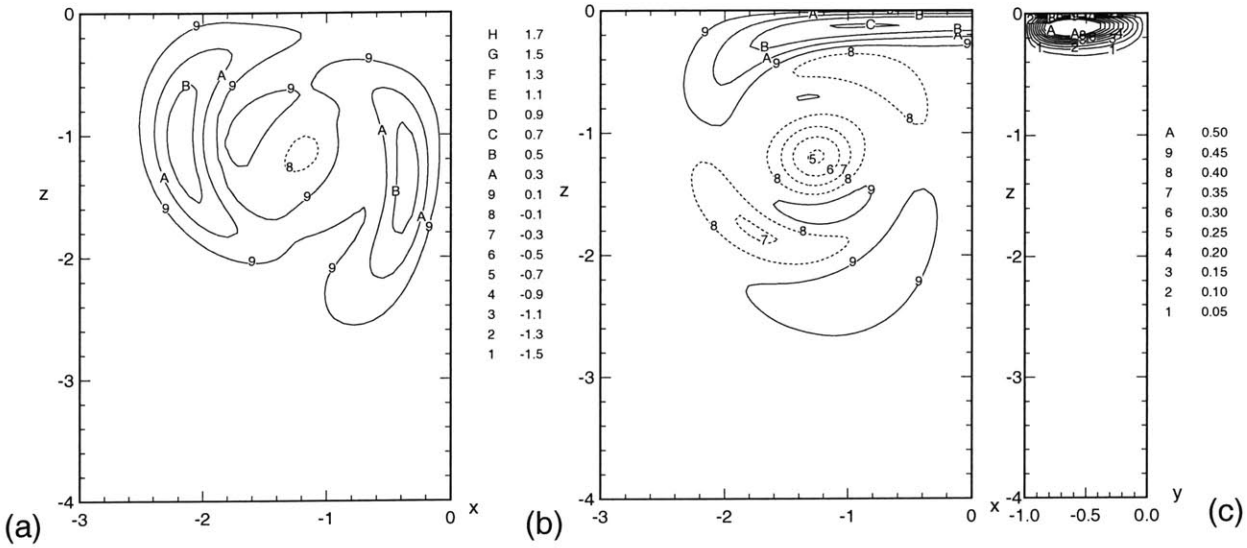

Figure 3-6: Surface normal ω_z and cross-axis vorticity ω_x distribution (t=6): (a) ω_z on $y = -0.5$; (b) ω_x on $y = -0.5$; (c) ω_x on $x = 0$. (a) and (b) use the same contour table between (a) and (b).

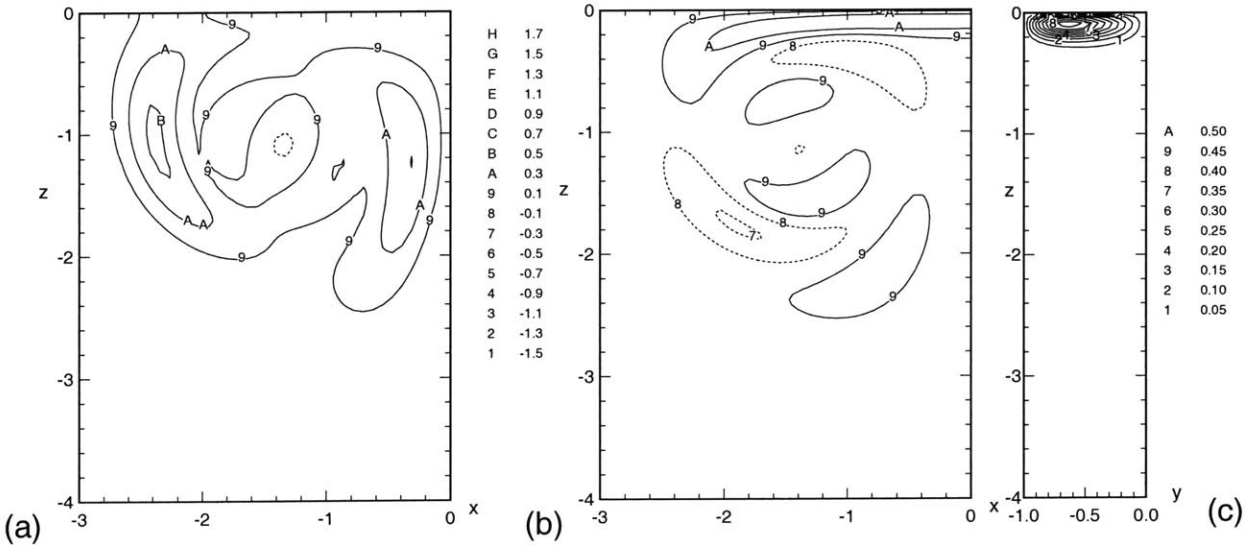

Figure 3-7: Surface normal ω_z and cross-axis vorticity ω_x distribution (t=7): (a) ω_z on $y = -0.5$; (b) ω_x on $y = -0.5$; (c) ω_x on $x = 0$.

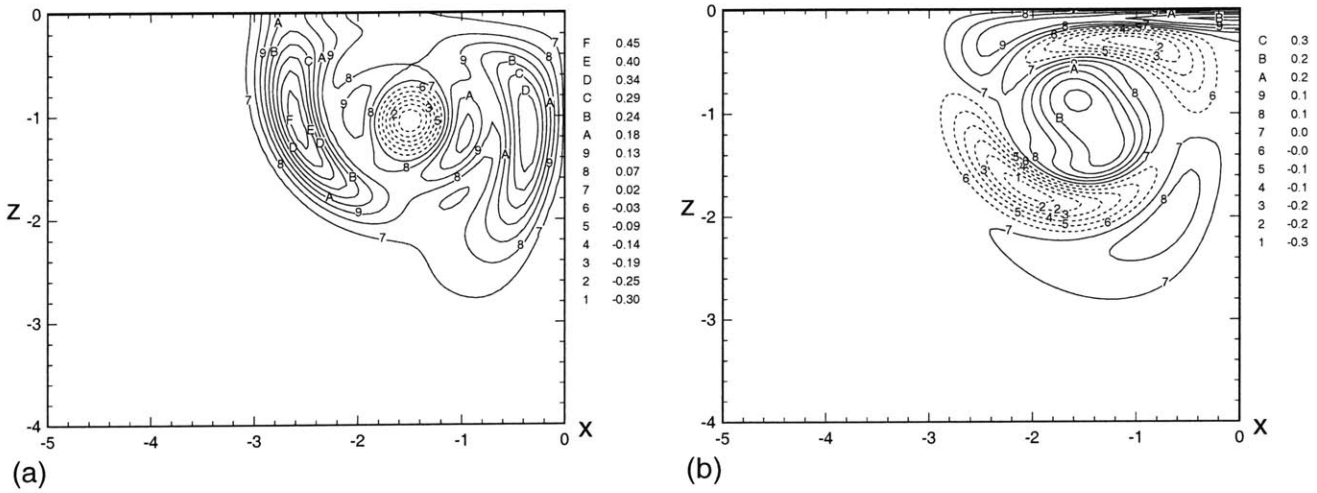

Figure 3-8: Surface normal ω_z and cross-axis vorticity ω_x distribution (t=7): (a) ω_z on $y = -0.5$; (b) ω_x on $y = -0.5$; (c) ω_x on $x = 0$.

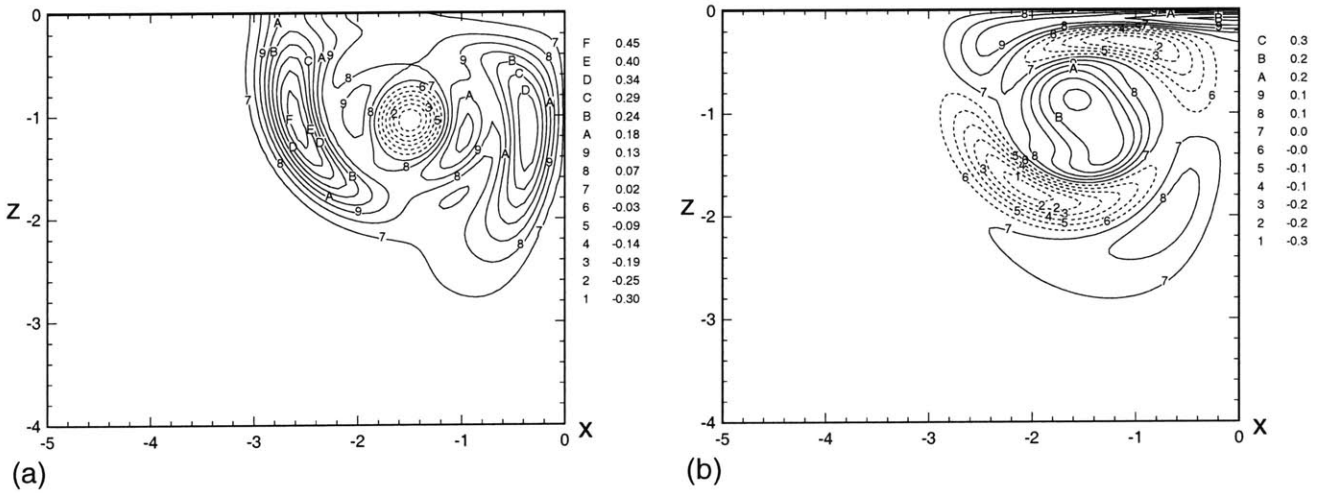

Figure 3-9: Surface normal ω_z and cross-axis vorticity ω_x distribution ($\mathcal{M}a = 0.0$, $t = 8$): (a) ω_z on $y = -0.5$; (b) ω_x on $y = -0.5$.

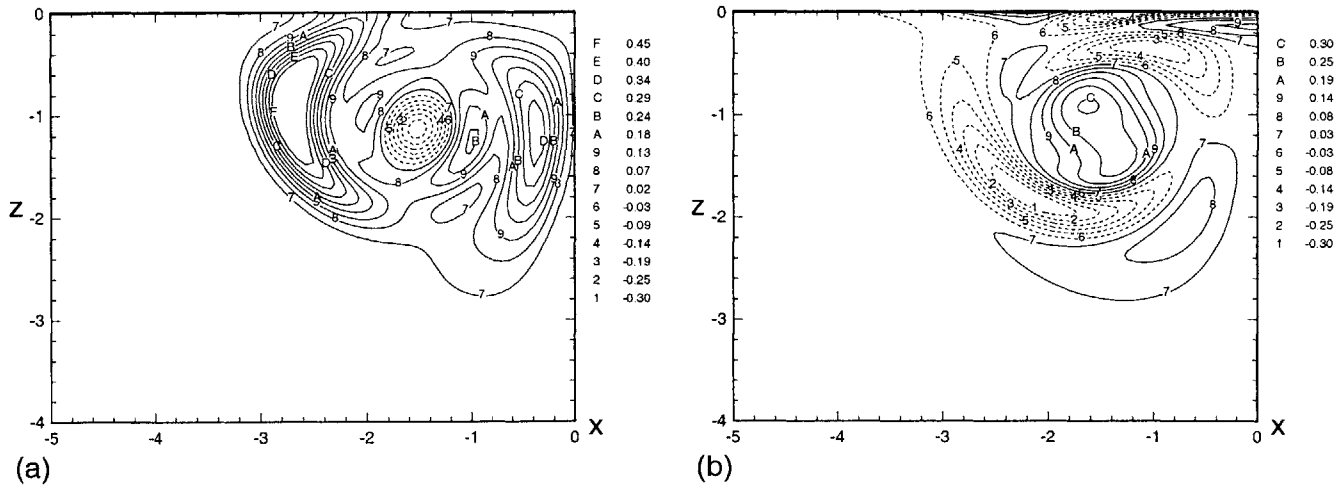

Figure 3-10: Surface normal ω_z and cross-axis vorticity ω_x distribution ($\mathcal{M}a = 0.4$, $t = 8$): (a) ω_z on $y = -0.5$; (b) ω_x on $y = -0.5$.

primary vortex as well. The spanwise curvature of the primary vorticity increases as the magnitude of the helical vorticity increases at the initial stage of evolution. The helical vorticity eventually connects to the free surface and the effects of the helical vorticity on the primary tube before and after connection are different. Before the connection, helical vorticity exerts a greater effect on increasing the curvature of the primary vortex because before connection the vorticity component ω_x that deforms ω_y filaments is the strongest. After the connection, the helical vorticity twists the primary tube in x-y plane and the effects decrease with time.

At this early stage of vortex evolution, the primary vortex is still in the process of ascending. Regarding the ω_x distribution on $x = 0$ plane, there is no vortex stretching for the helical vorticity in the x direction due to the horizontal primary vorticity motion for the time range $t < 8$. When vortex stretching does happen for ω_x because of the increased distance between the two primary vortex tubes, the helical vorticity already starts its interaction with the free surface.

As to the vortex structure representation in three dimensional space, isosurfaces of vorticity component(s) are used. It should be noted that an isosurface is not a material surface even in an inviscid flow. In our simulation, however, isosurface is a

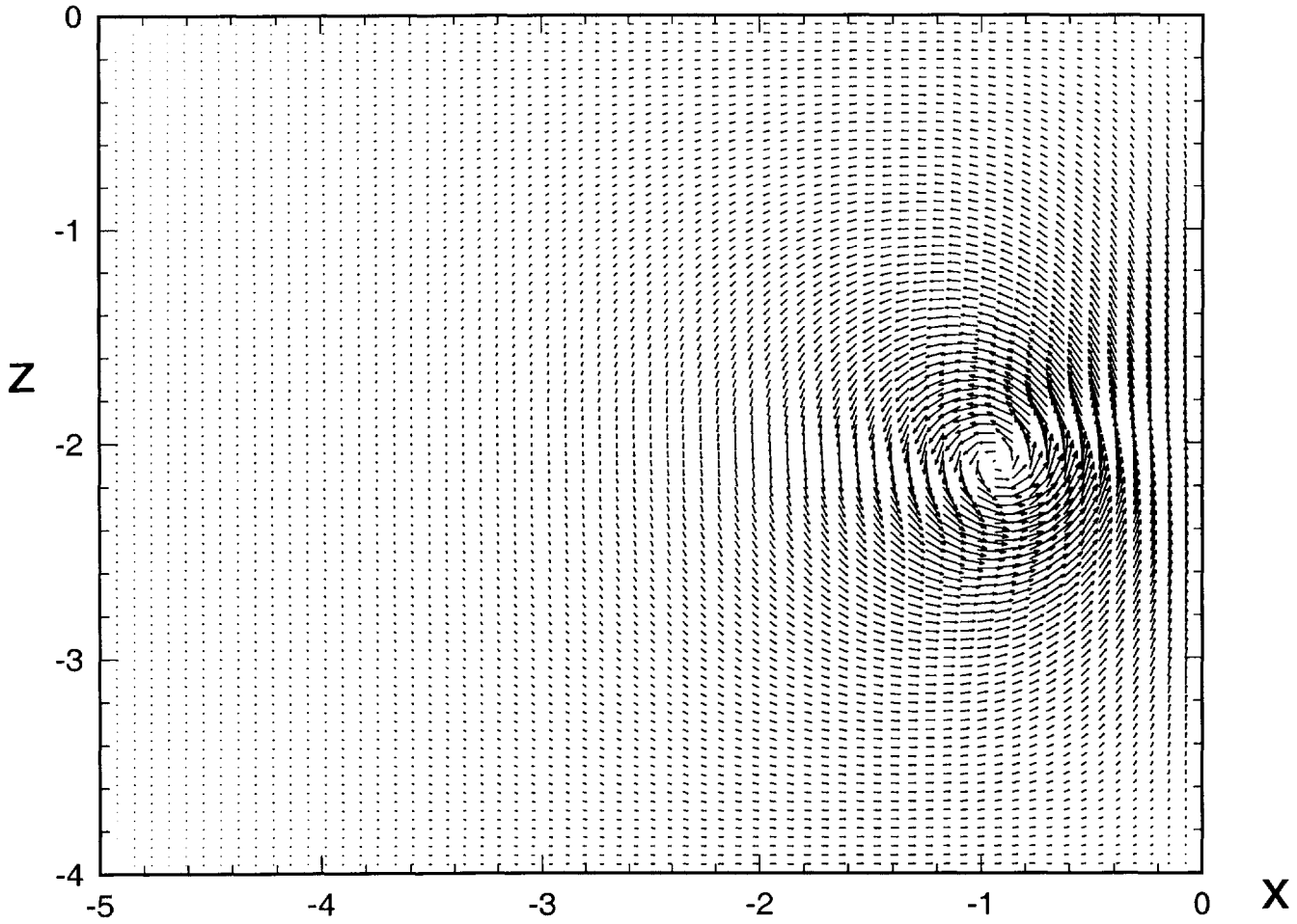

Figure 3-11: Velocity vector (u, w) induced by the primary vortex tube on $y = 0$ at $t = 0$. Because of symmetry, only half of the computational domain $x < 0$ is shown.

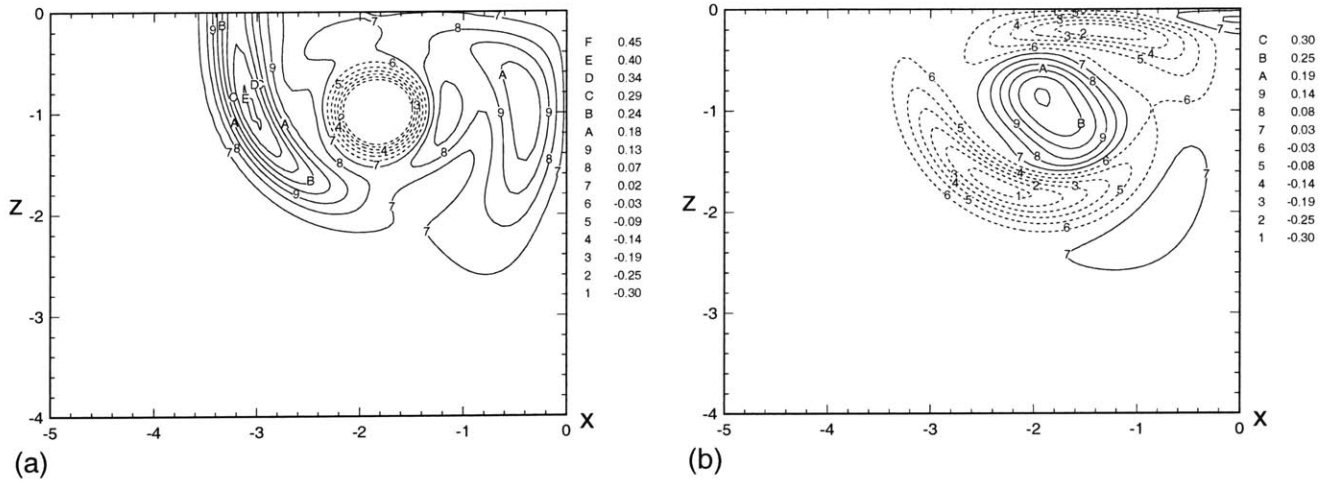

Figure 3-12: Surface normal ω_z and cross-axis vorticity ω_x distribution ($\mathcal{M}a = 0.0$, t=10): (a) ω_z on $y = -0.5$; (b) ω_x on $y = -0.5$.

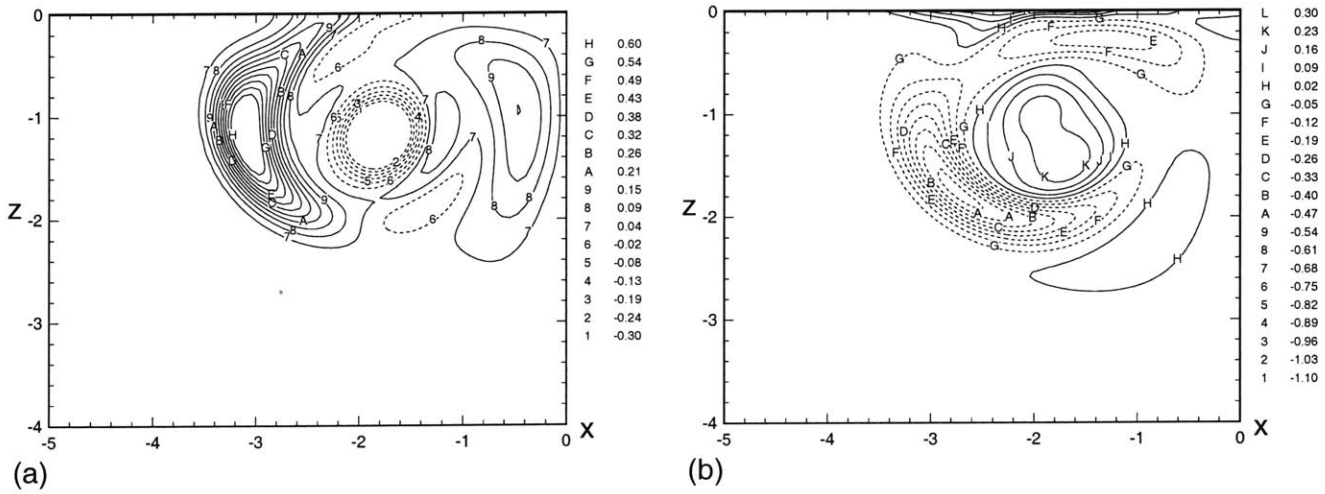

Figure 3-13: Surface normal ω_z and cross-axis vorticity ω_x distribution ($\mathcal{M}a = 0.4$, t=10): (a) ω_z on $y = -0.5$; (b) ω_x on $y = -0.5$.

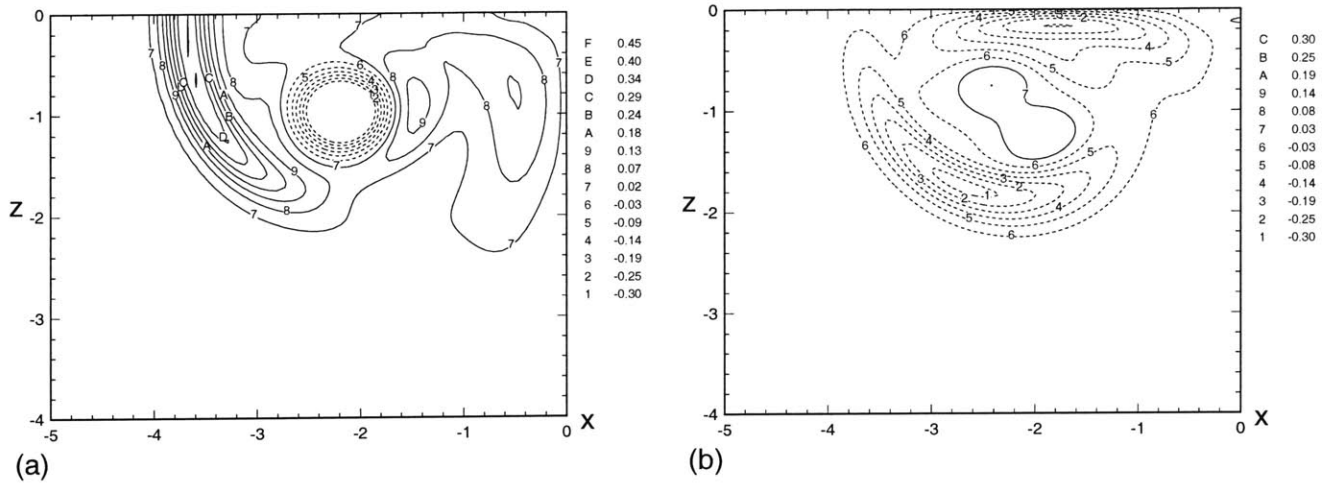

Figure 3-14: Surface normal ω_z and cross-axis vorticity ω_x distribution ($\mathcal{M}a = 0.0$, t=12): (a) ω_z on $y = -0.5$; (b) ω_x on $y = -0.5$.

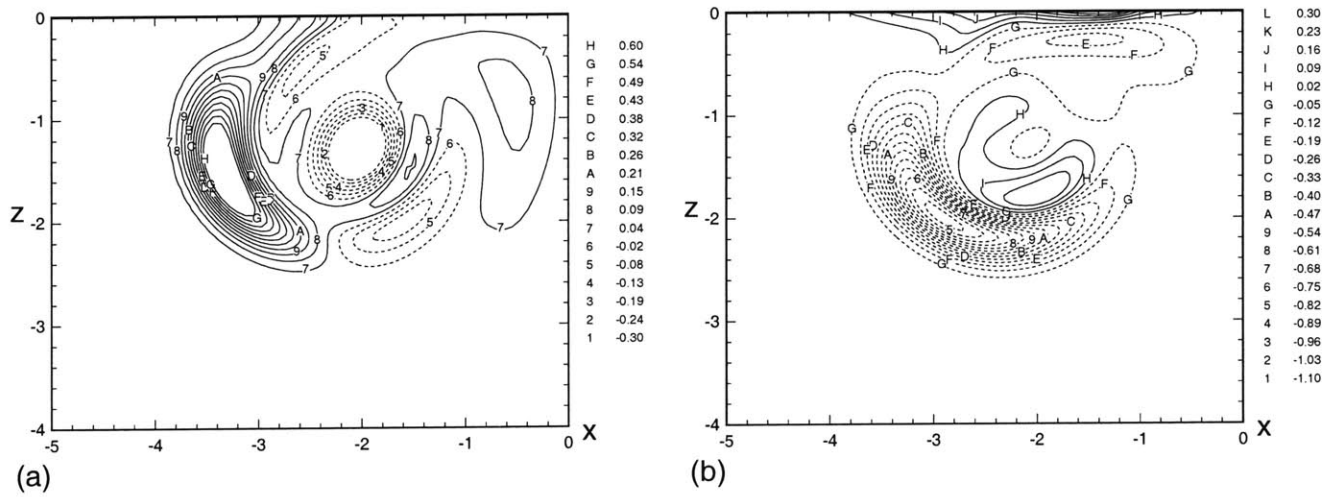

Figure 3-15: Surface normal ω_z and cross-axis vorticity ω_x distribution ($\mathcal{M}a = 0.4$, t=12): (a) ω_z on $y = -0.5$; (b) ω_x on $y = -0.5$.

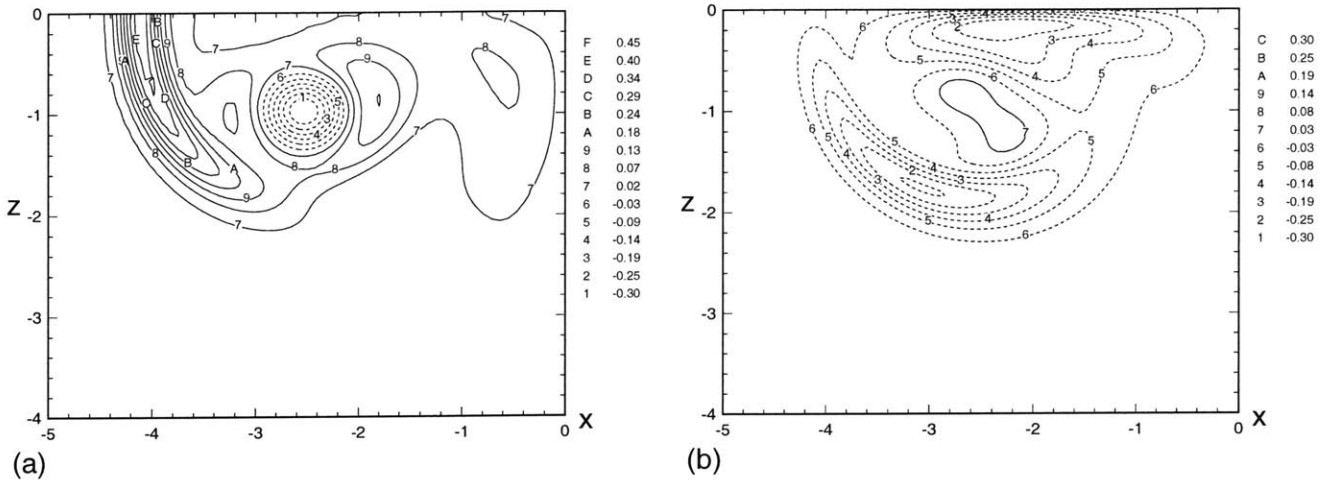

Figure 3-16: Surface normal ω_z and cross-axis vorticity ω_x distribution ($\mathcal{M}a = 0.0$, t=14): (a) ω_z on $y = -0.5$; (b) ω_x on $y = -0.5$.

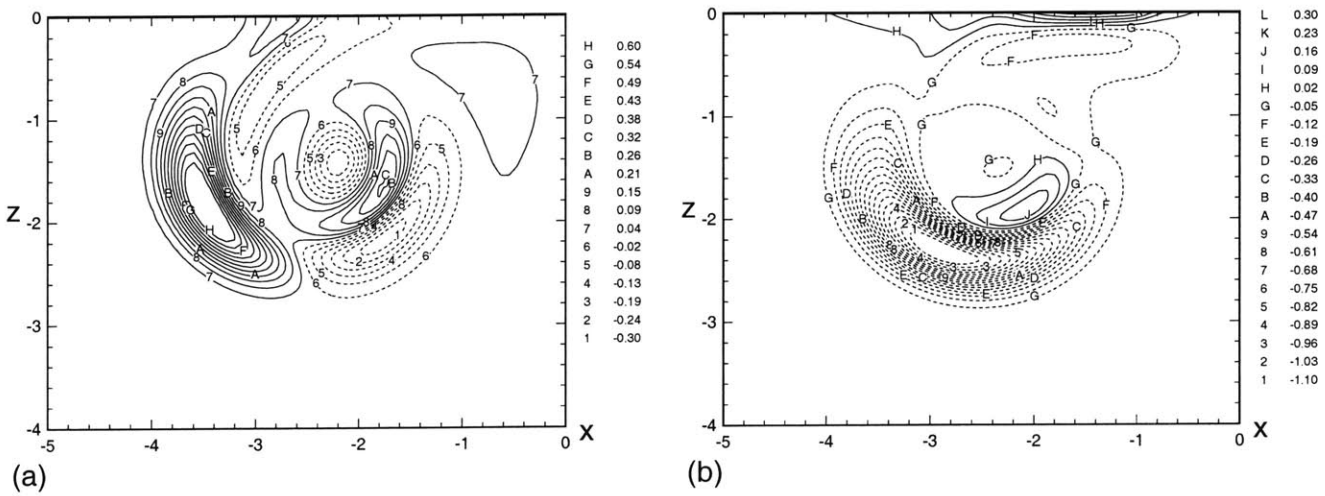

Figure 3-17: Surface normal ω_z and cross-axis vorticity ω_x distribution ($\mathcal{M}a = 0.4$, t=14): (a) ω_z on $y = -0.5$; (b) ω_x on $y = -0.5$.

good representation of the time evolution of a vortical structure because the structures are relatively isolated from one another and isosurface can easily identify them. The shortcoming of this approach is the separation of different vorticity components and somewhat non physical. Another problem is that only the scalar properties are studied, many important properties of the vorticity vector are missed in this approach.

In our three-dimensional plottings, isosurfaces of ω_y=-0.2, ω_y=0.2 and $\sqrt{\omega_x^2 + \omega_z^2} = 0.2$ are colored by green, red and light green, which represent primary, secondary and helical vortices, respectively. Secondary vorticity is generated on the free surface and bear direction opposite to the primary vorticity. The isosurface of ω_{xz} at $t = 1$ is shown in figure 3-20 (a). The connection over $x = 0$ intensifies a little bit at the initial stage of evolution, with circulation of ω_x increasing from 0.126 at $t = 0$ to 0.137 at $t = 1$. Isosurface description is used for now before switching to more accurate vortex filament approach. Isosurface does do an excellent job identifying structures when a new structure is induced. It offers a crude, yet overall picture of the flow.

In our case, detailed analysis shows that the helical vorticity is not defined by ω_{xz} only and vortex filament approach is needed to elucidate structural mechanisms involved. The deficiencies of the vortex line approach is that it is time-consuming to compute and one cannot get a complete flow field without computing a large amount of vortex lines. There is also the problem of extracting major vorticity structures from a complex flow field. These deficiencies do not hinder this analysis because the flow is laminar and the key structures can be manifested by a few vortex lines emanating from connection surfaces $z = 0$ and $x = 0$. The difficulty is identifying structures away from those two plane. One example is the ring structure created by the interaction between secondary vortex and helical vortex. The shape of the helical vorticity is not very clear before $t = 3$ because the structures are squeezed to one another. Because the initial flow field is characterized by two strong tubes, and the position of the helical vorticity coincides with the core of the primary tube, the helical vorticity translates with the primary tube and rotates around it, and unwind to develop itself into a more definite configuration.

The two-dimensional distribution of ω_z and ω_x for $t = 2$, $t = 3$, $t = 4$, $t = 5$,

$t = 6$ are shown in figures 3-2, 3-3, 3-4, 3-5, and 3-6. The helical vorticity continues to evolve and move closer to the free surface with the primary tube. During this period, the area occupied by the helical vorticity becomes larger on $y = -0.5$ and the positive and negative parts of both ω_x and ω_z gradually separate. The induced velocity of the primary tube causes the helical vorticity to spiral off.

3.2 Vortex pair interaction with a clean free surface

3.2.1 Interaction of fully developed helical vorticity with free surface

Clean interaction is considered in this section as a basis for later comparison with contaminated case. Before the helical vorticity isosurface is fully developed, the deformation of the free surface is still very small, so the initial development of the helical vorticity is a subsurface phenomenon, and is influenced little by the free surface. There are two wings located at the outer side of helical vorticity isosurface. This can be clearly seen in the two dimensional contour plot of ω_x in figure 3-6(b) and ω_z in figure 3-6(a) on $y = -0.5$ at $t = 6$. The interaction between the two tubes causes one set of wings to connect across the center plane $x = 0$. Due to the induced velocity, the primary tube continues to move upward. The free surface forms a hump near the center plane and a depression region on the sides. This is a two dimensional phenomenon. The surface elevation η near the center plane is not uniform along the y-axis because the vertical velocity component w induced by the primary vortex is modified periodically in the y direction by the x component of the helical vorticity shown in figure 3-22. Figure 3-19 shows the surface elevation and surface vertical velocity at $t = 3$ and there is correlation between the two. It is evident that the surface elevation is not uniform in the y direction. At $t = 6$, the x and z components of the helical vorticity are shown in 3-6. The ω_z forms the shoulder of the helical vorticity as observed in the isosurface representation.

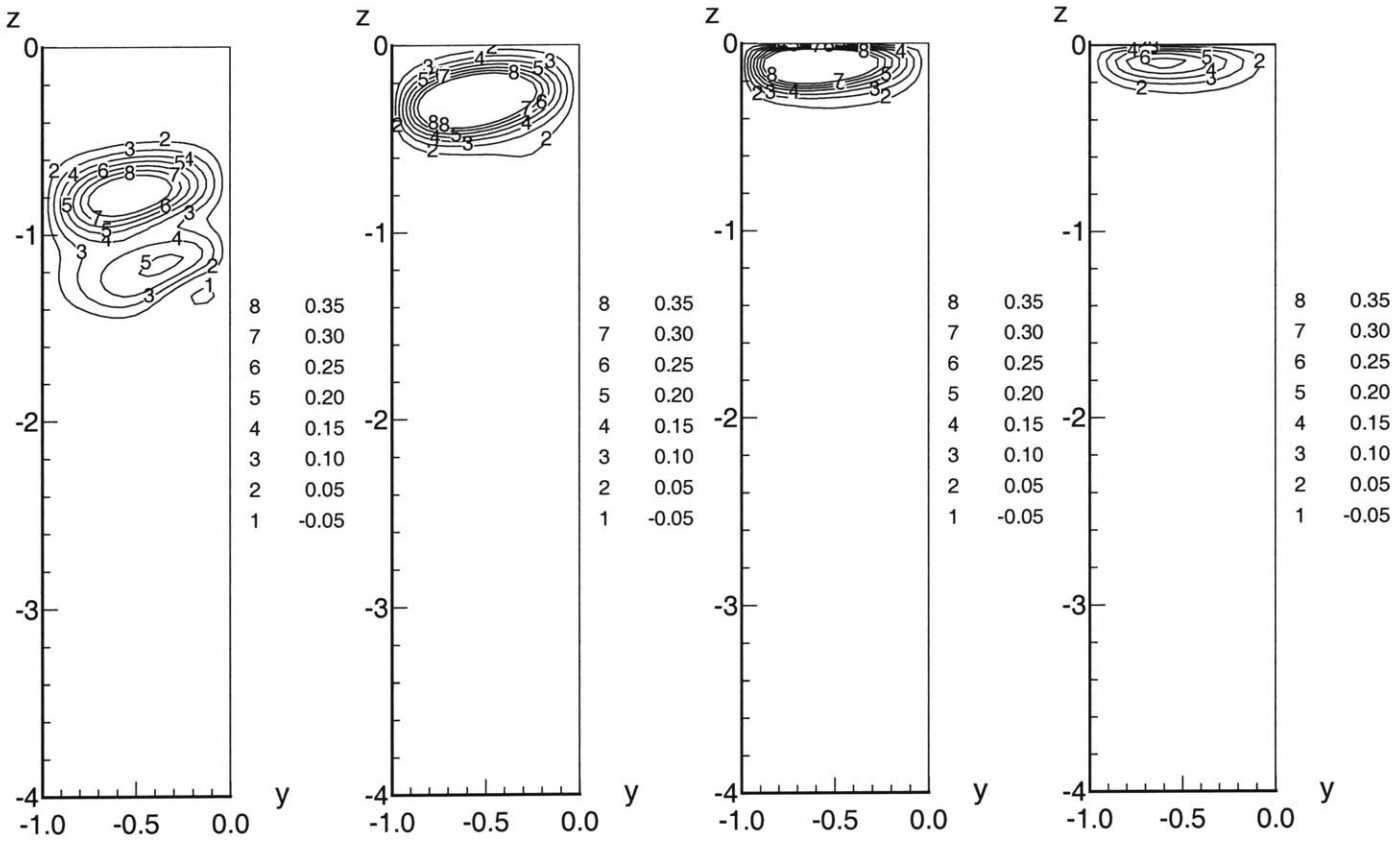

Figure 3-18: Vorticity connection ω_x across $x = 0$: (a) $t = 2$; (b) $t = 4$; (c) $t = 6$; and (d) $t = 8$.

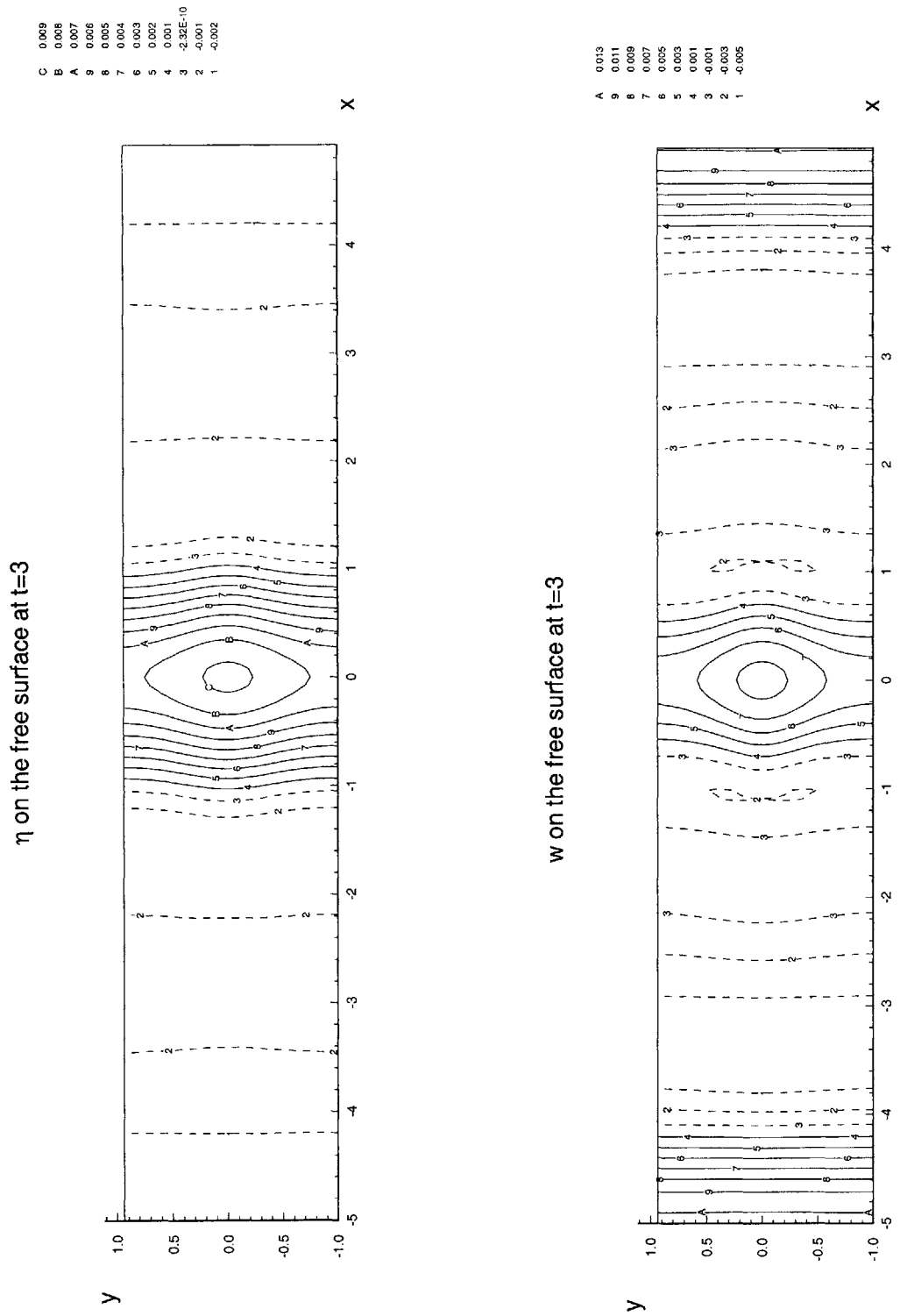

Figure 3-19: Surface elevation η (a) and surface normal velocity w (b) at $t = 3$.

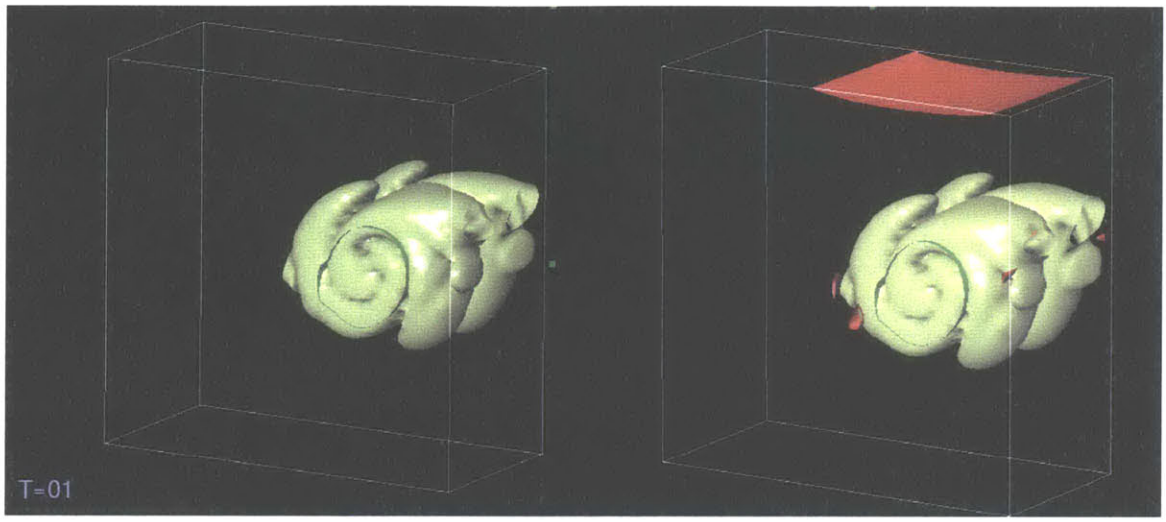

Figure 3-20: Isosurfaces of $\omega_y = -0.2$ (green), $\omega_y = 0.2$ (red) and $\sqrt{\omega_x^2 + \omega_z^2} = 0.2$ (light green) at $t = 1$. Clean $\mathcal{M}$a=0 case is shown on the left (a) and contaminated $\mathcal{M}$a=0.4 case is shown on the right (b).

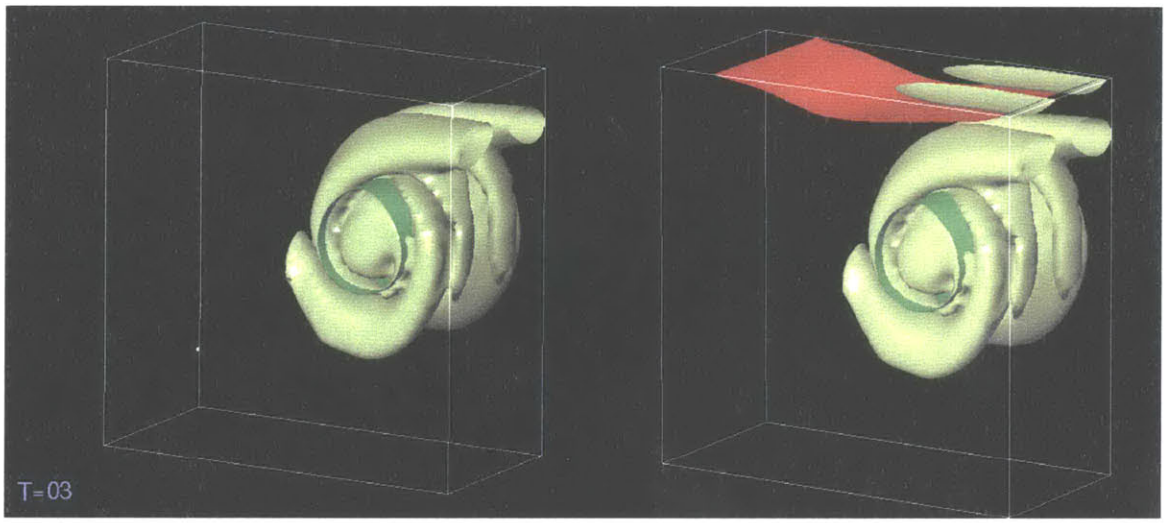

Figure 3-21: Isosurfaces of $\omega_y = -0.2$ (green), $\omega_y = 0.2$ (red) and $\sqrt{\omega_x^2 + \omega_z^2} = 0.2$ (light green) at $t = 3$. Clean $\mathcal{M}$a=0 case is shown on the left (a) and contaminated $\mathcal{M}$a=0.4 case is shown on the right (b).

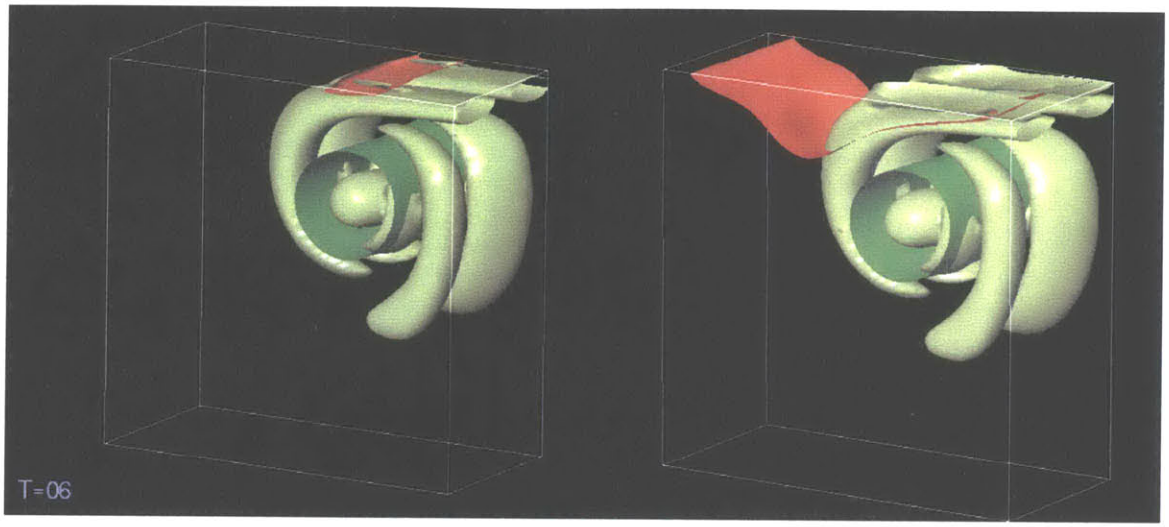

Figure 3-22: Isosurfaces of $\omega_y = -0.2$ (green), $\omega_y = 0.2$ (red) and $\sqrt{\omega_x^2 + \omega_z^2} = 0.2$ (light green) at $t = 6$. Clean $\mathcal{M}$a=0 case is shown on the left (a) and contaminated $\mathcal{M}$a=0.4 case is shown on the right (b).

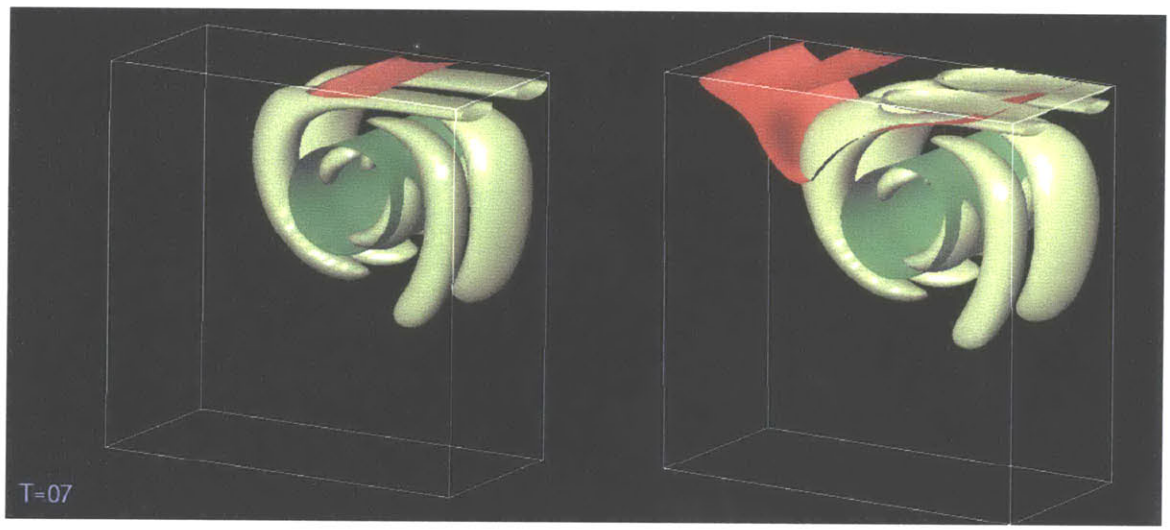

Figure 3-23: Isosurfaces of $\omega_y = -0.2$ (green), $\omega_y = 0.2$ (red) and $\sqrt{\omega_x^2 + \omega_z^2} = 0.2$ (light green) at $t = 7$. Clean Ma=0 case is shown on the left (a) and contaminated Ma=0.4 case is shown on the right (b).

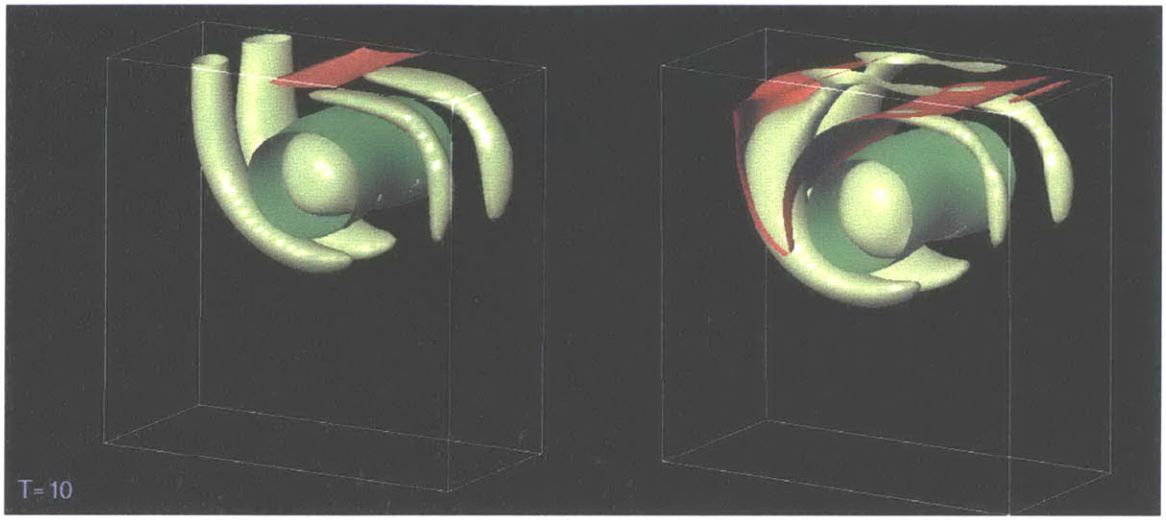

Figure 3-24: Isosurfaces of $\omega_y = -0.2$ (green), $\omega_y = 0.2$ (red) and $\sqrt{\omega_x^2 + \omega_z^2} = 0.2$ (light green) at $t = 10$. Clean Ma=0 case is shown on the left (a) and contaminated Ma=0.4 case is shown on the right(b).

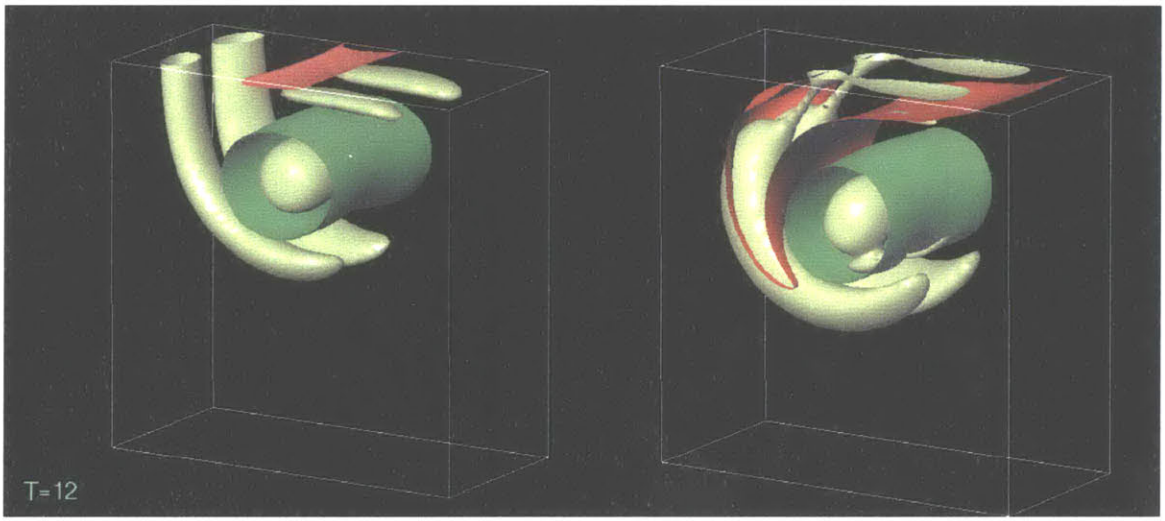

Figure 3-25: Isosurfaces of $\omega_y = -0.2$ (green), $\omega_y = 0.2$ (red) and $\sqrt{\omega_x^2 + \omega_z^2} = 0.2$ (light green) at $t = 12$. Clean Ma=0 case is shown on the left(a) and contaminated Ma=0.4 case is shown on the right(b).

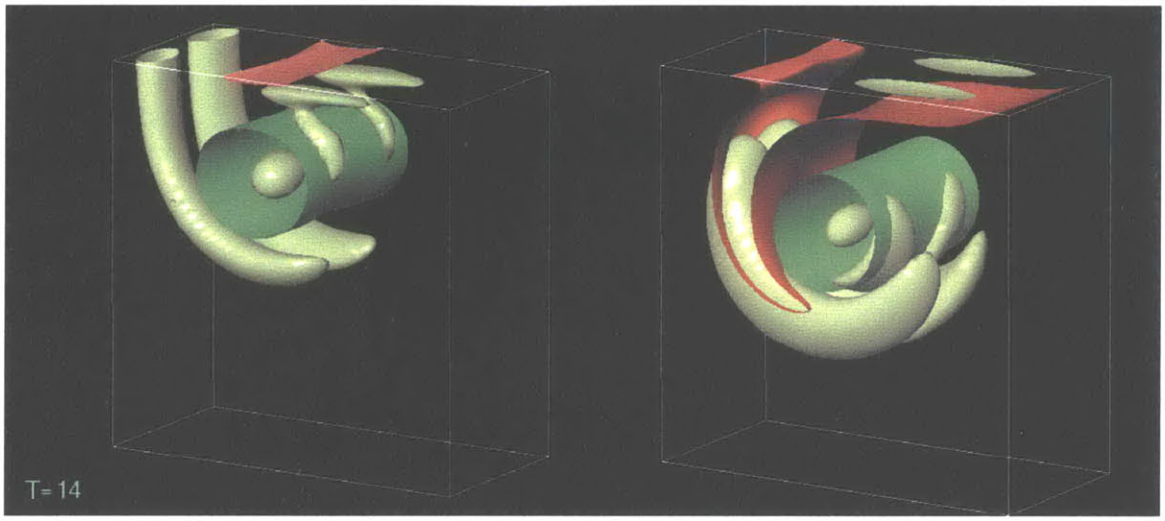

Figure 3-26: Isosurfaces of $\omega_y = -0.2$ (green), $\omega_y = 0.2$ (red) and $\sqrt{\omega_x^2 + \omega_z^2} = 0.2$ (light green) at $t = 14$. Clean Ma=0 case is shown on the left(a) and contaminated Ma=0.4 case is shown on the right(b).

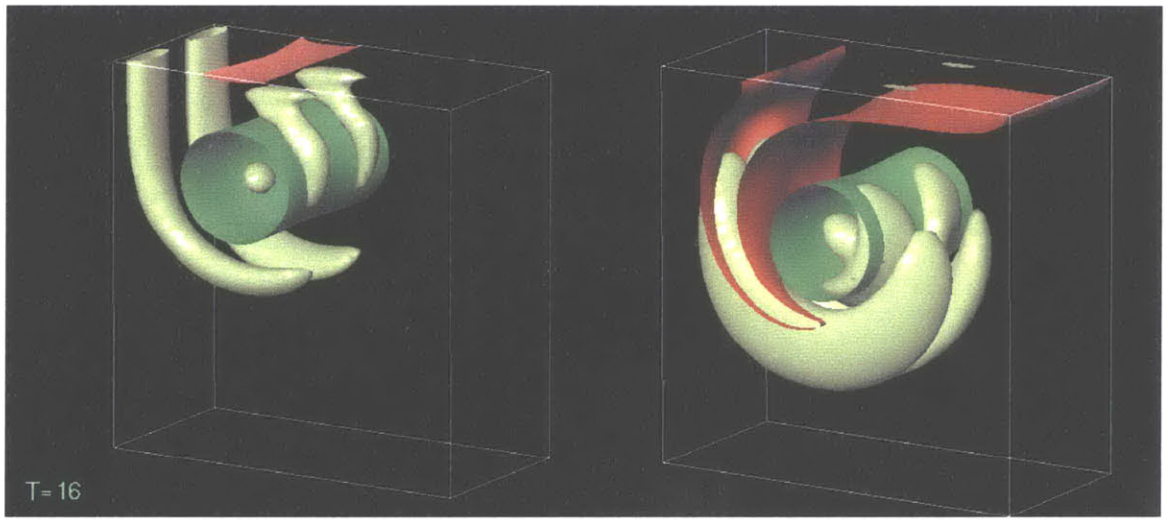

Figure 3-27: Isosurfaces of $\omega_y = -0.2$ (green), $\omega_y = 0.2$ (red) and $\sqrt{\omega_x^2 + \omega_z^2} = 0.2$ (light green) at $t = 16$. Clean Ma=0 case is shown on the left (a) and contaminated Ma=0.4 case is shown on the right(b).

Three dimensional helical vorticity can be shown as isosurface and the appearance of it near the center $x = 0$ can be perceived as vortex sheets. At $t = 6$, the top portion of helical vorticity begins to touch the free surface. It is now a well-formed cam-shaped structure. At this time, dissipation sets in in the interaction region. The large dissipation near the free surface decreases the ω_x dramatically. Cross-axis vorticity ω_x at $t = 2$, 4, 6, and 8 are shown in figure 3-18. The shape of the connection gets narrower in the z direction with time because of the mutual interaction between the helical vortex and its image vortex above the free surface under the free slip boundary condition. In this process, the connection is decreased between $t = 6$ and $t = 8$.

Figures 3-28,3-29,3-30 and 3-31 show the comparison of dissipation ($\frac{1}{2}\ s_{ij}s_{ji}$ on $x = 0$, where s_{ij} is the strain tensor) for clean and contaminated cases at t =2, 4, 5, 6. As the helical vortex continues to move up and interact with the surface, ω_x is squeezed in the surface region. This leads to the die-out of ω_x which is shown in the circulation on $x = 0$ of ω_x vs time given in 3-32. At $t = 4$, the maximum dissipation for clean case is 0.1116, while for contaminated case is 0.1237. At $t = 5$, the maximum dissipation for clean case is 0.1374, while for contaminated case is 0.1566. At $t = 6$, the maximum dissipation for clean case is 0.0772, while for contaminated case is 0.0750. Large dissipation of ω_x occurs in the center plane very near the free surface, especially between $t = 4$ and 6 (ω_x is the only non-zero vorticity component there). Because the x-component of the helical vorticity dissipates out as it rises to the free surface, the shoulder of the helical vorticity, which is mainly composed of ω_z, connects to the free surface. This connection can be explained by Melander & Hussain's cut-and-connect model. The decreased connection over $x = 0$ plane has to be terminated somewhere. It is shown later that the decreased connection is fed into the secondary vorticity and a new structure is created.

The relationship among secondary vorticity, normal connected vortex and surface horizontal velocity is shown in figure 3-33 at $t = 10$. Because of the creation of secondary vorticity, the horizontal displacement of helocal vorticity is significantly altered. At the time the dissipation occurs, connection is also in the process. For

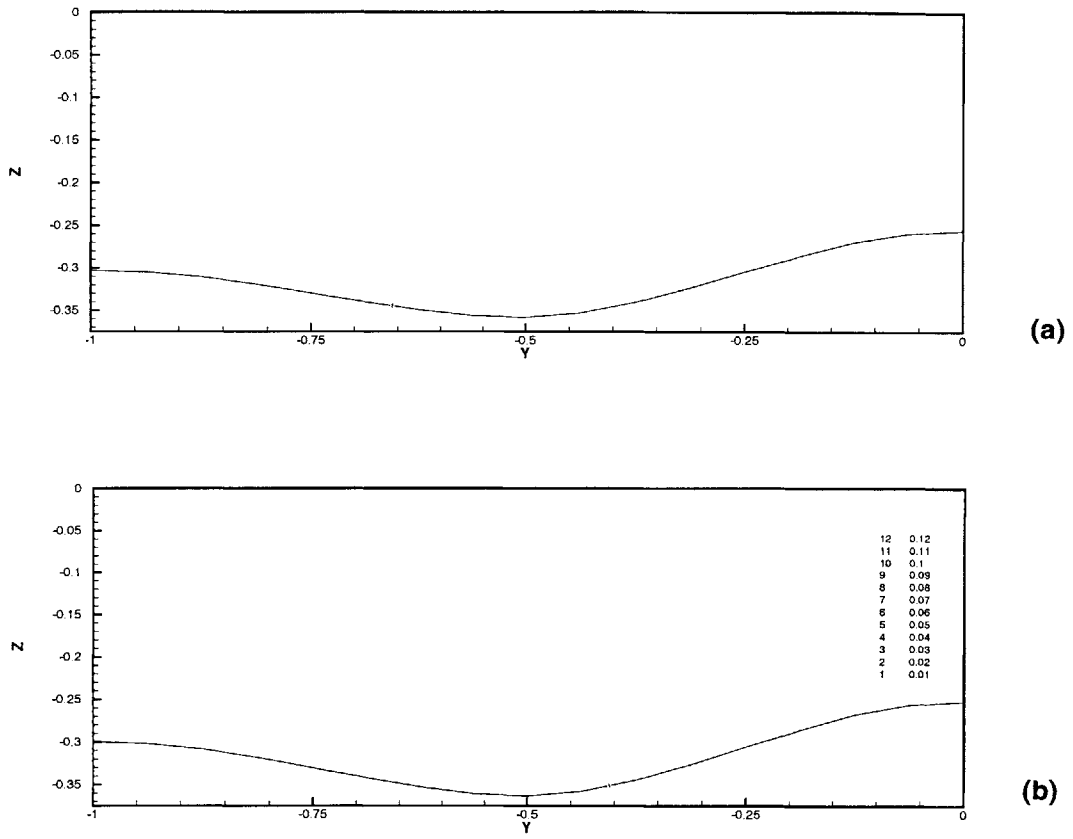

Figure 3-28: Viscous dissipation on $x = 0$ at $t = 2$. (a) Ma=0.0; (b) Ma=0.4. Contour line 1 denotes value 0.01 and the increment is 0.01.

vortex reconnection on the surface, in terms of vortex line approach, the vortex line has to terminate somewhere. And in terms of isosurface of total vorticity, there has to be a cut somewhere on the boundary. In another word, a cut of isosurface is a connection. Detailed discussion of figure 3-33 will be presented in the section on negative feedback mechanism.

From this point on, the major structures are clearly no longer intermixed. From ω_z at $t = 10$ (figure 3-12), the surface vortex connection is right at the shoulder. ω_x and ω_z for $t = 6$ (figure 3-6 is shown, at which time connection is in process. ω_z and ω_x compose two different parts of helical vorticity. The distribution of ω_z on $y = -0.5$ is far from uniform. The nearer to the center of the core, the larger the ω_z. Same plots for $t = 10$ are shown in figure 3-12. At that time the connection is fully completed and the core of ω_z nearly connects to the free surface. Shown in figure

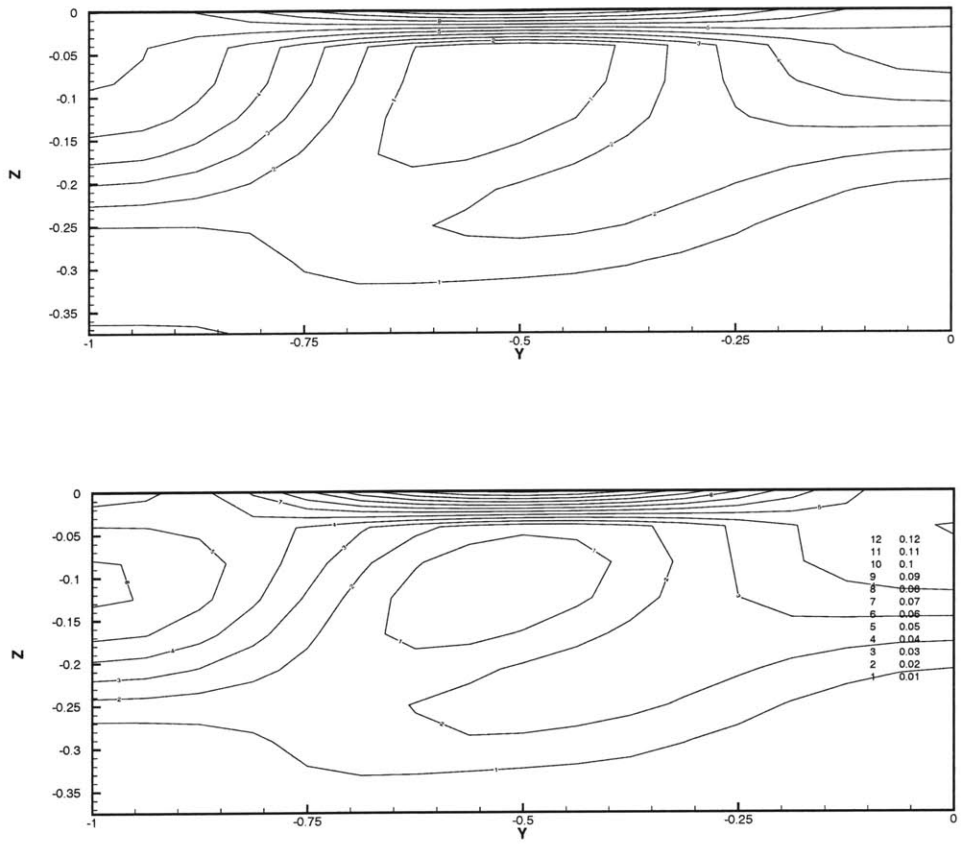

Figure 3-29: Viscous dissipation on $x = 0$ at $t = 4$. (a) Ma=0.0; (b) Ma=0.4. Contour line 1 denotes value 0.01 and the increment is 0.01.

3-32 is the circulation of the ω_z on the free surface. As Γ_x decreases, Γ_z increases. When the Γ_x approaches 0, the Γ_z also reaches its maximum value. The elliptical shape of ω_x tube near free surface is an indication of the interaction between ω_x and its image above the free surface. Before $t = 4$, the Γ_x decreases slowly because the interaction has not begun yet. After $t = 10$, the connected ω_z moves with the primary tube further downstream. The time evolution of the primary tube in $y = 0$ plane is shown in figure 3-34. So after connection, the primary tube moves almost parallel to the free surface for clean free surface, and the connection sustains. For contaminated surface, the primary vortex is rebounded from the free surface and at $t = 18$, the displacement of the core position is about 65% of that of the clean case.

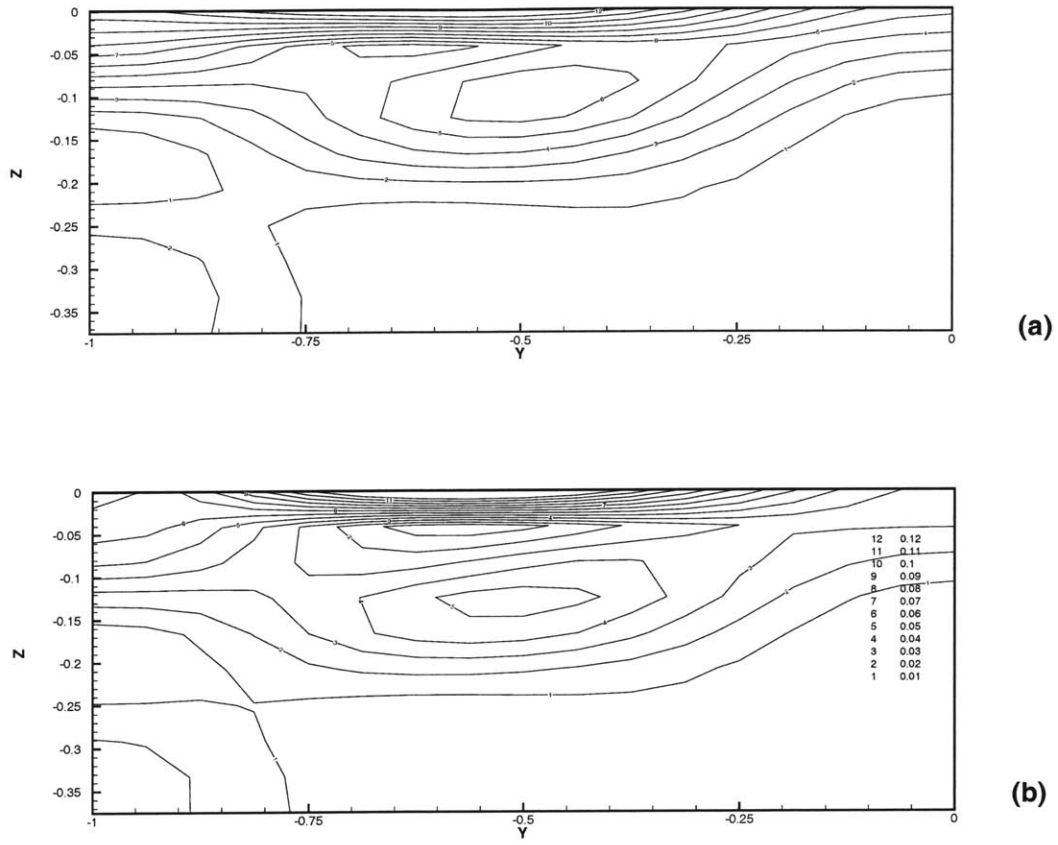

Figure 3-30: Viscous dissipation on $x = 0$ at $t = 5$. (a) Ma=0.0; (b) Ma=0.4. Contour line 1 denotes value 0.01 and the increment is 0.01.

3.2.2 Free Surface Features

The free surface behavior is affected by many factors. Vortex structures such as primary vortex, helical vortex and secondary vortex all play a role in determining the surface signature. In this section, all the surface features observed are described quantitatively.

As the primary vortex moves up to the free surface, the surface near the center forms an upwelling region with surface depression on the sides. Waves propagate away from the center plane ($x = 0$) as soon as the vortex pair starts to move up because of the pressure exerted on the surface due to the ascend of the primary structures. Because waves reflected from the sides would ruin the flow field due to the periodic boundary condition, the surface elevation is valid up to $t = 20$.

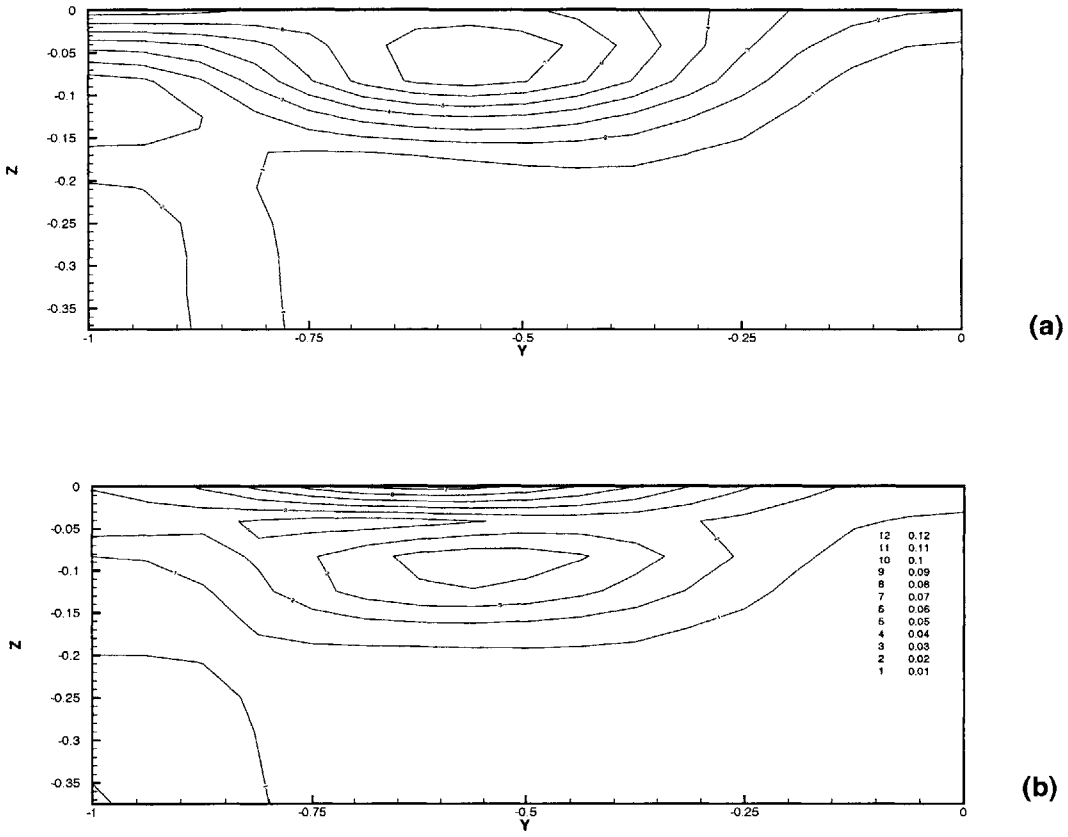

Figure 3-31: Viscous dissipation on $x = 0$ at $t = 6$. (a) Ma=0.0; (b) Ma=0.4. Contour line 1 denotes value 0.01 and the increment is 0.01.

In order to show the various aspects of the surface features as the vortex pair evolves, several quantities derived from the surface elevation are presented. First the mean surface elevation $\overline{\eta_0(t)} = \int_0^W \eta(0, y, t)dy$ at the center plane is shown in figure 3-35 for Ma=0.0 and Ma=0.4. This mean elevation $\overline{\eta_0(t)}$ reaches its peak value at about $t = 5.5$. The cross-axis vorticity ω_x on the surface reaches maximum at the same time (see figure 3-5). After $t = 7$, it is evident that for Ma=0.4, the surface elevation is significantly smaller. Surfactants have an effect of smooth a surface. This means that surface elevation exhibits an oscillating behavior with a time period about 2.

The same quantity at all x locations after connection occurs ($t > 8$) is shown in figure 3-36. The surface signature originated from the primary vortex tube motion is shown by averaging the surface elevation over y. The scale of the center upwelling

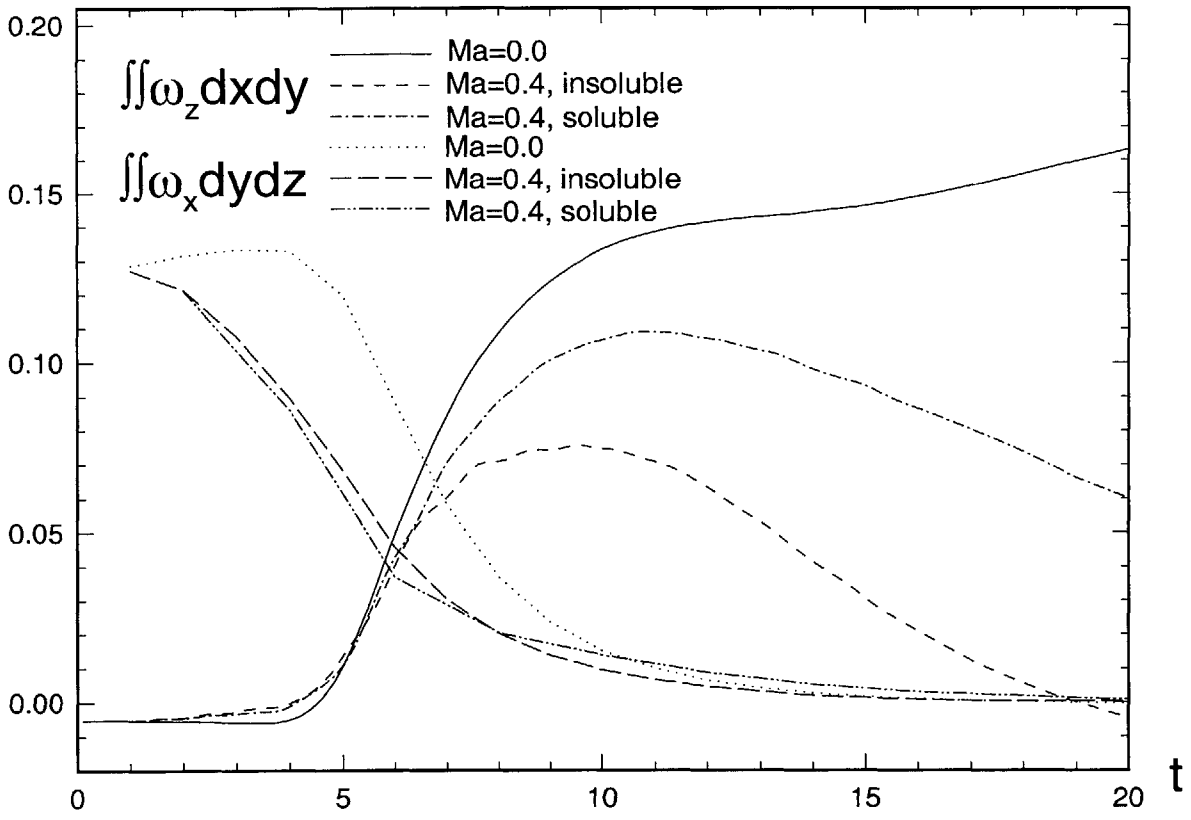

Figure 3-32: Circulations at two cross sections $x = 0$ and $z = 0$ for Ma=0.0, Ma=0.4 (soluble and insoluble surfactant).

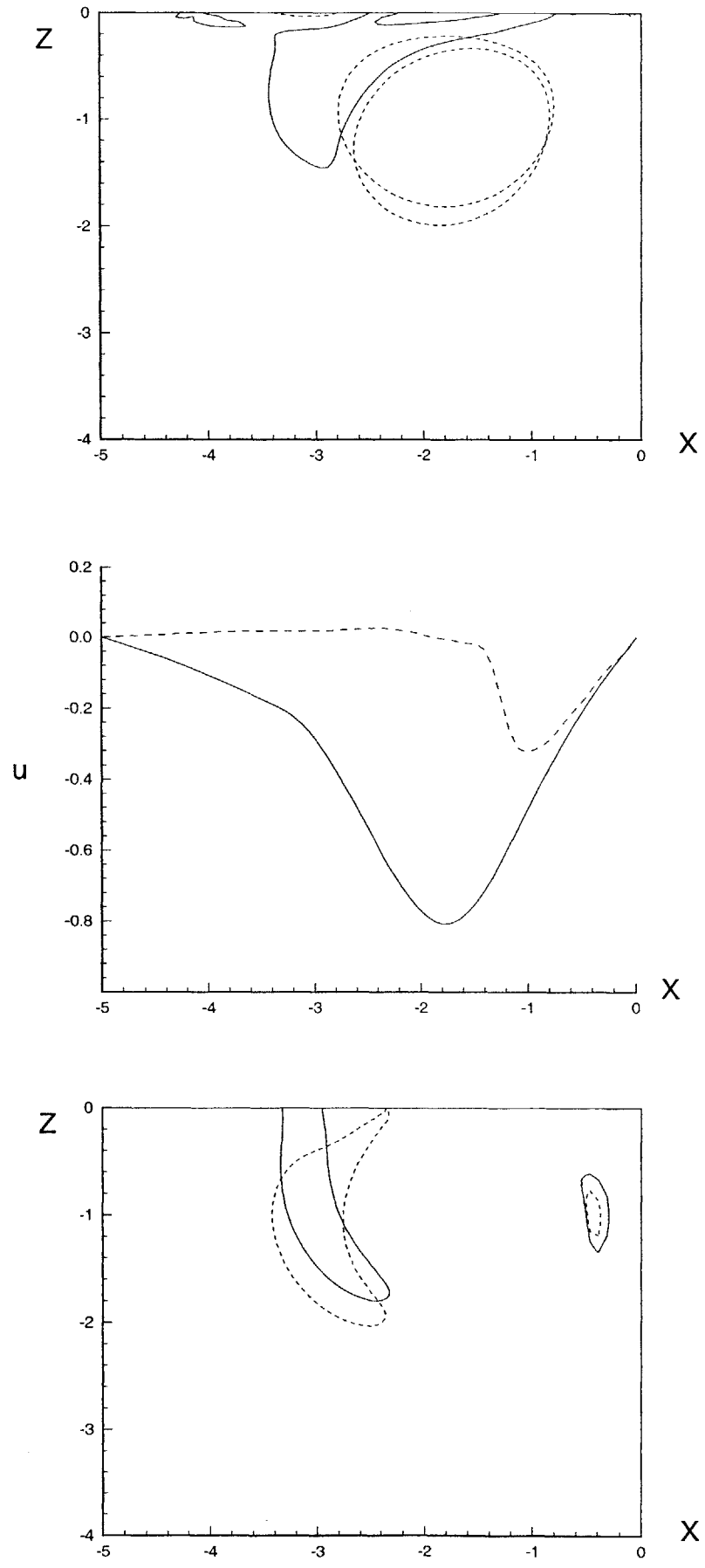

Figure 3-33: Comparison of connection location, secondary vorticity location (a) primary and secondary vorticity; Contours of $\omega_y = 0.4$ and $\omega_y = -0.4$ are shown. (b) surface horizontal velocity; and (c) ω_z. Solid lines are for clean case and dashed lines are for contaminated case.

region is similar to the distance between the two primary tubes. For $Ma = 0.0$, significant surface fluctuation can be observed throughout the whole surface region. But for contaminated case, this happens only in the central less contaminated region. Away from the center plane the effect of surfactant on surface elevation suppression is more significant because of increased surfactant concentration away from the center. For $Ma = 0.0$, the suppression on the sides moves gradually away from the center plane. For contaminated case, the suppression on the sides is not as concentrated and therefore does not appear to move outboard as the clean case.

Because surface striation is a three dimensional feature, it can be manifested by subtracting the representation of two dimensional feature $\overline{\eta(x,t)} = \int_0^W \eta(x,y,t)dy$ from the total surface elevation η. The distribution of $\eta(x,y,t) - \overline{\eta(x,t)}$ shows similar surface contour profile compared to that of ω_x and therefore striation is definitely caused by the ω_x near the surface. The intensification of striation can be seen from figure 3-37 and figure 3-38. Both the clean and contaminated cases are shown and it is evident that surfactant has a minimal effects on the surface striation.

From the plot of η with mean η (over y) subtracted in figures 3-37 and 3-38, it can be seen that at $t = 6$ there are depressions located in the region $(-2.8, -1.4) \times (-0.4, 0.4)$ on the free surface. Because η average is already negative there, the dotted lines denotes deeper depressions. One ω_z connection corresponds to one dimple. The effect of three dimensionality can be seen from the surface elevation with the mean η subtracted.

Note that the depressions are not where the whirls (vortex in the z direction) are on the free surface. There is a 90 degrees phase difference in the distribution of normal vorticity compared with that of surface depression. The maximum depression of the dimple is located on the line $y = 0$ and the maximum connection on the surface is located on $y = -0.5$ or $y = 0.5$. Figure 3-42 shows this feature for $t = 8$. This fact can be seen from the positions of the surface depressions. The maximum velocity on the free surface happens on $y = -1, 0, 1$, so the surface pressure is smallest at those locations, which leads to deepest surface depression. Even there exists this phase difference, surface features are closely related to the vortical structures.

In the connection process, we can regard the primary vortex (active vortex) as the driving vortex and the helical (passive) vortex as the vortex been driven. Due to the strong driving vortex, the helical vortex which is above the primary tube interacts with the free surface completely, while the primary tube interacts with the free surface by itself. Dissipation only happens at the outer part of the primary vortex. There is no extra force to push the primary structure further to the surface.

The initial disturbance imposed on the primary vortex tube is a good representation of the vortex pair instability, since surface features such as striations and scars from the simulation were observed in the experiments. The location of the striations is right between the centerline and the primary vortex and we obtained the width of the scar region described in Sarpkaya's paper. The striation becomes weak when there is surfactant and for both cases, there is no striation right at $x = 0$.

3.3 Effects of insoluble and soluble surfactants

When there is insoluble surfactant present, the induced velocity (u, v) on the free surface leads to a non-uniform distribution of γ, which generates shear due to the Marangoni effect. This shear leads to the generation of secondary vorticity downstream of the primary tube. In three dimensional flow, the situation becomes complicated because of the mutual interactions between the three major vortex structures. In addition to the primary and secondary vortices, we have helical vorticity, which is affected by the secondary vortex in a complex way, both directly and indirectly.

Generation of secondary vorticity

At the initial stage of vortex evolution, the primary flow dominates the surface horizontal velocity and surfactant gradient starts to build up rapidly. In three dimensional case, the helical vorticity generates secondary vorticity which has components in x direction, The mechanism of this secondary vorticity is the same as that of the primary secondary vorticity. The origin of this secondary vorticity is the ω_x component of the helical vorticity. This ω_x secondary vorticity is much weaker than the major

secondary vorticity.

Interaction of the helical vorticity with the secondary vorticity

Because the flow is viscous, vortex lines are not material lines and we need to interpret mechanisms by vortex line evolution with caution. However since in our simulation the vorticity is strong and the vortex line structures are isolated, we are able to present the vortex evolution in terms of vortex lines. Whenever there is no change in vortex configuration, we can rely on vortex lines to describe structural evolution. However, for laminar flow, it is still possible to build a connection between the two vortex configurations before and after vortex connection. For the interaction near the surface and the reconnection underneath the free surface, vortex line approach is not applicable, while at other locations where no vortex reconnection occurs, we can still treat the vortex line at a given time as quasi-material line.

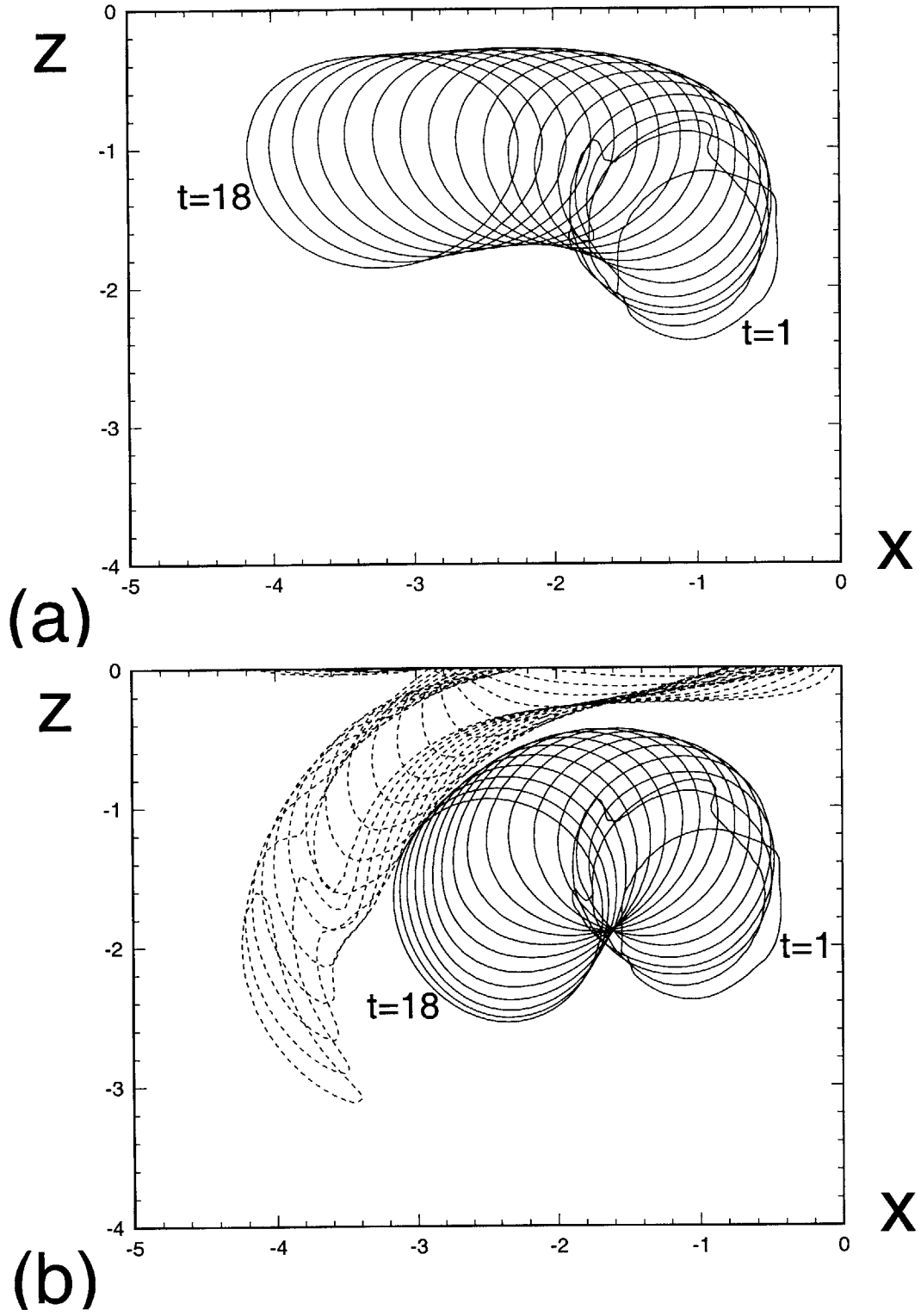

Figure 3-34: Secondary vorticity evolution. (a) Ma=0.0; (b) Ma=0.4. t = 1, 2, 3, 4, 5, 6, 7, 8, 9, 10, 11, 12, 13, 14, 15, 16, 17, 18. Contours of $\omega_y = 0.4$ (dashed line) and $\omega_y = -0.4$ (solid line) are plotted.

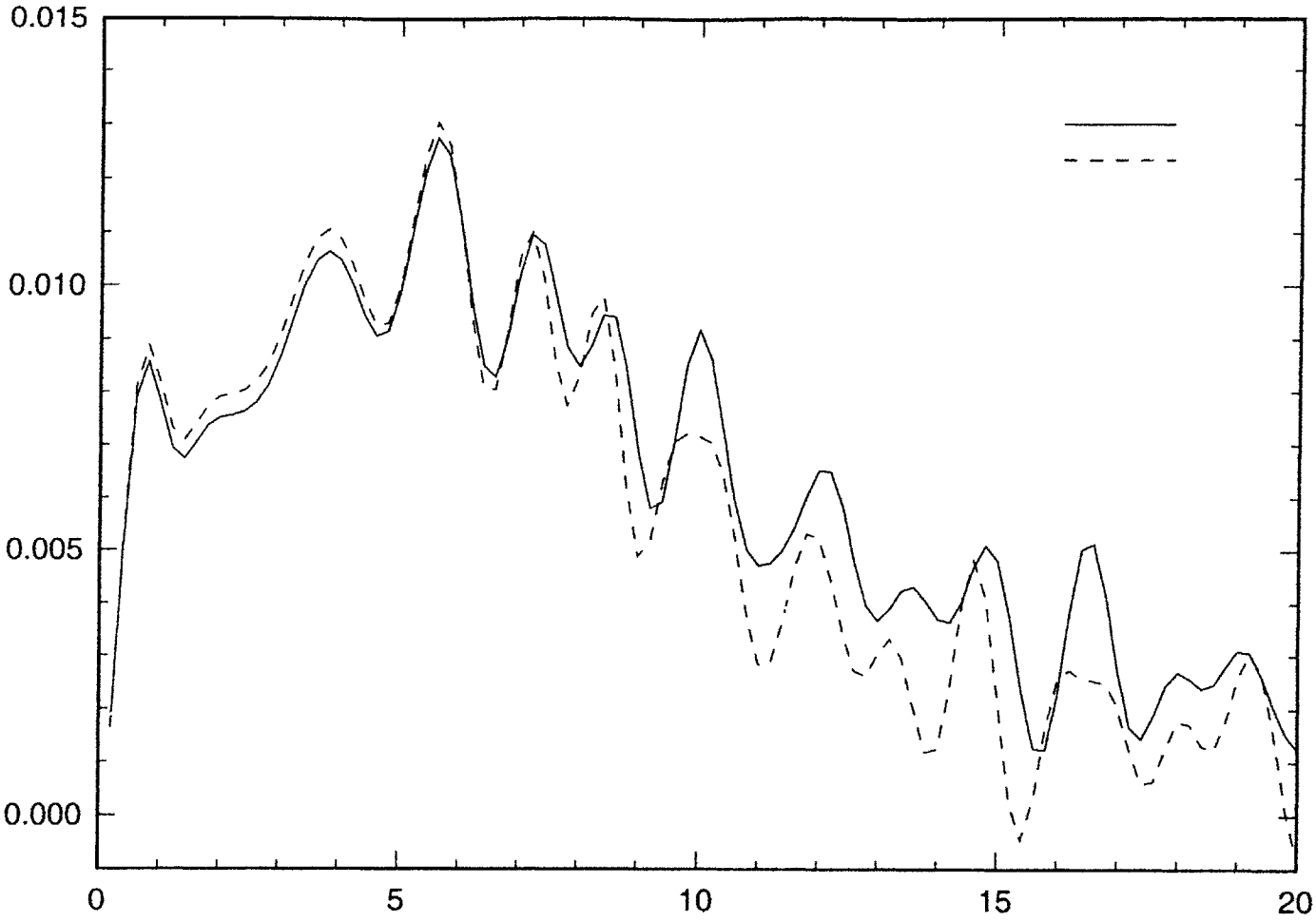

Figure 3-35: Surface mean elevation at the center plane. Solid line is for Ma=0.0 and dashed line is for Ma=0.4. The horizontal axis is time t.

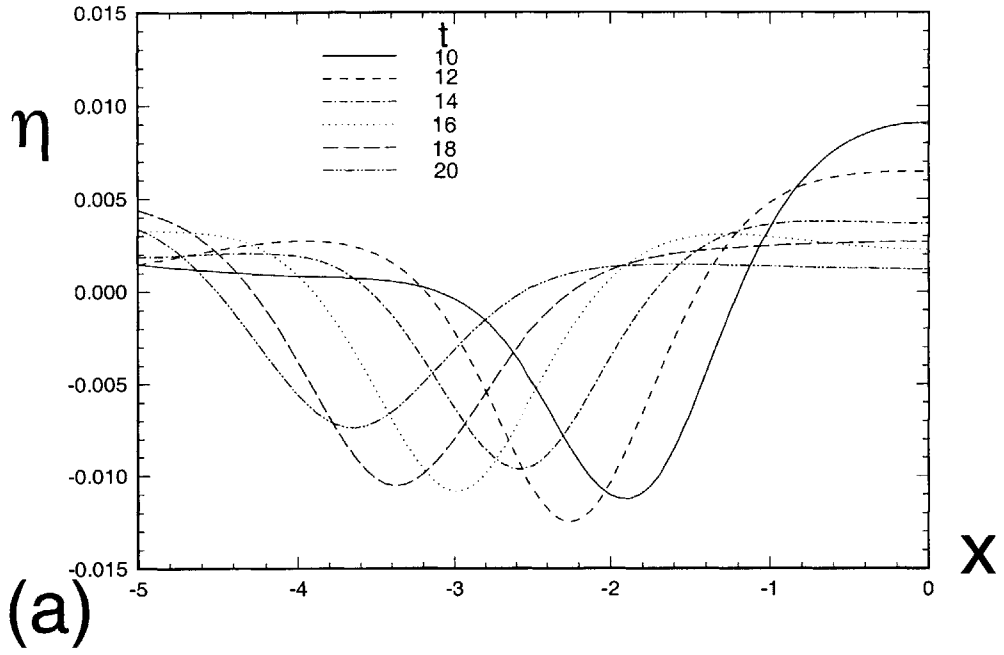

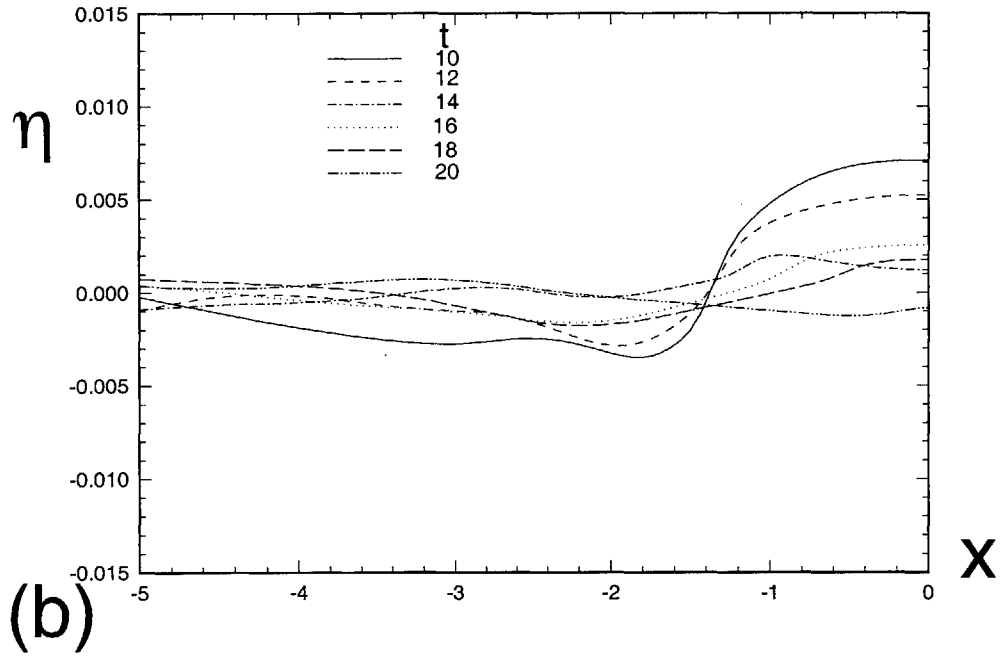

Figure 3-36: Transversely averaged free surface elevation time sequence: (a) Ma=0.0; (b) Ma=0.4.

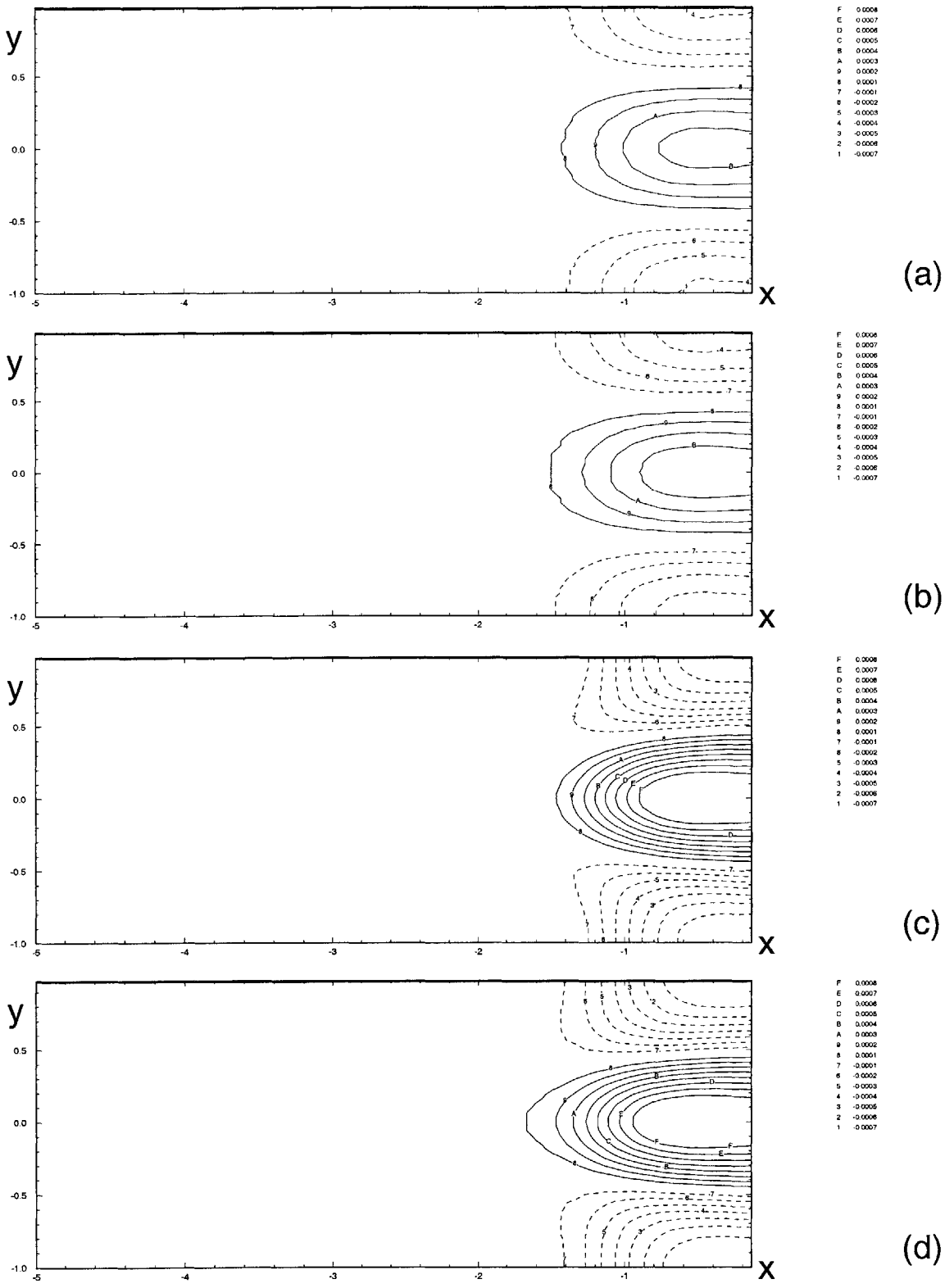

Figure 3-37: Surface elevation η with $\overline{\eta_y}$ subtracted. (a) t=2, Ma=0.0; (b) t=2, Ma=0.4; (c) t=4, Ma=0.0; (d) t=4, Ma=0.4. The contour extremes and increments are: -0.007 to 0.008 by 0.001.

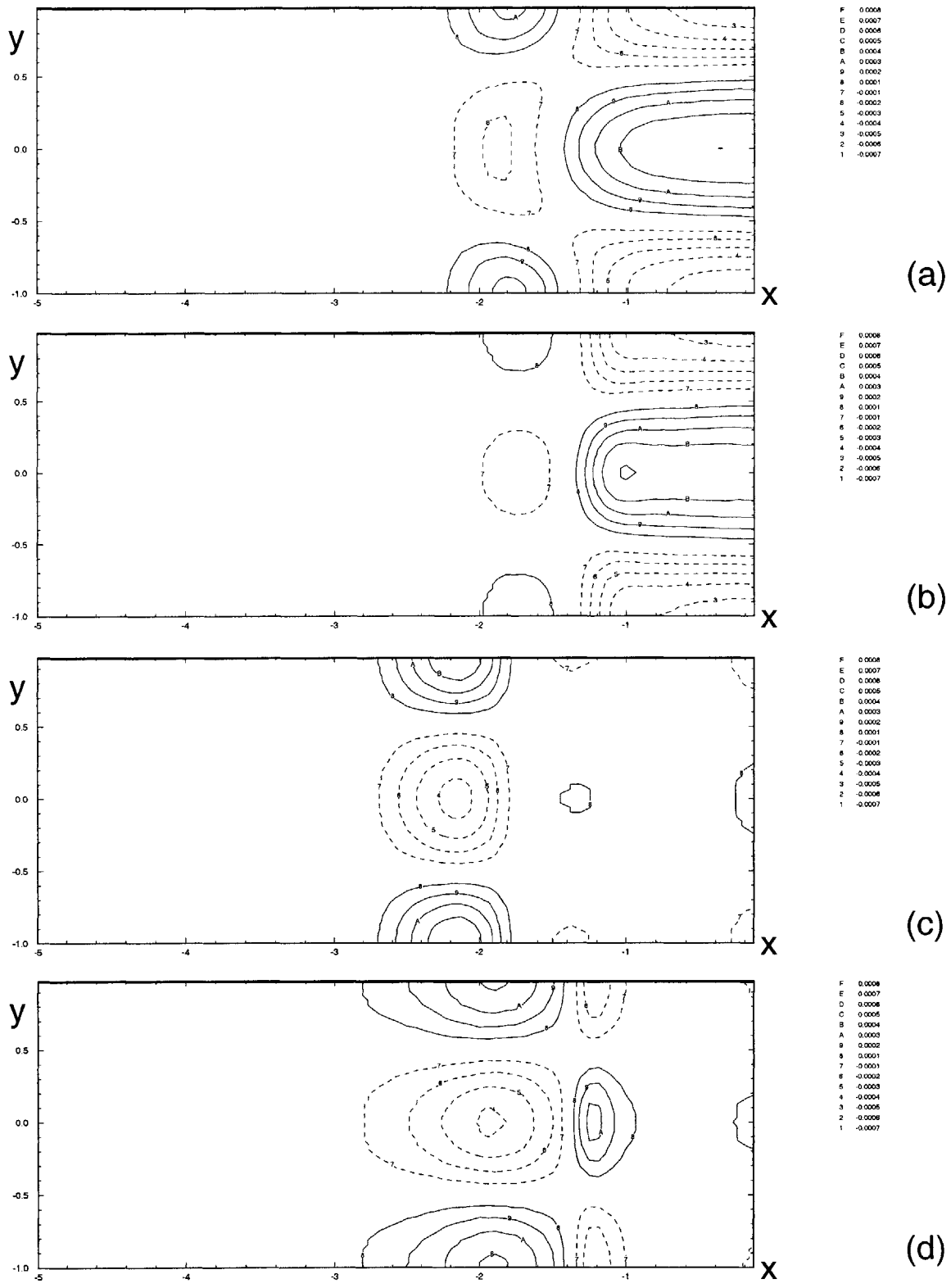

Figure 3-38: Surface elevation η with $\overline{\eta_y}$ subtracted. (a) t=6, Ma=0.0; (b) t=6, Ma=0.4; (c) t=8, Ma=0.0; (d) t=8, Ma=0.4. The contour extremes and increments are: -0.007 to 0.008 by 0.001.

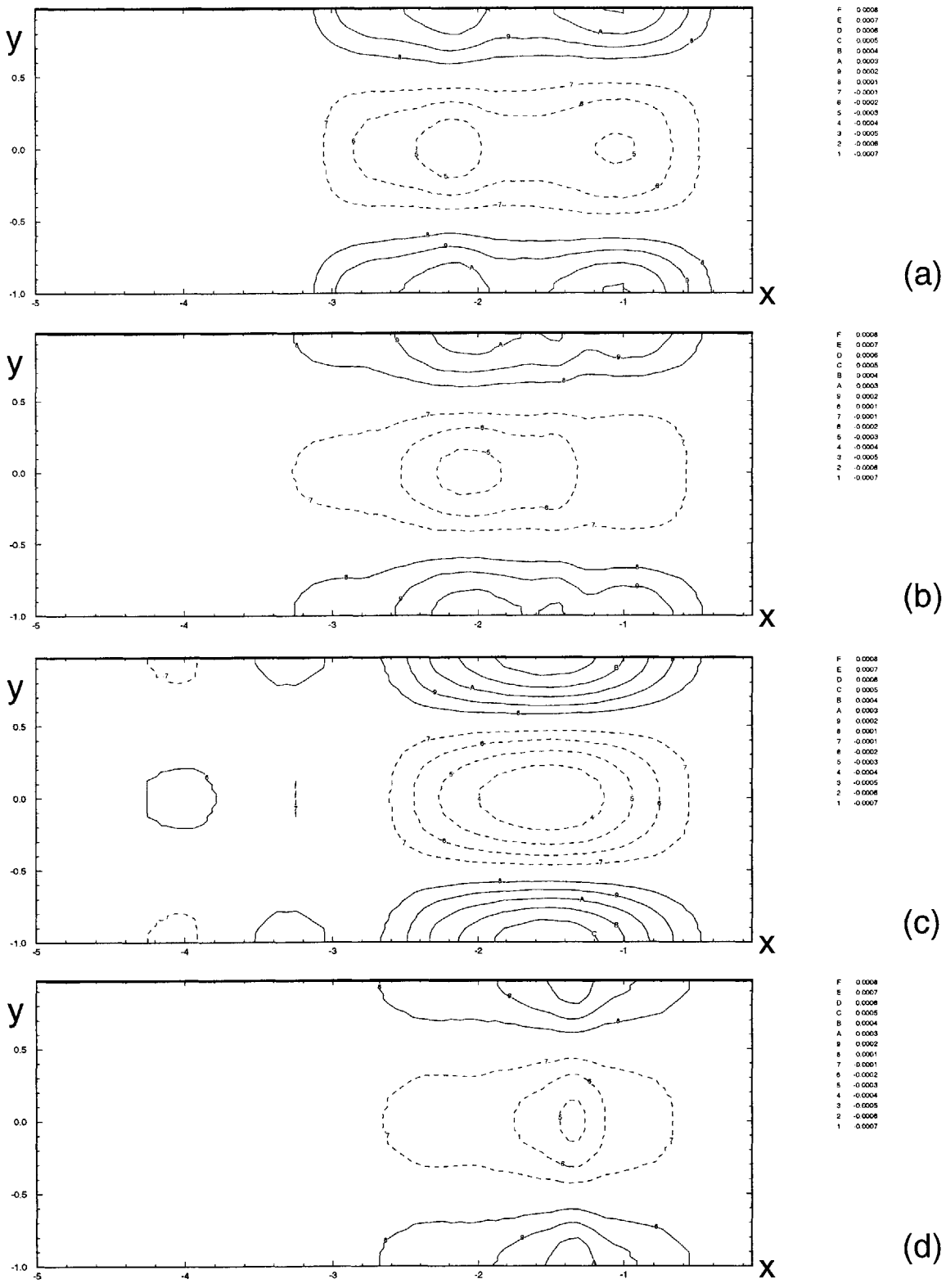

Figure 3-39: Surface elevation η with $\overline{\eta_y}$ subtracted. (a) t=10, Ma=0.0; (b) t=10, Ma=0.4; (c) t=12, Ma=0.0; (d) t=12, Ma=0.4. The contour extremes and increments are: -0.007 to 0.008 by 0.001.

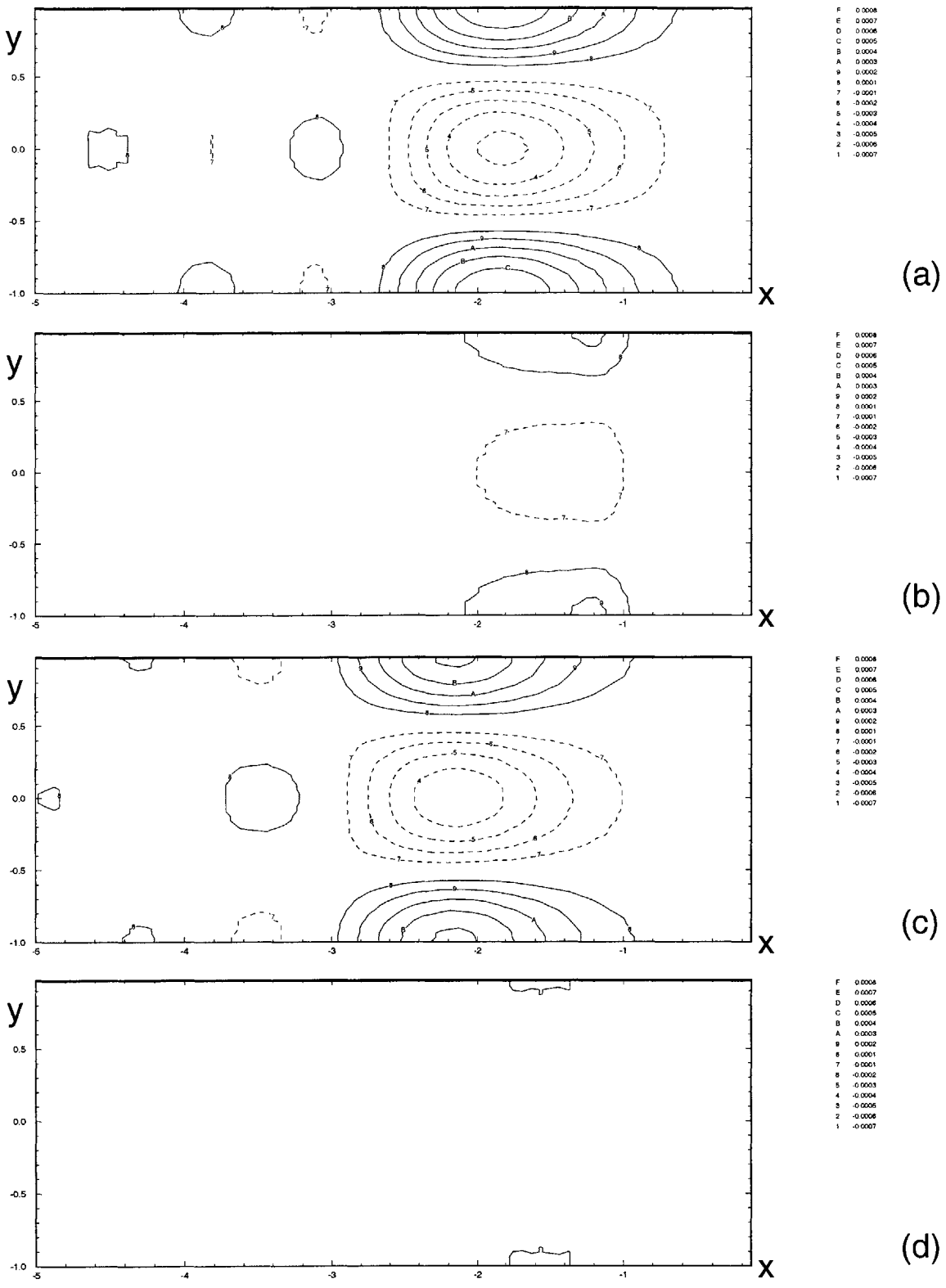

Figure 3-40: Surface elevation η with $\overline{\eta_y}$ subtracted. (a) t=14, Ma=0.0; (b) t=14, Ma=0.4; (c) t=16, Ma=0.0; (d) t=16, Ma=0.4. The contour extremes and increments are: -0.007 to 0.008 by 0.001.

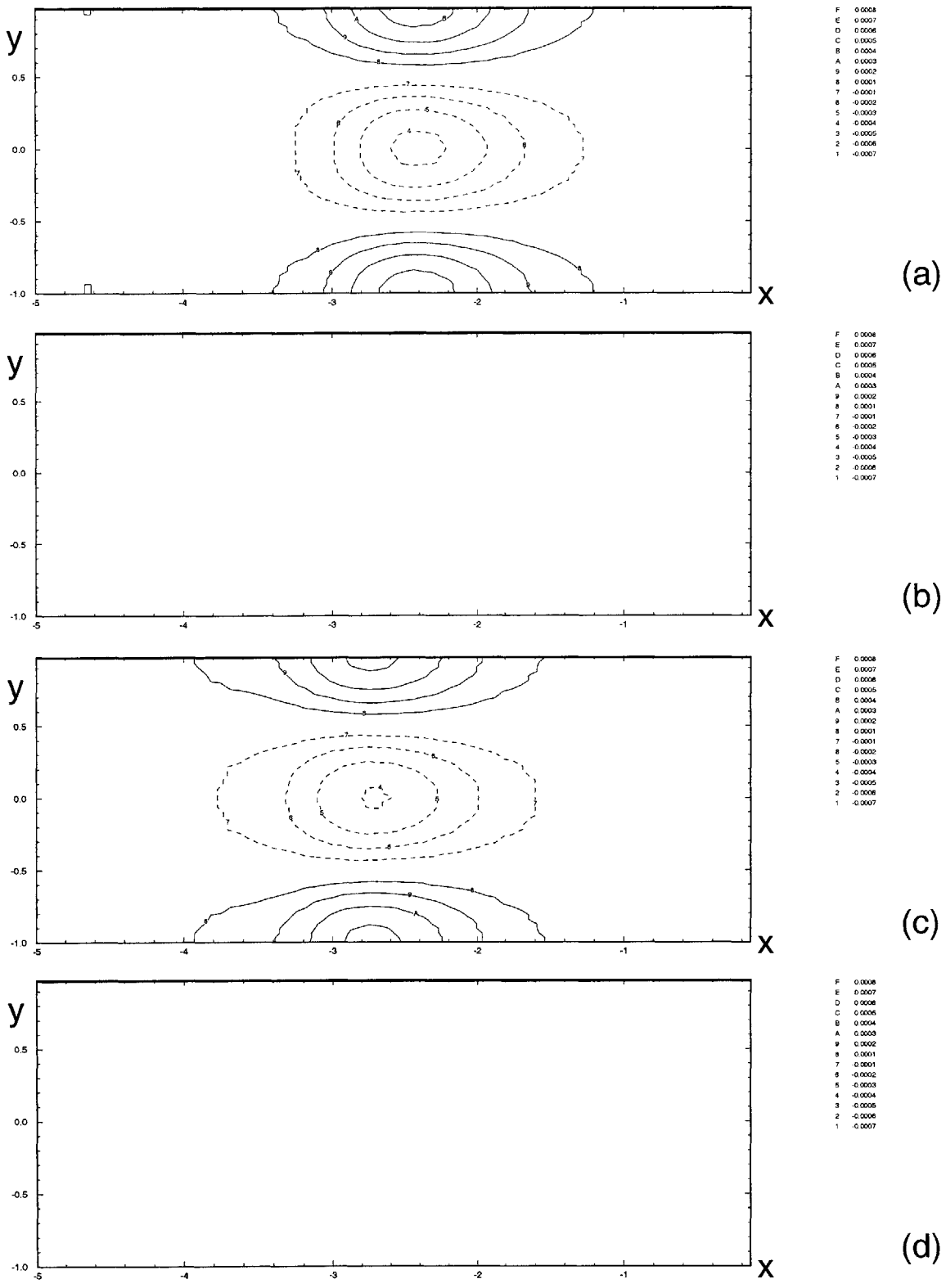

Figure 3-41: Surface elevation η with $\overline{\eta_y}$ subtracted. (a) t=18, Ma=0.0; (b) t=18, Ma=0.4; (c) t=20, Ma=0.0; (d) t=20, Ma=0.4. The contour extremes and increments are: -0.007 to 0.008 by 0.001.

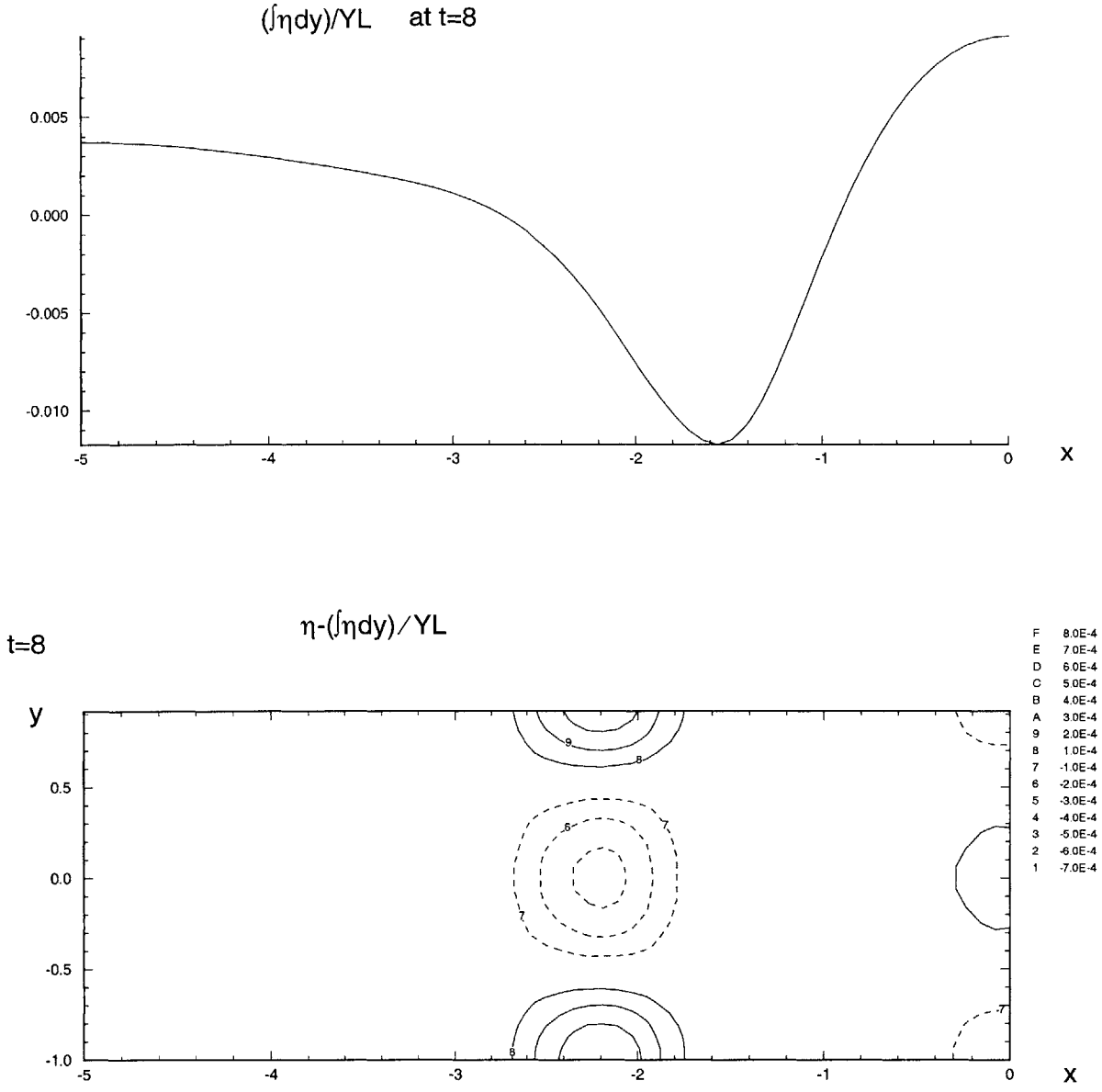

Figure 3-42: Surface mean elevation $\overline{\eta}_y(x,t)$ (a) and elevation fluctuation $\eta - \overline{\eta}_y(x,t)$ (b) at $t = 8$.

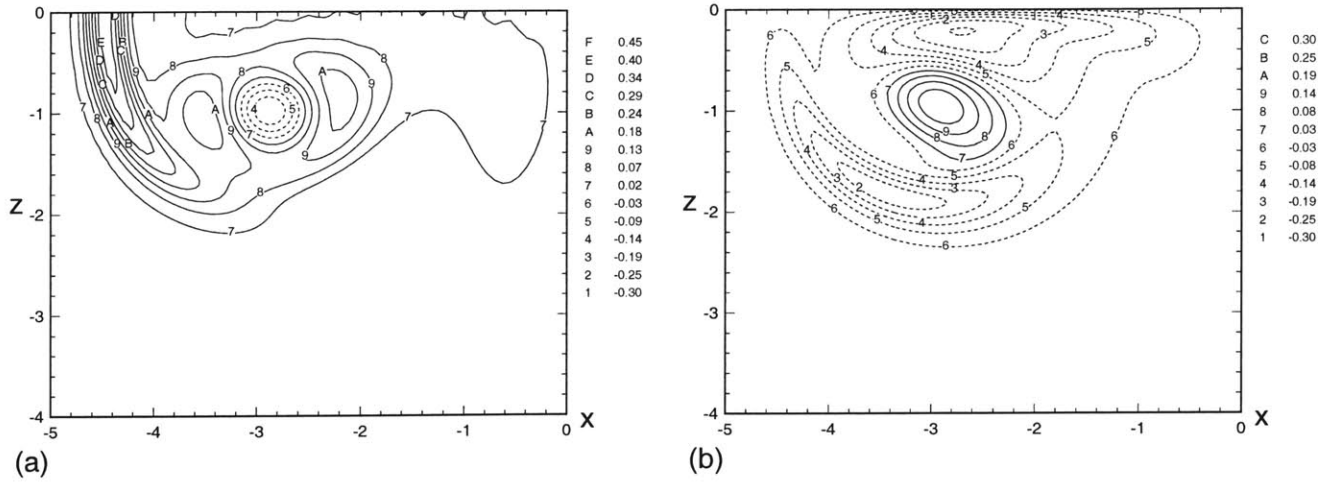

Figure 3-43: Surface normal ω_z and cross-axis vorticity ω_x distribution ($\mathcal{M}a = 0.0$, t=16): (a) ω_z on $y = 0$; (b) ω_x on $y = 0$.

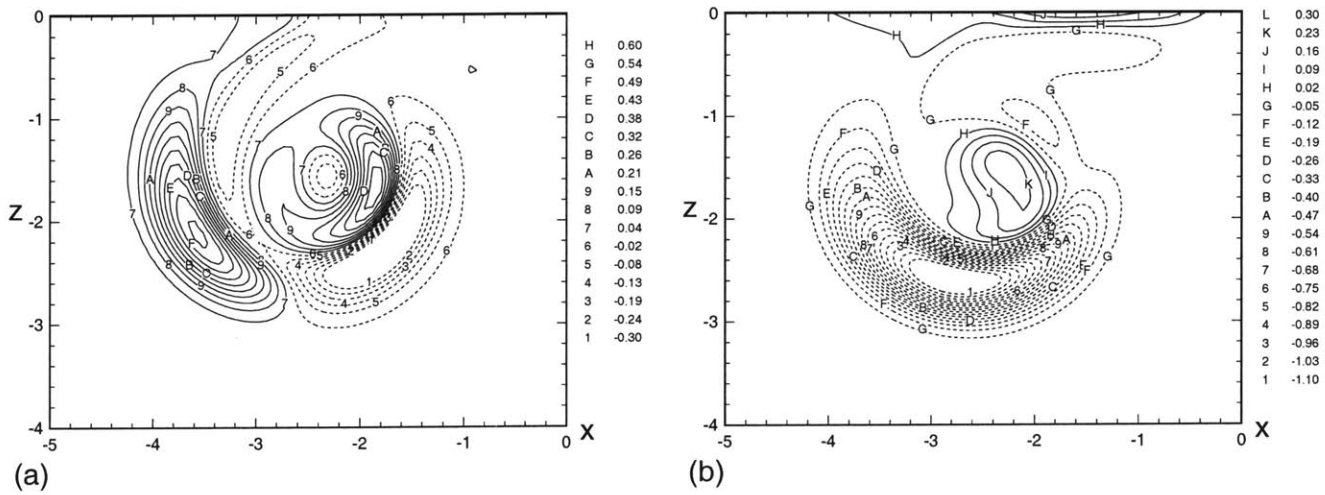

Figure 3-44: Surface normal ω_z and cross-axis vorticity ω_x distribution ($\mathcal{M}a = 0.5$, t=16): (a) ω_z on $y = 0$; (b) ω_x on $y = 0$.

The most important consequence of the interactions of these three vortices is that the secondary vorticity would block the horizontal motion of the primary tube and cause it to rebound from the free surface, as in the two dimensional case. Because the helical vorticity translates with the primary tube, the shoulder portion of the helical vorticity which is responsible for vortex connectionmoves with the primary vortex away from the free surface. The interaction of helical vorticity with the free surface is not as complete as in clean case. So the core (with the largest ω_z) of the ω_z contour cannot fully approach the free surface, and the connection is greatly diminished (figure 3-8). The reduction of u in the region downstream of the primary tube prevent top part of the helical vorticity from moving further downstream, thus the strain field caused by the secondary vorticity deforms the distribution of the helical vorticity by stretching it in both x and z directions. The induced velocity on the free surface due to the secondary vorticity prevents the connection position from getting further away from the centre plane compared with clean case shown in figure 3-45. When the helical vorticity interacts with the free surface, the secondary vorticity is just above the helical vorticity, so the interaction process has to involve the secondary vorticity. The interaction of helical vorticity and secondary vorticity underneath the free surface leads to significant dissipation in the contact zone. This large dissipation prompts the new structure to be generated. Because of surfactant, the helical vorticity is kept near the primary structure instead of remaining on the surface.

The contaminated free surface can sustain larger ω_x or ω_y than in clean case, thus from the point of view of vortex lines, the large ω_x on the free surface makes it difficult for vortex lines to dissipate and connect to its image above the free surface. The continuing rebound of the primary tube makes the connection last only a short time as shown in figures 3-46 and 3-47.

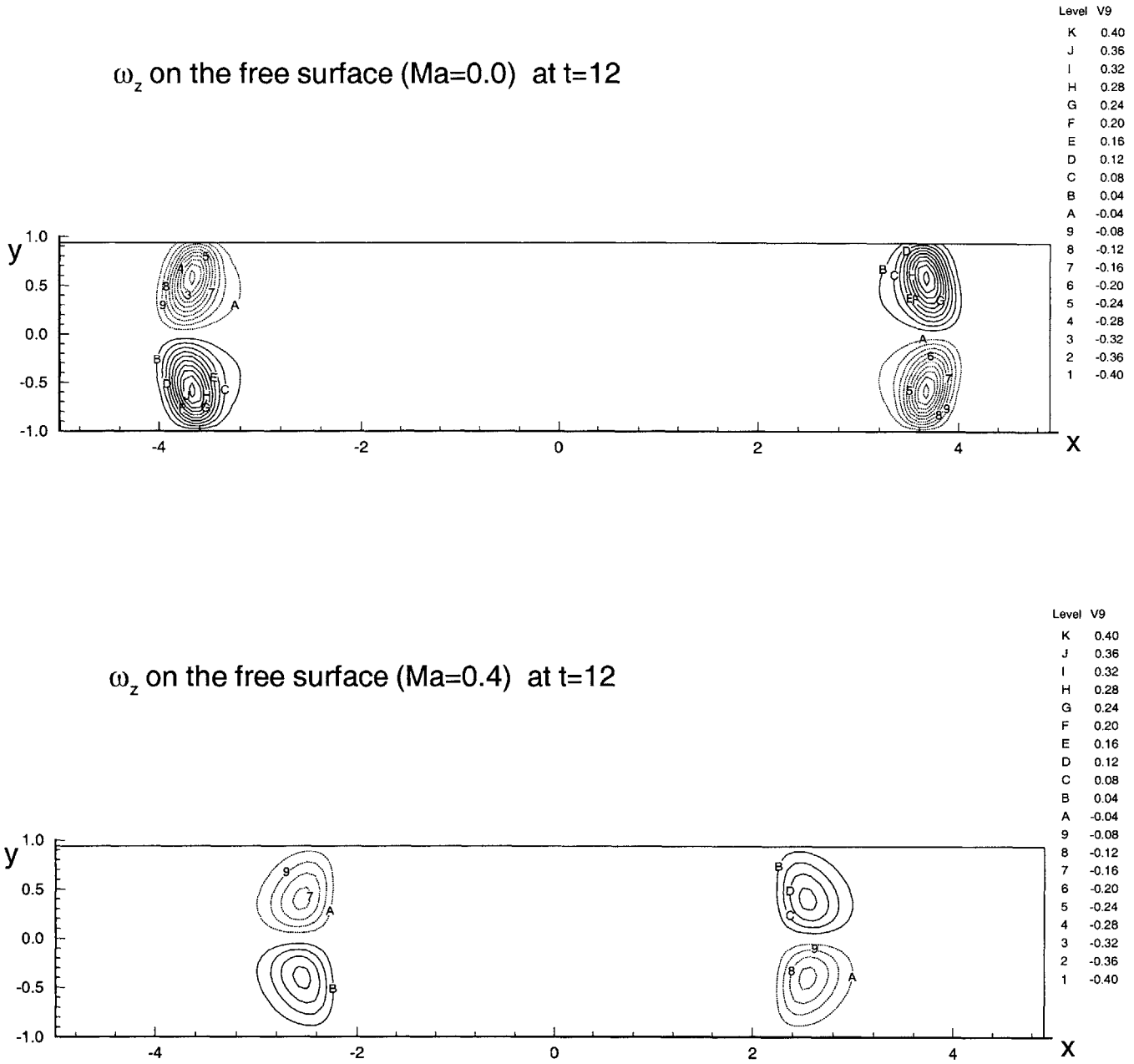

Figure 3-45: Surface normal vorticity ω_z comparison at $t = 12$. The upper figure is for $\mathcal{M}_a = 0.0$ and the lower figure is for $\mathcal{M}_a = 0.4$.

However even though the dissipation on the surface is decreased, there is interaction between the helical vorticity and the secondary vorticity. This can also be seen from the isosurface plots in figure 3-23 and 3-24. The circulation of ω_z on the free surface is shown in figure 3-32. The connection is small compared to that of clean case. The time evolution of the primary and secondary vortex on $y = 0$ plane is shown in figure 3-34, where the rebound of the primary tube is shown. The interaction of helical vorticity with the free surface comes later and weaker as shown by dissipation function in figure 3-30. Secondary vortex sheet is deformed by the helical vorticity and the non-uniform primary ω_y, as shown in above three-dimensional plots. Secondary vorticity does not connect to free surface nor does it connect to its neighbor branch.

Dissipation at the region ($x < 0$) is complicated by the existence of the primary tube. The interaction of the primary dissipation is the major part. Only at $x = 0$, no primary dissipation exists. However, one can tell from the behavior of ω_x, that dissipation do exist. Vortex line approach is more clear when applied for studying this connection.

For insoluble surfactant, small tertiary vorticity appears on the free surface if the secondary vorticity is strong enough to overtake the effect of the primary vortex in the region away from the center. The mechanism for tertiary vorticity generation is the same as that of secondary vorticity generation. For instance, at $t = 10$, the tertiary vorticity is seen on the free surface in the region $(-3.4, -2.8)$ in figure 3-48 (a). At $t = 10$, the surface surfactant concentration γ and its gradient is shown in figure 3-49 (a) and (b). Even though some secondary vorticity surrounds the tertiary vorticity, from figure 3-48 (b), the major portion of the secondary vorticity locates upstream of the tertiary vorticity. The tertiary vorticity is weak and does not have any effect on the vortex connection.

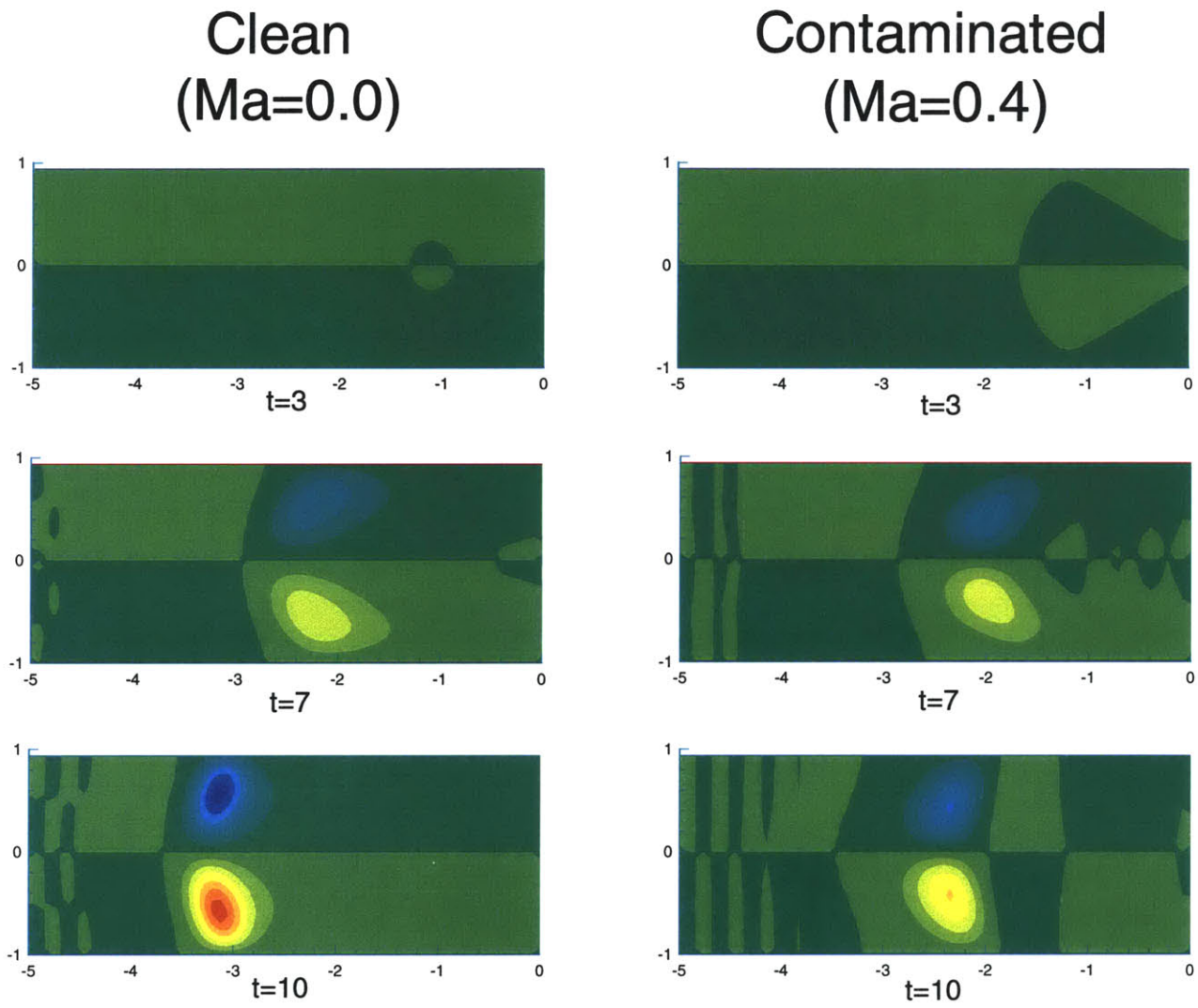

Figure 3-46: Surface distribution of ω_z at $t = 3$, 7, 10.

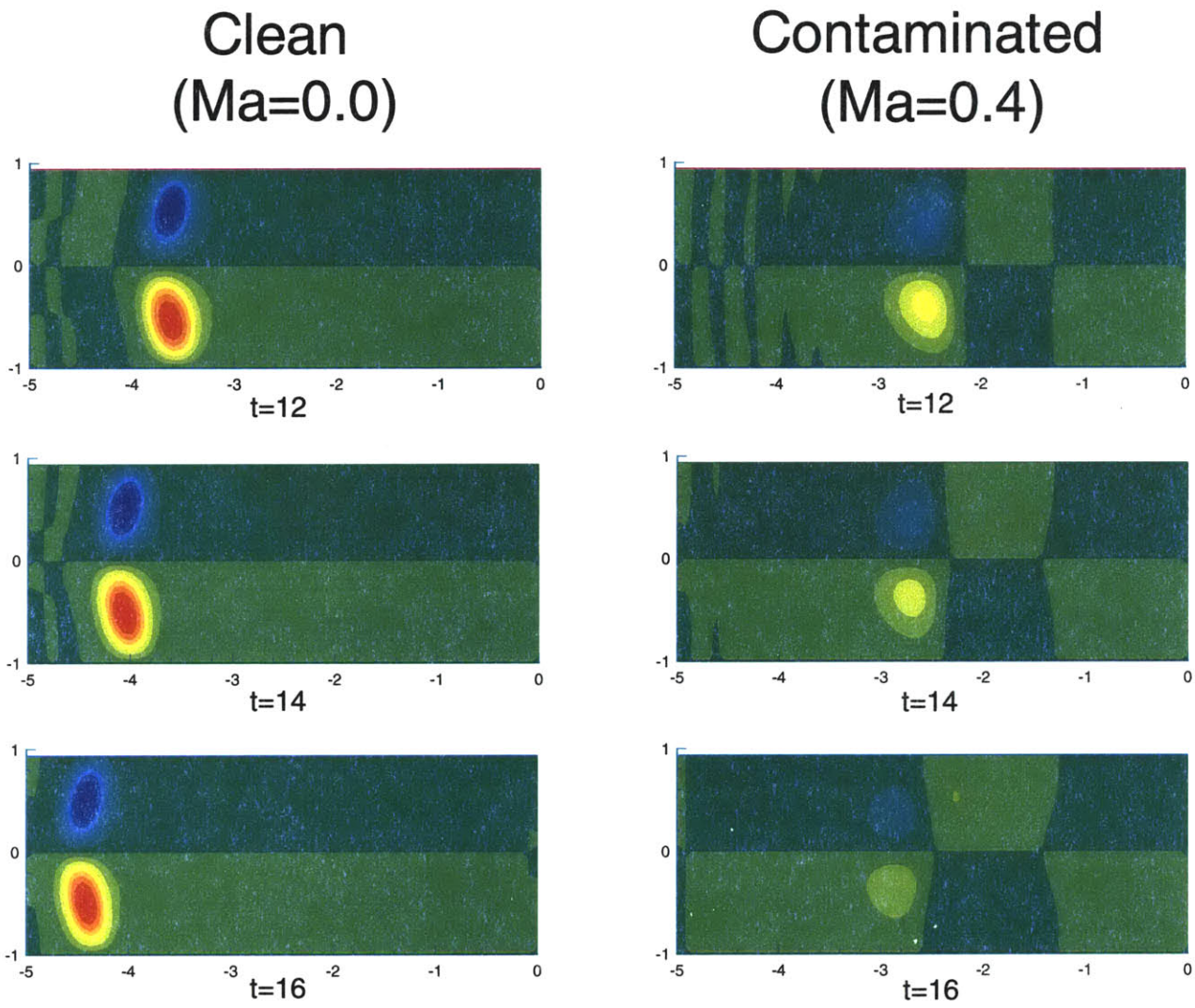

Figure 3-47: Surface distribution of ω_z at $t = 12$, 14, 16.

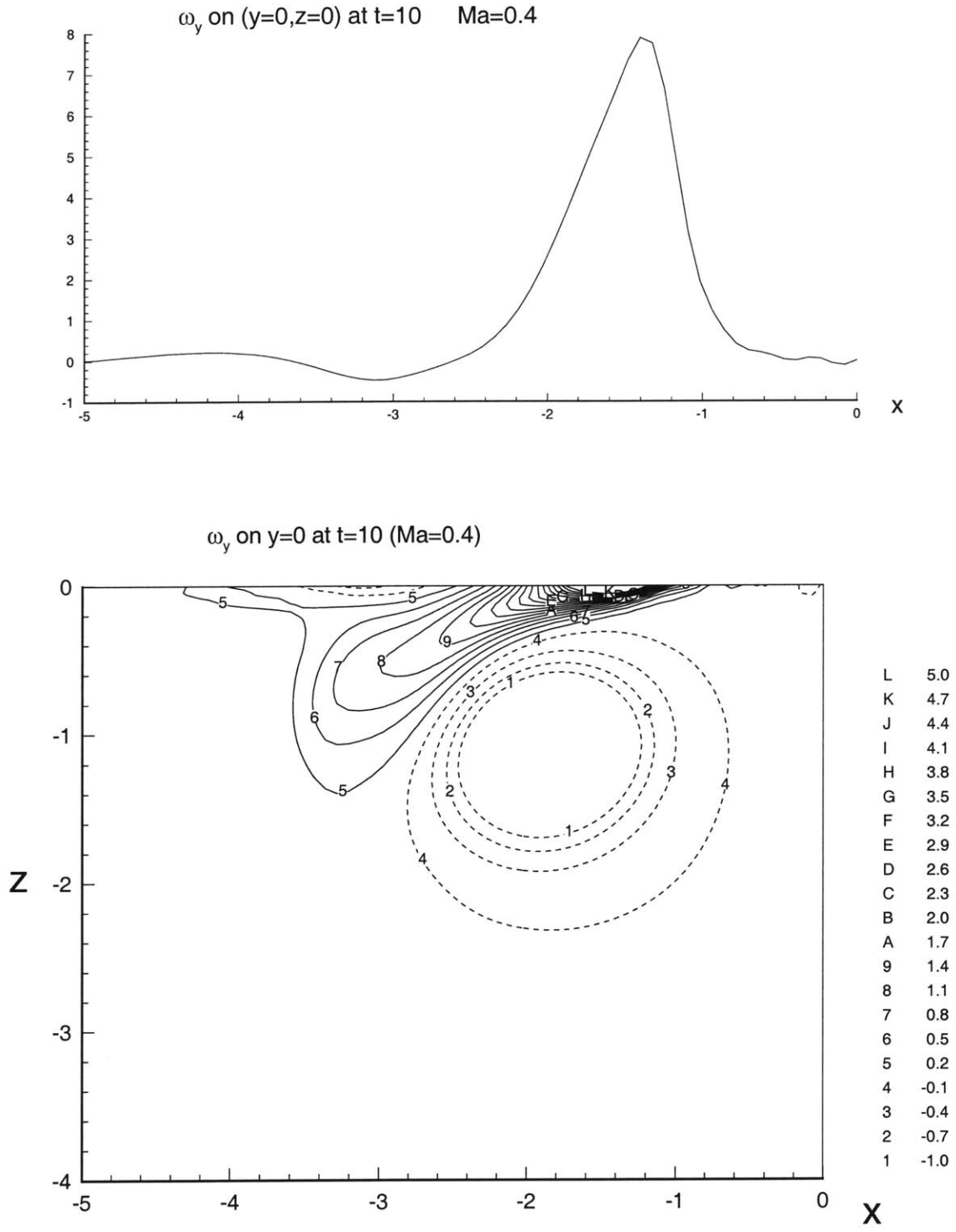

Figure 3-48: Existence of tertiary vorticity (t=10): (a) surface spanwise vorticity distribution ω_y on $y = 0$; (b) vorticity distribution ω_y on $y = 0$.

As have been discussed before, the striations on the surface are evidence of helical vorticity before connection. When there is no surfactant present, the motion of the helical vorticity is not blocked in the horizontal direction by the secondary vorticity. Therefore before connection, the horizontal extension of the helical vorticity must be smaller for contaminated case since the striation is caused by the ω_x part of the helical vorticity. This is shown in figures 3-37 and 3-38 of η with the mean along y axis subtracted. So on the free surface, the surfactant covered striation is narrower. The striations intensifies quickly from $t = 2$ to $t = 4$ for the clean case and has larger range (but barely observable) and exists for longer time. As to the strength of these three structures, there is a circulation ratio of 1:5:20 for the helical, secondary and primary vortices. The free surface serves as a vorticity sink. After connection, the ω_x portion of the helical vorticity only appears away from the center plane. From figures 3-39 and 3-40, the diminished striations exists until $t = 20$ for clean surface. At $t = 20$, there is no surface feature induced by ω_x near the connection region (see figure 3-41). For $t < 8$, the above figures show the striation and for $t > 8$, the above figures show the surface connection. It is clear that the 90-degree phase change from striation to connection-induced swirls. At $t = 6$ both the striation and connection can be observed for clean case.

When the surfactant is soluble, the secondary vorticity on the free surface becomes weaker and the new structure may not be created depending on the strength of the secondary vorticity. The surface connection strength is between the two extreme cases as shown in figure 3-32. Shown in figure 3-36 is the averaged surface elevation. The surfactant suppresses the surface deformation, especially in the region far away from the center where the surfactant concentration is high.

Closed-loop interaction

The closed-loop interaction of surfactant transport and vortex generation leads to a feedback process. The gradient of surfactant concentration γ generated because of the primary tube is the source of secondary vorticity on the free surface. The induced velocity on the free surface due to the secondary vorticity counteracts that

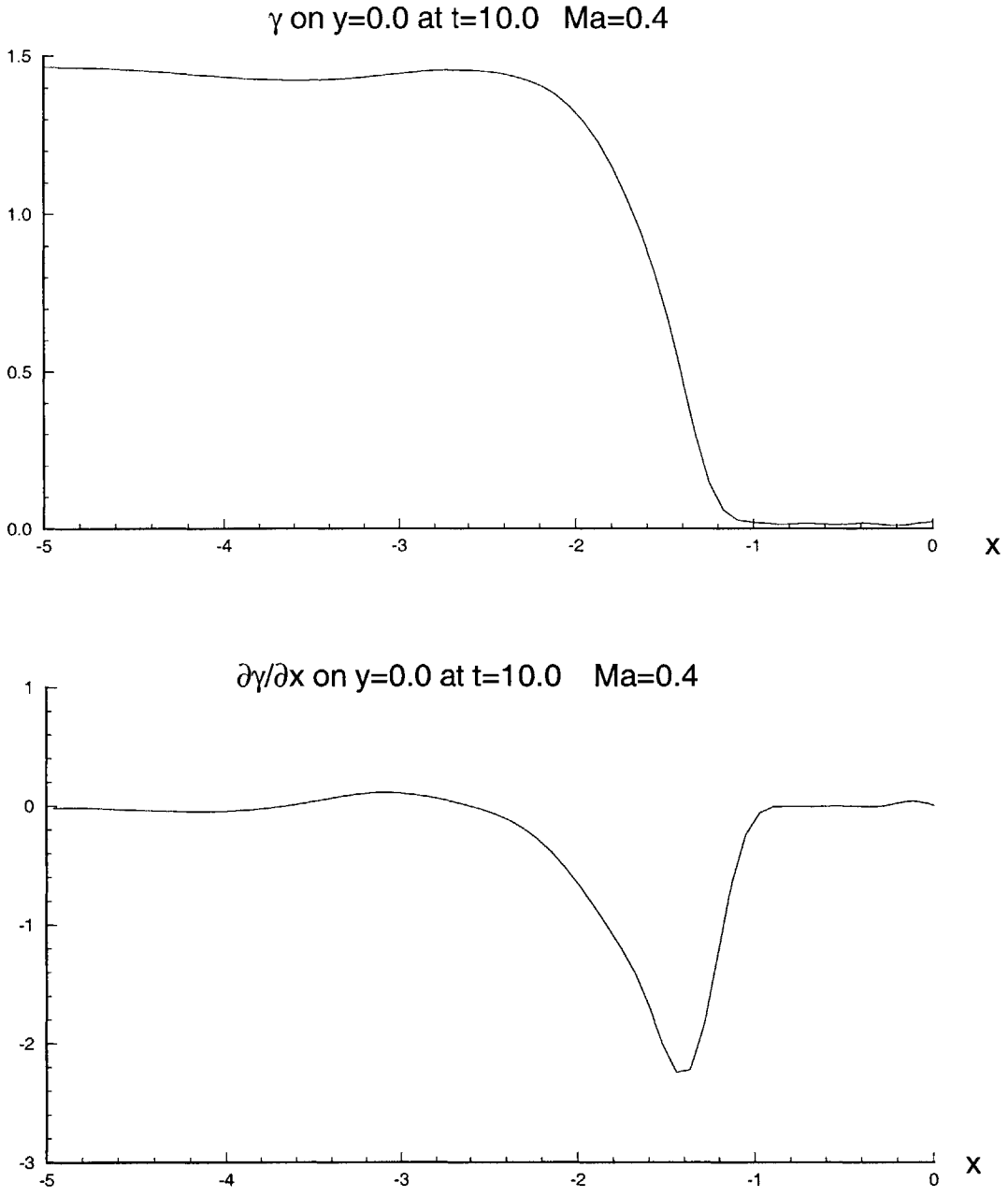

Figure 3-49: Dynamical behavior of surfactant distribution (t=10). (a) surfactant concentration on $y = 0$; (b) surfactant concentration gradient.

of the primary tube. So the surfactant gradient cannot be built into infinity. When γ reaches maximum, the velocity induced by the secondary vorticity on the free surface surpasses the velocity induced by the primary vorticity, and the horizontal velocity downstream of the free surface changes direction. At this moment, the γ gradient begins to decrease, and so does the secondary tivevorticity. The effect of γ gradient leads to the decrease of itself, which is a typical negative feedback phenomenon. The closed loop sketchy plot of the feedback mechanism is shown in figure 3-50. Figure 3-51 shows the total induced horizontal velocity u, surface vorticity ω_y and surfactant concentration γ at $t = 5$, 10 and 15. The rebounding of the primary vortex tube plays a significant role in this feedback process. If there is no rebounding of the primary vorticity, the effect of secondary vorticity would not take over the effect of the primary vorticity. The increase in concentration buildup cannot go indefinitely.

Bulk fluid motion near an interface has the effect of disturbing the homogeneity of the interfacial surfactant composition that would otherwise exist in the absence of flow. The ensuing interfacial tension gradients act in a manner such as to restore the interface to its homogeneous, equilibrium state by engendering flow in the proximity of the interface.

3.4 Detailed mechanisms

Initial conditions

In order to study the detailed vortex connection and interaction mechanisms, we need to resort to the vortex line approach. The primary structure with its meandering property has all three vorticity components. This leads to inaccuracy of the isosurface description, although we can still have a story based on that.

At $t = 0$, the major vortex structures are shown in figure 3-52. The dimensions in the figure are $(-3, 0) \times (-1, 1) \times (-3, -1)$. If we consider the right half $x > 0$, the helical vortex can be considered as a vortex ring sitting between a pair of primary vortex.

Figure 3-66 shows the helical vorticity bundle, which has the shape of an elongated

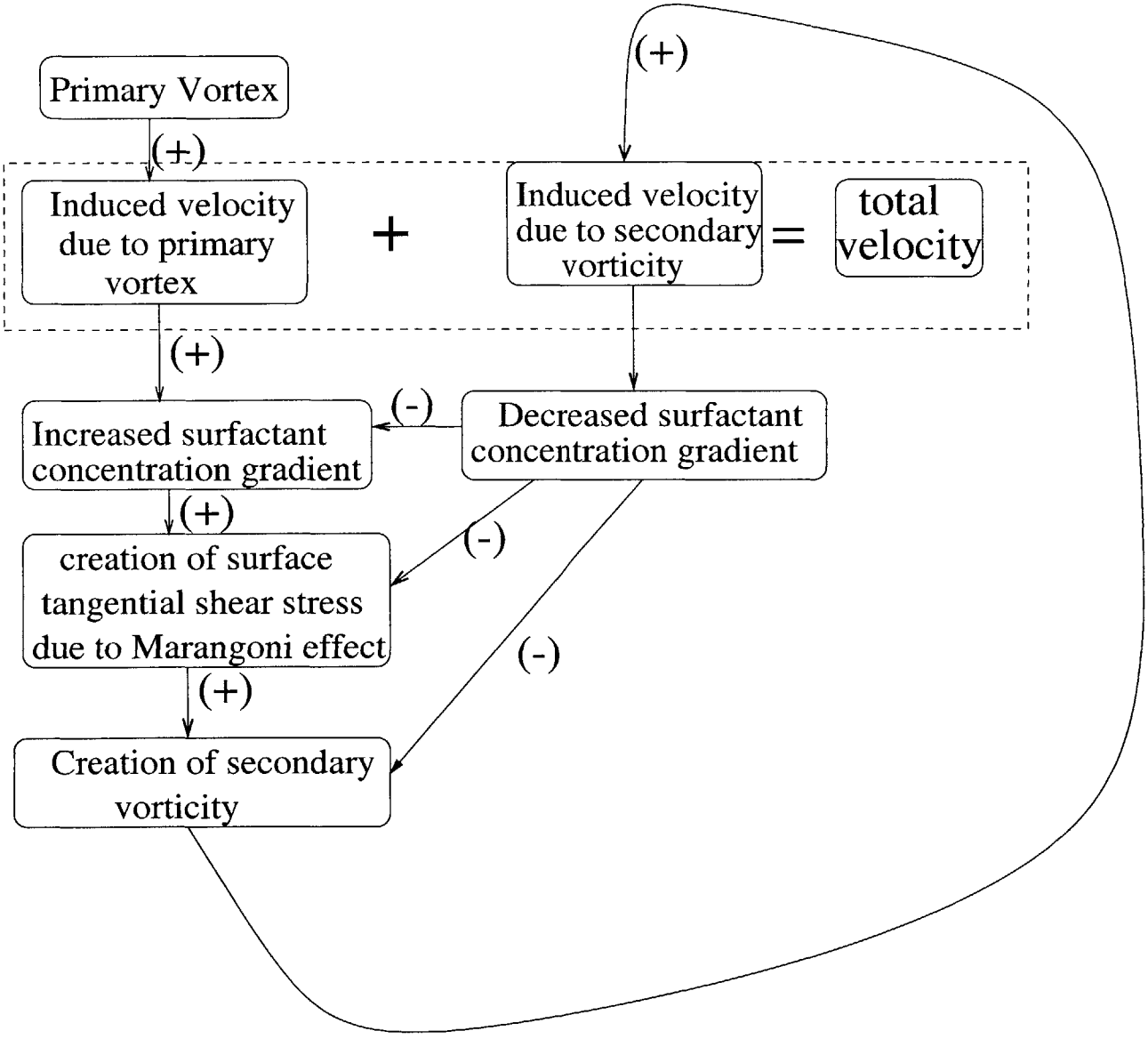

Figure 3-50: Closed loop feedback mechanism

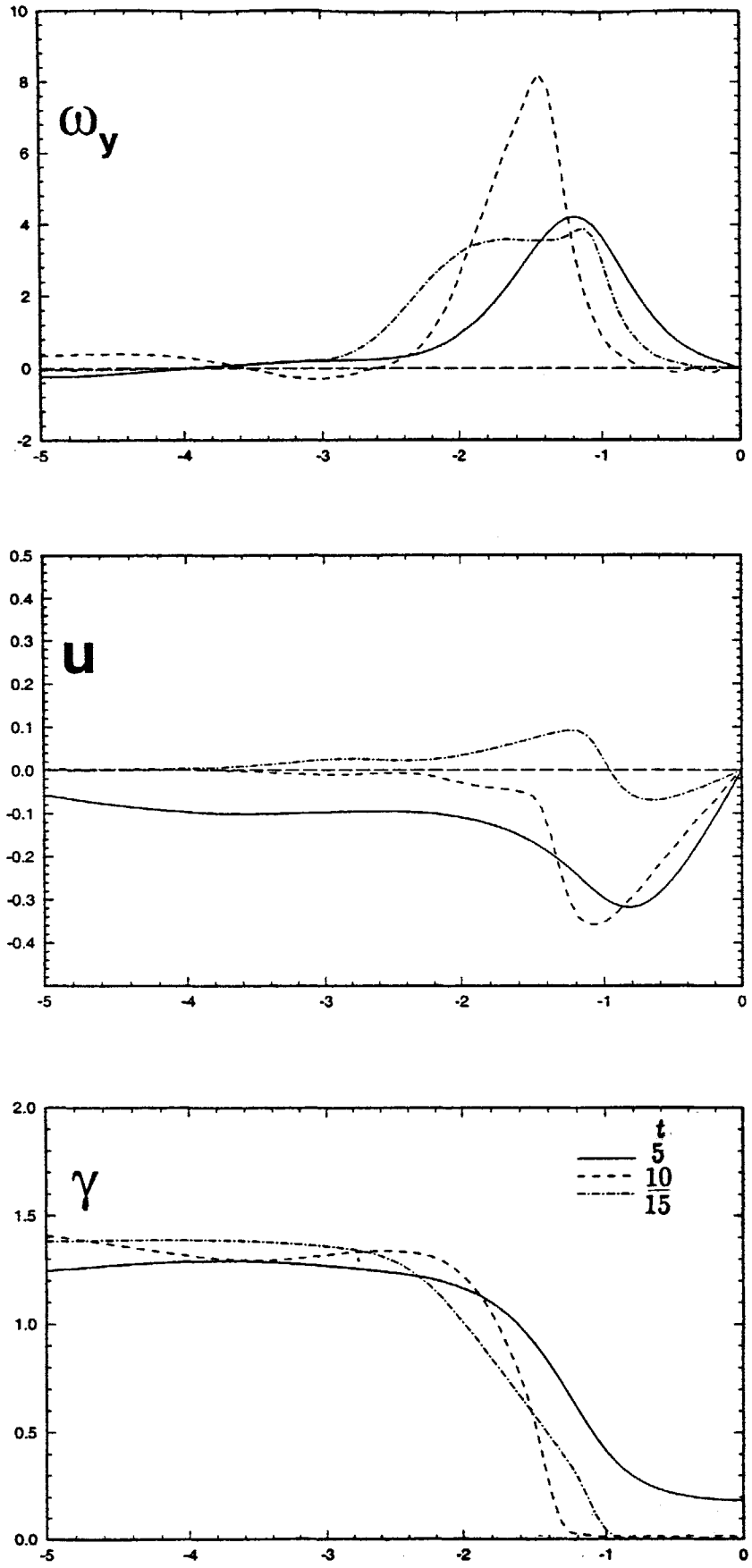

Figure 3-51: Feedback mechanism of surfactant transport and secondary vorticity generation. ($t = 5$, 10, 15): (a) surface transverse vorticity ω_y; (b) surface horizontal velocity u; (c) surfactant concentration on the surface γ

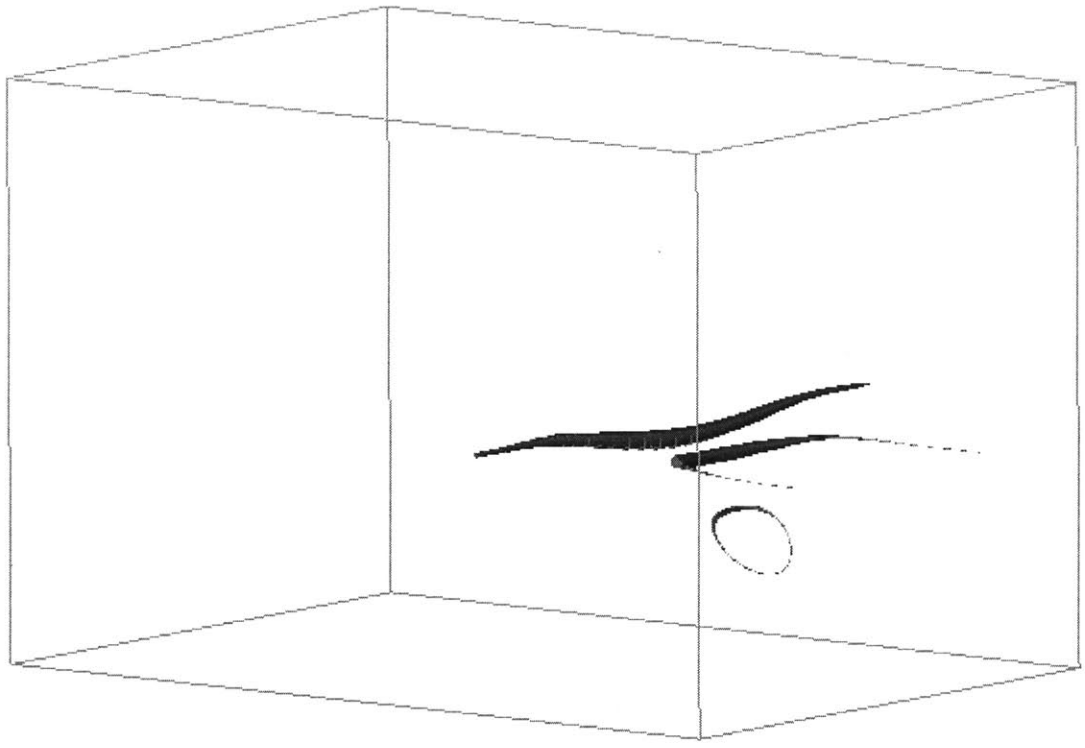

Figure 3-52: Initial flow configuration: ring structure near the center plane. The dimension of the box is $(-3, 0) \times (-1, 1) \times (-3, -1)$.

ring with small curvature in the middle near the center line. So a better name for helical vorticity is circumferential vorticity. A ring structure can be seen located at the right lower part of the primary vortex. This ring structure possesses a circulation of 0.1553 which is of the same order of the circulation of the helical vorticity 0.1264, but is considerably smaller compared with that of the primary tube 3.3617. This ring is not important in our connection process. The spatial relation of the three structures can be seen more clearly in the three dimensional plot in figure 3-52.

At $t = 0$, the whole helical vorticity remains almost on the same vertical level and has not been distorted by the primary vortex. The helical vorticity locates between the primary vortex tubes and they are all on the same vertical level. All the initial vortical lines belong to one of the three groups.

The sequence of the evolution of the vortical structures are shown in figures 3-53, 3-54, 3-55, 3-56, 3-57, 3-58, 3-59, 3-60, 3-63. It is clear that a new structure is created during $t = 6$ and $t = 7$ for contaminated flow. The vortex line patterns at $t = 10$ are

shown in figure 3-61 and 3-62.

In order to show the scale of the ring structure underneath the surface, two vortex lines are shown in figure 3-64. These two vortex lines start at the location from the edge at a vorticity magnitude 20% of maximum vorticity.

Connection mechanism

The major difference for clean and contaminated interaction lies in the fact that the evolutions of the helical vorticity are totally different. For clean interaction the whole elongated ring evolves into two U-shaped vortices with connection on the free surface. For contaminated case, the helical vorticity splits into two parts. One branch connects to the free surface as in clean case. Another branch connects with itself underneath the free surface, and forms another set of rings. Thus connection on the free surface is much decreased. Comparison of clean and contaminated cases is shown in three dimensional figure 3-61 and figure 3-62. The dimensions in that figure are $(-5, 0) \times (-1, 1) \times (-4, 0)$. So part of the helical vorticity feeds into the secondary vorticity, which leads to smaller and shortened connection. The induced velocity due to the primary vortex and secondary vortex Larger speed of the ring due to the secondary vorticity.

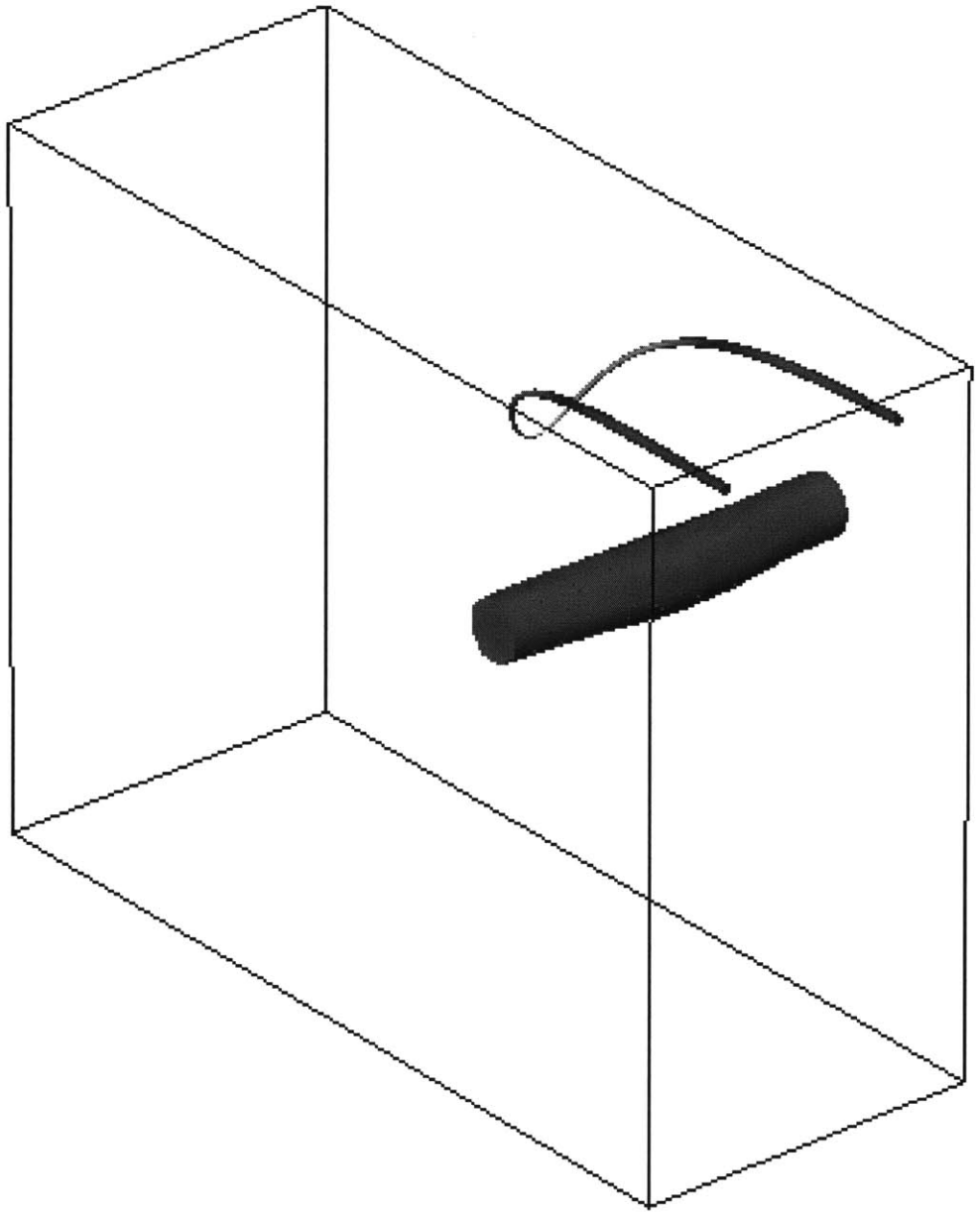

Figure 3-53: Vortex line representation of the primary and helical vortices. ($t = 6$, Ma=0)

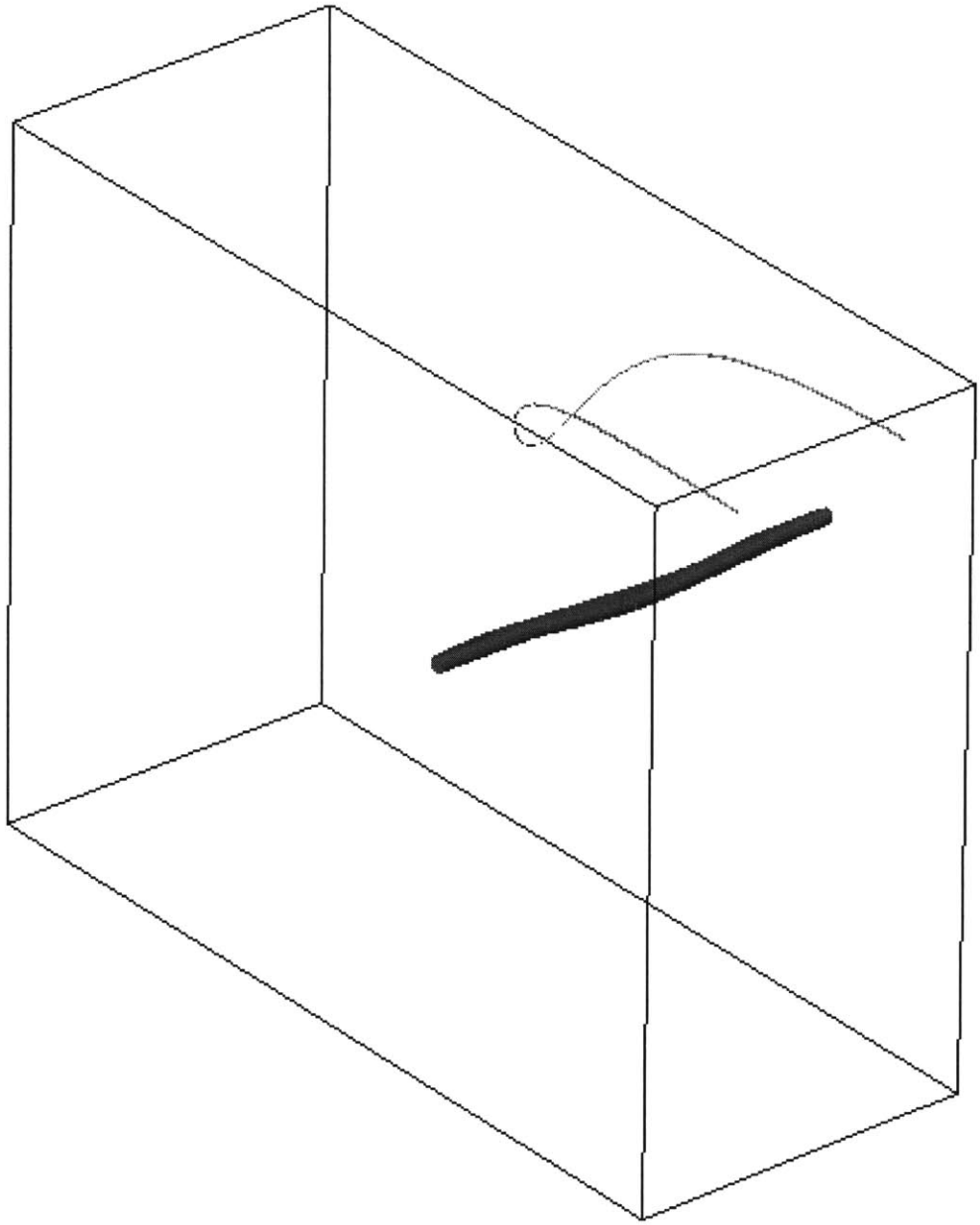

Figure 3-54: Vortex line representation of the primary and helical vortices. Secondary vorticity is shown as $\omega_y = 0.4$ isosurface. ($t = 6$, Ma=0.4)

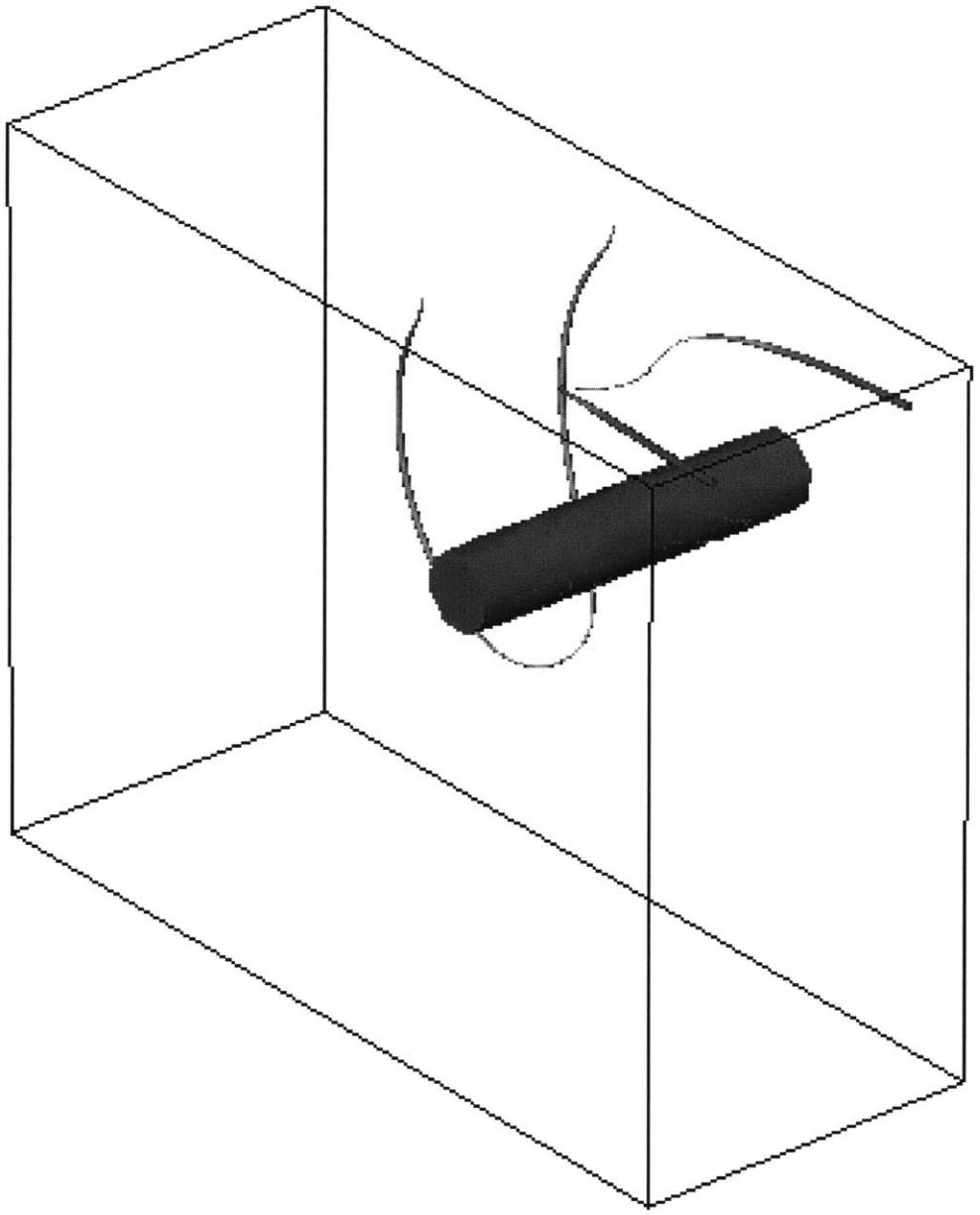

Figure 3-55: Vortex line representation of the primary and helical vortices. ($t = 7$, Ma=0)

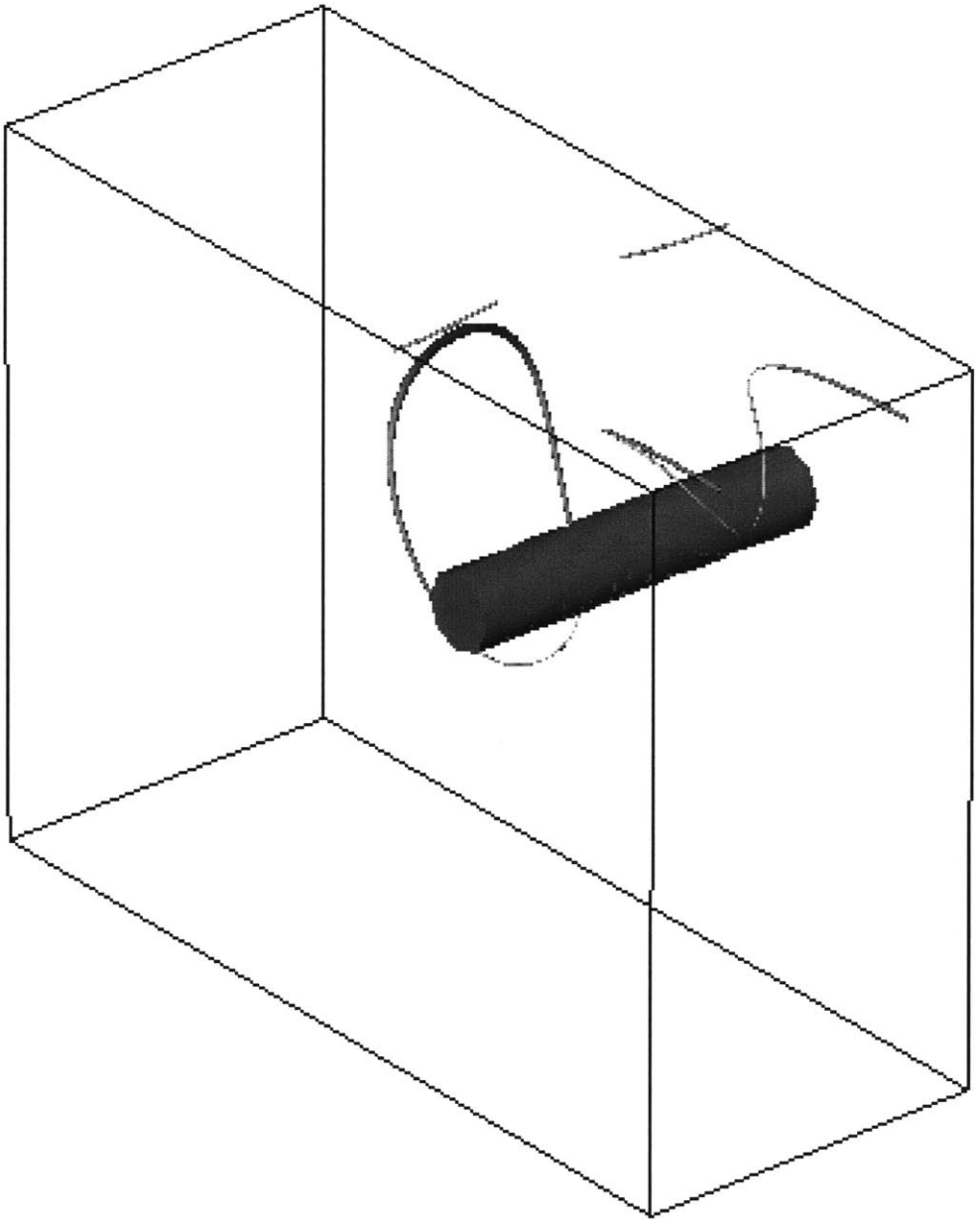

Figure 3-56: Vortex line representation of the primary and helical vortices. At $t = 7$, the interaction of helical vorticity and secondary vorticity leads to weakened connection (A+, A-) and a new ring structure (B). ($t = 7$, Ma=0.4)

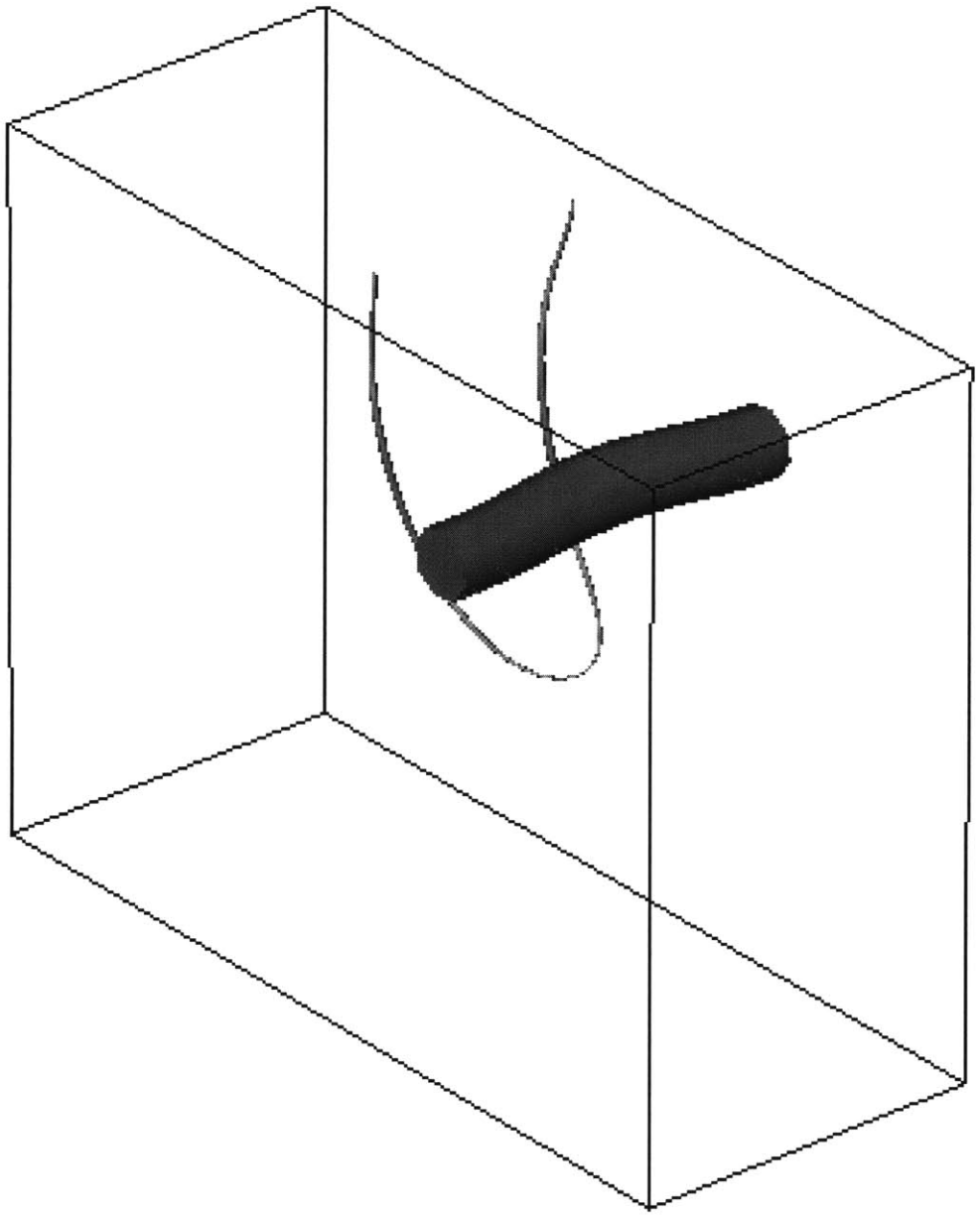

Figure 3-57: Vortex line representation of the primary and helical vortices. ($t = 8$, Ma=0)

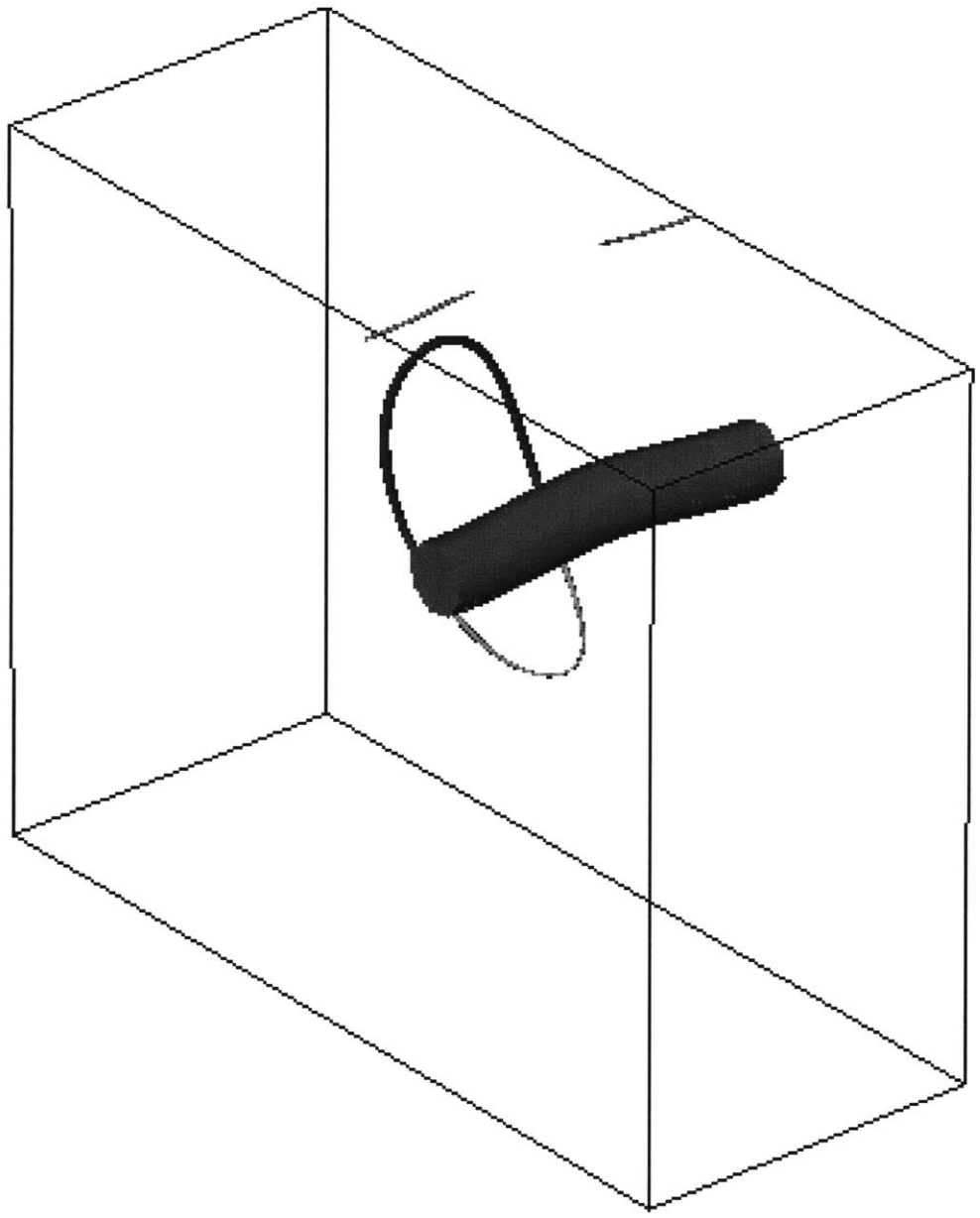

Figure 3-58: Vortex line representation of the primary and helical vortices. At $t = 8$, the interaction of helical vorticity and secondary vorticity leads to weakened connection (A+, A-) and a new ring structure (B). ($t = 8$, Ma=0.4)

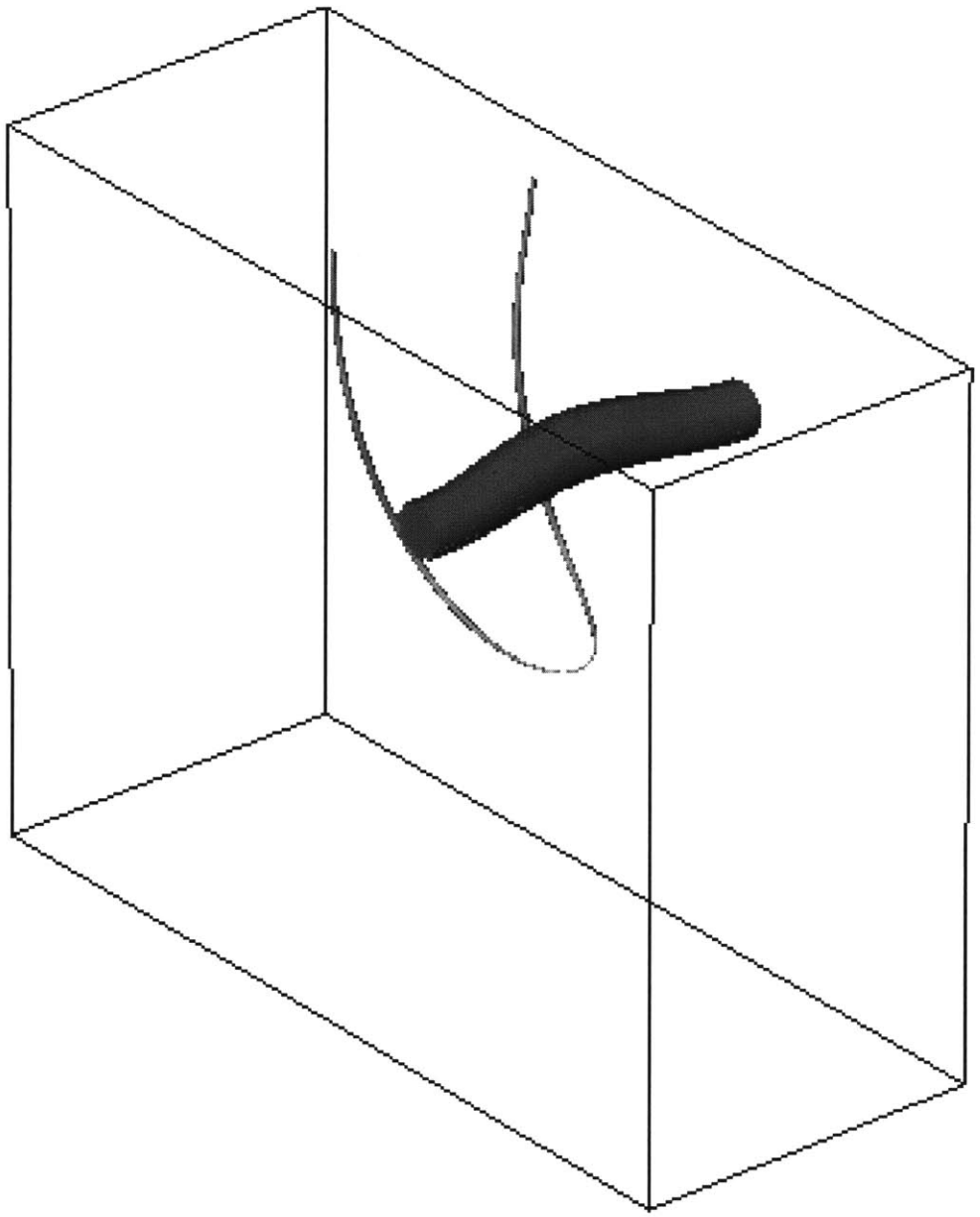

Figure 3-59: Vortex line representation of the primary and helical vortices. ($t = 9$, Ma=0)

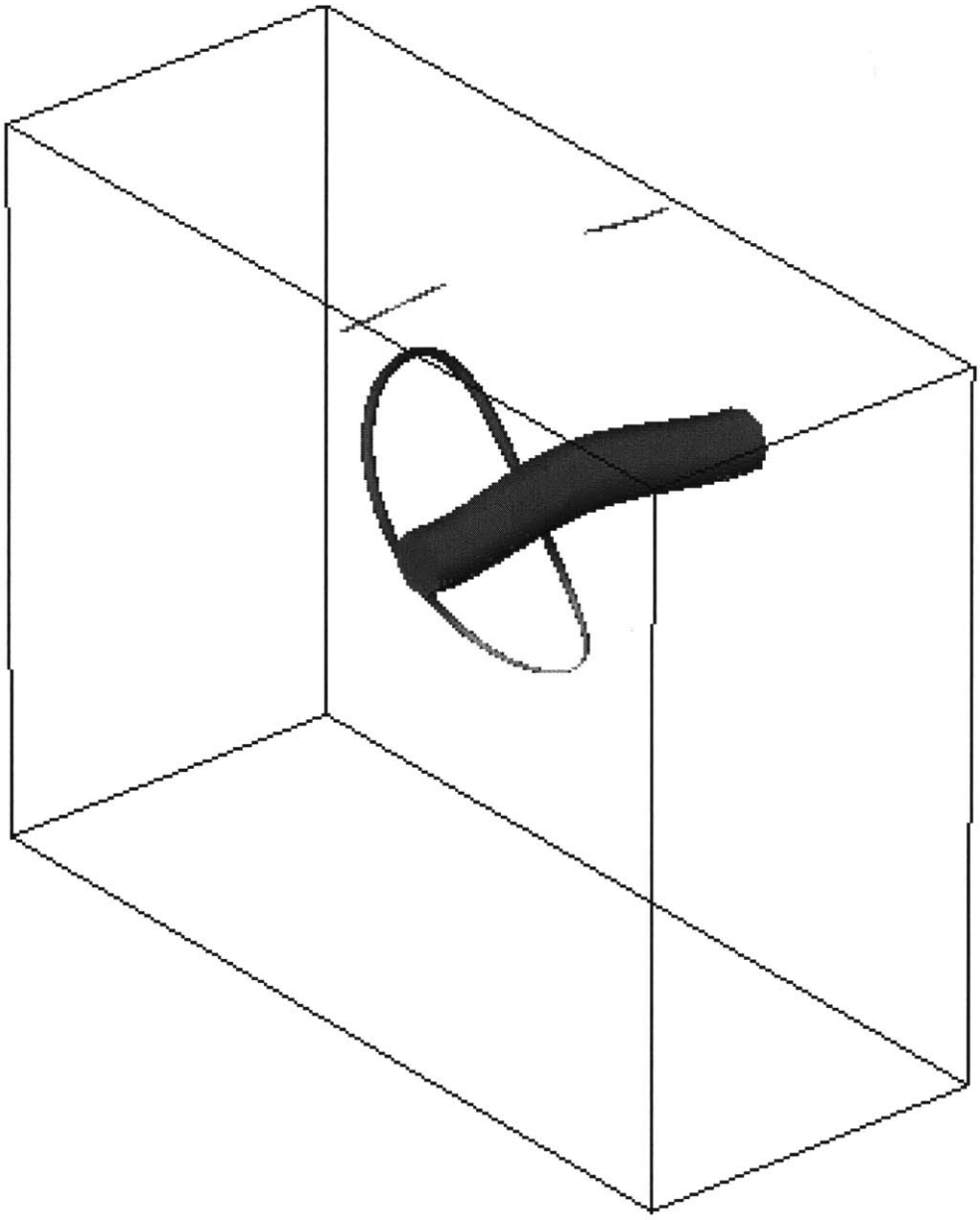

Figure 3-60: Vortex line representation of the primary and helical vortices. At $t = 9$, the interaction of helical vorticity and secondary vorticity leads to weakened connection (A+, A-) and a new ring structure (B). ($t = 9$, Ma=0.4)

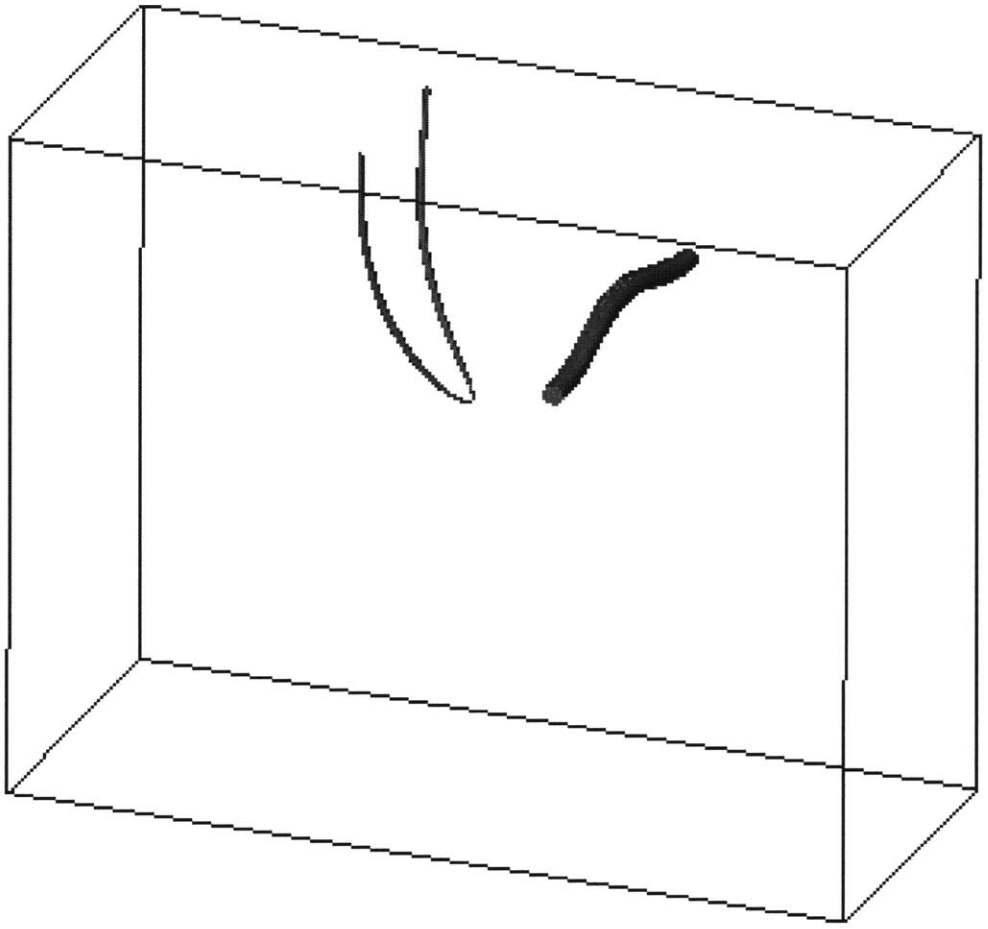

Figure 3-61: Vortex line representation of the primary and helical vortices. ($t = 10$, Ma=0)

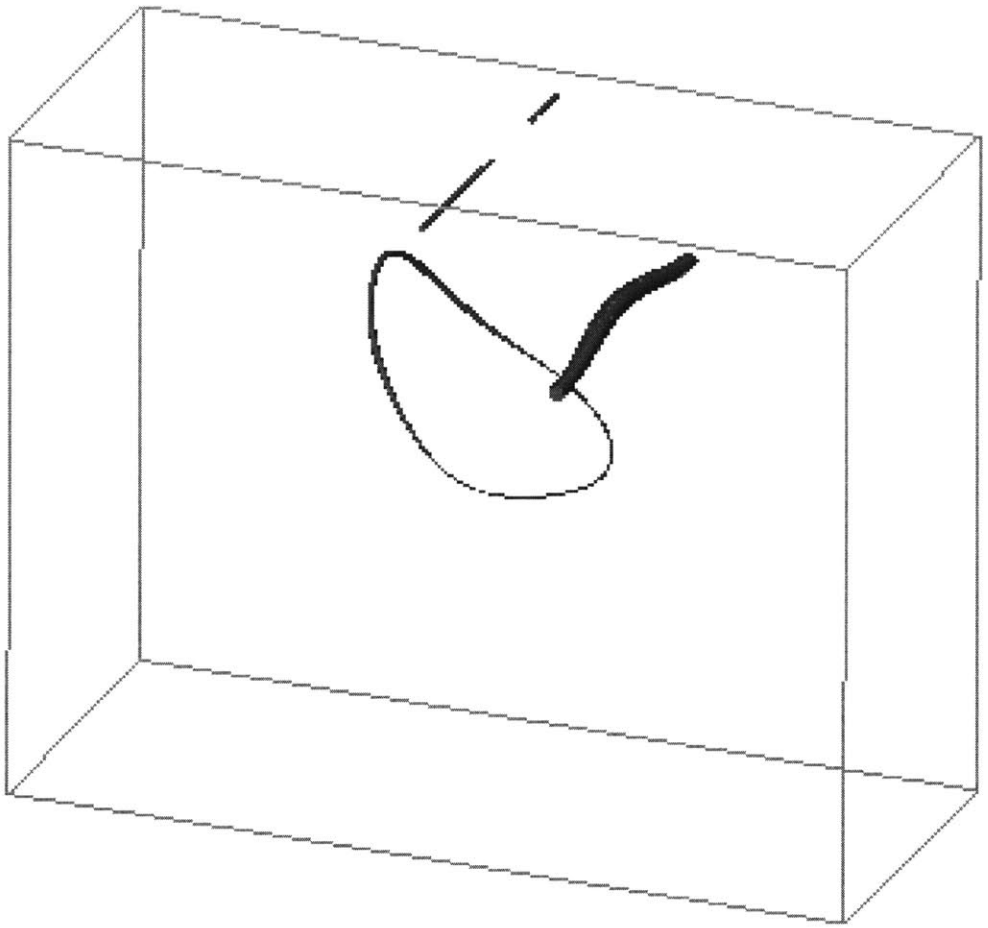

Figure 3-62: Vortex line representation of the primary and helical vortices. At $t = 8$, the interaction of helical vorticity and secondary vorticity leads to weakened connection (A+, A-) and a new ring structure (B). ($t = 10$, Ma=0.4)

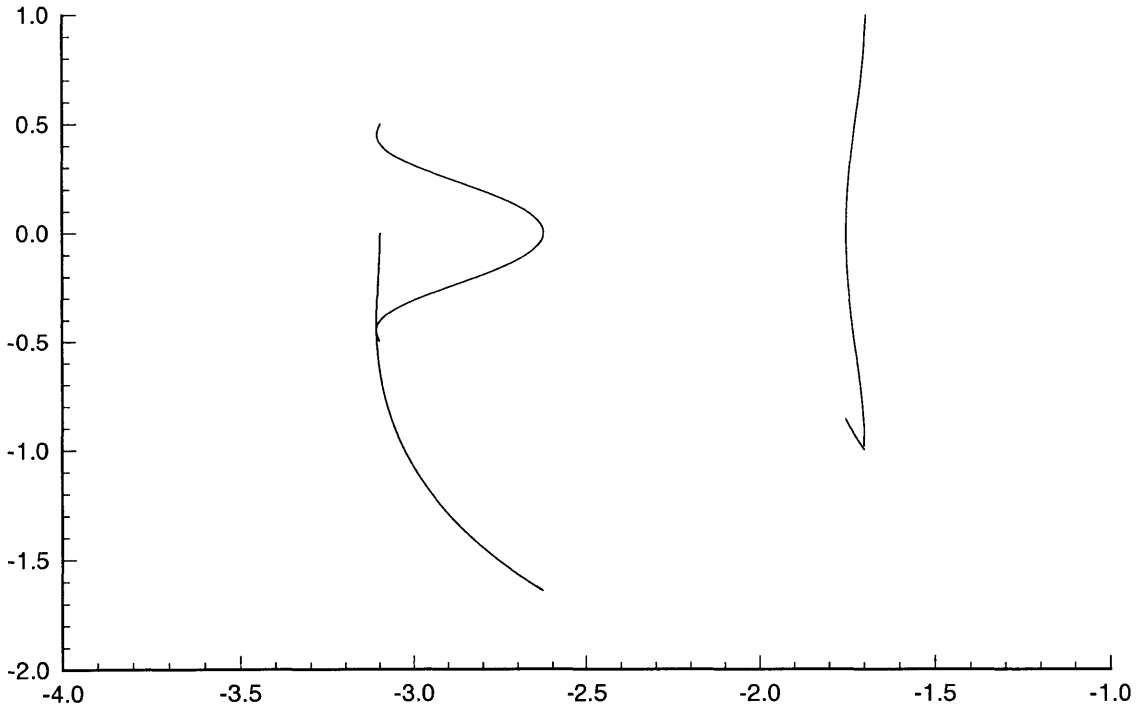

Figure 3-63: Primary connection and helical projection on $x - z$ and $x - y$ plane. (Vortex line representation of the primary and helical vortices.) ($t = 10$, Ma=0.0)

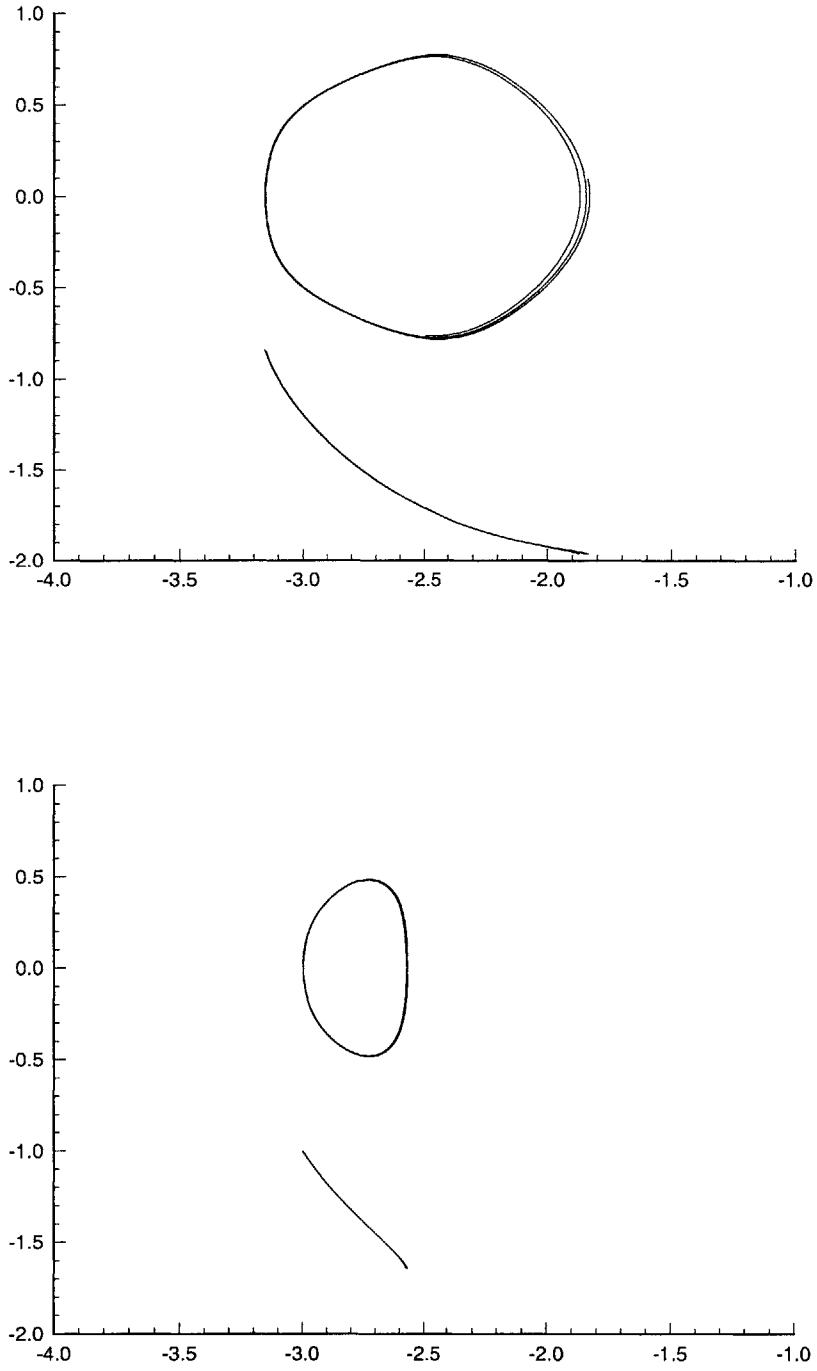

Figure 3-64: Surface spanwise elevation and mean elevation. (a) outer portion of the vortex ring; (b) inner portion of the vortex ring.

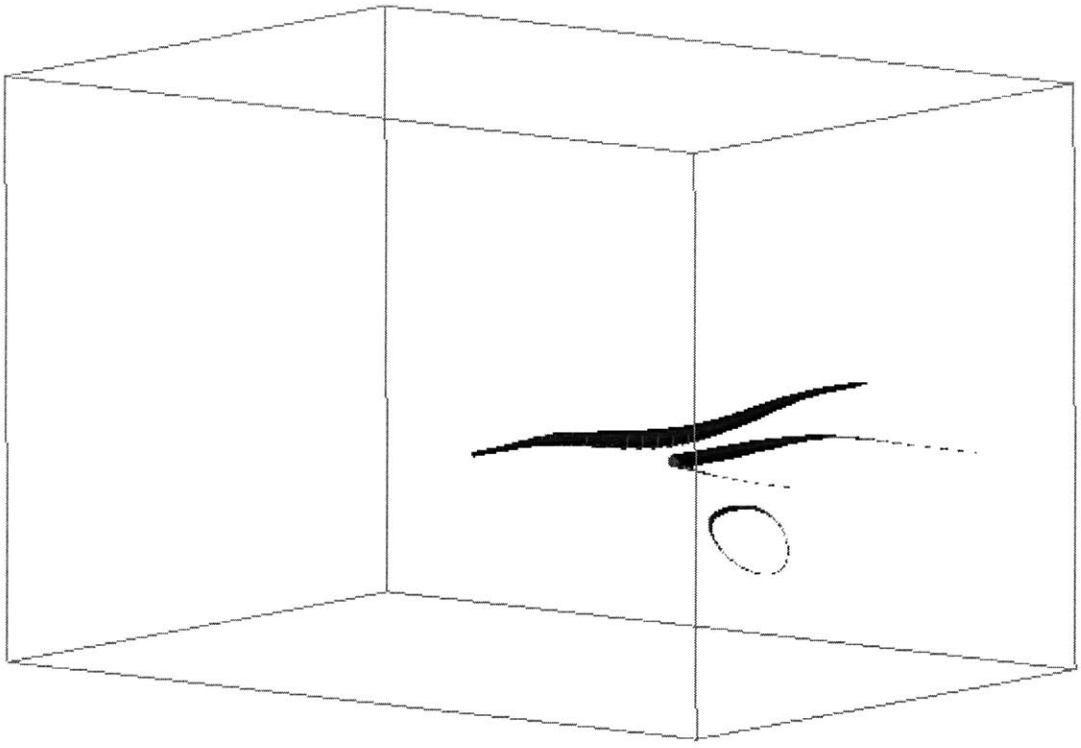

Figure 3-65: Transverse vorticity distribution

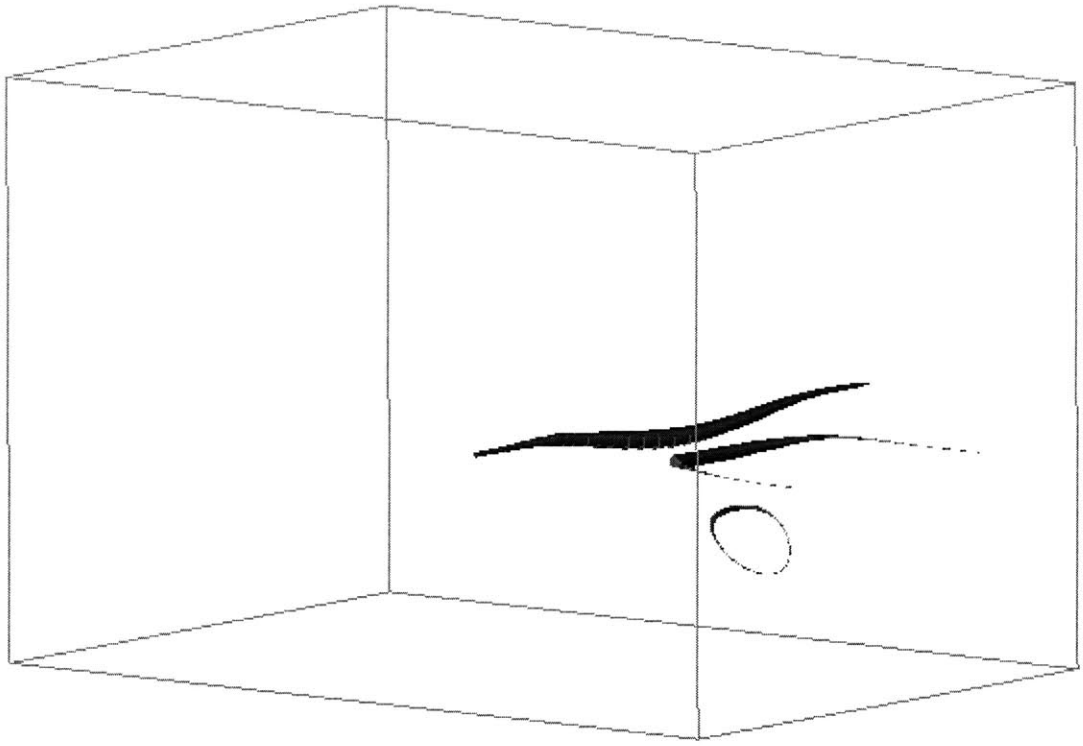

Figure 3-66: Helical vorticity bundle (a) projection of vortex lines on z plane; (b) projection of vortex lines on y plane; (c) vorticity magnitude along the vortex lines.

At the connection region, ω_z reaches its maximum at a small distance below the free surface (figure 28 for $\mathcal{M}a = 0$). This also shows the existence of a surface layer. Tangled vortex lines near the connection region can also be seen in figure 28, which convinces that the vortex cancellations do exist. In order to show that the vortex cancellation exists, one needs to use cross-diffusion, not dissipation.

3.5 Conclusions

We consider the effects of soluble and insoluble surfactants on laminar three dimensional vortical flows. Our surfactant model includes the convection-diffusion-sorption processes governing the evolution the evolution of bulk and surface surfactant concentration and their coupling to the free-surface vortical flow through the stress boundary conditions. The presence of surfactant decreases the connection of helical vorticity on the free surface. A new structure is generated because of the interaction between the helical vorticity and the secondary vorticity. For contaminated surface, only the

surface residue of the helical vorticity connects to the free surface. We anticipate that in free surface turbulence this kind of new structure will dominate the surface region.

Primary vortex driven secondary-helical vortices interaction is typical in the three dimensional surfactant flows. For the rebounding mechanism, in the ascending process, the major structure does not depend on the surfactant too much. When the primary vorticity reaches its top position, the surfactant effects take over. There is no head-tail on the structures in our simulation. There is also no thread and legs in our simulation. For Ma=0.4, the small connected vortices cannot sustain large dissipation and finally disappear.

For clean case, dissipation plays a minor role in the behavior of connected vortex. For contaminated case, the dissipation becomes significant because there is no strong vortex underneath the free surface to sustain the connection. In both cases, no threads exist (remnants of the primary tube). The interaction depends on the strength of the primary tube much more than on the viscous interaction time scale. New mechanism for helical vorticity interaction with secondary vorticity are presented in this thesis.

The above mechanisms have implications for turbulent flows and also provide possible approach in controlling near surface turbulence. If we adjust the location of secondary vortex by modifying surfactant concentration, the connection can be controlled.

Bibliography:

BARKER, S. J. & CROW, S. C. 1977, The motion of two-dimensional vortex pairs in a ground effect *vol. 82 J. Fluid. Mech.*

BERNAL, L.P., HIRSA, A., KWON, J.T. & WILLMARTH, W. W. 1989, On the interaction of vortex rings and pairs with a free surface for various amounts of surface active agent. *Phys. Fluids A1*, 2001-2004

GAINES, G.L. 1966, Insoluble Monolayers at Liquid-Gas Interface, Interscience.

SAFFMAN P.G. 1979, The approach of a vortex pair to a plane surface in inviscid fluid. *J. Fluid Mech.*, **92**, 47

OHRING S. & LUGT H. 1991, Interaction of a viscous vortex pair with a free surface.

J. Fluid. Mech., **227** 47

TSAI, W.T. & YUE, D.K.P. 1995, Effects of soluble and insoluble surfactant on laminar interactions of vortical flows with a free surface *J. Fluid Mech.*, **289**, 315-349

SARPKAYA T. 1983, Trailing vortices in homogeneous and density stratified media *J. Fluid Mech.*136, 85-109.

SARPKAYA T.& HENDERSON 1985, Surface scars ans striations. AIAA paper No. 85-0445.

SARPKAYA T. & SUTHON P. 1991, Interaction of a vortex couple with a free surface *Experiments in Fluids* 11, 205-217.

HIRSA A. AND WILLMARTH W. W. 1994, Measurements of vortex pair interaction with a clean or contaminated free surface *vol. 259 J. Fluid Mech.*

WILLERT, C.E. 1992, The Interaction of modulated vortex pairs with a free surface. Ph.D thesis, University of California, San Diego.

EDWARDS, D.A., BRENNER, H., &WASAN, D.T. 1991, Interfacial Transport Processes and Rheology, Butterworth-Heinemann.

DOMMERMUTH D.G. 1993, The laminar interactions of a pair of vortex tubes with a free surface *vol. 246 J. Fluid Mech.*

TRYGGVASON, G., ABDOLLAH,-ALIBEIK, J., WILLMARTH, W.W., & HIRSA, A. 1992, Collision of a vortex pair with a contaminated free surface *Phys. Fluids A 4, 1215-1229*

MELANDER & HUSSAIN 1990, Topological aspects of vortex connection. In *Topological Fluid Mechanics* (ed. H. K. Moffatt & A. Tsinober), pp 485-499. Cambridge University Press.

ANANTHAKRISHNAN & YEUNG 1994, Nonlinear interaction of a vortex pair with clean and surfactant-covered free surfaces. Wave Motion, 19, 343-365.

KIDA, TAKAOKA & HUSSAIN 1991, Vortex Ring Collision. *vol. 230 J. Fluid. Mech.*

Part II

Turbulent Flow over a Flexible Body Undergoing Fish-like Swimming Motion

Chapter 4

Introduction

Turbulent flow over a wavy wall undergoing traveling wave motion transversely to an incoming flow is intrinsically related to fish swimming. Taneda (1974) demonstrated in his experiment that when the wave velocity is smaller than the external flow, the boundary layer separates at the back of the wave crest, but when the wave velocity is larger than the uniform flow velocity, the boundary layer does not separate. He also observed that the traveling wave motion has a tendency to laminarize the flow and the fluid motion in the wave direction is accelerated. These striking results offer a challenge to turbulence researchers for theoretical understanding and also opportunity for engineers because of the new approach of turbulence control. His work motivated us to test his conclusions and to obtain detailed quantitative mechanisms. Few other publications on turbulence over traveling wavy wall exists other than Taneda's experiment. Benjamin (1959) provided a linear analysis for fixed, traveling, wavy motion between two fluids. Later Kendall (1970) studied experimentally the effects of traveling wavy wall for $ka = 0.18$. Even for this relatively small wave slope he observed a decrease in the pressure perturbation compared to flow over a fixed wavy wall.

Before considering a wavy wall, we review some results pertaining to flow over a curved surface. Measurements of turbulent boundary layers along a convex surface obtained by So & Mellor (1973) indicated that Reynolds stress was decreased on the convex side. Experimental work on boundary layer over concave surface are not as

extensive. but the opposite effect was observed by Eskinazi & Yeh (1956) for a concave surface. The effects of stabilizing or destabilizing forces on the turbulent motion by curved surface was first discussed by Prandtl (1930). Normal pressure gradients generated by centrifugal force can suppress surface normal momentum exchange for convex surfaces. Görtler (1940) observed that high Reynolds number laminar boundary layer flow over a concave surface develops an alternating sequence of rolling structures under certain conditions. Stability of this kind of flow falls into the Taylor and Görtler inertial instability which concerns rotating fluids. Bradshaw (1969) showed that an analogy between buoyancy-induced instability and curvature-induced instability can be achieved by using Richardson number. However, his analysis is only valid for non-separated flows. For compressible flow over a curved wall, Rotta (1967) calculated the contribution of the Coriolis force to energy production and found that compressibility enhances the wavy wall effects.

The flow over a wavy surface is subject to the effects of alternating convex and concave curvatures. A more complicated flow over surface with curvature is over wavy surface. This kind of flow is of importance because many natural surfaces consist of waves. The wavy motion strongly modifies all the flat wall turbulence results such as log law, streak and bursting structures. The effects of both convex and concave surfaces appear and separation may occur. Maass and Schumann (1994) obtained numerically turbulent flow field over a fixed wavy wall with small wave amplitude. An increase in the mean friction velocity at the wavy surface, compared to a flat surface, was observed. A few experiments were performed on the flow over fixed wavy boundary. Zilker *et al.* (1977, 1979) and Buckles *et al.* (1984) studied separated and non-separated turbulent flows over fixed wavy wall. They identified separation and reattachment points.

There are few published works available on turbulence near a flexible traveling surface merits further research in the subject. The traveling wave motion adds complexity to the problem because the surface motion is not simply the translation or rotation of a solid body surface since there are non-uniform surface extension or compression ($\nabla_s \cdot \boldsymbol{v} \neq 0$, where ∇_s is surface divergence operator and $\boldsymbol{v}$ is surface

velocity vector). This problem is of physical importance because it may offer a new approach to controlling turbulence, obtaining drag reduction, and generating thrust. The energy input to and extracted from the flow by the boundary motion becomes significant and the mechanisms are not well known. There are several additional kinematic and dynamic parameters involved in flexible boundary turbulence, for example, more length scale from wave amplitude and wave length, more velocity scale (wave speed) and time scale (wave period) to complicate the already multiscale wall turbulence problem. This flow configuration has implications in fish swimming because of similarity in boundary movement with certain type of fish swimming mode. It has been observed that fish surface undergoes wavy motion at a phase speed slightly higher than its forward moving speed when swimming at a fixed speed. There is evidence that fish is capable of achieving high efficiency in thrust production, drag reduction, and wake control through evolution. In order to apply fish locomotion mechanism to the design of new generation underwater vehicle, one needs to accurately predict drag, thrust, transition and turbulence level.

There are two types of drag reduction techniques available – passive and active techniques. Passive approach requires no energy input and a net gain can be achieved. Active approach usually involves body motion or suction/blow of fluid and can achieve higher level of drag reduction. LEBU (large eddy break-up devices) is showing enormous promise.

There are several key differences of this flow from fixed wavy wall flow. The traveling wavy motion of the surface which is normal to the incoming flow displaces the boundary layer non-uniformly and may generate pressure thrust or drag which is absent in flat wall flow. The surface normal pressure gradient which is proportional to c^2 increases dramatically with c and we expect that flow field displays great deviation from fixed wavy wall case. Typical evidence of the effects of surface normal pressure gradient is the flow over an angular oscillating cylinder, in which case separation is suppressed. Drag coefficient of stationary cylinder is 1.35, while for a motioncontrolled cylinder, the drag coefficient is only 0.2. It will be shown that the flow over a wavy wall exhibits similarity to flow over a rotationally oscillating cylinder. The phase speed c

of the wave can also be interpreted as Strouhal number in the sense that if there is vortex shedding, c corresponds to vortex shedding rate. Wavy wall motion generates extra near surface vorticity (positive or negative) and the shedding of this vorticity may create a thrust. If viewed in a system moving with wave speed, the surface slides non-uniformly in its tangential direction. Longuet-Higgins (1969) showed that sinusoidal shear stress is dynamically equivalent to a pressure force on the wave. Our periodic and non-periodic simulations confirm that. Pressure distribution mechanism over wavy surface without separation is discussed by Miles' inviscid theory (1957, 1959).

In the area of steady, live fish locomotion, Gray (1936) observed that c/U decreases as wave speed increases. He also showed that the distribution of wave speed is non-uniform and reaches its maximum at the tail. Wu (1961) developed a theory for the swimming propulsion mechanism of a plate moving at variable forward speed in an inviscid fluid. Barrett *et al.* (1999) showed experimentally that the power required to propel a swimming body is smaller than the power needed to tow the straight-rigid body at the same speed U. In order to understand fish swimming propulsion, there are two interdependent aspects of the problem need to be studied: (1) the nature of the force resisting the motion, and (2) the mechanisms that lead to the thrust force. The usually defined "flapping foil" mechanism can be further divided into two cases. One is sinusoidal motion in amplitude, and another is sinusoidal motion in orientation. Total different mechanisms are present for these two cases and our simulations focus on amplitude oscillation. We believe, in most experiments, the observed drag reduction is in fact due to thrust generation.

This paper applies direct numerical simulation (DNS) to study turbulent boundary layer flow over a traveling wavy wall. One of the key issues is the effect of c/U on turbulence amplification and suppression. Due to the multi-parameter nature of the problem, considerable amount of simulation is needed for a reasonable understanding of the turbulence behaviors involved. In this paper, we emphasize on the comparison for the effects of c/U, rather than on the flow analysis of one particular c/U case. We first study flow properties for small amplitude wave to obtain leading order effects

which are easier to interpret. Then we go on to nonlinear large wave amplitude, for which case separation occurs at $c/U = 0$. The flow is simulated in both periodic and non-periodic streamwise coordinate systems. Two aspects of this problem which will be discussed which are: (1) the effects of wavy motion on the turbulent properties, and (2) the averaged force and power balance on the body (wavy surface). For a steady swimming motion maintained by pressure thrust created over the whole body, the vorticity shed at the tail is not important for thrust generation. Some relevant questions are answered in this paper, such as whether turbulence decays uniformly as a function of c/U, or any local minimum and maximum of laminarization exist. This analysis, if applied to fish swimming, can resolve some existing misunderstandings about drag reduction. The paper is organized as follows: the problem definition and numerical method is stated in §2. §3 contains results which include statistics, Reynolds evolution analysis, force and power balance, and Reynolds number effects. §4 summarizes and discusses the results.

Chapter 5

Problem definition and numerical method

In this chapter, we first define the physical problem studied in this paper, which is the turbulent flow over a flexible wall. Coordinate systems, governing equations and boundary conditions are given. Then we introduce the numerical scheme and its validation.

5.1 Problem definition and governing equations

We consider the motion of a three dimensional incompressible boundary layer flow near a wall undergoing sinusoidal motion. As shown in figure 5-1, the flow is in the frame (x', y', z') where x', y' and z' are streamwise, vertical and spanwise coordinates, respectively. Developed turbulent boundary layer flow or uniform turbulent flow enter the frame from the left. The surface is undergoing a one-dimensional wavy motion. Its amplitude can vary as a function of time and streamwise location. The surface profile shown in figure 5-1 has a wave magnitude proportional to the distance from the leading edge. This motion resembles what is observed in a live tuna. Even though only flow over one side of a two dimensional body is simulated, the results are reliable for the understanding of power dynamics of fish swimming if three dimensional effects are insignificant and there is no wake.

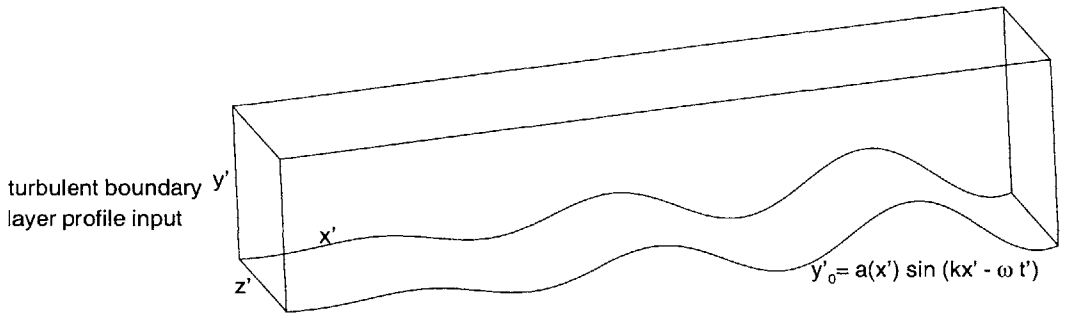

Figure 5-1: Sketch of the physical problem (fixed with wall). The coordinate system x'-y' is fixed in space. Turbulent inflow enters at the left boundary.

Two approaches can be used to simulate this problem. The simpler one is to follow the wave crest, ignore wave amplitude variation, and use periodic streamwise boundary condition. The advantage of this approach is its numerically simplicity because it is a steady simulation in terms of boundary conditions and there is no turbulence inflow condition. For periodic simulation, two methods are available in terms of boundary conditions. The one used by existing fixed wavy wall simulation is to modify channel flow simulation by replacing one flat wall with a wavy wall. The disadvantage of this approach is that it limits the simulation to shear flow over an infinite wave train and the turbulent shear stress is different from that of boundary layer flow. Another periodic approach is to use free slip boundary condition at the far field and impose boundary layer profile and velocity fluctuations at the start of the simulation. A time-dependent streamwise pressure gradient has to be imposed to maintain the mean flow. A much more complicated approach is through non-periodic simulation which describes turbulent boundary layer profile and its development more accurately and is able to provide various upstream inflow conditions. We discuss periodic simulation first, and then go on to non-periodic simulation.

The geometric configuration of the physical flow field is shown in figure 5-1. The problem involves a uniform flow U over a flexible wavy wall specified by the sinusoidal

function

$$y_0' = a(x')\sin(kx' - \omega t') = a(x')\sin k(x' - ct'), \tag{5.1}$$

where $k = 2\pi/\lambda$ is the wave number, ω the frequency and $a(x')$ the wave amplitude. The flow is from left to right. In this study, the propagation direction of the wave (positive ω/k) is chosen to be the same as that of the uniform flow. In this laboratory coordinate system, any point on the wall possesses an up-down oscillation with velocity components given by

$$\begin{cases} u'_{wall} = 0, \\ v'_{wall} = -\omega\, a(x')\cos(kx' - \omega t'), \end{cases} \tag{5.2}$$

Thus the motion of the wall behaves like a traveling wave of phase speed $c = \omega/k$. Here u'_{wall} and v'_{wall} are the horizontal and vertical velocity components, respectively.

For convenience, we define a moving coordinate system x-y which moves horizontally at the wave speed c if the wave amplitude $a(x')$ is a constant. Clearly the x-y coordinate system is related to the fixed x'-y' system by the Galilean transformation

$$x = x' - ct',\ y = y',\ t = t'. \tag{5.3}$$

In the moving coordinate system, the wall position becomes fixed ($y = a\sin(kx)$) and the velocity field on the wall becomes steady:

$$\begin{cases} u_{wall} = -c, \\ v_{wall} = -\omega\, a\cos(kx). \end{cases} \tag{5.4}$$

Notice

$$\frac{\partial v_{wall}}{\partial x}|_{wall} = \omega\,(ka)\sin(kx), \tag{5.5}$$

this velocity gradient contributes to surface shear generation, which will be discussed in later sections.

Since

$$\frac{v_{wall}}{u_{wall}} = \frac{-\omega a\cos(kx)}{-c} = (ka)\cos(kx) = \frac{dy}{dx}, \tag{5.6}$$

the velocity on the wall is along the tangential direction with space varying magnitude

$V_t(x)$:

$$|V_t| = [c^2 + (c\,(ka)\cos(kx))^2]^{1/2} = c[1 + (ka)^2\cos^2(kx)]^{1/2} \geq c, \tag{5.7}$$

and the normal velocity on the wall $V_n(x)$ is always zero. At wave nodal points, V_t reaches its maximum value of $c[1 + (ka)^2]^{1/2}$, and at crest and trough, V_t retains its minimum c. Therefore there is a tangential acceleration along the wall.

The flow is assumed to be homogeneous in the spanwise direction and the boundary is always periodic in that direction. For periodic simulations, the above velocity field (4) is used on the wall as no-slip boundary condition. Uniform shear or free slip condition can be applied on the upper boundary. In the horizontal direction, only one or two wavelengths of the flow is simulated because simulation of larger domain shows similar features and most of the scales are smaller than one wavelength by comparing velocity correlation function with runs with more wavelengths. Two methods are available to impose random initial flow condition. One is to add random velocity fluctuations to flat wall mean velocity profile and gradually increase wave amplitude until the desired amplitude is reached. Another way is to apply initial random flow to wavy wall laminar profile and let the simulation proceed. The second method is applied in our periodic simulation because the first approach leads to longer simulation and thus stronger turbulence decay.

The motions of the flow are described by the Navier-Stokes equations

$$\frac{\partial \boldsymbol{u}}{\partial t} + \boldsymbol{u} \cdot \nabla \boldsymbol{u} = \frac{1}{\mathcal{R}_e}\nabla^2 \boldsymbol{u} - \nabla p, \tag{5.8}$$

together with the continuity equation

$$\nabla \cdot \boldsymbol{u} = 0, \tag{5.9}$$

where $\boldsymbol{u}$ is the velocity vector with components u, v, w in x, y and z directions respectively, p the dynamic pressure, $\mathcal{R}_e = UL/\nu$ the Reynolds number, and ν the kinematic viscosity. The equations have been normalized by a characteristic length L, a velocity scale U, and the density of the bulk fluid ρ. For our numerical formulation, U is incoming flow velocity and L is wavelength $2\pi/k$, where k is wave number of the

surface wavy motion. Mean values are denoted by $<>$ or overbar. Averaging over z is denoted by $<>_z$ and averaging over both y and z is denoted by $<>_{yz}$ We use u, u_{rms}, u' to denote instantaneous velocity, root mean square fluctuating velocity and fluctuating velocity respectively.

5.2 Numerical methods and validation

The primitive-variable form of Navier-Stokes equations and continuity equation are solved numerically as an initial-boundary-value problem. We first use a projection method, which couples the continuity equation with the momentum equations, to obtain a Poisson equation with a divergence correction for the pressure. The Poisson equation for the pressure is solved at each time step. The simulation is then advanced implicitly to next step.

For our moving boundary problem, we need to use the following coordinate transformation to achieve fine grid distribution in the boundary layer.

$$\begin{cases} x = x(\xi, \eta), \\ y = y(\xi, \eta), \end{cases} \tag{5.10}$$

where (x, y) are the variables in the physical domain and (ξ, η) are those of transformed domain. The governing equations and Poisson equation can thus be written as follows by the above transformation:

$$\begin{aligned} \tilde{\Delta} p = &-[(y_\eta u_\xi - y_\xi u_\eta)^2 + 2(x_\xi u_\eta - x_\eta u_\xi)(v_\xi y_\eta - v_\eta y_\xi) + (x_\xi v_\eta - x_\eta v_\xi)^2]/J^2 \\ &+(y_\eta u_\xi - y_\xi u_\eta + x_\xi v_\eta - x_\eta v_\xi)/(J\Delta t), \end{aligned} \tag{5.11}$$

$$\begin{aligned} u_t + \frac{uy_\eta - vx_\eta}{J} u_\xi + \frac{vx_\xi - uy_\xi}{J} u_\eta + w\frac{\partial u}{\partial z} \\ = -\frac{y_\eta p_\xi - y_\xi p_\eta}{J} + \frac{1}{Re}\tilde{\nabla} u, \end{aligned} \tag{5.12}$$

$$v_t + \frac{uy_\eta - vx_\eta}{J} v_\xi + \frac{vx_\xi - uy_\xi}{J} v_\eta + w\frac{\partial v}{\partial z}$$

$$= -\frac{x_\xi p_\eta - x_\eta p_\xi}{J} + \frac{1}{Re}\tilde{\nabla} v, \tag{5.13}$$

$$w_t + \frac{uy_\eta - vx_\eta}{J} w_\xi + \frac{vx_\xi - uy_\xi}{J} w_\eta + w\frac{\partial w}{\partial z} = -\frac{\partial p}{\partial z} + \frac{1}{Re}\tilde{\nabla} w, \tag{5.14}$$

where

$$\tilde{\nabla} A = (\alpha A_{\xi\xi} - 2\beta A_{\xi\eta} + \gamma A_{\eta\eta})/J^2 + [(\alpha x_{\xi\xi} - 2\beta x_{\xi\eta} + \gamma x_{\eta\eta})(y_\xi A_\eta - y_\eta A_\xi) + (\alpha y_{\xi\xi} - 2\beta y_{\xi\eta} + \gamma y_{\eta\eta})(x_\eta A_\xi - x_\xi A_\eta)]/J^3, \tag{5.15}$$

$$J = x_\xi y_\eta - x_\eta y_\xi, \tag{5.16}$$

$$\alpha = x_\eta^2 + y_\eta^2, \tag{5.17}$$

$$\beta = x_\xi x_\eta + y_\xi y_\eta, \tag{5.18}$$

$$\gamma = x_\xi^2 + y_\xi^2. \tag{5.19}$$

For our simulation, the boundary layer thickness is less than or comparable to the wave amplitude. For periodic case, since the shear rate near the flexible boundary is not the same for every c/U case, initial turbulence cannot be scaled by local shear rate if we want to make a direct comparison of turbulent intensities. Doing so we are not imposing the same amount of turbulence to the flow field. For periodic simulations, at the same location, the same fluctuation (relative to mean flow velocity) was added to the initial laminar wavy wall velocity field for every c/U. Like flow over cylinder, there is Reynolds number constraint in numerical simulation. For flat surface such constraint is less severe. For periodic simulation, in order to avoid rapid decrease in turbulent energy for the Reynolds number simulated, in the initial stage of simulation, larger time-decreasing Reynolds numbers are used. The validity of streamwise dimension is confirmed by scale analysis. Since our priority is to compare turbulence behavior for various c/U values, it is not crucial to have a fluctuation field which is perfectly appropriate for a particular case. The initial condition is set to be similar to available turbulent boundary layer flow results.

For non-periodic case, there is a need to input turbulence at the inflow boundary. The wall shear stress or the friction velocity are both functions of time. Two separate runs are needed for non-periodic simulation. The first run generates the boundary conditions at the inflow boundary for the second run which really simulates the boundary layer wavy wall flow. First run can be boundary layer over flat wall or homogeneous turbulence depending on the input requirement. Because of the no-slip boundary, it takes much longer for the near surface features to cover the whole computational domain and thus the second run is time consuming.

Procedures for simulating non-periodic turbulent boundary layer flow are explained as follows. (1) Set up a mean flow field in the computation domain. This mean flow field is determined by the turbulent boundary layer at the given Reynolds number. This mean flow field will evolve laminarly before turbulence arrives. (2) Run flat wall turbulence input with periodic boundary conditions. The Reynolds number is set to be equal to the leading edge Reynolds number of the wavy wall. The run stops when the surface layers are apparent. For this simulation, much less grid is applied outside the boundary layer, so that longer streamwise dimension can be achieved. (3) Obtain input condition $p, u, v, w(x = x_0, y, z, t)$ from (2). (4) Match the initial flow field input $p, u, v, w(x = x_0, y, z, 0)$ with the laminar input in (1). Artificially impose the fluctuating velocity at a few vertical layers near the left boundary. (5) Keep inputing turbulence at the inflow boundary as the simulation goes on. (6) Stop when the input data runs out. Based on the above procedures, the streamwise growth of boundary layer is determined numerically. The Kolmogorov length scale $\eta = (\mu/\epsilon)^{1/4}$ is the smallest scale that needs to be resolved and in our simulation is about the same as the minimum vertical grid scale. For all these simulations, results along four stations on the wall are shown. The viscous wall region is well resolved assuming the smallest scales for wavy motion is comparable to the flat wall case. If the structures generated in the trough region can be sustained in non-periodic simulation, there is not too much difference in global flow properties for periodic and non-periodic cases. For non-periodic boundary condition, the end portion of the flow field is discarded for accuracy in calculating total force.

For periodic boundary condition, the pressure gradient on the wavy wall can be written as

$$p_\eta = (x_\eta \tilde{\Delta} u^{n+1} + y_\eta \tilde{\Delta} v^{n+1})/Re - (x_\eta u_\eta^{n+1} + y_\eta v_\eta^{n+1}) \frac{v^n x_\xi - u^n y_\xi}{J} - y_\eta v_\xi^{n+1} \frac{u^n y_\eta - v^n x_\eta}{J}. \quad (5.20)$$

For non-periodic boundary condition case, the pressure boundary can be written as ($u = 0$ on the wall):

$$p_\eta = (x_\eta \tilde{\Delta} u^{n+1} + y_\eta \tilde{\Delta} v^{n+1})/Re - y_\eta v_t \quad (5.21)$$

$$- y_\eta v \frac{v_\eta^{n+1} x_\xi - v_\xi^{n+1} x_\eta}{J}, \quad (5.22)$$

where $\tilde{\Delta}$ is the Laplace operator in the transformed frame. Because most of the flow properties remain the same at certain wave phase, we usually show flow field for one wave length because that is enough to describe the flow field at any surface locations.

The numerical simulation cost increases at wave amplitude increases. The simulation of $ka = 0.75$ costs 20 times more than a flat wall simulation. All the simulations use variable grid spacings with maximum resolution near the bottom surfaces. Most results are presented for wave amplitude 0.5 or 0.75 and the wave length is 1 in terms of wavelength λ. The computational domain non-dimensionalized by the wavelength is $2.5 \times 1 \times 1$ in the x, y and z directions, respectively. The resolution of the simulation is $L_x \times L_y \times L_z = 256 \times 121 \times 120$. We assume the flow is homogeneous over z axis, and averaging over z is usually performed first. In order to show near surface feature, only the bottom portion of the flow field is shown and for certain features, one or less than one wavelength is shown. Our typical run is for a Reynolds number based on the boundary layer thickness is in the range of 2400, corresponding to a global Reynolds number (length scale $L = \lambda$) of 6000. The first grid point away from the wall is at $y^+ = 0.1$, and is comparable to the corresponding grid spacing used by Kim *et al.* (1987) for their channel flow simulation. The maximum grid spacing is about $\Delta y^+ = 5.0$. There are about five grid points between $0 < y^+ < 1$ and about eight grid points between $1 < y^+ < 10$.

Chapter 6

Results

Wave phase speed relative to mean velocity c/U and wave slope ka are two major parameters that control wavy motion characteristics. Wave slope induces expansion and contraction of streamlines which result in pressure gradient in both surface tangential and normal directions. As wave speed increases, the centrifugal pressure gradient induced by the wavy motion takes control and determines the total force.

Statistical presentation of the flow field is provided in this section. Because the statistical quantities are not uniform in x-y plane, physical quantities are first averaged over spanwise direction and in time to give statistics that are functions of both x and y. If necessary, they are integrated over y and then x to show the streamwise dependence and collective effects. Because we are interested in discovering the effects of c/U, some of the statistics are compared between $c = 0.4U$ ($c < U$) and $c = 1.2U$ ($c \geq U$). However, for some turbulent properties, $c = 0.4U$ is not typical of all $c < U$ cases. When necessary, cases with other c/U values are provided to elucidate certain features. Mean velocity, turbulent intensities, effects of small wave amplitude, surface pressure, friction distribution and power balance are studied.

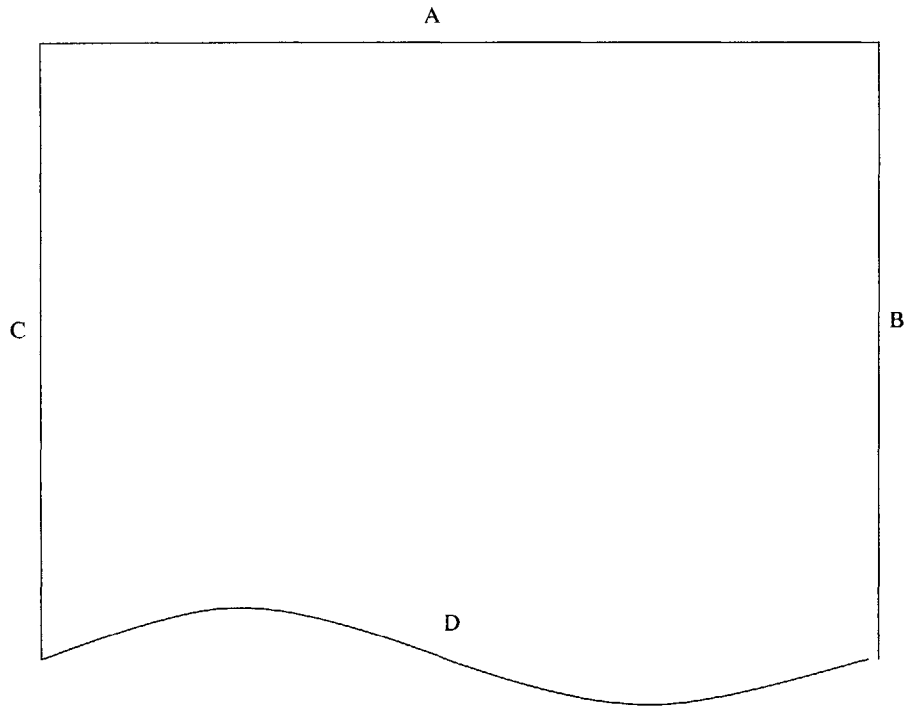

Figure 6-1: Total vorticity calculation.

6.1 Some basic features of wavy wall motion

The total vorticity in the domain is affected by the wavy motion. We can study the circulation for one wavelength, as seen in figure 6-1. On the four sides of the domain. On the path B and C, the total circulation is zero, on the path A, the circulation is $\Gamma_A = \int_A v dl = (U - c)\lambda$. The velocity integral over path D is $\Gamma_D = \int_D v dl = \int_0^\lambda c\sqrt{1 + (\frac{dy}{dx})^2}\sqrt{1 + (\frac{dy}{dx})^2}dx = c\lambda(1+0.5(ka)^2)$. So the total vorticity over a wavelength is $\Gamma = (U-c)\lambda + c\lambda(1+0.5(ka)^2) = U\lambda + 0.5c\lambda(ka)^2 = 2\pi U(\frac{1}{k} + 0.5\frac{a^2kc}{U})$.

From the above formula, we can see that if U, a, c are fixed, the circulation reaches minimum at $k = \frac{1}{a}\sqrt{\frac{2U}{c}}$.

6.2 Mean flow profile

The mean streamline pattern of the flow over traveling wavy wall is affected strongly by the wave speed especially in the wave trough region. For $c/U = 0$, streamlines do

not start or end on the surface, and separation can be determined just by locating dividing streamlines. For non-zero c/U, streamlines emanating from the surface have to end on the surface as well.The variation of mean streamline and mean velocity magnitude ($\sqrt{< u >_z^2 + < v >_z^2}$) contour patterns with wave velocity is shown in figure 6-2. Here the average is taken over z and a few phases. Streamline patterns are shown on the left and velocity magnitude contours are shown on the right. Arrows on the streamlines denote the flow direction. For $c/U = 0$, the streamlines (a1) clearly show that there is separation bubble at the wave trough and a free shear layer exists. The recirculating zone reaches maximum thickness of 0.18 at $x/\lambda = 0.68$. Velocity magnitude distribution shown in figure 6-2(a2) indicates that away from the separation region maximum velocity gradient is very close to the boundary. Downstream the separation point the velocity magnitude contours scatter as is typical of the flow field after separation. Because of the interaction between successive waves, the diverged velocity magnitude contours converge after reattachment point. The separation extends approximately from $x = 0.44$ to $x = 0.86$ from the streamline pattern. For $c/U = 0.4$, the separation bubble disappears and the streamlines near the wave trough bear the same curvature (concave as shown in the figure) as the wave profile. The velocity gradient downstream the wave crest decreases dramatically at this c/U and increase again downstream of the wave trough. For $c/U = 1.2$, the streamlines near the wave trough exhibit a curvature to the opposite direction of the wave trough and surprisingly, maximum velocity gradient does not happen on the surface, but rather at a small distance away from the wave crest. From $c/U = 0.0$ to $c/U = 1.2$, the streamline pattern near the wave trough changes from closed separation bubble to open streamlines with both ends on the surface. The region with open streamlines expands as c/U increases and at $c/U = 1.2$, occupies the whole surface. Another feature for $c/U = 1.2$ is that the velocity distribution is less scattered as other two cases. The mean flow pattern for these three c/U values show distinct flow features which affect turbulent behavior. If the streamlines and velocity magnitude contours are examined at the same time, one can notice that there is strong acceleration and deceleration in the mean flow near the boundary. Generally speaking, for streamlines emanating from the surface, a fluid particle first accelerates before

reaches maximum velocity and then decelerates to wall velocity. This behavior is more clear for $c/U = 1.2$. Near the wave crest, for $c/U = 1.2$, velocity contours are closed with both ends on the surface. The velocity magnitude contour configuration is complicated for big c/U because total velocity magnitude on the surface varies from 0 to $(ka)c$ and increases with c. One key difference of separating flow near a fixed and a flexible body is that for the latter case the separation and reattachment points, if they exist, are not located on the surface. Based on our simulation, there is no separation (mean reverse flow) for $0.35 < c/U < 1.60$. Because of the boundary motion, the location with zero shear stress on the surface does not mean separation. At locations with zero mean shear there may be a velocity deflection point. However, as long as the boundary is moving and there is a positive velocity component in the tangential direction on the surface, flow separation does not happen.

For uniform flow near flexible wall, negative mean velocity is one indication of separation. For flow near flexible boundary, the separation criteria for fixed surface, such as negative mean shear stress, are not valid. Usually, separated region is highly disturbed and exhibits very large fluctuations. The contours of $< u >_z$ and $< v >_z$ are shown in figure 6-3. Notice for $c/U = 0$, near the wave trough there is negative $< u >_z$ which is a consequence of separation. For other two cases, there is no negative $< u >_z$. The vertical velocity contour $< v >_z$ in (b2) and (b3) confirms the sign of curvature of the streamlines near wave trough in figure 6-2(b1) and (c1).

If the streamlines are plotted in a frame moving with the wave, the flow pattern totally changes. In the moving frame, the body is fixed with surface sliding velocity. Physically it is still a reasonable frame to observe the flow. Plotted in figure 6-4 are the mean streamline patterns in the moving frame for $c/U = 0.4$ and 1.2. It is evident that there is trapped vortex located near the negative wave slope region for $c = 0.4U$. This trapped vortex does not exist even in moving frame for $c = 1.2U$.

Because of separation and possible turbulent suppression and amplification involved with wavy wall motion, it is expected that the log law is no longer valid. However, we can calculate surface shear velocity and obtain the profile and make a

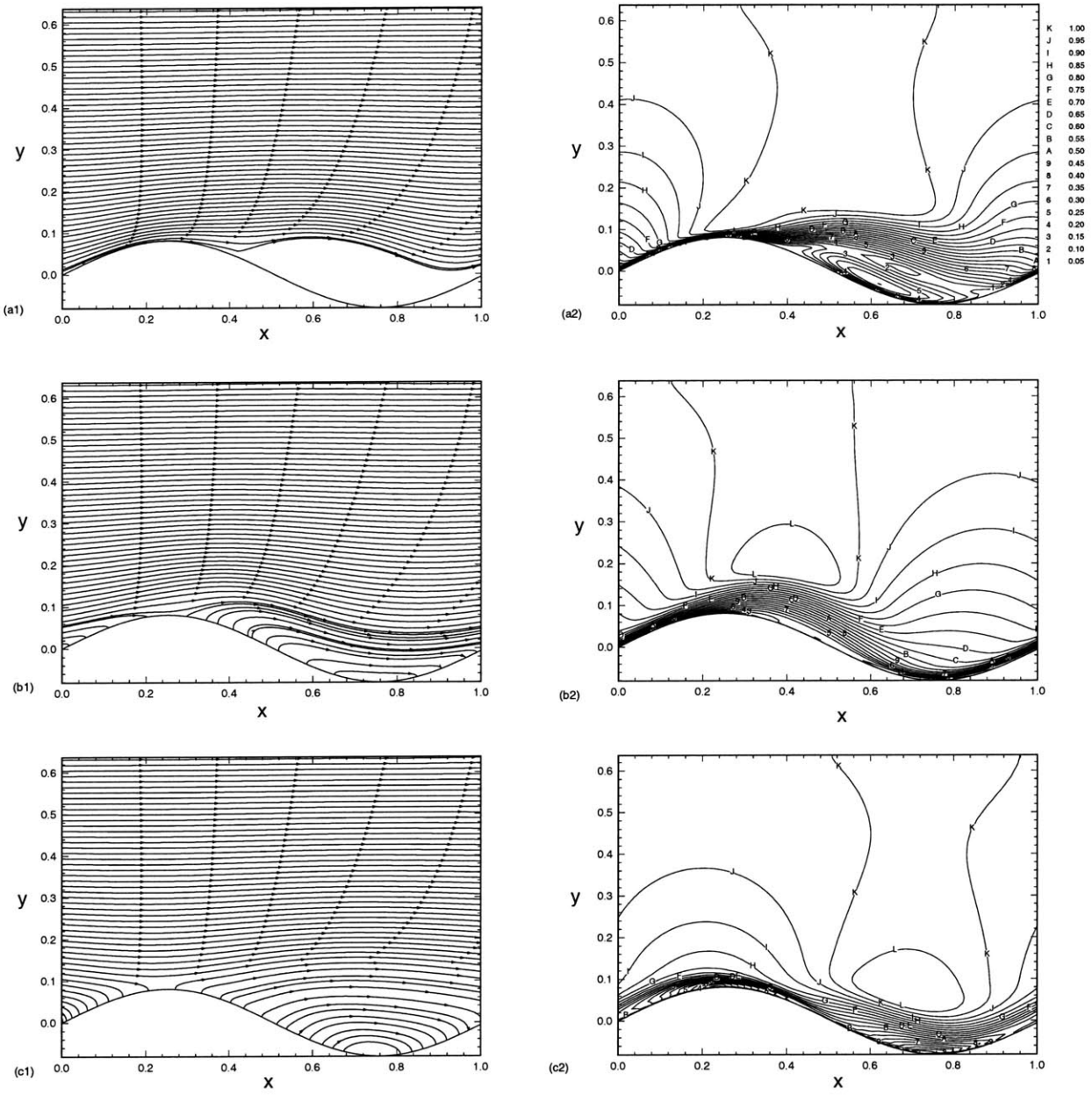

Figure 6-2: Streamline pattern for c/U = (a1) 0.0, (b1) 0.4, (c1) 1.2; and velocity magnitude distribution for c/U = (a2) 0.0, (b2) 0.4, (c2) 1.2.

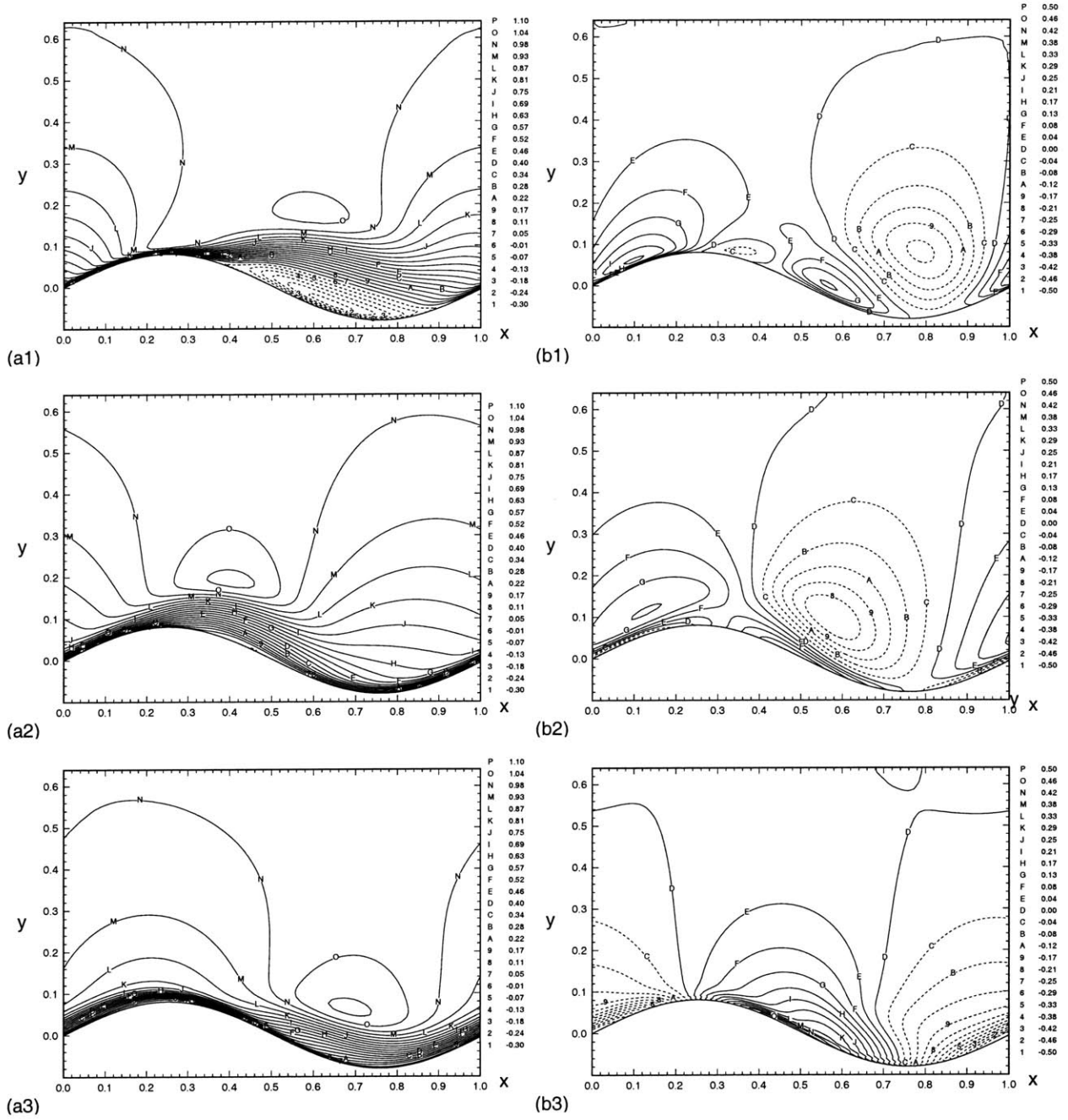

Figure 6-3: Mean velocity distribution $< u >_z$ for c/U = (a1) 0.0, (a2) 0.4, (a3) 1.2; and $< v >_z$ for c/U = (b1) 0.0 (b2) 0.4, (b3) 1.2. Dashed lines are for negative values.

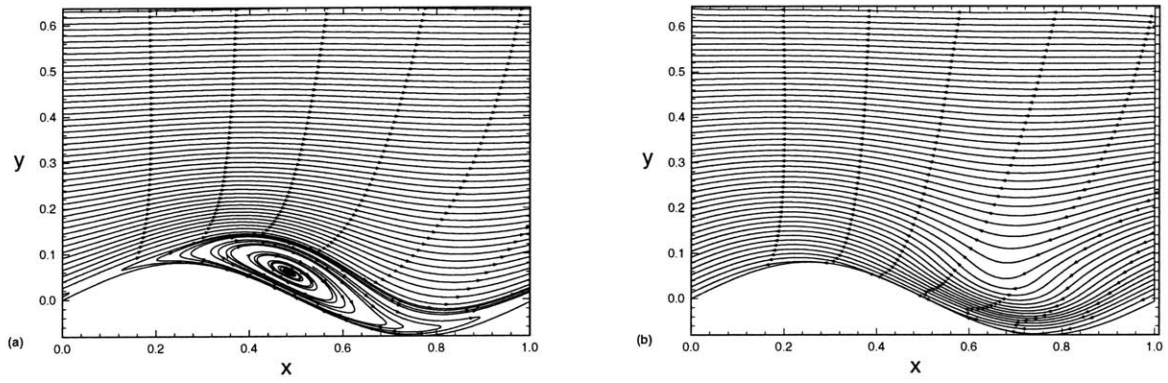

Figure 6-4: Streamlines in the moving frame for $c/U = 0.4$(a); 1.2(b).

comparison. The velocity shown in figure 6-5 is the velocity component to the normal of the surface. Notice not only averaging over z but also averaging over several phases are performed. The log law is shown with constants $\kappa = 0.41$ and $C = 5$. There exists a significant difference for $c/U = 0.4$ and $c/U = 1.2$, especially at the wave crest c. Greater deviation from log law means greater decrease in turbulent shear stress. For $c/U = 1.2$, the turbulence experiences a laminarization process. However this process is not uniform along the surface. At location d, it appears that the turbulence is less laminar from u^+ profile than at c. For $c = 0.4U$, at location d, the profile is slightly above the log law. This means that there is noticeable turbulence decay going on as well. It should be stressed that this figure can not always be plotted for all c/U values because at certain locations the friction velocity could become very small or even change sign. The flow field near location c is the most reliable in terms of representing the mean flow. Because of the wavy motion, the mean flow profile is not intrinsically the same for the two c/U cases, and the increase in normalized mean flow for $c/U = 1.2$ is not caused solely by strong laminarization. From u^+ plot, it can be assumed that at location a there exists an extended viscous inner layer. It may be true that wave crest or wave trough or nodal points are not typical locations for measuring mean velocity profile to show laminarization. For very big c/U there is a need to increase grid resolution because the interaction between the surface motion and outer flow creates big velocity gradient near the surface downstream the wave crest. At location c, profile for $c/U = 0$ is meaningful because it is not in the sep-

arated region and the profile is shown as hollow circles with other two cases and is closer to the flat wall log law. The outperforming of u^+ for $c = 1.2U$ also implies that the thrust generation is stronger. There are larger regions near the surface with horizontal velocity exceeds far field mean velocity.

There are several parameters contributing to the behavior of the log law, including curvature radius and surface acceleration. Because of the surface sliding, there is another surface velocity parameter, which is the phase speed c. For c very small, the flow field is controlled by the outflow for the same amplitude a. For big c, the near wall flow field is controlled by the body motion. For even higher c/U, there exists a reverse flow region near the wave crest as shown in figure 6-6. At this c/U, the flow induced by the wall is so strong that the dividing streamlines (can be seen in figure 6-2(c1)) near the wave crest are pushed further away from the wall and a new stagnation point appears near the wall. Figure 6-6(a) shows the local streamline distribution and the reverse flow region is clearly shown. Figure 6-6(b) shows the contour of horizontal velocity component. Obviously there is a slender near surface region with negative horizontal velocity component. The closed streamlines form a small pocket above the wave crest. Downstream of the this small pocket, fluid particles initially move in the direction opposite to the outer flow direction and finally make a turn and move in the outer flow direction. For fluid upstream of the pocket, fluid particles initially move in the direction of the outer flow direction and then turn to the direction opposite to the outer flow. By comparing the streamlines at this c/U to those of $c/U = 1.2$ in figure 6-2 (c1), one may observe the relocation of "stagnation point" in the flow pattern near the wave crest. One implication of this change is that the mean shear stress can be zero on the surface for certain c/U, and viscous sublayer is destroyed. This is indeed true and will be shown in the discussion of pressure and friction force. Zero shear stress on the wall contributes to smaller turbulent kinetic energy because of decreased energy production on the surface.

In order to show the location of the separation bubble, we plotted the geometrical center of the separation bubble in figure 6-7. The center of vortex bubble moves

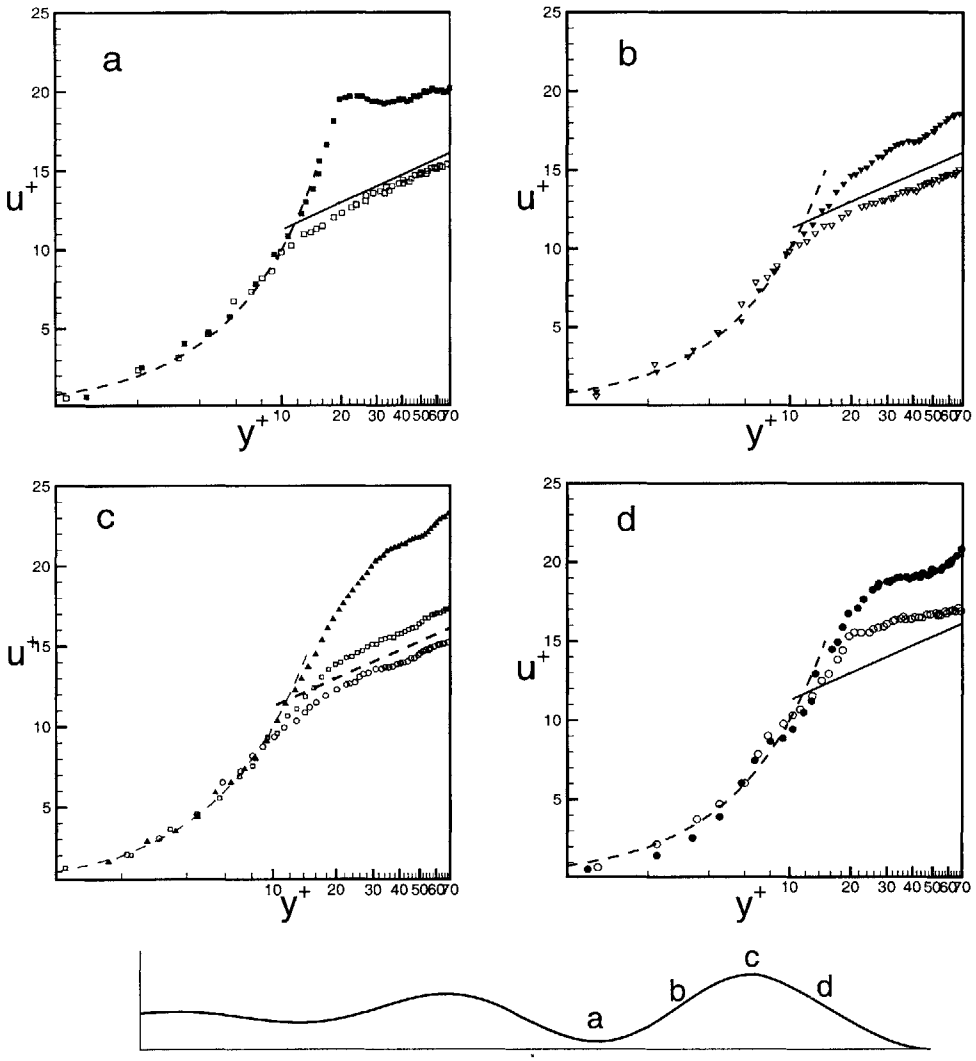

Figure 6-5: Transverse averaged longitudinal velocity profiles at four locations at a particular phase of a plate undergoing a wavy motion (see inset). The maximum amplitude a=0.032L (L is the plate length), the wavelength is λ=0.4L and the phase speeds of the motion are c/U= 0.4 (hollow symbols) and 1.2 (filled symbols). At location c, hollow circles are for $c/U = 0$. U is the speed of the incoming turbulent stream. The Reynolds number based on L is 6000. The instantaneous (transversely averaged) friction velocity u_*/U at the 4 different locations are, for c/U=0.4: (a) 0.039; (b) 0.049; (c) 0.046; (d) 0.029; and for c/U=1.2: (a) 0.037; (b) 0.044; (c) 0.040; (d) 0.053. For the circle symbol ($c/U = 0$) shown at location c, the friction velocity is 0.055

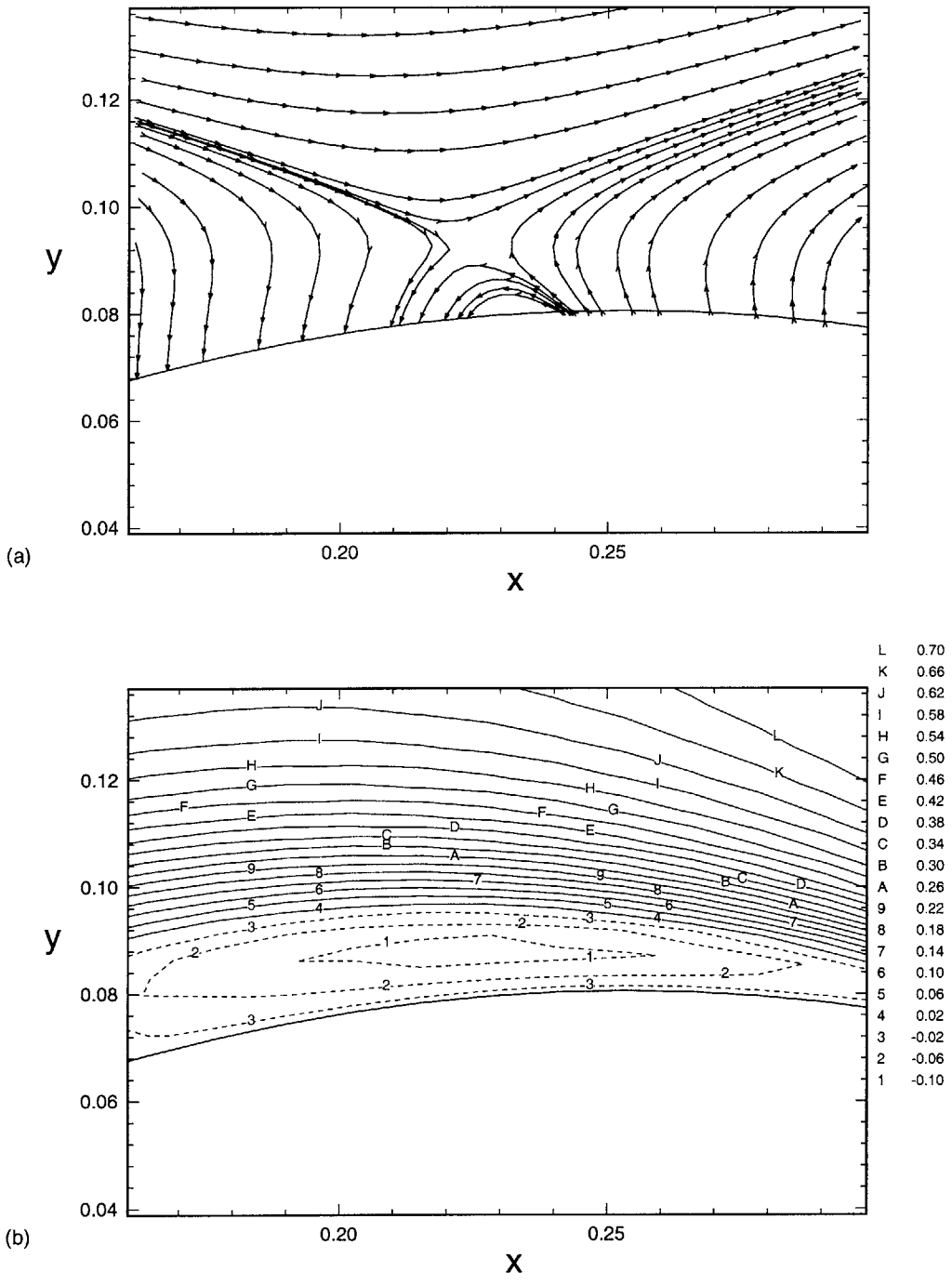

Figure 6-6: Streamline pattern (a) and horizontal velocity contour (b) for $c/U = 2$.

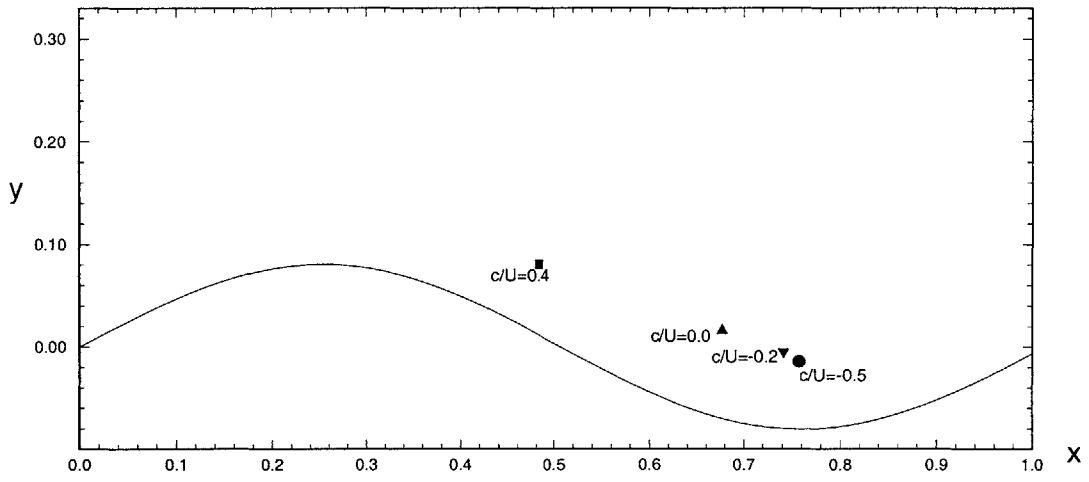

Figure 6-7: Geometrical center of recirculating streamlines.

upstream as c/U increases. Also worth mentioning is the flow field for $c/U < 0$. For this case the flow direction is to the opposite of the wavy motion. Figure 6-8 shows the streamline pattern, and the separation bubble still exists and is pushed away from the surface by the secondary flow generated by the wavy motion near the wave trough. The secondary flow consists of streamlines emanating from and ending on the surface. For negative c/U, the secondary flow near the trough is in the same direction as that of the lower portion of the separation bubble so small negative c/U does not eliminate the separation bubble. Near the wave crest, a similar secondary flow is created. For even bigger negative $c/U = -2$, the separation bubble may disappear and create a strong shear layer which is shown in figure 6-9. Because the secondary flows near both the wavy crest and the wave trough are strong enough, the separation bubble is suppressed.

The mean horizontal velocity distribution at the wave crest, trough and nodal points are shown in figure 6-10. It can be seen that there is energy increase in the horizontal direction and the mean flow profile is fuller for $c/U = 1.2$. From this figure it is seen that the law of the wall is not applicable for this case. As can be shown later, the absence of momentum defect is due to the elimination of drag.

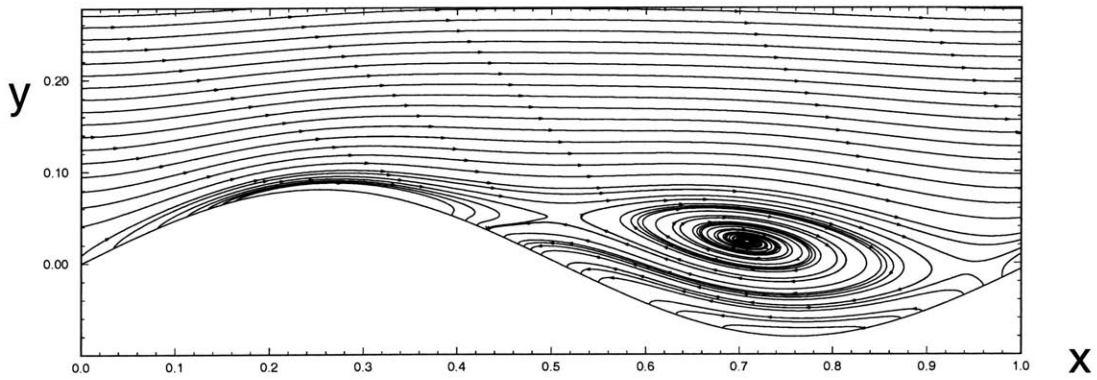

Figure 6-8: Streamline pattern for $c/U = -0.2$.

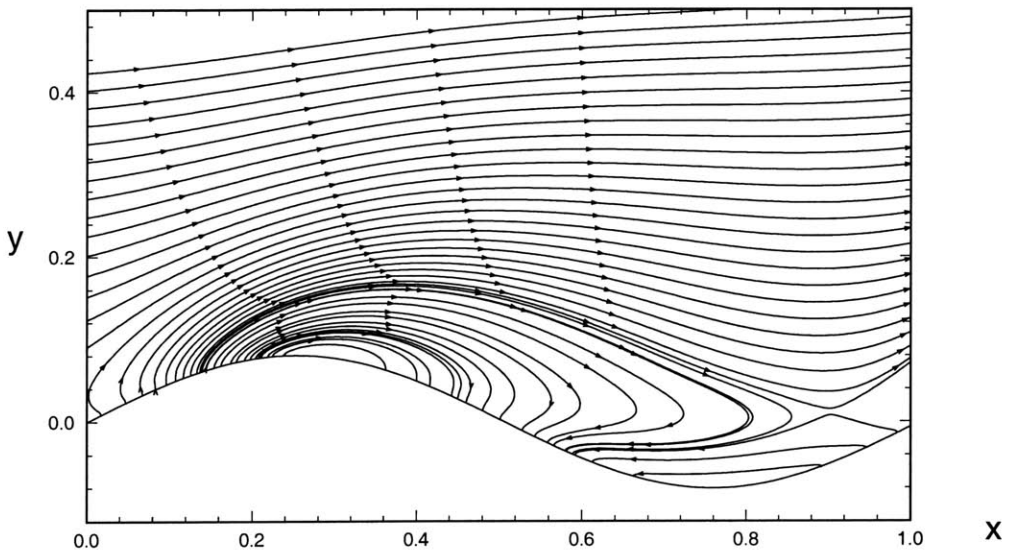

Figure 6-9: Streamline pattern for $c/U = -2$.

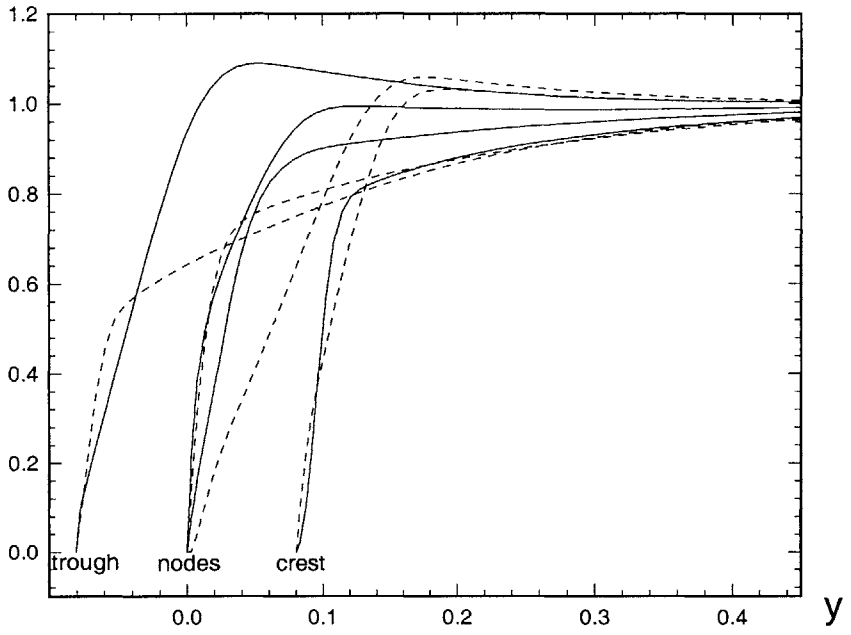

Figure 6-10: Mean horizontal velocity plotted as a function of vertical dimension y. Solid lines are for $c/U = 1.2$ and dashed lines are for $c/U = 0.4$.

For positive c/U, as the recirculating zone disappears, the surface motion inputs energy into the mean flow. For c/U negative, the recirculating zone still exists and the fluid energy is increased as well. The total mean energy of the flow is shown in figure 6-11. Here the total energy in the whole computational domain is shown. If the total energy in a smaller region (say, $y^+ < 100$) is shown, the difference is more significant. The total mean energy increase is equal to the thrust generated minus any energy losses. It can be anticipated that for big c/U and steep wavy motion, the boundary layer profile does not matter much. Because of energy input to the mean flow, at the trailing edge, the mean profile deviates significantly from boundary layer profile.

Because of the unsteady motion of the boundary transversely to the flow direction, the mean streamline pattern does not resemble the mean particle streakline pattern, especially near the surface. The streamline pattern does provide a simpler presentation of the flow. One of the advantages of viewing the flow in a moving frame is

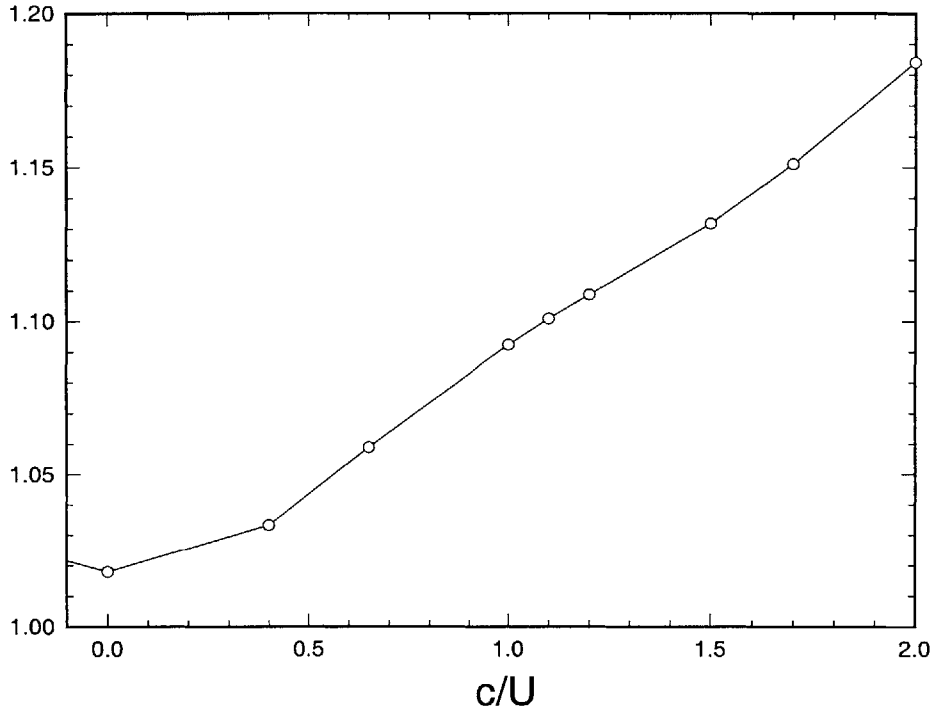

Figure 6-11: Total mean energy as a function of c/U.

that the streakline and streamline are identical. Streakline pattern is shown in figure 6-12. Very near the surface in (c), particles moves with larger amplitude and smaller wave length. Away from the surface in (a), particles moves with smaller amplitude and larger wave length. If the flow is viewed in a frame that moves with a particular surface location, especially near the wavy nodal points, the flow has the profile of a boundary layer flow.

For higher Reynolds number, the separation pattern for $c/U = 0$ changes greatly because of the shift in separation location and the scale of the separation bubble. Figure 6-13 shows the streamline pattern for Re=18,000. The small c/U case is largely affected by the change in separation pattern due to the increase in Reynolds number. There are two separation bubbles with the smaller one appearing first. It can be anticipated that the total force balance would change more for the separated $c/U = 0$ case than $c/U = 1.2$ case. When separation is suppressed, the flow is less sensitive to Reynolds number. Because the flow is affected more by the Reynolds

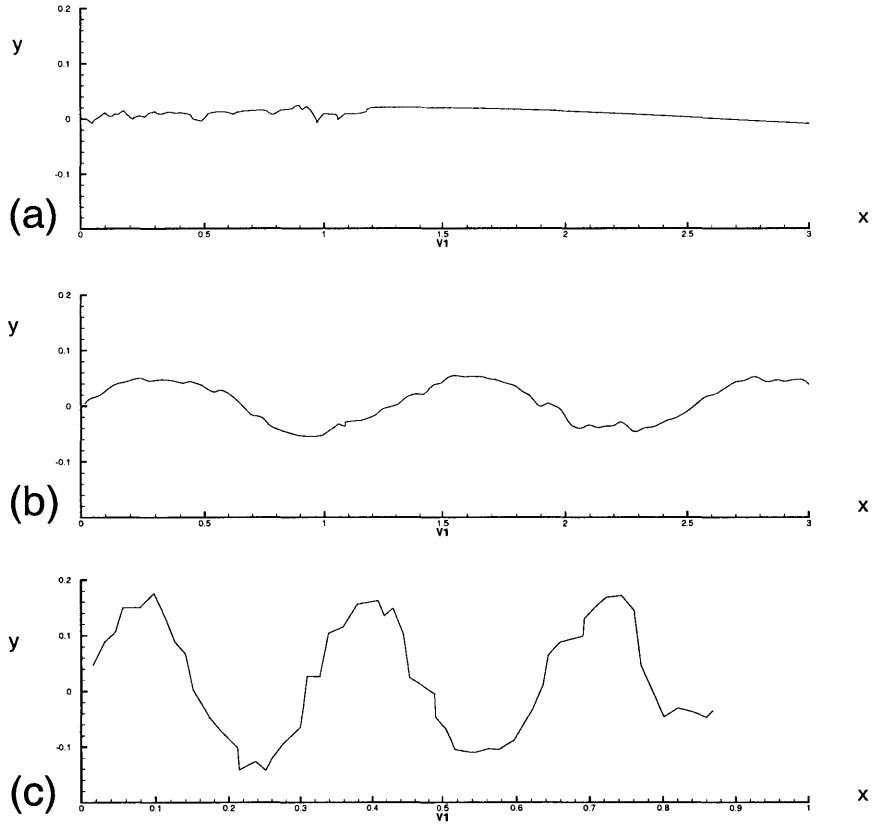

Figure 6-12: Streaklines emanating from three locations: $y^+ = 150$ (a); 30 (b); 10 (c).

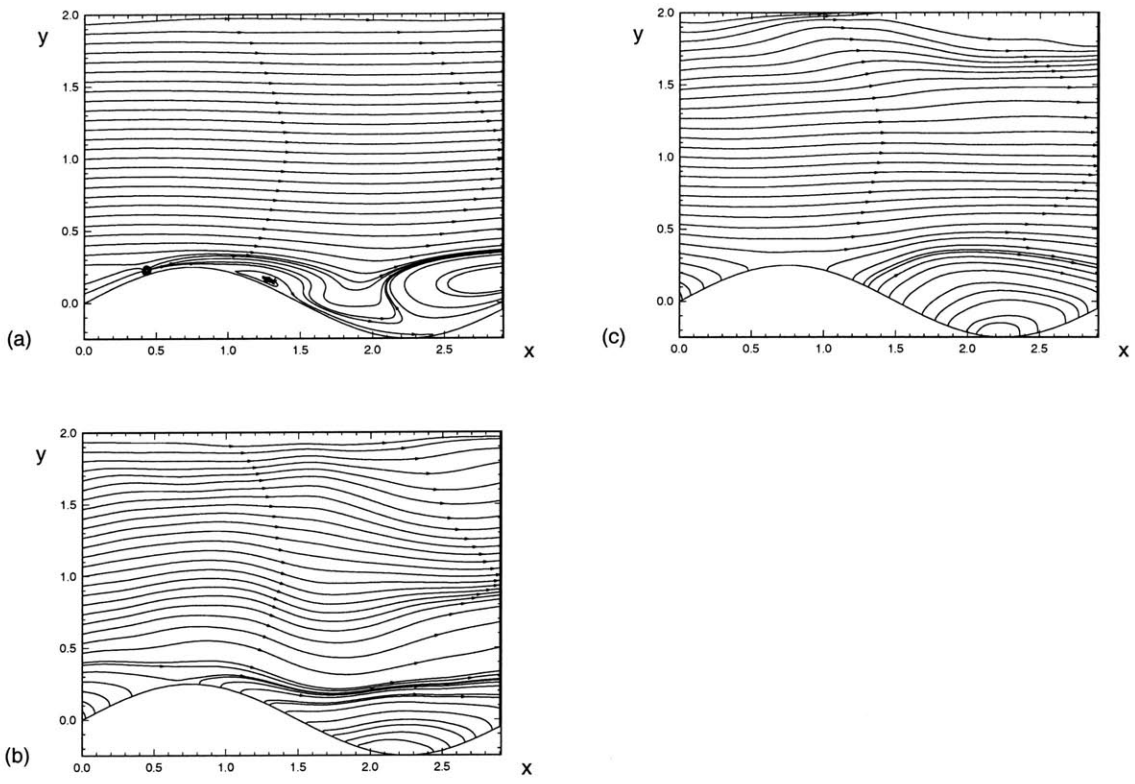

Figure 6-13: Streamline pattern for Re=18,000, $c/U = 0.0$ (a); 0.8 (b); 1.2 (c).

number for smaller c/U, the behavior in figure 6-30 will change significantly only for small c/U values. Flow configuration changes little for large c/U.

The critical Reynolds number at which separation disappears is not sensitive to Reynolds number. just as flow over a rotating cylinder.

6.3 Turbulence statistics

Wavy wall motion strongly modifies not only the mean flow but also the turbulence intensities. The mean flow profile is more time invariant, but the fluctuation contours are less spatially organized. Figure 6-14 shows the turbulent intensities averaged over the spanwise direction. In our discussion, turbulent intensities mean root mean square of fluctuating velocity.

All three components of turbulent kinetic energy are shown. It can be observed that for $c = 1.2U$, the turbulent intensities are smaller at most locations. Moreover, the distribution for $c = 1.2U$ is much less uniform. At certain locations there is a bigger laminar region. For example, ahead of the wave crest for $c/U = 1.2$, the region with small turbulence is bigger even near the surface. If more averaging is performed, the distribution can be more organized with clearer maximum and minimum locations. Some of the comparisons are made between $c/U = 0.4$ and $c/U = 1.2$ and others are between $c/U = 0.0$ and $c/U = 1.2$ because different features manifest themselves best at different c/U. A preferable way is to include all the c/U values which is not feasible. We also face a question whether a local maximum of turbulent intensity can be determined and how organized the mean kinetic energy distribution can be. If the streamwise amplitude variation is strong, organized structures can be obtained.

The turbulent shear stress $- < uv > /u_0^2$ is shown in figure 6-15. It is evident that for $c = 1.2U$, the turbulent shear stress is significantly smaller, especially near the wave crest. In order to show the overall distribution of turbulent intensities as a function of x, we averaged the intensities shown in figure 6-14 over y. The results are shown in figure 6-16. Even though there are locations at which turbulence intensities are bigger for $c = 1.2U$, the overall turbulent distribution is smaller. In order to show the turbulence distribution on the horizontal domain, we plotted in figure 6-17 the turbulent intensities integrated over the vertical dimension. It shows clearly the nonuniform distribution of turbulent intensity for $c/U = 1.2$. The distribution of turbulent intensities as a function of y is shown in figure 6-18. Table 6.1 shows the total turbulent intensities integrated over the whole domain. So in the range of moderate Reynolds number, the Reynolds number does not affect the turbulence suppression very much. At relative low Reynolds number other effects plays a role.

For a glimpse of instantaneous vorticity behavior, we show $\omega_x'(x; (y-Y)_i; z_0, t_0)$ at several distances away from the wall in figure 6-19. Clearly for $c/U = 1.2$, fluctuation is smaller. However at $4 < x < 6$, there are also big fluctuations for $c = 1.2U$, especially far away from the surface. As c increases, the turbulent region in the crest portion decreases. while in the trough region, the turbulent region increases. For

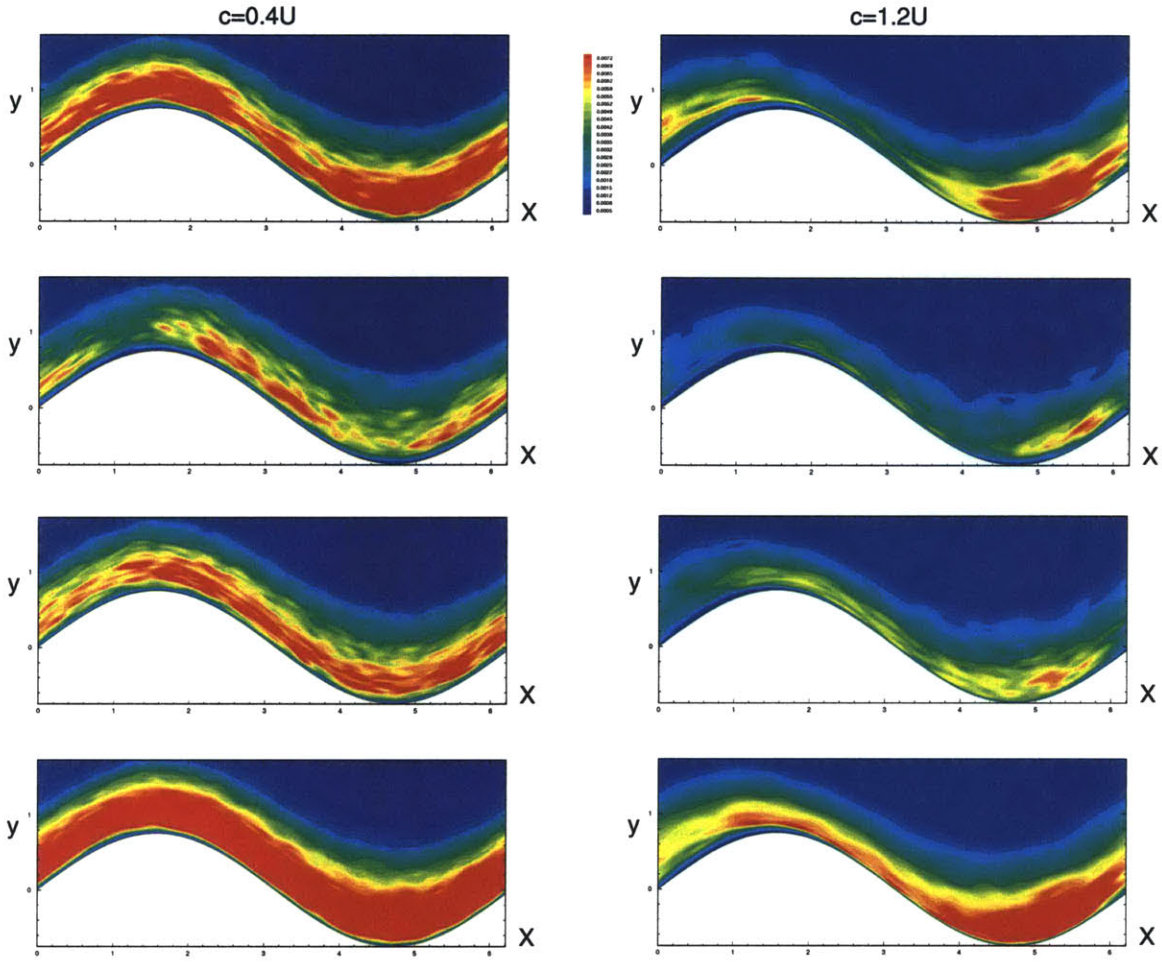

Figure 6-14: Transverse-averaged turbulent kinetic energy intensities of flow over a plate undergoing a wavy motion. The kinetic energy components are (from top to bottom) streamwise; vertical ("average wall" normal); span-wise; and total.

	Re=3000			Re=6000		
	(a) c=0.4U	(b) c=1.2U	(b)/(a)	(a) c=0.4U	(b) c=1.2U	(b)/(a)
$E_u = \int u'^2 dV$	1.128	0.881	0.781	1.365	1.078	0.789
$E_v = \int v'^2 dV$	0.968	0.678	0.701	1.106	0.717	0.648
$E_w = \int w'^2 dV$	0.895	0.694	0.775	1.018	0.768	0.712
E_k (kinetic energy)	1.495	1.127	0.756	1.744	1.282	0.732

Table 6.1: Total turbulent intensities integrated over the whole domain.

$c/U = 1.2$, the computed shear stress at the wall shows streaky patterns appear only at downstream slope and the patterns are less regular patters elsewhere. For c/U large, the streaky pattern is highly irregular, and non-uniformly distributed. Because of the variation in turbulence input at the inflow boundary, the turbulent kinetic energy at the input cross section is not steady. The numerical values of the turbulent intensities discussed above should be compared with the values obtained with similar turbulent input only. As separation disappears, the distribution of turbulent intensity also changes. For c/U small the biggest turbulence intensities are away from the wall, especially after separation. But, for c/U large, the biggest turbulence intensities are very near the wall on the whole surface. We show in figure 6-20 the instantaneous velocity field as a function of normal dimension for one wavelength at thirty equal horizontal locations.

6.4 Reynolds stress evolution analysis

The turbulent behavior discussed in the above section can be analyzed in detail by applying Reynolds evolution equation. Compared to flat wall turbulence, the wavy motion induced both surface pressure gradient and velocity gradient, which contribute significantly to energy balance.

The Reynolds evolution equation near the surface can be written as:

$$\frac{\partial \overline{u^2}}{\partial t} = -\frac{\partial}{\partial s}(U\overline{u^2} + \overline{u^3}) - \frac{\partial}{\partial n}[h(V\overline{u^2} + \overline{uv^2})] - \overline{u^2}\frac{\partial U}{\partial s} \\ -\overline{uv}\frac{\partial U}{\partial n} + \kappa(UV + \overline{uv}) + \overline{u\frac{\partial p}{\partial s}} - \epsilon_{uu}, \tag{6.1}$$

$$\frac{\partial \overline{v^2}}{\partial t} = -\frac{\partial}{\partial s}(U\overline{v^2} + \overline{uv^2}) - \frac{\partial}{\partial n}[h(V\overline{v^2} + \overline{v^3})] - \overline{v^2}\frac{\partial V}{\partial s} - \overline{uv}\frac{\partial V}{\partial n} \\ -\kappa(2U\overline{uv} + \overline{u^2 v}) + h\overline{v\frac{\partial p}{\partial s}} - \epsilon_{vv}, \tag{6.2}$$

$$\frac{\partial \overline{uv}}{\partial t} = -\frac{\partial}{\partial s}(U\overline{uv} + \overline{u^2 v}) - \frac{\partial}{\partial n}[h(V\overline{uv} + \overline{uv^2})] - \overline{u^2}\frac{\partial V}{\partial s} - \overline{uv}\left(\frac{\partial U}{\partial s} + h\frac{\partial V}{\partial n}\right) - \overline{v^2}\frac{\partial hU}{\partial n} \tag{6.3}$$

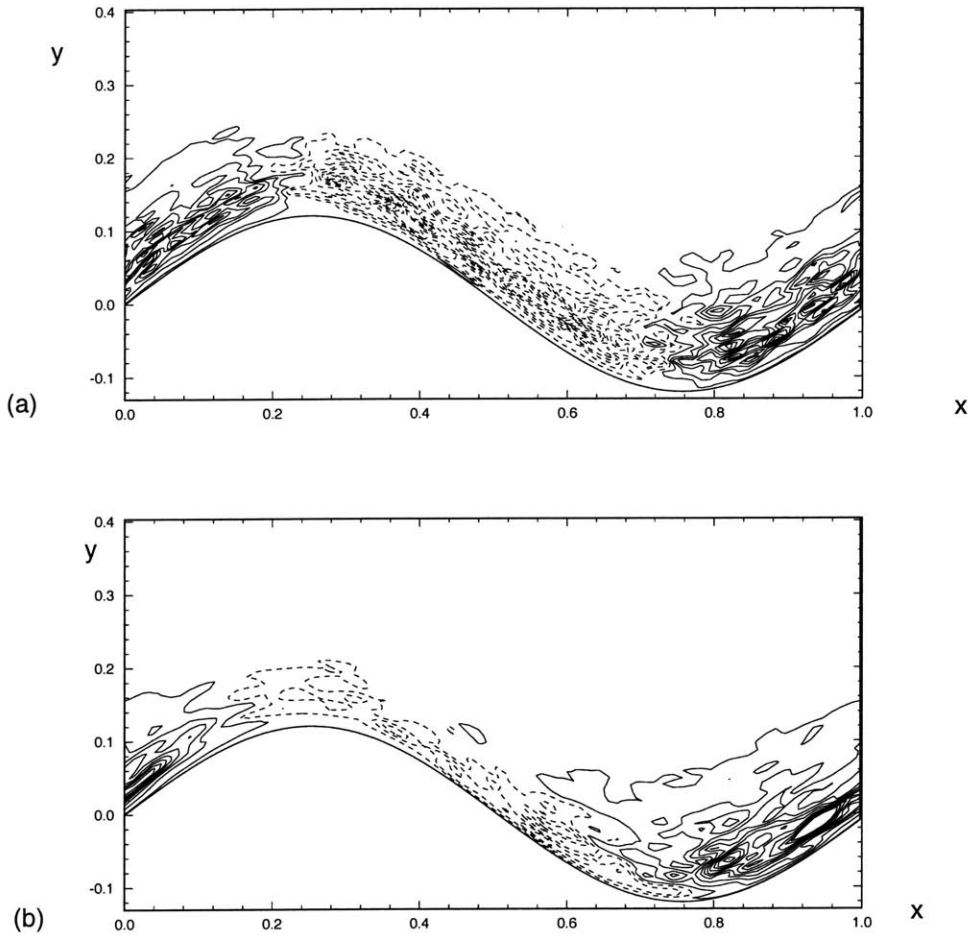

Figure 6-15: Transversely averaged turbulent shear stress for c/U = (a) 0.4, (b) 1.2.

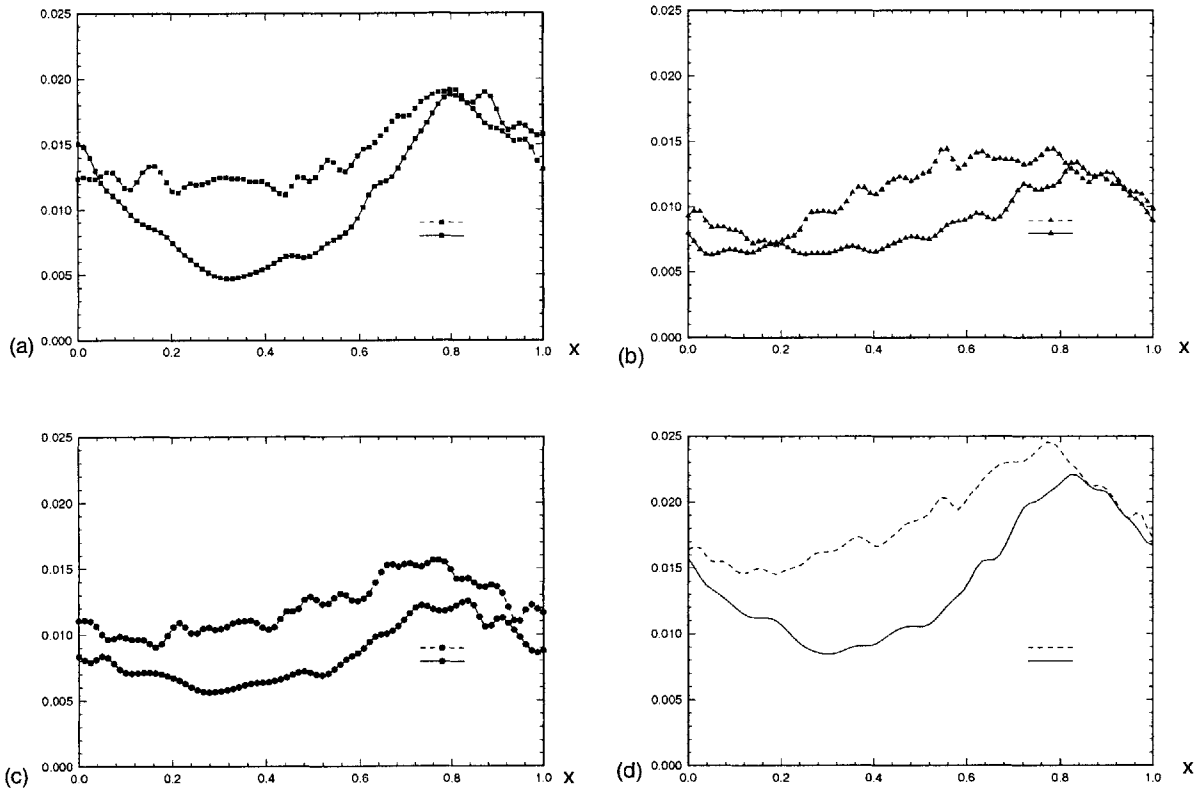

Figure 6-16: Transversely and longitudinally averaged turbulent shear stress. (a,b,c,d) are for streamwise, vertical, spanwise intensities and total kinetic energy. Solid lines are for $c/U = 1.2$.

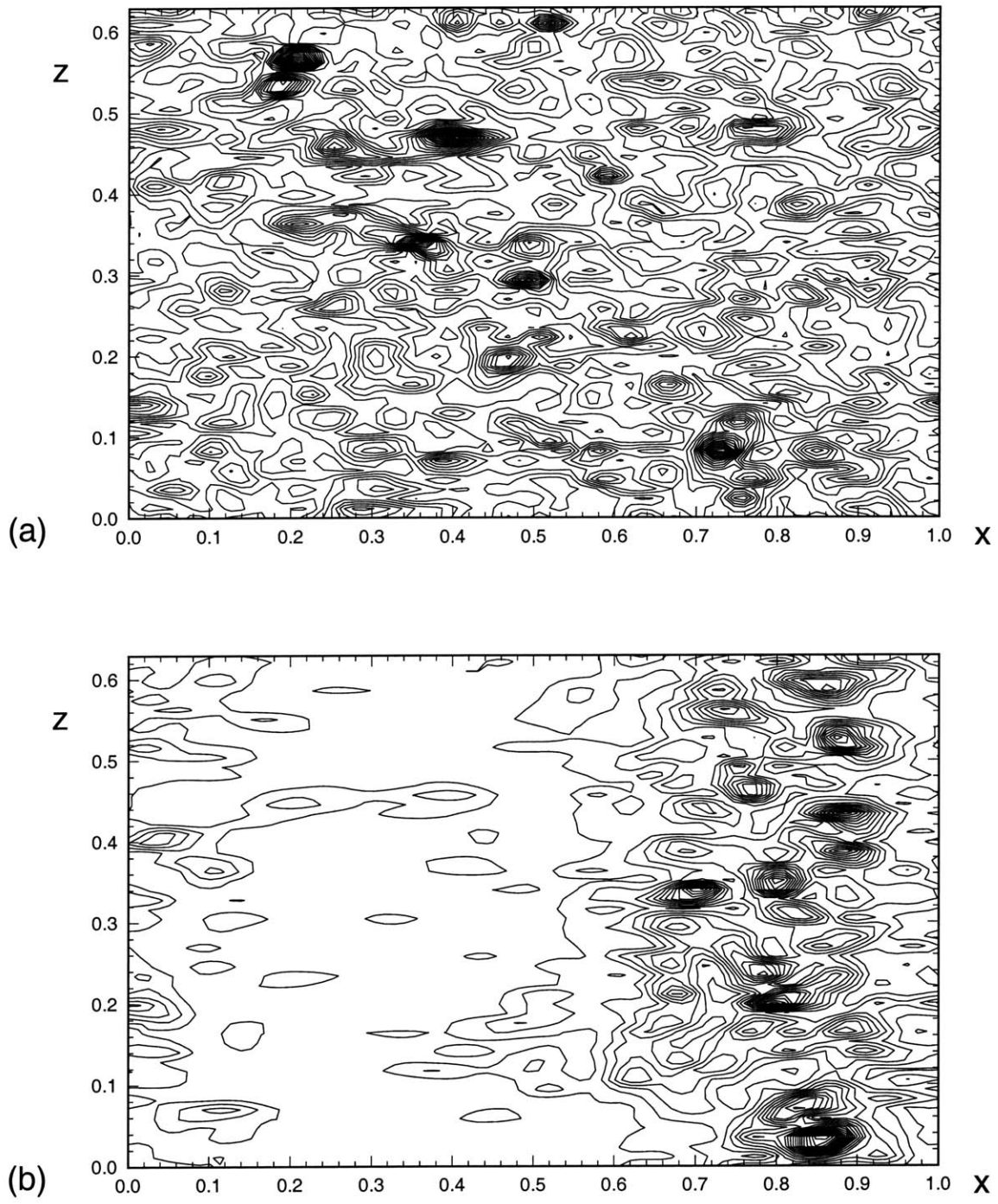

Figure 6-17: Turbulent kinetic energy as a function of x-z. $c/U = 0.4$ (a); and 1.2(b).

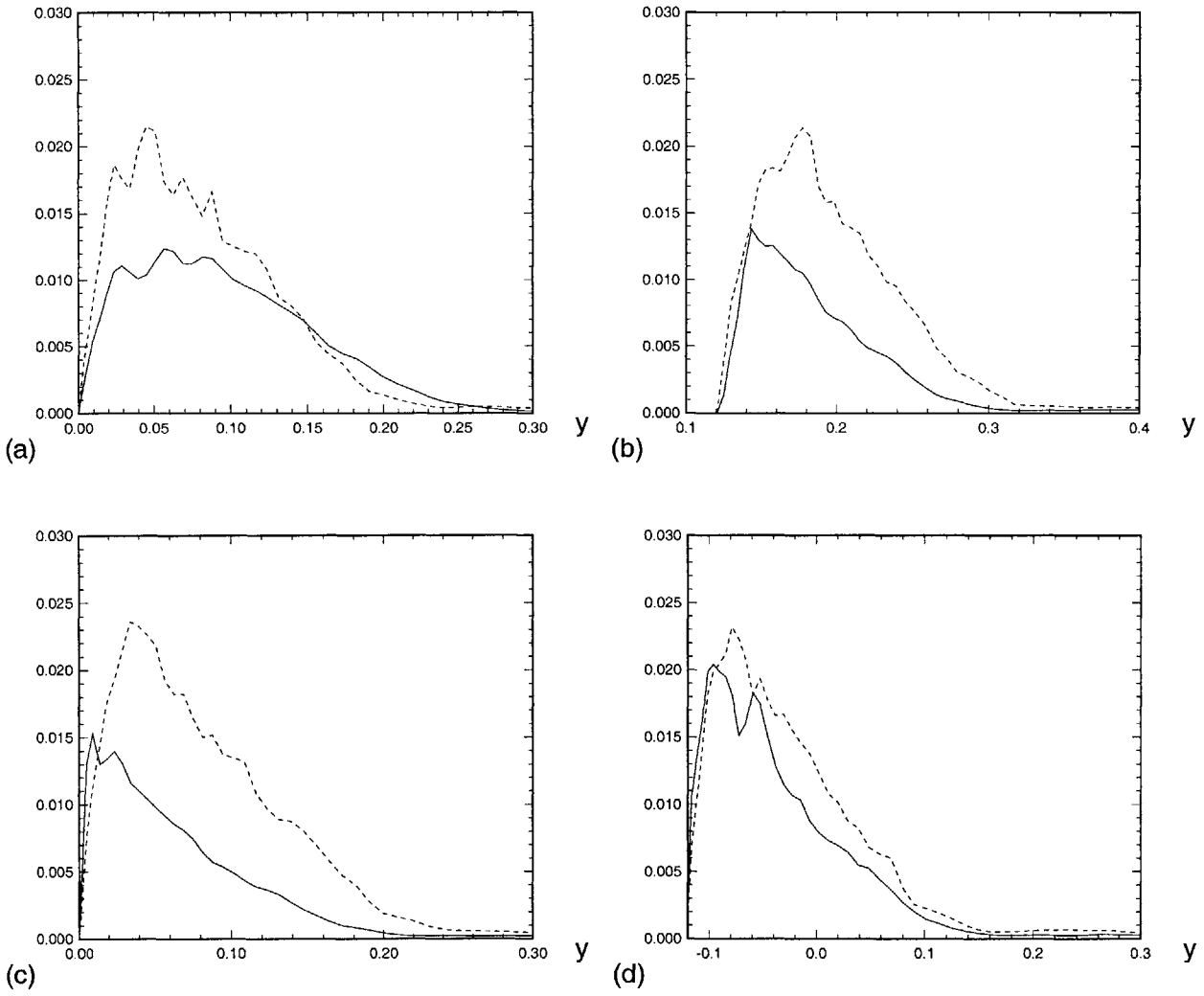

Figure 6-18: Vertical turbulent kinetic energy at wave crest, trough and nodal points. Solid lines are for $c/U = 1.2$ and dashed lines are for $c/U = 0.4$.

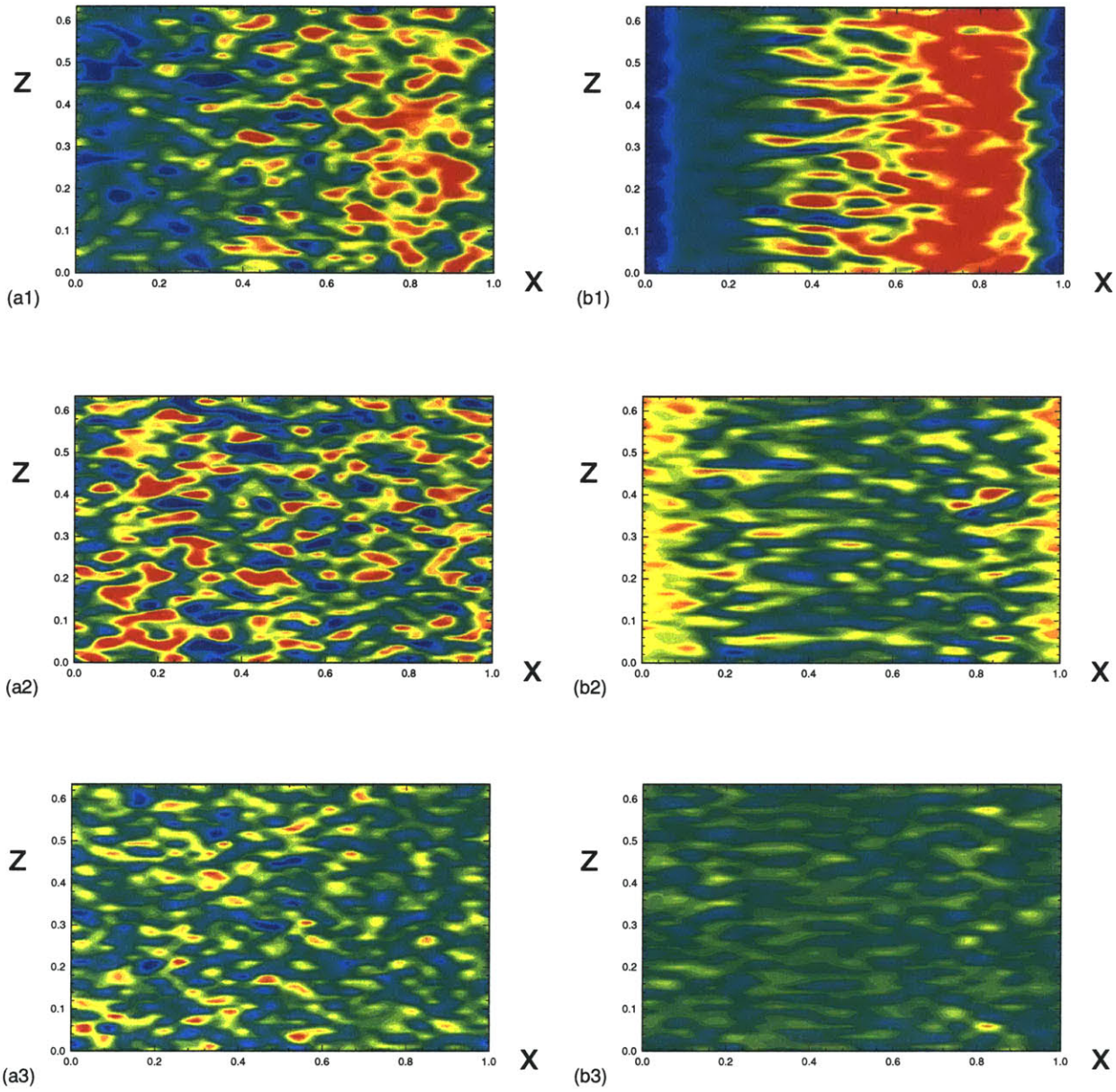

Figure 6-19: Instantaneous horizontal vorticity at three distances away from the wall (a1, b1) are closer to the wall and (a3, b3) are 4.5 times further away. Left figures are for $c/U = 0.4$, and right figures are
for $c/U = 1.2$.

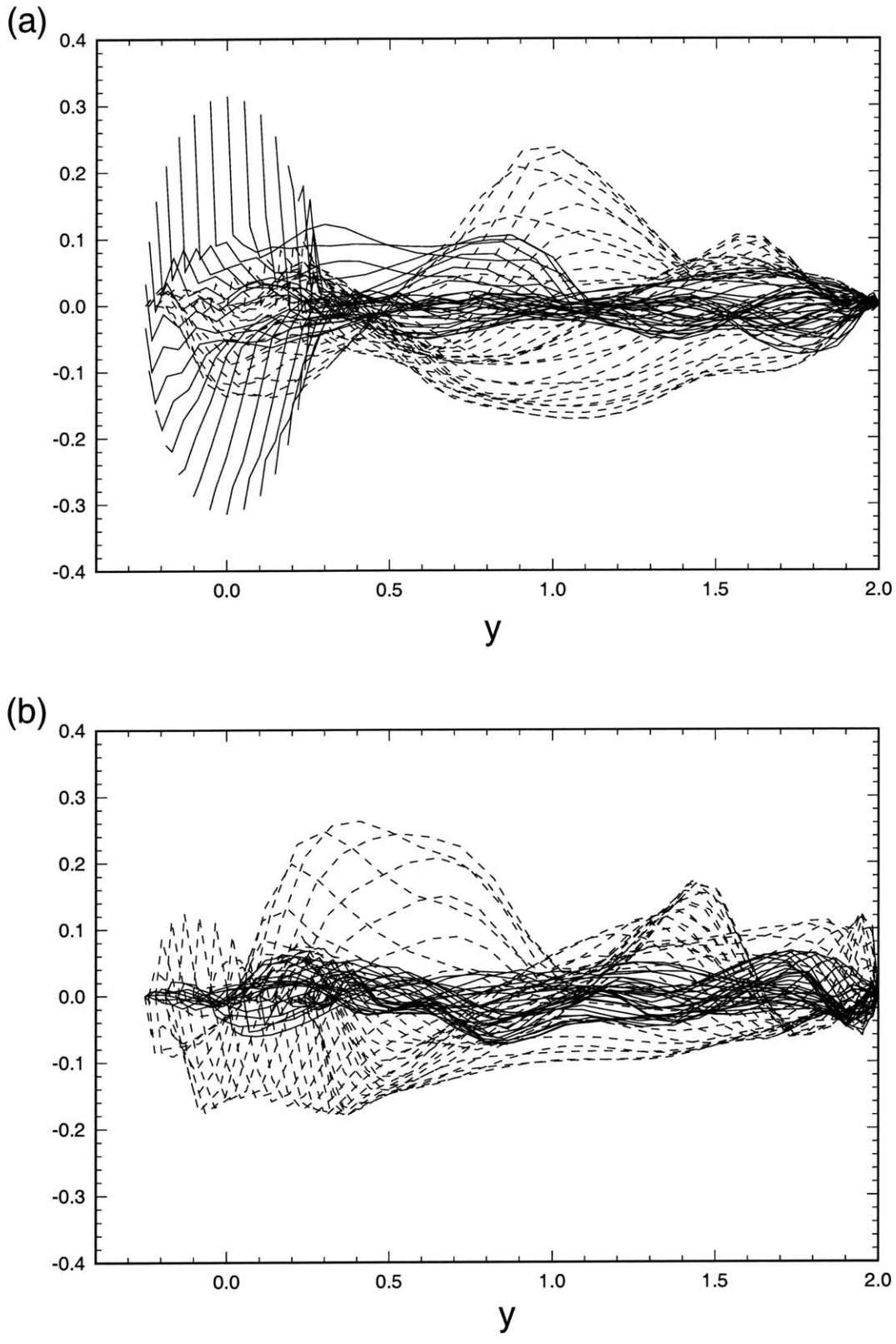

Figure 6-20: Instantaneous velocity distribution (a) vertical (b) spanwise. Dashed lines are for $c/U = 0.0$ and solid lines are for $c/U = 1.2$. The left side is the wavy boundary.

$$+\kappa(2U\overline{u^2}+\overline{u^3}-\overline{uv}V-\overline{uv^2})+h\left(\overline{v\frac{\partial p}{\partial s}}+\overline{hu\frac{\partial p}{\partial n}}\right)-\epsilon_{uv}(6.4)$$

Here U, V, W are averaged velocity components in the curvilinear system, s the arc length, and κ the surface local curvature. n is the surface normal. First two terms on the right side are turbulent transport and the fourth terms are turbulent production. ϵ denotes dissipation.

For flat surface, the total turbulent production goes directly to streamwise fluctuation. The other two energy components get their energy by the means of pressure strain correlation. For our simulation, turbulent production exists for both streamwise and vertical components. Energy production in the vertical component increases as c increases. From boundary condition, one can deduce that the extra vorticity induced by the wavy motion in the domain is a linear function of c. It is evident that for $c = 0.4U$, the diffusion rate is bigger, and this leads to decreased dissipation and increased turbulent intensities. The basic physics is that, for $c/U = 1.2$, there is less overall turbulence production and the diffusion near wave trough increases the turbulent dissipation. We show in figure 6-21 the averaged turbulent production distribution $-\overline{uv}(\frac{\partial U}{\partial n}+\frac{\partial V}{\partial n})$ in the vertical plane. For $c/U = 0.0$, the production is significantly bigger and less clustered to the wall. For wavy motion, the tendency to isotropy is stronger before the wave crest than after the wave crest. The variation of surface shear stress greatly affect energy production. There are two terms contributed to the production, one to horizontal component, another to vertical component. Away from the separation regime, the maximum fluctuations appear near the wavy boundary. For fixed wavy wall the maximum fluctuation happens at the boundary. Surface wavy motion effectively decreases the injection of flow impinging on the surface, thus reduces pressure fluctuations. The distribution of turbulent intensities is not symmetric with respect to wave crest and wave trough even though the streamlines are symmetric for large c/U because the mean velocity magnitude is not symmetric.

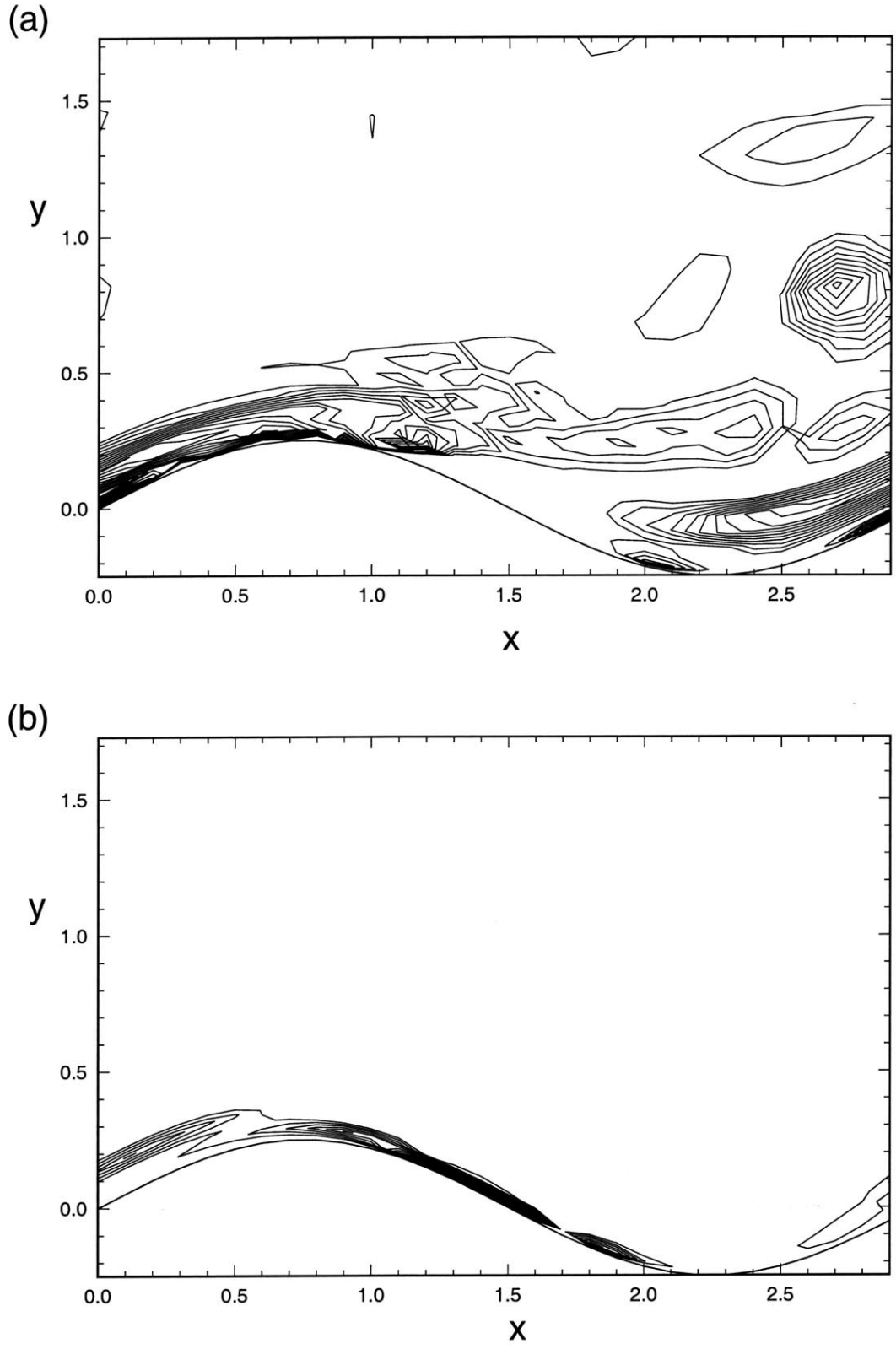

Figure 6-21: Turbulent production for c/U = (a) 0.0; (b) 1.2.

6.5 Pressure and friction force distribution

Pressure and friction distribution for flow over wavy wall with very small slope $ka = 0.05$ is discussed first for leading order effect of wave slope ka. Because there is no separation, this flow can be compared with flat wall results. Numerical results show that nonlinear deviations become significant as c increases even for this small ka.

The spanwise and temporally averaged surface pressure and friction fields are shown in figure 6-22. Since the wave slope is very small, the pressure distribution is approximately sinusoidal (single harmonic) for small c/U. The pressure variation on the surface decreases as c/U increases for this ka even when c/U is up to 1.2. For $c/U = 0.0$ and 0.4, the minimum (maximum) pressure is located downstream the wave crest $x = 0.25$ (wave trough $x = 0.75$) and the two distributions are similar. The phase difference has to appear in the manner which is shown. A phase shift in the other direction implies thrust which is not physical because there is no energy input. However, for c/U=1.2, the pressure profile changes greatly with maximum located near $x = 0.45$. It can be easily seen that for all three cases the pressure force is a drag. The total pressure force is proportional to $\sin(\alpha)$ where α is the phase angle shift between the pressure and surface profile under the assumption that the pressure is pure sinusoidal. For this small ka, pressure drag is not caused by separation. As to the friction distribution, phase shift as a function of c/U is more significant and total friction force is always drag and reaches maximum between $c/U = 0$ and $c/U = 1.2$. However, because the wave amplitude is small and there is no separation, the total friction only varies slightly. The total pressure force is a stronger function of c/U in terms of amplitude.

Note that the smallest friction force on the boundary does not happen at the wave trough for $c/U = 0$. A small increase in c/U near $c/U = 0$ decreases both the pressure and friction variations. The evolutions of pressure and friction distribution with c/U on the surface are different not only in phase but also in magnitude. At $c/U = 1.2$, the pressure variation is smaller than that of $c/U = 0.4$, but the friction variation is

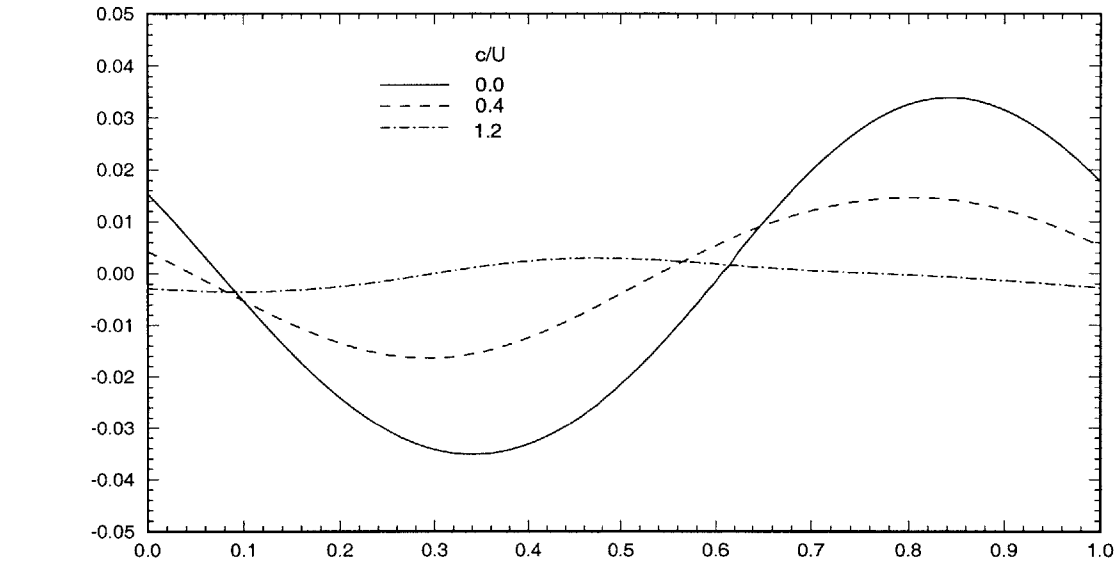

(a)

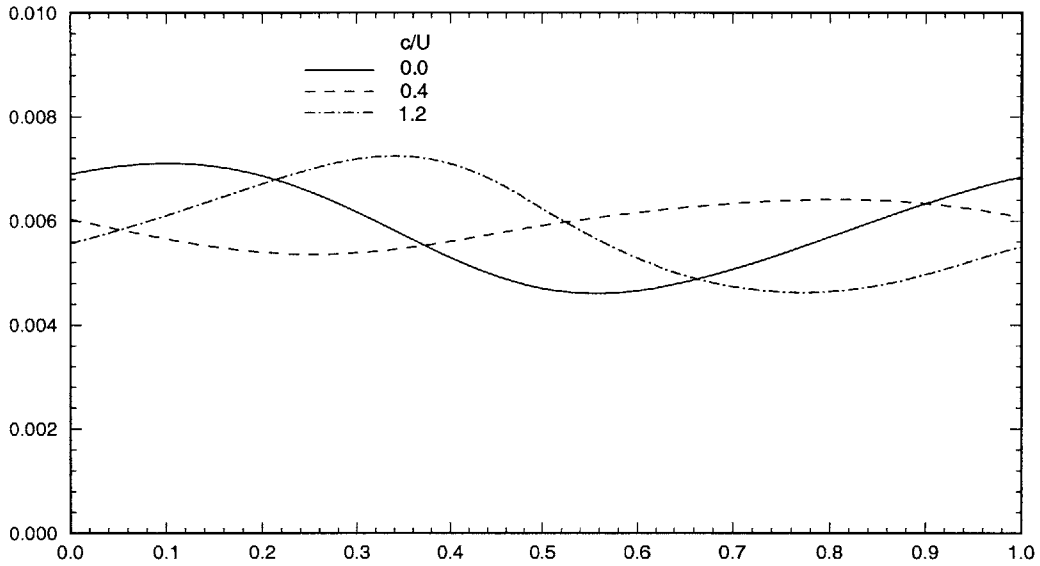

(b)

Figure 6-22: (a) surface pressure distribution $0.5c_p$, (b) surface friction distribution c_f.

c/U ($ka = 0.05$)	pressure force $\int C_{p_x} dx$	friction force $\int C_f dx$	total force
0.0	0.000280	0.003681	0.0039610
0.4	0.0000602	0.003722	0.0037822
1.2	-0.0000443	0.003672	0.0036277

Table 6.2: Pressure and friction force for $ka = 0.05$.

bigger than that of $c/U = 0.4$ after initial decrease between $c/U = 0$ and 0.4. As will be shown later, the pressure variation will finally increase when c/U is big enough. It is evident that different mechanisms play major roles for different values of ka. For this small ka, the effect of centrifugal force is not important, and the change in the thickness of the boundary layer is insignificant in terms of force distribution. Table 6.2 shows the integrated pressure and friction forces. For all three values of c/U, the total force is a drag force and the friction force is much bigger than the pressure force. Note for $c = 1.2U$, there exists a small thrust pressure force. The friction force changes little from $c/U = 0$ to $c/U = 1.2$ because the surface slope is too small to change velocity profile. In order that the wavy motion generate a significant thrust, the wave amplitude has to be increased.

The pressure coefficient is given by

$$C_{Dp} = \boldsymbol{i} \cdot \int_0^l (-C_p \boldsymbol{n}\, ds) = \int_0^l C_p \frac{dy}{dx} dx \tag{6.5}$$

The friction for flat surface is 0.00351, 4.8% smaller than wavy surface at this wave slope. There are two effects contributing to the increase in friction for $c/U = 0$: (1) increase in surface area, (2) change in local shear. The effects of turbulence level on pressure and friction drag are different. There is a greater effect of turbulence on friction drag than on pressure force.

For large positive c/U, significant pressure thrust can be generated. In order to show the generation of thrust, we look into $c/U = 2$ and $c/U = -2$ cases with $ka = 0.5$. There is an obvious difference in the phase shift of pressure distribution with

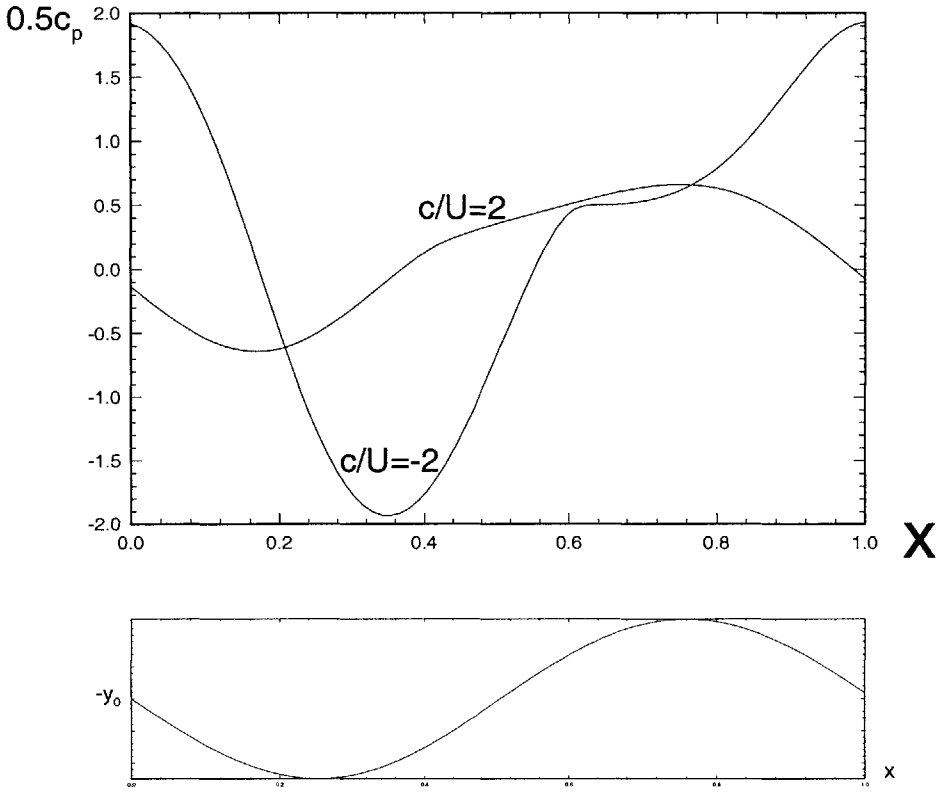

Figure 6-23: Comparison of difference in phase shift in surface pressure for $c/U = 2$ and -2.

respect to the surface profile for $c = 2U$ and $c = -2U$ in that the former generates thrust and the latter generates a drag. The top figure in figure 6-23 shows the mean surface pressure distribution and the bottom of figure 6-23 shows the negative of surface profile $-y_0$. The pressure for $c/U = 2$ is closer to sinusoidal shape because of the disappearance of separation.

One way to understand the phase shift of the pressure distribution is to examine the flow field in the moving frame. For $c/U = 2$ and $c/U = -2$, the tangential sliding velocity magnitude on the wall is the same in the moving frame, but the pressure distribution is not. If we view the flow field from the moving coordinate system, for $c/U = -2$, the outer flow velocity is half the sliding velocity and for $c/U = -2$, the outer flow velocity is one and half of the sliding velocity. Figure 6-24 sketches velocity comparison on and away from the wall and the location of

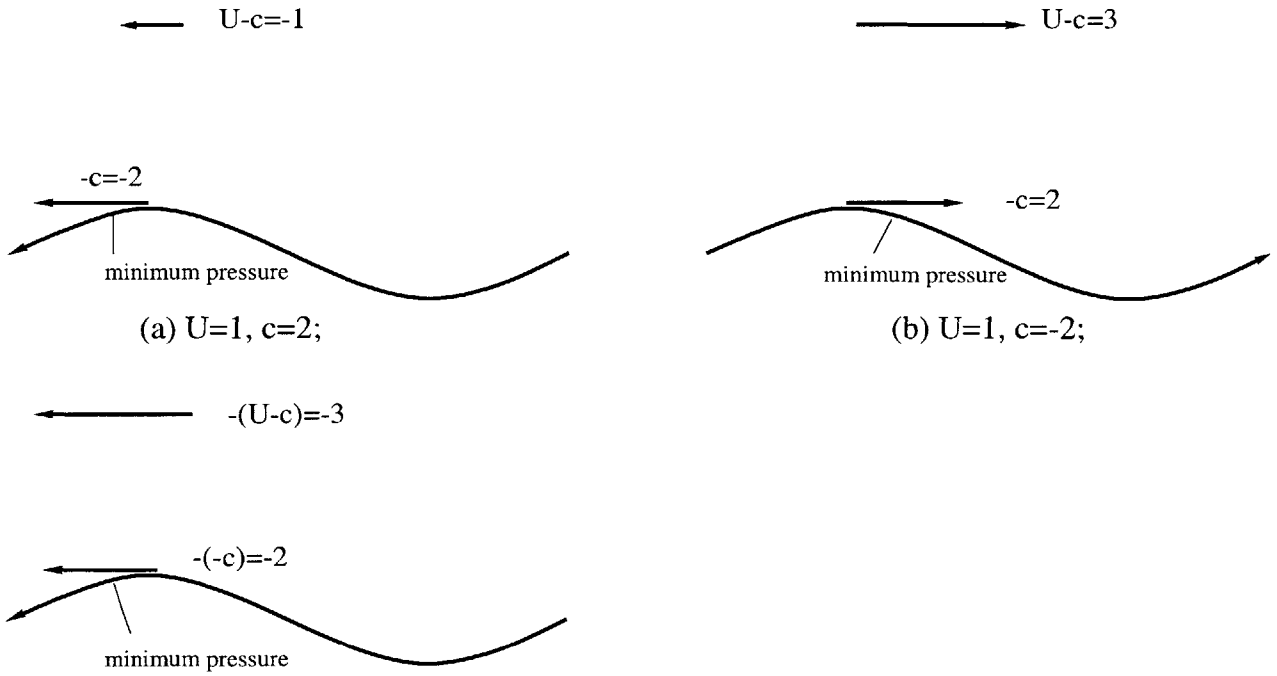

(a) U=1, c=2;

(b) U=1, c=-2;

(c) same as (b) with the direction of horizontal axis reversed.

Figure 6-24: Relative surface and outer flow velocity distribution in the moving frame and minimum pressure location for $c/U = 2$ and -2.

the minimum pressure for these two c/U values. In the moving frame, the outer flow velocity is $U - c$ which can be negative if $c > U$. This outer flow velocity is denoted in the figure away from the wavy wall. A velocity vector is shown on the wave crest to denote surface sliding direction and magnitude $(-c)$. Numerical values are shown if $U = 1$. Figure 6-24 (a) and (b) shows the distributions for $c/U = 2$ and $c/U = -2$, respectively. Figure 6-24 (c) is the horizontal reversal of (b) and we can easily see the similarity between (a) and (c) because the only difference is the magnitude of the outer velocity. From this figure, the location of the minimum pressure is determined by c and the magnitude of the pressure is determined by the interaction between the surface pressure gradient induced by surface sliding and the outer flow. The distribution of maximum pressure shows similar features. For $c/U = -2$, the maximum pressure occurs near $x = 1$, which is not far away from the stagnation point $(0.9, 0.03)$ shown in figure 6-9. Near the wavy trough at which the secondary flow is present, the pressure is flat for $c/U = -2$.

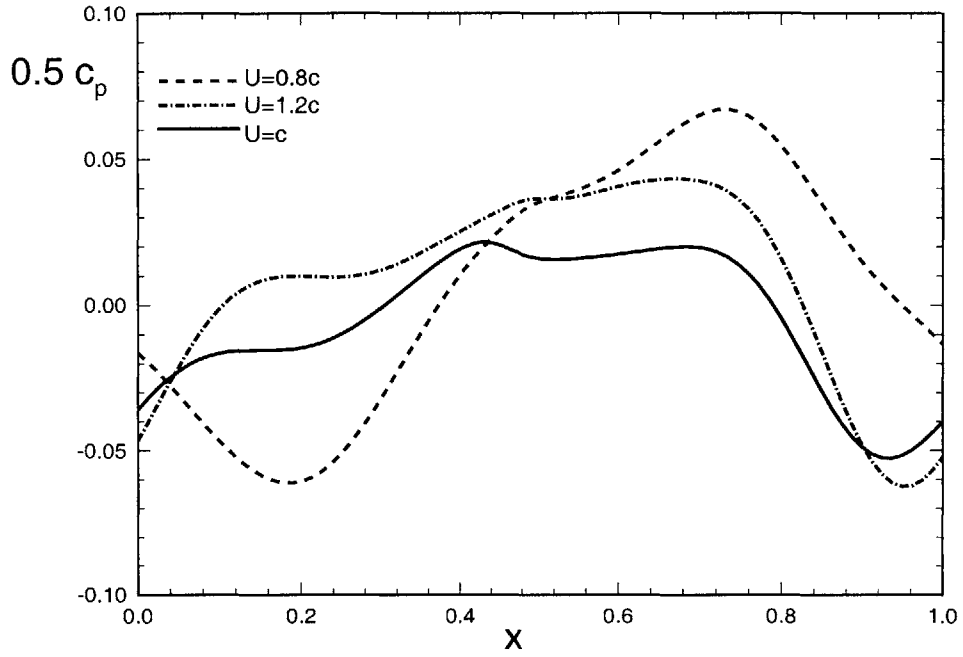

Figure 6-25: Surface pressure distribution for fixed c.

In order to show the effects of outer flow velocity on the sliding body pressure distribution, we show in figure 6-25 the pressure for same $c = 1$ for different U/c. The outer flow does not affect the pressure as much as the variation in c. Only for big c/U can pressure be shown with distinct maximum and minimum. For a fixed c, pressure variation increases as a function of c/U.

After examining the thrust generation for cases with extreme c/U, we study surface pressure and friction for moderate $ka = 0.5$ and c/U which is shown in 6-26. The increase in pressure variation from $c/U = 1.2$ to $c/U = 2$ is much more striking than that from $c/U = 0.0$ to $c/U = 1.2$. Maximum pressure location coincides with the reattachment point. If there is separation, the effective wave steepness is decreased. Figure 6-27 shows the friction for four c/U values. For large c/U, the variation of c_f on the surface can be as twice as much the flat wall value, and at this value the surface friction is controlled by body motion and is not affected by the outer flow condition. The recirculation zone de-attaches from the surface as c increases. In the range $1.2 < c/U < 2U$, as c increases, the friction decreases. This can be explained

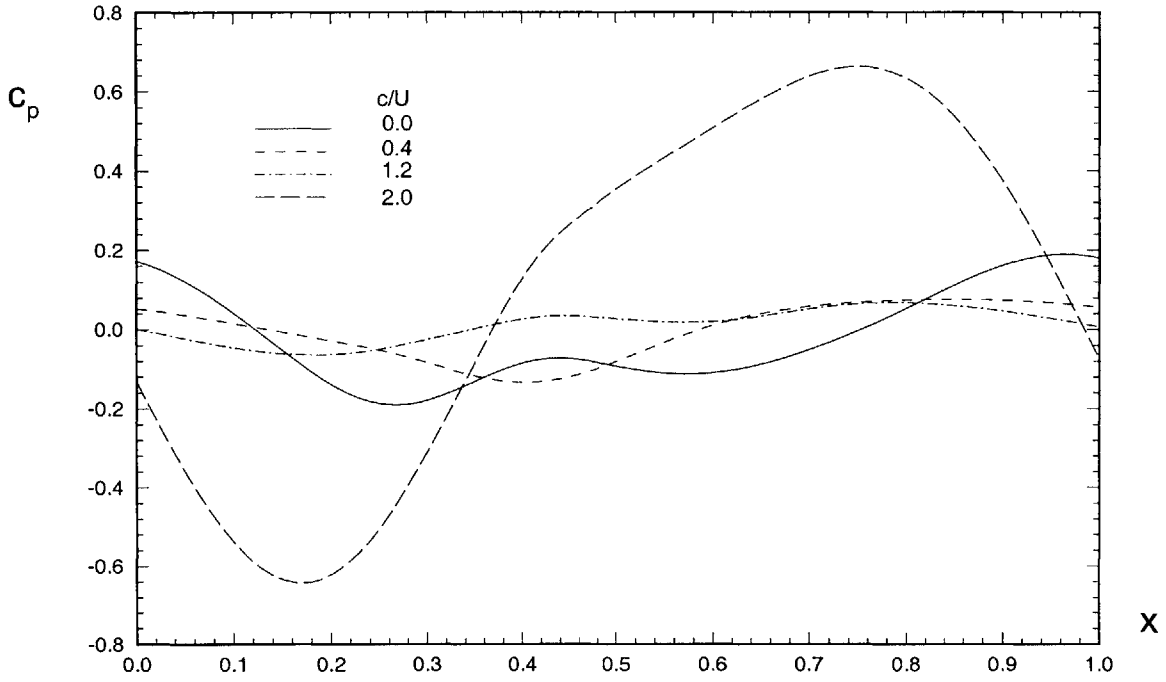

Figure 6-26: Surface pressure distribution.

by examining the tangential velocity on the wall and the mean velocity.

Thrust generation and accompanied drag reduction in our case is not the same as common drag reduction mechanisms, which are mostly passive and with no involvement of pressure force.

Now we examine the pressure force again which is given in (6.5). In order that a thrust exists, for positive wave slope, small pressure is desirable. For negative slope, big pressure is desirable. If local horizontal pressure component $c_p n_x > 0$, it is a force in x direction. So if the integral is positive, the force is a drag and negative value means thrust. Same sign notion is applied here for friction force. For $c/U = 0.0$, pressure in the preceding half of the separation region is almost constant over the central portion of the bubble. The pressure near the reattachment point is similar to that which would be produced by a stagnation-point flow with impingement at an oblique angle to the surface. The reattachment can be defined using shear stress as well as mean streamlines or pressure maximum. The reattachment point defined by these three are not the same due to the unsteadiness of the flow. Away from

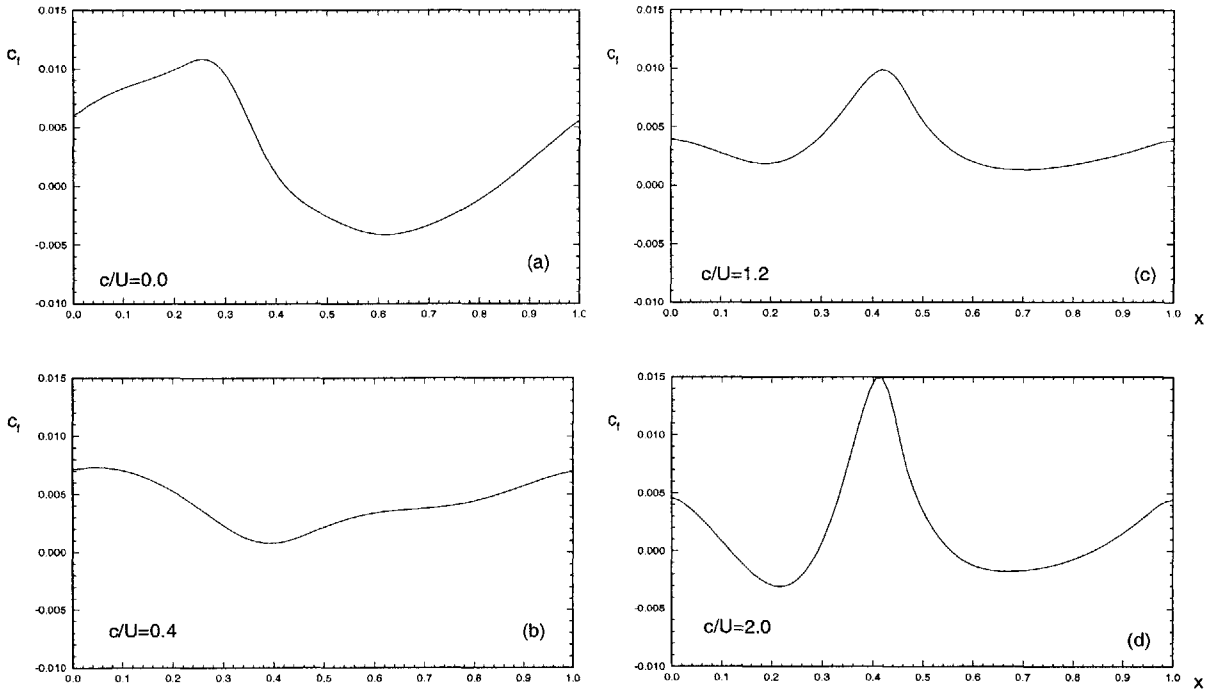

Figure 6-27: Surface friction distribution (a) $c/U = 0.0$, (b) $c/U = 0.4$, (c) $c/U = 1.2$, (d) $c/U = 1.2$.

the separation region, the boundary layer highly depends on the outer flow. From $c = 0$ to $c/U = 2$, the flow field changes from separation controlled to centrifugal force controlled pressure distribution. Local pressure variation as a function of c/U is shown in figure 6-28. The local contribution to pressure coefficient $c_p \frac{dy}{dx}$ is shown in figure 6-29. The pressure variation on the surface decreases about 50% from $c/U = 0$ to $c/U = 1.2$. When c/U is greater than 1.5, pressure changes dramatically, and the profile is controlled by centrifugal force. For $c = 2.0U$, thrust is generated on 70% of the surface. As c increases from 0 to $1.2U$, the maximum of the pressure keeps almost the same, but it is the distribution change that generates thrust, as shown in figure 6-29. For boundary layer flows, the variation in pressure drag is not as significant at for shear flow case.

As may be expected, such traveling wavy motions effects have a direct implication on the overall dynamics of the "swimming" motion. Table 6.5 summarizes the DNS calculations for a range of c/U for the wavy plate. All quantities shown are time

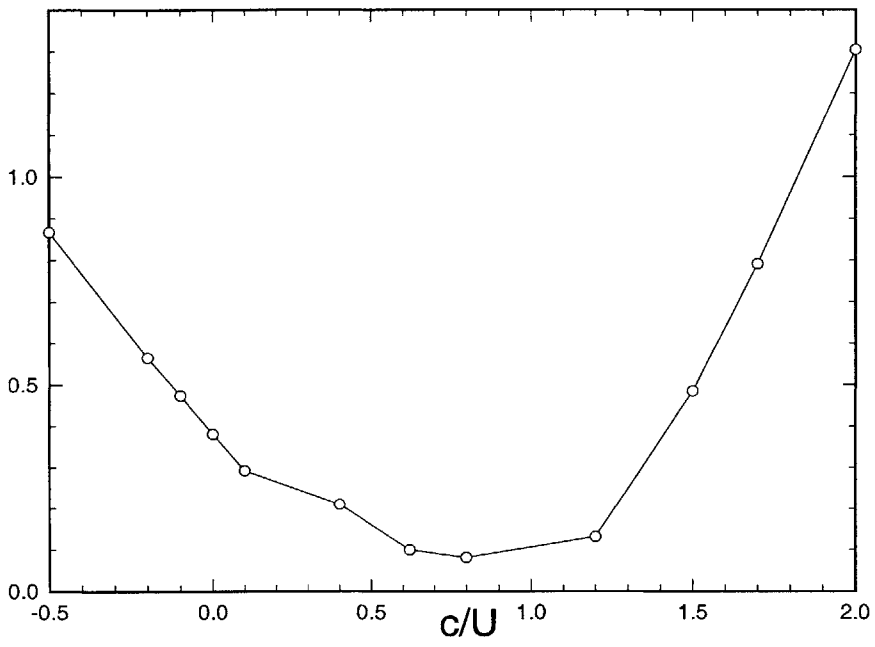

Figure 6-28: Pressure variation on the surface as a function of c/U.

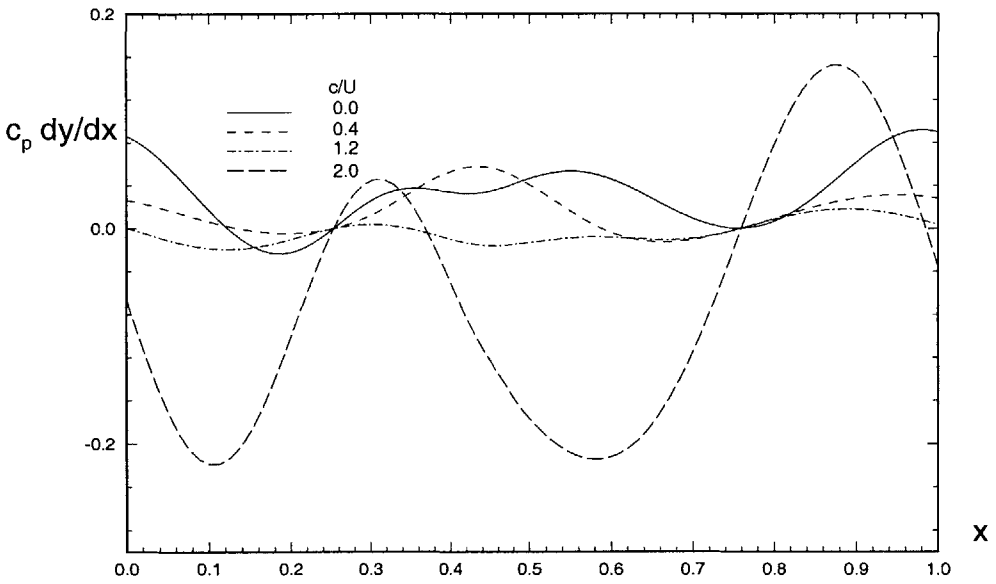

Figure 6-29: Contribution on pressure force

c/U	$F_p = \int C_{p_x} dx$	$F_f = \int C_f dx$	$F_T = F_p + F_f$	P_S	$P_T = P_S + UF_T$
0.0	0.127	0.010	0.137	0	0.137
0.4	0.064	0.017	0.081	0.050	0.131
0.8	-0.030	0.018	-0.012	0.048	0.036
1.2	-0.015	0.015	0.000	0.035	0.035
2.0	-0.262	0.008	-0.254	0.970	0.716

Table 6.3: Force and power required to propel a plate undergoing wavy motions with different phase speeds c/U. The maximum amplitude of wavy plate motion is a/L=0.032. The Reynolds number based on L for all cases is 6000.

(over one period) and laterally averaged values. The total longitudinal force on the plate F_T=$F_p + F_f$, where F_p, F_f are respectively the components in the longitudinal direction due to pressure and friction (viscous stress). Also calculated are the averaged total power required to execute the swimming motion P_S ($=\int C_y(x)\dot{Y}(x)dx$ where C_y is the vertical force coefficient and $Y(x)$ is the instantaneous vertical position of the plate); and the total power required to move the body $P_T \equiv P_S + UF_T$.

The most interesting case is for c/U=1.2 where F_p and F_f almost cancel completely resulting in $F_T \approx 0$, i.e., condition for steady motion. Remarkably, the total power for this motion is smaller by factors of approximately 3.8, respectively, than that required for the fixed plate (c/U=0) of the same length and moving at the same speed.

Swimming energy is shown in figure 6-32. The total pressure and friction forces as a function of c/U are also shown in figure 6-30. Pressure force decreases as c/U increases, at about $c = U$, the pressure force is zero, and then it becomes negative, which means thrust. Zero total force is achieved at about $c = 1.2U$ at this wave slope. It can be seen that for $c/U = 1.2$, the total swimming energy reaches a local minimum.

The linear approach deviates as c increases because pressure gradient increases as c^2. From the pressure distribution for $c/U = 0$, one can design a surface motion that absorbs energy from the flow, and small positive wavy motion fit that requirements. That surface motion has to have a leading harmonic component which corresponding

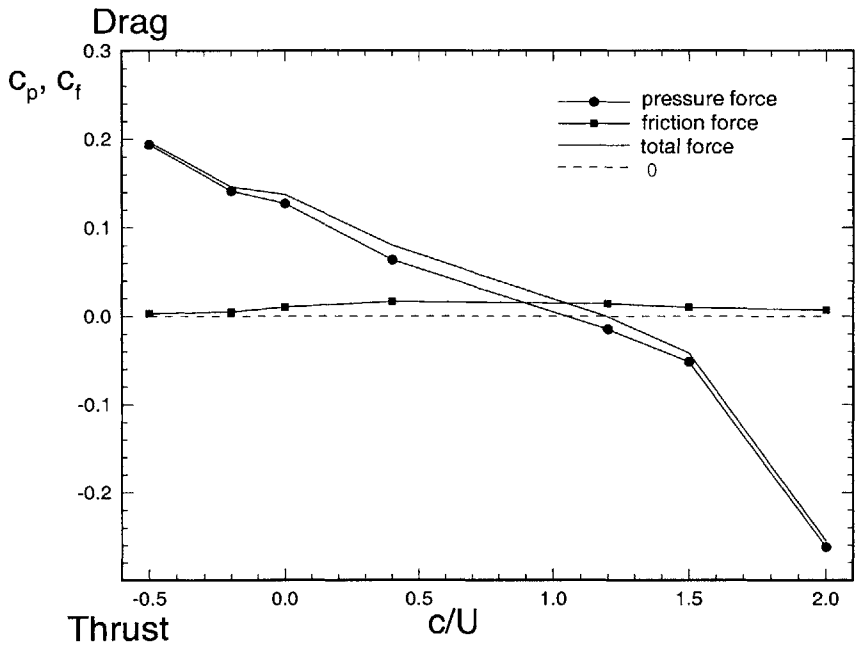

Figure 6-30: Pressure and friction force distribution

wavy motion in the flow direction. So for small c/U, the energy is extracted from the flow to the wavy wall, as long as the wavy motion is slow enough that it does not change the pressure profile of the flow. However, for c/U big, the pressure changes dramatically, and there has to be power input. There exists a c/U for every surface amplitude, the total swimming energy is zero. So for $c/U = -\delta$ and $c/U = \delta$, the energy is to the opposite direction. In the mean time, the drag is decreased. However, the energy that can be extracted from the wavy wall is small. What are the key differences for a flow over a traveling wavy wall at different wave speed. This means that wavy motion can input energy from the flow. Figure 6-31 shows surface pressure for $c/U = 0.1$ for comparison. It's clear that for $c/U = 0.1$, the pressure drag is decreased. The basic shape of the pressure profile is unchanged. Because for c/U with 0.1 and -0.1, the velocity vector on the surface is of the opposite sign, it is obvious one of the flow can extract energy from the wavy motion.

The mean pressure contour is shown in figure 6-33. For $c/U = 1.2$, the pressure variation is closer to the surface and organized distribution of pressure is obvious on the surface. For large c/U, the friction is very small, because the surface motion is

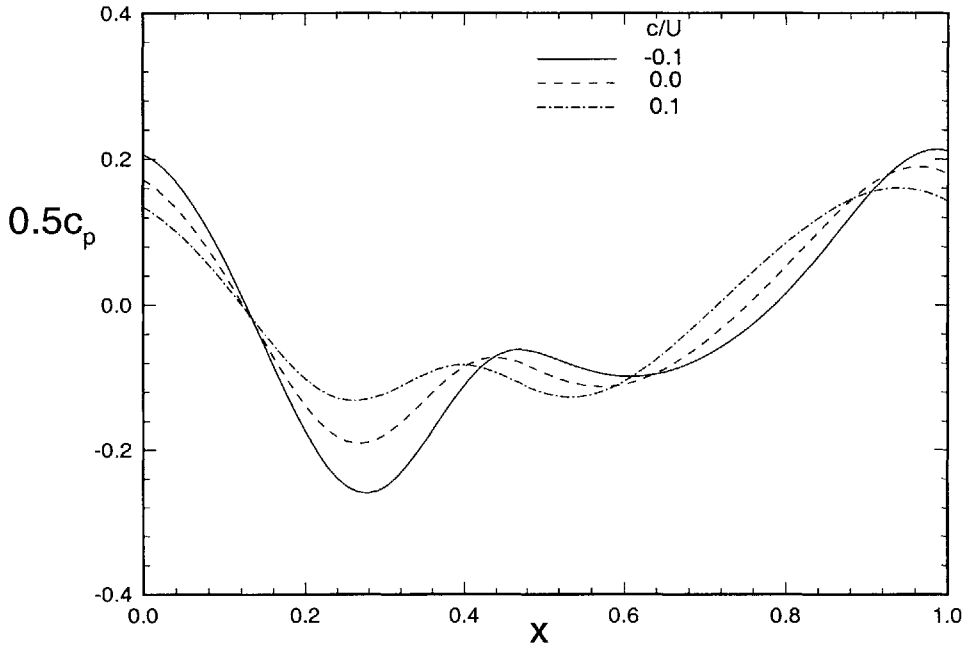

Figure 6-31: Surface mean pressure coefficient distribution for small c/U values.

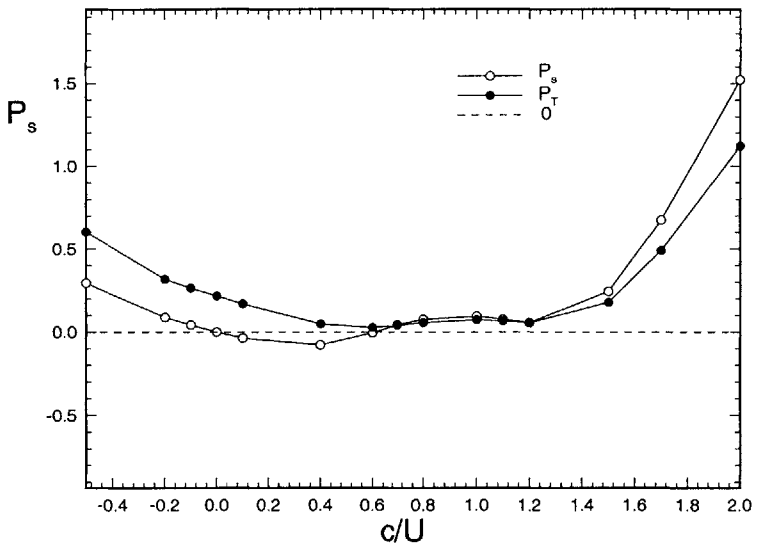

Figure 6-32: Swimming energy (P_S) and total energy (P_T) as a function of c/U.

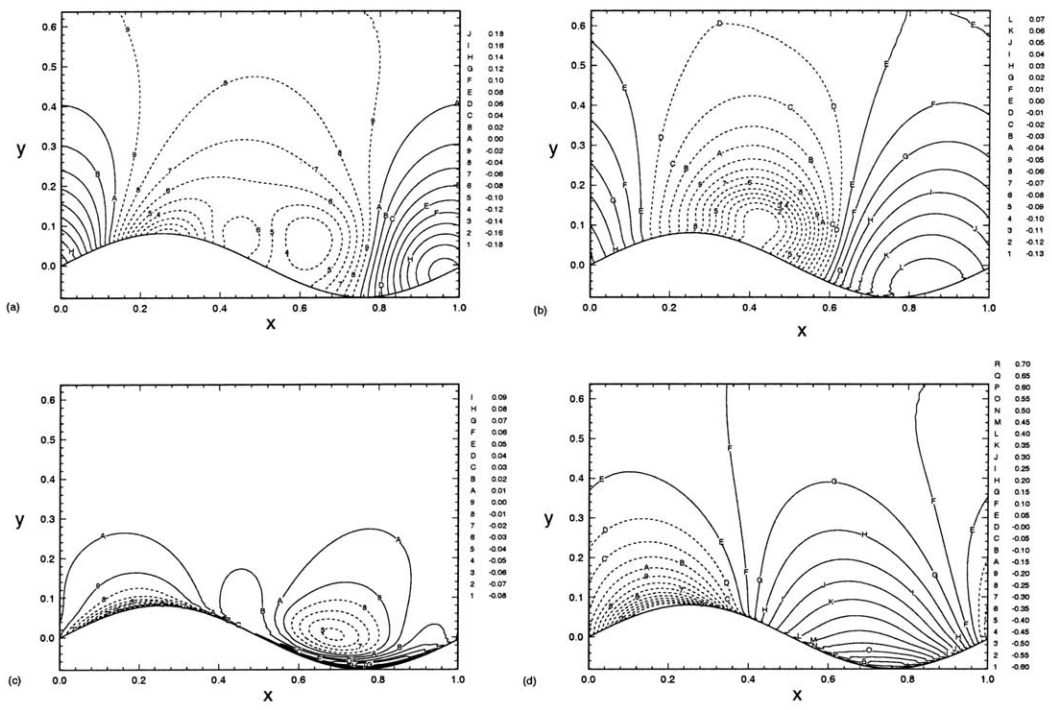

Figure 6-33: Mean pressure contour (a) $c/U = 0.0$, (b) $c/U = 0.4$, (c) $c/U = 1.2$, (d) $c/U = 2.0$.

nearly normal to the wall and no friction exists. So for very large c/U, turbulence plays a minor role in determining the shear stress. As Reynolds number increases, separation is delayed and the shear layer is extended because of the thickness of boundary layer is of less importance. Fish swimming mechanism is a combination of wavy wall mechanism and flapping foil mechanism. There are differences between the two mechanisms. For different fish, different mechanism plays a major role. Wavy motion generate near uniform thrust to propel the body and the flapping foil generate transient fores of high amplitude or create momentum for turning. However there are two criteria: (1) generate thrust, (2) minimize lateral force. Now we explain why the pressure difference decreases as c/U increases slightly from 0. The reason for this is that for small c/U, the pressure is controlled by variation in streamline and for big c/U, the pressure is controlled by centrifugal force. One should be clear that the thrust is generated along the fish body, not only at the tail portion of the fish. It is amazing that the pressure force and drag force can be balanced for nearly all Reynolds numbers for given c/U values.

In order to increase pressure thrust, the pressure should increase as much as possible after decrease near the wave crest before the wave trough to increase the thrust. The wavy motion does just that. Also in wave crest region, the wavy motion increases the surface pressure near wave crest and decrease the drag portion of the pressure force. For fixed a, as c increases, the friction drag first increases, then decreases, reaches minimum at about $c = U$ and then increase again. As c increases, the pressure drag decreases and becomes negative (thrust). Our key observations are:

(1) For c=0.0U and c=0.4U, both pressure and friction drags are positive (no thrust).

(2) For c=0.4U, if the body is free to move, it will decelerate, and thus c=0.4U motion cannot be sustained. So when a fish reduces its wavy motion speed, it has to slow down.

(3) For c=1.2U, the pressure thrust is approximately equal to the friction drag. The system is balanced. In other words, a fish can maintain its motion with constant speed.

(4) For c=2.0U, pressure thrust >> friction drag. If the body is free to move, it will accelerate and finally reach $U \approx c$. (Another way to show the effects of wavy motion is to show the forces as a function of U/c (fixed c) instead of c/U).

(5) Friction is similar for $c = 0.4U$ and $c = 1.2U$, which confirms Taneda's experiment.

(6) From $c = 0$ to $c = 0.4U$, there is a big increase in friction drag.

Because in experiments, drag is measured as the summation of pressure force and viscous friction force and the two cannot be separated from one another. In our simulation, we can easily identify the two forces. In experiment, one can measure friction for a fixed body, and then measure the total drag for a swimming body. But the friction drag in swimming case is already changed. Our simulation shows that there exists a dividing line on which the velocity gradient is zero so that zero total force

is achieved. For small c/U, the flow field induces flow in the wave trough region and the contraction of streamlines near wave crest becomes less significant and pressure in that region increases. In the mean time, the maximum pressure decreases. For non-separated flow, the decrease is uniform (see figure 6-22(a). For separated flow, the pressure maximum near reattachment point decreases as well, but more complex than non-separated case. For even larger c/U, the centrifugal force take over and pressure variation increases again with c/U.

For wavy wall motion, the mean pressure variation on the surface increases as c/U increases, but r.m.s. pressure fluctuations decreases. The fluctuation is well correlated with the mean pressure. Big r.m.s. pressure fluctuation can be attributed to the flow impinging on the wall near stagnation point. For wavy wall flow, that kind of interaction does not exist.

6.6 Applicability of boundary layer theory to wavy wall flow

Boundary layer theory is not valid any more for big c/U and boundary layer approximation cannot be applied because one of the basic boundary assumption regarding normal pressure gradient is not valid any more. Also not valid is the implied assumption in boundary layer theory that the surface tangential pressure gradient can be calculated by the far field velocity. The shape parameter changes as a function of c/U. At $c = 0$, maximum shape parameter is greatest. But for $c = 1.2U$, the shape parameter is more uniformly distributed.

For large c/U and ka, there is a large normal pressure gradient especially near the wave crest and wave trough. This implies that there exists a significant surface normal pressure gradient on the wall. This result is not compatible with the standard boundary layer conclusion that the pressure variation across the boundary may be neglected. It turns out that, viewing the problem in a moving frame, the centrifugal force dominates the surface pressure distribution when both the wall sliding velocity

and surface curvature radius are large. The periodic interchange of favorable and adverse pressure gradients and reversal of the mean flow and the shear stress determine the shift of surface pressure distribution. The centrifugal force increases the pressure near the trough while displacement of boundary decrease the pressure in the same region, so this effect reduces pressure drag. For $c = 2U$, the strong interaction between surface flow and outer flow generates a double layer. Friction velocity is twice as larger at location f than location g. Potential flow theory cannot account for the term $\frac{V_t^2}{R}$ in normal momentum equation, where R is curvature radius. No matter how fast a surface particles slide over a curved surface, the potential flow field cannot feel the motion. So potential theory is inadequate here to describe flow near flexible surface. For example, for $c = U$ case, potential theory predicts the dynamic pressure is zero everywhere. However when there is viscosity, the surface normal pressure gradient is of order $O(1)$ with $ka = 0.75$ and $Re = 6000$. In potential theory, wavy wall flow of phase velocity $c > U$ is equivalent to wavy wall flow of phase velocity $c - U$. The only difference is the flow direction. For $c = 2U$, the acceleration is too strong that a second layer exists.

6.7 Coherent structures

Wall turbulence research is interested in quasi-streamwise vortices. Spatial variation of vortex in streamwise direction is much slower than the characteristic variation in the transverse direction. We are interested in the streak pattern in the presence of turbulence laminarization.

The horizontal velocity with spanwise mean subtracted at a location $y^+ = 12$ is shown in figure 6-34. The velocity pattern for $c/U = 0$ clearly shows long streaky pattern with fast and slow motion side by side. For larger c/U, the decay in turbulence affects streak structures as well. The intensity in terms of $u(x, z)$ decreases. Streaky pattern is only evident in the trough region. Previous study of curvature effects does not account for pressure gradient effects. For a surface where both convex and concave curvatures are present, a streamwise pressure gradient is inevitable. The bigger the c,

the bigger the pressure gradient. The flow returns to isotropy when y is big for $c > U$ while for $c < U$ isotropy exists almost up to the wall. It is well known that streaky pattern exists in wall-bounded turbulent flows that are . The streamwise pressure gradient affects the velocity acceleration which affects the flow properties.

Flow over a concave surface is not stable while flow over a convex surface is stable. It thus can be deduced that the intensity of turbulence should increase on concave surfaces and decrease on convex surfaces. Usually when people talk about convex and concave surface, they refer to static surface. However for our simulation, in the moving frame, the boundary is sliding in its tangential direction. When c is large, this sliding velocity is of the same order and we can anticipate the centrifugal force (proportional to v_t^2/R, v_t the velocity along the streamline, R the curvature radius of the streamline) is much bigger than that of the flow over the same static surface. So we are to see stability properties change also according to c/U. In figure 6-35, we show the Taylor-Görtler instability criterion for sliding boundary. v_0 is the surface sliding velocity. For our case it is the composite velocity of wave phase speed and oscillating velocity. v_δ is the velocity at a small distance away from the wall. For flow over a convex surface, if $v_\delta > v_0$, the flow is stable; while if $v_\delta > v_0$, the flow is unstable. Because of the stabilizing mechanism, the surface normal velocity component should show the strongest stabilizing effect. This is indeed the case when we take both the horizontal and normal fluctuation components and project them to the surface normal direction. As c/U varies, the stabilizing and destabilizing regions on the surface are relocated and the scales of the effects are modified. The overall effect is determined by the competition between the stabilizing and destabilizing effects.

For separated flow, turbulence decreases form drag. For non-separated flow, turbulence does not reduce form drag, but reduce friction drag. Wavy motion eliminate separation and turbulence laminarization does not affect the form drag. Our numerical simulation shows that only for certain boundary thickness can the trapped vortex be kept in the trough region. The trapped vortex may slide on the wavy boundary and the pressure on the flexible surface is affected. From $c = 0$ to $c = 2U$, the control of pressure field changes from trapped vortex controlled to centrifugal force

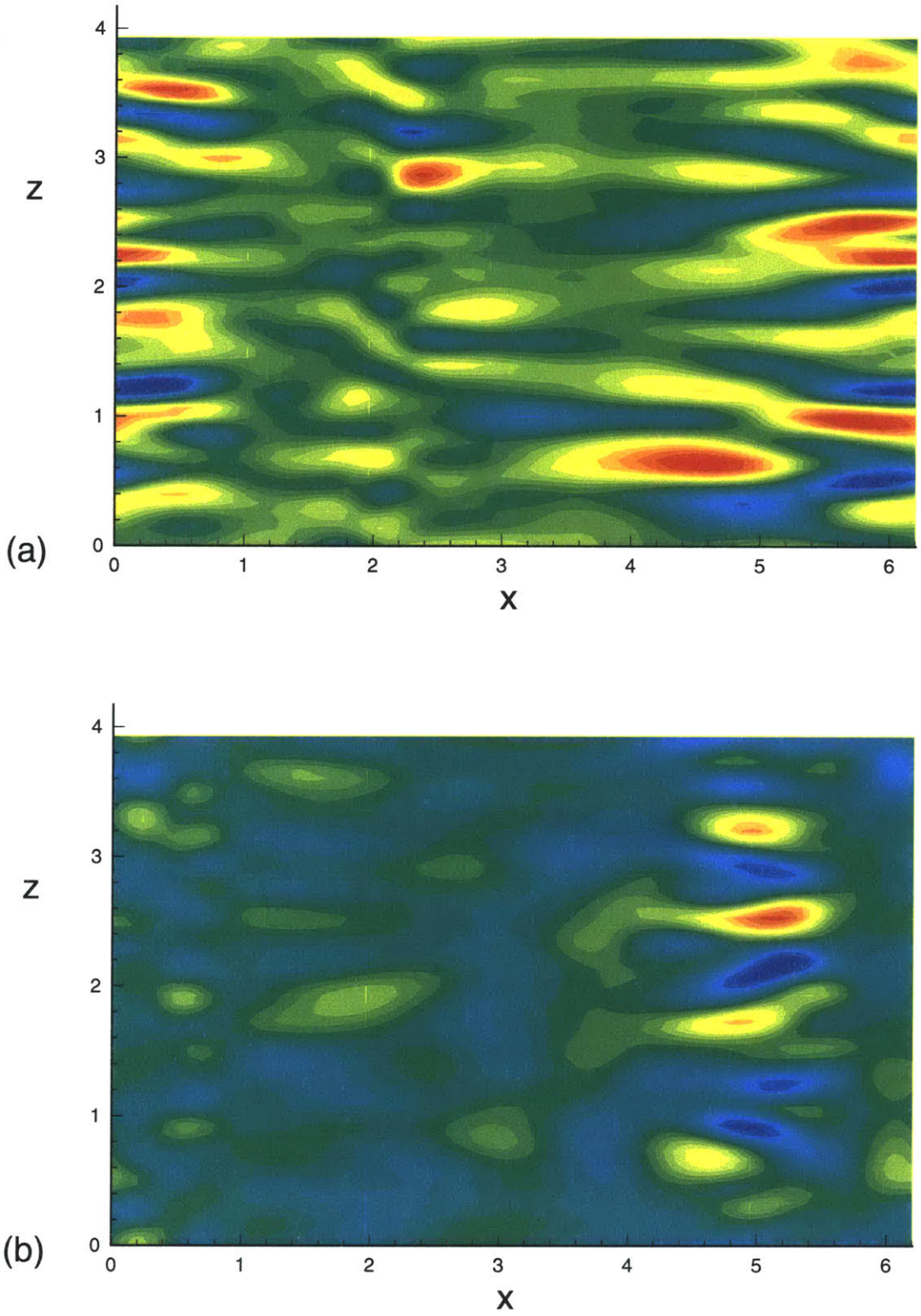

Figure 6-34: Instantaneous u^+ distribution at $y^+ = 12$: (a) $c/U = 0.0$, (b) $c/U = 1.2$.

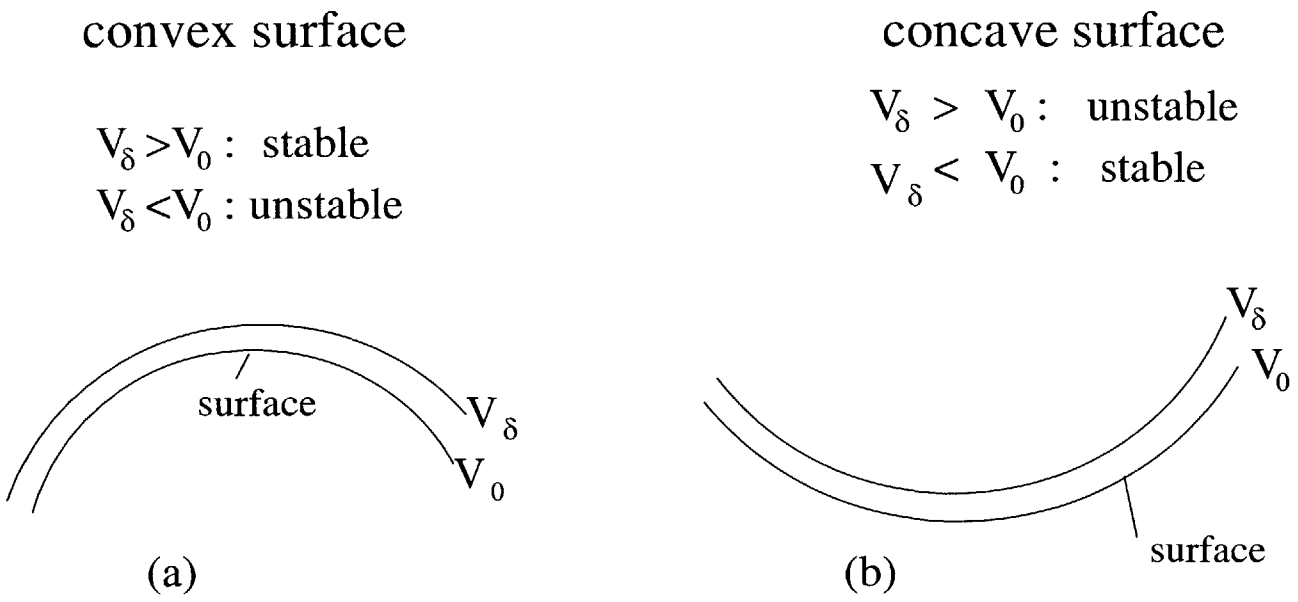

Figure 6-35: Taylor-Gortlor instability criterion: local near surface velocity comparison.

controlled.

6.8 Three dimensional flow over a flexible ribbon

The remarkable success in turbulence suppression by wavy motion observed in the above chapters raised a new question. Can we apply the same mechanism to a cable to modify the flow to achieve certain dynamical advantage? It is beneficial to have a reduced turbulence for cables with communication tasks. Lueptow investigated turbulent boundary layer on a cyliner in axial flow.

A cable with elliptical cross section is simulated. The fluctuating vorticity distribution in the central streamwise cross section is shown in figures 6-36 and 6-37. Our preliminary research shows that there is reduced vorticity fluctuation for $c/U = 1.2$. Because noise reduction is more important for the ribbon problem, we plot in figure 6-38 the pressure fluctuation for the two cases and there is obvious reduction in pressure fluctuation.

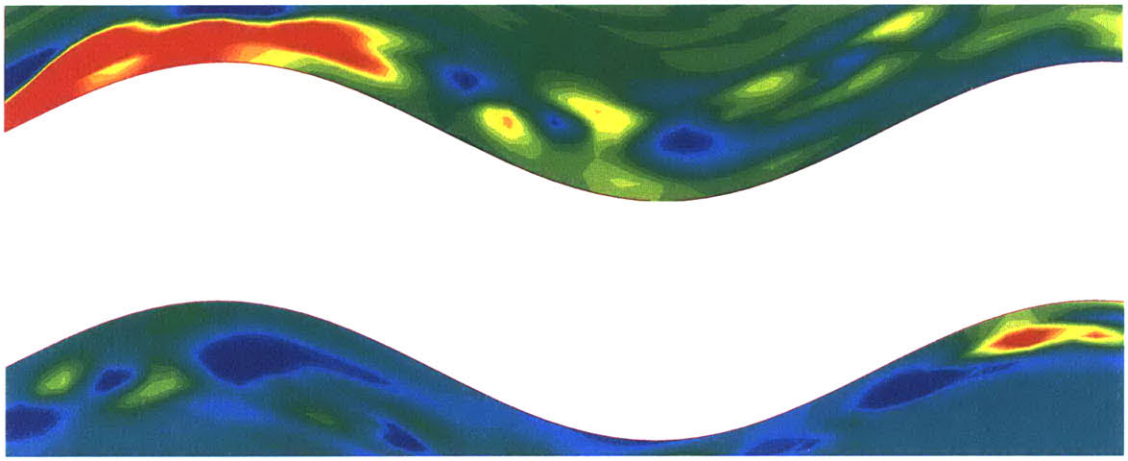

Figure 6-36: Fluctuating vorticity contour on central streamwise cross section, $c/U = 0.3$).

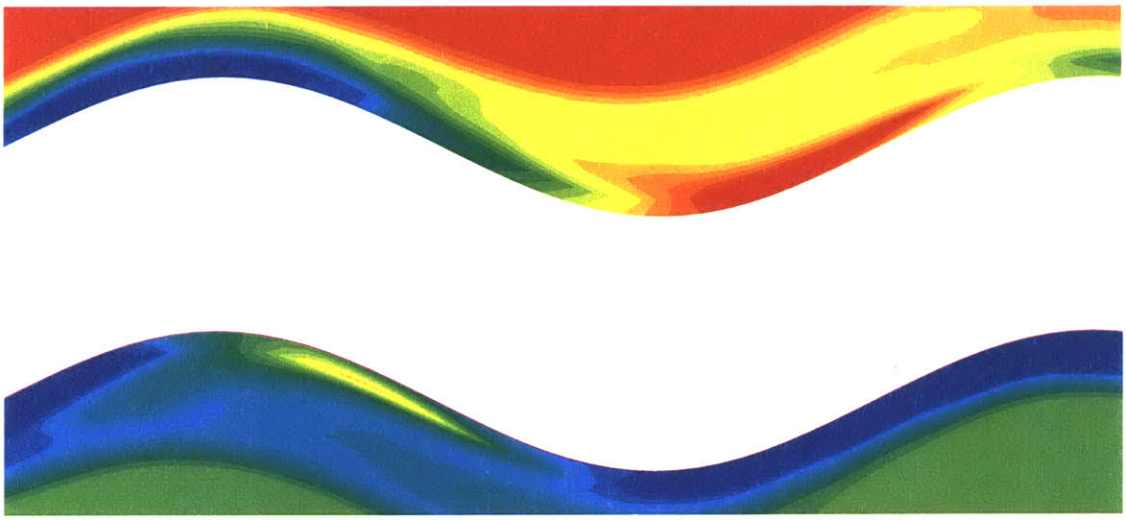

Figure 6-37: Fluctuating vorticity contour on central streamwise cross section, $c/U = 1.2$).

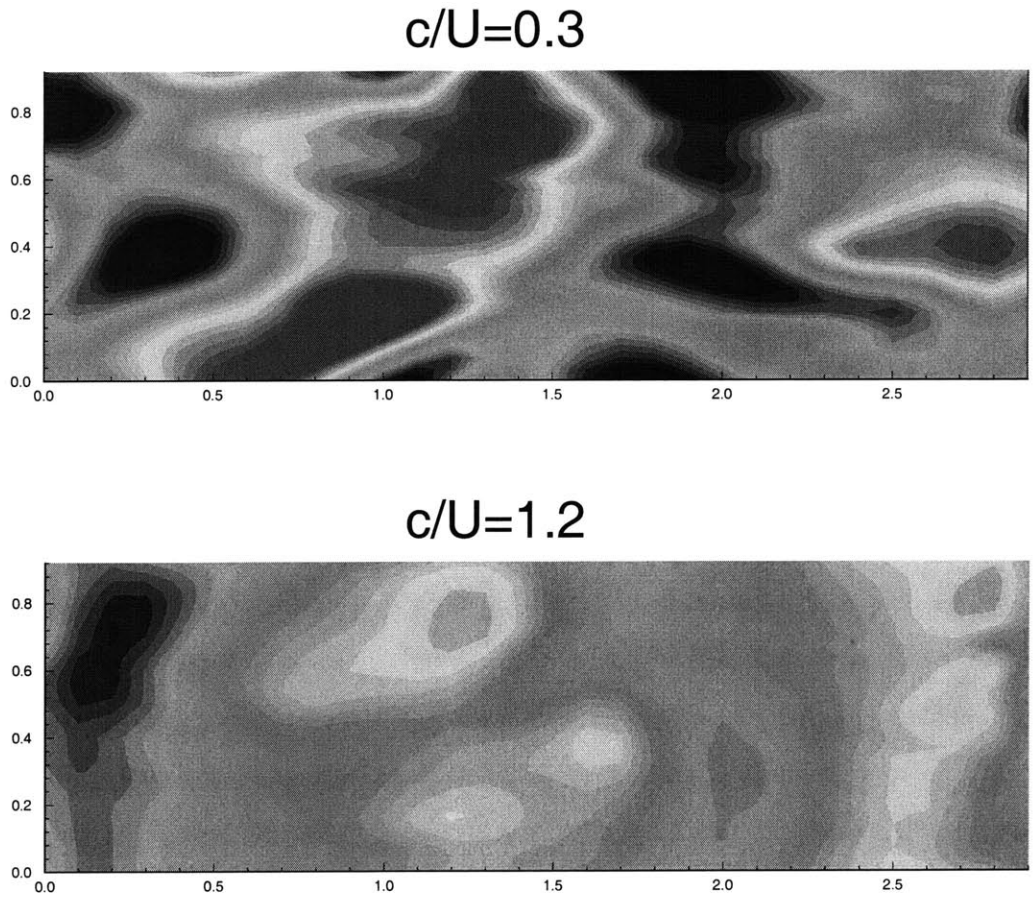

Figure 6-38: Surface pressure fluctuation (with local average subtracted)

Chapter 7

Summary and concluding remarks

Direct numerical simulation of turbulent flow over a flexible surface was performed. One objective of this work is to eliminate some of the existing controversies regarding the efficiency of fish swimming. We believe that key source of fish propulsion has been captured and fish forward swimming mechanism is thoroughly explained. This work quantitatively elucidates locomotion mechanism of fast fish swimming in anguilliform mode. This research confirms that major functionality of boundary motion is to create a pressure thrust, and at the same time get drag reduction and turbulence suppression if possible. Because of the disappearance of separation, the body appears to be more streamlined and does not generate a wake flow that would increase pressure drag. So optimal wavy motion not only generates thrust but also eliminates undesirable wake.

Because the pressure is not the same for crest and wave trough, there is transverse flow (converging or diverging)on the sides. The flow pattern is a strong function of c/U. For $c = 0$, there are features like separated region, attached boundary layer, and free shear layer. The pressure gradient created on the surface is balanced by viscous force in the momentum equation. For $c/U = -0.2$, the separation point and reattachment point move away from the wall but the separation bubble persists. Secondary flow exists both at the wave crest and wave trough. For $c/U > 0$, the pressure gradient is not balanced by viscous stress only, but also by centrifugal force. Separation and reattachment points move away from the wall but not as far away as

$c/U < 0$ case. As c increases, the separation bubble disappears at a certain c value. For $c/U = 2$, there is a secondary reverse flow near the wave crest and local friction velocity becomes very small. For large ka at $c/U = 0$, the flow is not sensitive to ka because separation location does not change much and outer flow cannot feel the difference.

Only viscous flow simulation can explain fish swimming, since for potential flow the viscous friction is omitted and no steady state can be achieved. However, some other fish swimming features may be related to potential effects, such as turning, etc. Without considering viscous effect, pressure force cannot be calculated correctly. We showed how the friction evolves as a function of c. Friction force reaches maximum at a wave speed slightly smaller than U. We verified Taneda's conclusion that the swimming motion accelerates the flow near the surface in the wave direction and suppress the turbulent fluctuations.

Turbulence is effectively reduced by the wave motion. If it were not for the laminarization, fish would be swimming at, say $c = 1.3U$. If ambient turbulence is strong, fish must exert strong wavy motion to achieve same speed. An experiment would be helpful in confirming this assumption. Production of thrust and turbulence suppression are both important for efficient fish swimming.

Some of the features we did not simulate include three dimensional effect, wake (if any) and body turning. For real fish the pressure and friction away from the flipping region should play a role. The mucus (viscous protective lubricant coating) secreted by fish skin gland is not considered, as well as skin elasticity. It is anticipated that these features can enhance drag reduction and maneuverability. The laminarization and separation suppression are striking because few examples were discovered that separation can be eliminated by body motion.

The mean velocity profile of a cylindrical boundary layer is substantially different from that of a planar boundary as the ratio between the boundary thickness and the radius of the cylinder δ/a becomes large. The mean velocity is fuller than in the planar case. Based on two-dimensional wall simulation, the three dimensional flow

over a ribbon with ellips cross section is performed.

It turns out vortex does not play an important role as was suggested before. Vortices are generated on the surface and travel along the body of the fish. The vortices are eventually shed from the surface and may be manipulated by the caudal fin. In wavy wall motion, laminarization does not present itself as reduced friction drag as much as reduced turbulence intensities. We observed that swimming energy is negative for c/U slightly bigger than zero. In this simulation, no rotational motion of the body is considered. Future research can be performed to include that freedom of motion and examine the effect on turbulence and force balance. The question whether wavy propulsion can achieve much better efficiency than stiff propulsion still merits further investigation.

Future work includes the stability analysis of boundary layer on a wavy wall, large eddy simulation, and flow over a compliant wavy wall. Another aspect of work can be performed on flow with a distinct wake effect. Gray's paradox of fish propulsion still merits further investigation.

Bibliography:

BENJAMIN, T. B., 1959, Shearing flow over a wavy boundary, *J. Fluid Mech.*, **6**, 161.

BARRETT, D.S., TRIANTAFYLLOU, M.S., YUE, D.K.P., GROSENBAUGH, M.A., WOLFGANG, M.J., 1999, Drag reduction in fish-like locomotion, *J. Fluid Mech.*, **392**, 183.

BRADSHAW, P., 1969, The analogy between streamline curvature and buoyancy in turbulent shear flow, *J. Fluid Mech.*, **36**, 177.

BUCKLES, J., G.W., HANRATTY, T.J., ADRIAN, R.J., 1984, Turbulent flow over large-amplitude wavy surfaces, *J. Fluid Mech.*, **140**, 27.

CHERUKAT, P., NA, Y., T.J. HANRATTY, J.B. MCLAUGHLIN, 1998, Direct Numerical Simulation of a Fully Developed Turbulent Flow over a Wavy Wall *Theoret.*

Comput. Fluid Dynamics, **11** 2, 109-134.

ESKINAZI, S. & YEH, H., 1956, An investigation on fully developed turbulent flows in a curved channel *J. Aero. Sci.*, **23**, 23.

GÖRTLER, H., 1940, On the three-dimensional instability of laminar boundary layers on concave walls, *Tech. Mem. Nat. Adv. Comm. Aero. Wash.*, No. 1375 (1975).

GRAY, J., 1936, Studies in animal locomotion, *J. Experi. Bio.*, **13**, 192.

KENDALL, J.M., 1970, The turbulent boundary layer over a wall with progressive surface waves, *J. Fluid Mech.*, **41**, 259.

KIM, J., MOIN P., & MOSER R., 1987, Turbulent statistics in fully developed channel flow at low Reynolds number, *J. Fluid Mech.*, **177**, 133.

LONGUET-HIGGINS, M.S., 1969, Action of a variable stress at the surface of water waves, *Phys. Fluids*, **12**, 737.

LUEPTOW, R.M., 1990, Turbulent Boundary Layer on a Cylinder in Axial FLow, *AIAA Journal*, vol**28**, No.10, 1705.

MAASS, C. & SCHUMANN, U., 1994, Numerical simulation of turbulent flow over a wavy boundary, *Direct and Large-Eddy Simulation, Voke, P.R. et al. (eds.)*, p.287.

PRANDTL, L. 1930, Vorträge auf dem Gebiet der Aerodynamik und verwandter Gebiete, *Gesammelte Abhandlungen zur angewandten Mechanik, hydround Aerodynamik, 1961*, **2**, 778.

ROTTA, J.C., 1967, Effect of streamwise wall curvature on compressible turbulent boundary layers, *Phys. Fluids*, **12**, S174.

SIMPSON, R.L., CHEW, Y.-T. & SHIVAPRASAD, B.G., 1981, The structure of a separating turbulent boundary layer. Part I. Mean flow and Reynolds stresses. *J. Fluid. Mech.*, **113**, 23-51.

SIMPSON, R.L., CHEW, Y.-T. & SHIVAPRASAD, B.G., 1981, The structure of a

separating turbulent boundary layer. Part II. Higher order turbulence results. *J. Fluid. Mech.*, **113**, 53-73.

So R.M.C. & Mellor G.L., 1973, Experiment on convex curvature effects in turbulent boundary layers, *J. Fluid Mech.*, **60**, 43.

Spalart, P. R., 1988, Direct simulation of a turbulent boundary layer up to $R_\theta = 1410$, *J. Fluid. Mech.*, **187**, 61.

Taneda, S. & Tomonari, Y., 1974, An experiment on the flow around a waving plate,
J. Phys. Soc. Japan, **36**, 1683-1689.

Triantafyllou, M. S. *et al.* , 1991, Wake mechanics for thrust generation in oscillating foils. *Phys. Fluids A*, **3**(12), 2835-2837.

Wu. T.Y. Swimming of a waving plate, 1961, *J. Fluid Mech.*, **10**, 21.

Zilker, D.P., Cook, G.W., Hanratty, T.J., 1977, Influence of the amplitude of a solid wavy wall on a turbulent flow. Part. 1. Non-separated flows, *J. Fluid Mech.*, **82**, 29-51.

Zilker, G.W., Hanratty, T.J., 1979, Influence of the amplitude of a solid wavy wall on a turbulent flow. Part. 2. Separated flows, *J. Fluid Mech.*, **90**, 257.

Appendix A

Derivation of the fully nonlinear boundary stress conditions

A.1 Exact equations and approximation

In this appendix, free surface boundary conditions are expressed in tensor form, fully nonlinear form, and weakly linear form. First we present dynamic boundary condition for weakly nonlinear case. Note that the mean free surface is at $z = 0$.

• Normal-stress boundary condition:

$$-\boldsymbol{n} \cdot \|\overline{\boldsymbol{P}}\| \cdot \boldsymbol{n} = 2H\sigma + \mu^s(\boldsymbol{b} - 2H\boldsymbol{I}_s):\nabla_s \boldsymbol{v}^o + 2H(\kappa^s + \mu^s)\nabla_s \cdot \boldsymbol{v}^o \qquad \text{(A.1)}$$

$$\begin{aligned} &-P + 2\mu[w_z + \eta w_{zz} - \eta_x(u_z + w_x) - \eta_y(w_y + v_z)] \\ &= (\eta_{xx} + \eta_{yy})\sigma + \mu^s(-\eta_{yy}u_x + \eta_{xy}u_y + \eta_{xy}v_x - \eta_{xx}v_y) \\ &\quad +(\kappa^s + \mu^s)(\eta_{xx} + \eta_{yy})(u_x + v_y) + O(\epsilon^2) \end{aligned}$$

•Tangential-stress boundary condition:

$$-\boldsymbol{n} \cdot \|\overline{\boldsymbol{P}}\| \cdot \boldsymbol{I}_s = \nabla_s\sigma + (\kappa^s + \mu^s)\nabla_s\nabla_s \cdot \boldsymbol{v}^o \qquad \text{(A.2)}$$

$$+\mu^s\{\boldsymbol{n} \times \nabla_s[(\nabla_s \times \boldsymbol{v}^o) \cdot \boldsymbol{n}] + 2(\boldsymbol{b} - 2H\boldsymbol{I}_s) \cdot (\nabla_s \boldsymbol{v}^o) \cdot \boldsymbol{n}\} \qquad \text{(A.3)}$$

(1) on $x-z$ plane:

$$\begin{aligned}
&\mu[-2\eta_x(u_x-w_z)+w_x+\eta w_{xz}+u_z+\eta u_{zz}-\eta_y(v_x+u_y)]\\
&=\sigma_x+(\kappa^s+\mu^s)(u_{xx}+\eta u_{xxz}+\eta_{xx}u_z+\eta_x u_{xz}+v_{xy}\\
&\quad+\eta v_{xyz}+\eta_{xy}v_z+\eta_y v_{xz}+\eta_{xx}w_x+\eta_x w_{xx}+\eta_y w_{xy}+\eta_{xy}w_y+\eta_x u_{xz}\\
&\quad+\eta_x v_{yz})+\mu^s(-\eta_y v_{xz}+\eta_y u_{yz}+\eta_{xy}w_y+\eta_x w_{yy}-\eta_{xy}v_z\\
&\quad-\eta_x v_{yz}+\eta_{yy}u_z+\eta_y u_{yz}-\eta_{yy}w_x-\eta_y w_{xy}-v_{xy}+u_{yy}-\eta v_{xyz}+\eta u_{yyz})\\
&\quad+2\mu^s(-\eta_{xx}w_x+\eta_{xy}w_y)+O(\epsilon^2)
\end{aligned}$$

(2) on $y-z$ plane:

$$\begin{aligned}
&\mu[-2\eta_y(v_y-w_z)+w_y+\eta w_{yz}+v_z+\eta v_{zz}-\eta_x(v_x+u_y)]\\
&=\sigma_y+(\kappa^s+\mu^s)(u_{xy}+\eta u_{xyz}+\eta_x u_{yz}+\eta_{xy}u_z+v_{yy}\\
&\quad+\eta v_{yyz}+\eta_y v_{yz}+\eta_{yy}v_z+\eta_{xy}w_x+\eta_x w_{xy}+\eta_{yy}w_y+\eta_y w_{yy}+\eta_y u_{xz}\\
&\quad+\eta_y v_{yz})+\mu^s(-\eta_x u_{yz}+\eta_x v_{xz}+\eta_{xy}w_x+\eta_y w_{xx}-\eta_{xy}u_z\\
&\quad-\eta_y u_{xz}+\eta_{xx}v_z+\eta_x v_{xz}-\eta_x w_{xy}-\eta_{xx}w_y+v_{xx}+\eta v_{xxz}-u_{xy}-\eta u_{xyz})\\
&\quad+2\mu^s(\eta_{xy}w_x-\eta_{xx}w_y)+O(\epsilon^2)
\end{aligned}$$

Fully nonlinear expressions

- Normal stress boundary condition($z = \eta$) :

$$
\begin{aligned}
&-P + \frac{2\mu}{\mathcal{N}^2}[\eta_x^2 u_x + \eta_y^2 v_y + w_z + \eta_x\eta_y(v_x + u_y) - \eta_x(u_z + w_x) - \eta_y(w_y + v_z)] \\
&= \frac{(1+\eta_y^2)\eta_{xx} + (1+\eta_x^2)\eta_{yy} - 2\eta_x\eta_y\eta_{xy}}{\mathcal{N}^3}\sigma + \frac{\mu^s}{\mathcal{N}^3} \\
&\quad [-\eta_{yy}u_x + \eta_{xy}u_y + (\eta_y\eta_{xy} - \eta_x\eta_{yy})u_z + \eta_{xy}v_x - \eta_{xx}v_y + (\eta_x\eta_{xy} - \eta_y\eta_{xx})v_z \\
&\quad +(\eta_y\eta_{xy} - \eta_x\eta_{yy})w_x + (\eta_x\eta_{xy} - \eta_y\eta_{xx})w_y + (2\eta_x\ \eta_y\eta_{xy} - \eta_{yy}\eta_x^2 - \eta_{xx}\eta_y^2)w_z] \\
&\quad +\frac{(1+\eta_y^2)\eta_{xx} + (1+\eta_x^2)\eta_{yy} - 2\eta_x\ \eta_y\eta_{xy}}{\mathcal{N}^5}(\kappa^s + \mu^s)[(1+\eta_y^2)u_x - \eta_x\ \eta_y u_y \\
&\quad +\eta_x u_z + \eta_y v_z - \eta_x\ \eta_y v_x + (1+\eta_x^2)v_y + \eta_x w_x + \eta_y w_y + (\eta_x^2 + \eta_y^2)w_z]
\end{aligned}
$$

- Tangential stress boundary condition:

(1) on $x - z$ plane($z = \eta$):

$$
\begin{aligned}
&\frac{\mu}{\mathcal{N}}[-2\eta_x(u_x - w_z) + (1 - \eta_x^2)(w_x + u_z) - \eta_y(v_x + u_y) - \eta_x\ \eta_y(v_z + w_y)] \\
&= \sigma_x + (\kappa^s + \mu^s)[\frac{1}{\mathcal{N}^2}(\varphi_x + \eta_x\varphi_z) - \frac{\varphi}{\mathcal{N}^4}(2\eta_x\eta_{xx} + 2\eta_y\eta_{xy})] \\
&\quad +\frac{2\mu^s}{\mathcal{N}^4}(-\eta_x D_1 u - \eta_y D_1 v + D_1 w - \eta_x^2 D_3 u - \eta_x\ \eta_y D_3 v + \eta_x D_3 w) \\
&\quad +\mu^s[\frac{1}{\mathcal{N}^2}\Phi - \frac{\Pi\Omega}{\mathcal{N}^4}]
\end{aligned}
$$

(2) on $y - z$ plane(z=η):

$$
\begin{aligned}
&\frac{\mu}{\mathcal{N}}[-2\eta_y(v_y - w_z) + (1 - \eta_y^2)(w_y + v_z) - \eta_x(v_x + u_y) - \eta_x\ \eta_y(u_z + w_x)] \\
&= \sigma_y + (\kappa^s + \mu^s)[\frac{1}{\mathcal{N}^2}(\varphi_y + \eta_y\varphi_z) - \frac{\varphi}{\mathcal{N}^4}(2\eta_x\eta_{xy} + 2\eta_y\eta_{yy})] \\
&\quad +\frac{2\mu^s}{\mathcal{N}^4}(-\eta_x D_2 u - \eta_y D_2 v + D_2 w - \eta_y^2 D_3 v - \eta_x\ \eta_y D_3 u + \eta_y D_3 w) \\
&\quad +\mu^s[\frac{1}{\mathcal{N}^2}\Theta - \frac{\Pi\mathcal{R}}{\mathcal{N}^4}]
\end{aligned}
$$

A.2 Definitions and derivations

Some definitions used in the above nonlinear expressions

$$\varphi = (1+\eta_y^2)u_x - \eta_x\ \eta_y u_y + \eta_x u_z - \eta_x\ \eta_y v_x + (1+\eta_x^2)v_y + \eta_y v_z + \eta_x w_x + \eta_y w_y + (\eta_x^2+\eta_y^2)w_z$$

$$\begin{aligned}\Phi = {} & \eta_x\ \eta_y w_{yz} - \eta_x\ \eta_y v_{zz} + \eta_y^2 u_{zz} - \eta_y^2 w_{xz} - \eta_y v_{xz} + \eta_y u_{yz} + \eta_{xy} w_y + \eta_x w_{yy} - \eta_{xy} v_z \\ & -\eta_x v_{yz} + \eta_{yy} u_z + \eta_y u_{yz} - \eta_{yy} w_x - \eta_y w_{xy} - v_{xy} + u_{yy} + \eta_x^2 \eta_{xy} w_y + {\eta_x}^3 w_{yy} \\ & -\eta_x^2 \eta_{xy} v_z - {\eta_x}^3 v_{yz} + \eta_x^2 \eta_{yy} u_z + \eta_x^2 \eta_y u_{yz} - \eta_x^2 \eta_{yy} w_x - \eta_x^2 \eta_y w_{xy} - \eta_x^2 v_{xy} + \eta_x^2 u_{yy} \\ & -\eta_x\ \eta_y \eta_{xx} w_y - \eta_x^2 \eta_y w_{xy} + \eta_x\ \eta_y \eta_{xx} v_z + \eta_x^2 \eta_y v_{xz} - \eta_x\ \eta_y \eta_{xy} u_z - \eta_x \eta_y^2 u_{xz} \\ & +\eta_x\ \eta_y \eta_{xy} w_x + \eta_x \eta_y^2 w_{xx} + \eta_x\ \eta_y v_{xx} - \eta_x\ \eta_y u_{xy}\end{aligned}$$

$$\begin{aligned}\Theta = {} & \eta_x\ \eta_y w_{xz} - \eta_x\ \eta_y u_{zz} + \eta_x^2 v_{zz} - \eta_x^2 w_{yz} - \eta_x u_{yz} + \eta_x v_{xz} + \eta_{xy} w_x + \eta_y w_{xx} - \eta_{xy} u_z \\ & -\eta_y u_{xz} + \eta_{xx} v_z + \eta_x v_{xz} - \eta_x w_{xy} - \eta_{xx} w_y + v_{xx} - u_{xy} + \eta_x\ \eta_y \eta_{xy} w_y + \eta_x^2 \eta_y w_{yy} \\ & -\eta_x\ \eta_y \eta_{xy} v_z - \eta_x^2 \eta_y v_{yz} + \eta_x \eta_y \eta_{yy} u_z + \eta_x \eta_y^2 u_{yz} - \eta_x\ \eta_y \eta_{yy} w_x - \eta_x \eta_y^2 w_{xy} \\ & -\eta_x \eta_y v_{xy} + \eta_x\ \eta_y u_{yy} - \eta_y^2 \eta_{xx} w_y - \eta_x \eta_y^2 w_{xy} + \eta_{xx} \eta_y^2 v_z + \eta_x \eta_y^2 v_{xz} - \eta_{xy} \eta_y^2 u_z \\ & -{\eta_y}^3 u_{xz} + \eta_y^2 \eta_{xy} w_x + {\eta_y}^3 w_{xx} + \eta_y^2 v_{xx} - u_{xy} \eta_y^2\end{aligned}$$

$$\Pi = -\eta_x w_y + \eta_x v_z - \eta_y u_z + \eta_y w_x + v_x - u_y$$

$$\Omega = -\eta_x \eta_{xy} - \eta_y \eta_{yy} - {\eta_x}^3 \eta_{xy} + \eta_x \eta_y^2 \eta_{xy} + \eta_x^2 \eta_y (\eta_{xx} - \eta_{yy})$$

$$\mathcal{R} = \eta_x \eta_{xx} + \eta_y \eta_{xy} - \eta_x^2 \eta_y \eta_{xy} + {\eta_y}^3 \eta_{xy} + \eta_x \eta_y^2 (\eta_{xx} - \eta_{yy})$$

$$D_1 = -\eta_{yy} \frac{\partial}{\partial x} + \eta_{xy} \frac{\partial}{\partial y} + (-\eta_x \eta_{yy} + \eta_y \eta_{xy}) \frac{\partial}{\partial z}$$

$$D_2 = \eta_{xy} \frac{\partial}{\partial x} - \eta_{xx} \frac{\partial}{\partial y} + (\eta_x \eta_{xy} - \eta_y \eta_{xx}) \frac{\partial}{\partial z}$$

$$D_3 = (\eta_y \eta_{xy} - \eta_x \eta_{yy}) \frac{\partial}{\partial x} + (\eta_x \eta_{xy} - \eta_y \eta_{xx}) \frac{\partial}{\partial y} + (2\eta_x \eta_y \eta_{xy} - \eta_{xx} \eta_y^2 - \eta_{yy} \eta_x^2) \frac{\partial}{\partial z}$$

$$\mathcal{N} = (1+\eta_x^2 + \eta_y^2)^{1/2}$$

Mean surface curvature is defined as: $2H = -\nabla_s \cdot \boldsymbol{n} = -\nabla \cdot \boldsymbol{n}$, and can be written in terms of principal curvatures: $H = \frac{1}{2}(\kappa_1 + \kappa_2)$.

Surface curvature dyadic $\boldsymbol{b} = -\nabla_s \boldsymbol{n}$

If free surface elevation is given by $z = \eta(x, y, t)$, some geometrical parameters can be obtained as follows:

unit normal $\boldsymbol{n}$: $\boldsymbol{n} = \frac{(-\eta_x, -\eta_y, 1)}{\sqrt{\eta_x^2 + \eta_y^2 + 1}}$

tangent vector in (y, z) plane: $\boldsymbol{t}_x : \boldsymbol{t}_x = \frac{(1, 0, \eta_x)}{\sqrt{\eta_x^2 + 1}}$

tangent vector in (x, z) plane: $\boldsymbol{t}_y : \boldsymbol{t}_y = \frac{(0, 1, \eta_y)}{\sqrt{\eta_y^2 + 1}}$

base vectors:

$\boldsymbol{a}_1 = (1, 0, \eta_x), \boldsymbol{a}_2 = (0, 1, \eta_y), \boldsymbol{n} = (n_x, n_y, n_z)$

$\boldsymbol{a}^1 = \frac{(1+\eta_y^2, -\eta_x \eta_y, \eta_x)}{1+\eta_x^2 + \eta_y^2}$

$\boldsymbol{a}^2 = \frac{(-\eta_x \eta_y, 1+\eta_x^2, \eta_y)}{1+\eta_x^2 + \eta_y^2}$

$(\boldsymbol{a}^1, \boldsymbol{a}^2, \boldsymbol{n})$ denote the set reciprocal to $(\boldsymbol{a}_1, \boldsymbol{a}_2, \boldsymbol{n})$

$$\boldsymbol{n}\,\boldsymbol{n} = \frac{1}{1+\eta_x^2+\eta_y^2} \begin{bmatrix} \eta_x^2 & \eta_x \eta_y & -\eta_x \\ \eta_x \eta_y & \eta_y^2 & -\eta_y \\ -\eta_x & -\eta_y & 1 \end{bmatrix}$$

$$\nabla = \begin{bmatrix} \frac{\partial}{\partial x} \\ \frac{\partial}{\partial y} \\ \frac{\partial}{\partial z} \end{bmatrix}$$

Surface idemfactor:

$$\boldsymbol{I}_s = \boldsymbol{a}^1\boldsymbol{a}_1 + \boldsymbol{a}^2\boldsymbol{a}_2 = \frac{1}{1+\eta_x^2+\eta_y^2}\begin{bmatrix} 1+\eta_y^2 & -\eta_x\,\eta_y & \eta_x \\ -\eta_x\,\eta_y & 1+\eta_x^2 & \eta_y \\ \eta_x & \eta_y & \eta_x^2+\eta_y^2 \end{bmatrix}$$

$$\nabla_s = (\boldsymbol{I}_s \cdot \nabla) = \frac{1}{1+\eta_x^2+\eta_y^2}\begin{bmatrix} (1+\eta_y^2)\frac{\partial}{\partial x} - \eta_x\eta_y\frac{\partial}{\partial y} + \eta_x\frac{\partial}{\partial z} \\ -\eta_x\eta_y\frac{\partial}{\partial x} + (1+\eta_x^2)\frac{\partial}{\partial y} + \eta_y\frac{\partial}{\partial z} \\ \eta_x\frac{\partial}{\partial x} + \eta_y\frac{\partial}{\partial y} + \left(\eta_x^2+\eta_y^2\right)\frac{\partial}{\partial z} \end{bmatrix}$$

$$-\nabla_s \cdot \boldsymbol{n} = \frac{\eta_{xx}+\eta_{yy}+\eta_{xx}\eta_y^2+\eta_{yy}\eta_x^2-2\eta_x\eta_y\eta_{xy}}{(1+\eta_x^2+\eta_y^2)^{(3/2)}}$$

surface curvature dyadic $\boldsymbol{b} = -\nabla_s\boldsymbol{n}$

$$\boldsymbol{b} = \frac{1}{(1+\eta_x^2+\eta_y^2)^{(5/2)}}\begin{bmatrix} b_{11} & b_{12} & b_{13} \\ b_{21} & b_{22} & b_{23} \\ b_{31} & b_{32} & b_{33} \end{bmatrix}$$

$$b_{11} = (1+\eta_y^2)^2\eta_{xx} - 2\eta_x\,\eta_y\eta_{xy}(1+\eta_y^2) + \eta_x^2\eta_y^2\eta_{yy}$$

$$b_{12} = 2\eta_x^2\eta_y^2\eta_{xy} + (\eta_x^2+\eta_y^2)\eta_{xy} - \eta_x\eta_y(\eta_{xx}+\eta_{yy}) + \eta_{xy} - \eta_x\,\eta_y(\eta_x^2\eta_{yy}+\eta_y^2\eta_{xx})$$

$$b_{13} = (1+\eta_y^2)(\eta_x\eta_{xx}+\eta_y\eta_{xy}) - \eta_x\eta_y(\eta_x\eta_{xy}+\eta_y\eta_{yy})$$

$$b_{22} = (1+\eta_x^2)^2\eta_{yy} - 2\eta_x\eta_y\eta_{xy}(1+\eta_x^2) + \eta_x^2\eta_y^2\eta_{xx}$$

$$b_{23} = \eta_x^2\eta_y\eta_{yy} + \eta_x{}^3\eta_{xy} + \eta_y\eta_{yy} + \eta_x\eta_{xy} - \eta_x^2\eta_y\eta_{xx} - \eta_x\eta_y^2\eta_{xy}$$

$$b_{33} = \eta_x^2\eta_{xx} + 2\eta_x\eta_y\eta_{xy} + \eta_y^2\eta_{yy}$$

$\boldsymbol{b} = -\nabla_s\boldsymbol{n}$ is symmetric, so $b_{31} = b_{13}, b_{32} = b_{23}, b_{21} = b_{12}$

Another way to calculate $\boldsymbol{b} = -\nabla_s\boldsymbol{n}$:

$$\boldsymbol{r} = (x, y, \eta)$$

$$L = \boldsymbol{n} \cdot \boldsymbol{r}_{xx} = \frac{\eta_{xx}}{\sqrt{1+\eta_x^2+\eta_y^2}}$$

$$M = \boldsymbol{n} \cdot \boldsymbol{r}_{xy} = \frac{\eta_{xy}}{\sqrt{1+\eta_x^2+\eta_y^2}}$$

$$N = \boldsymbol{n} \cdot \boldsymbol{r}_{yy} = \frac{\eta_{yy}}{\sqrt{1+\eta_x^2+\eta_y^2}}$$

second fundamental form:

$$-d\boldsymbol{r} \cdot d\boldsymbol{n} = Ldx^2 + 2Mdxdy + Ndy^2$$

$$\boldsymbol{b} = -\nabla_s \boldsymbol{n} = L\boldsymbol{a}^{\,1}\boldsymbol{a}^{\,1} + M(\boldsymbol{a}^{\,1}\boldsymbol{a}^{\,2} + \boldsymbol{a}^{\,2}\boldsymbol{a}^{\,1}) + N\boldsymbol{a}^{\,2}\boldsymbol{a}^{\,2}$$

$$= \boldsymbol{b}_L + \boldsymbol{b}_M + \boldsymbol{b}_N$$

$$\boldsymbol{b}_L =$$

$$\frac{\eta_{xx}}{\Delta}\begin{bmatrix} \left(1+\eta_y^2\right)^2 & -\eta_x\,\eta_y(1+\eta_y^2) & \eta_x(1+\eta_y^2) \\ -\eta_x\eta_y(1+\eta_y^2) & \eta_x^2\eta_y^2 & -\eta_x^2\eta_y \\ \eta_x(1+\eta_y^2) & -\eta_x^2\eta_y & \eta_x^2 \end{bmatrix}$$

$$\boldsymbol{b}_M =$$

$$\frac{\eta_{xy}}{\Delta}\begin{bmatrix} -2\,\eta_x\,\eta_y\,(1+\eta_y^2) & (1+\eta_x^2)(1+\eta_y^2)+\eta_x^2\eta_y^2 & \eta_y(1+\eta_y^2)-\eta_x^2\eta_y \\ (1+\eta_x^2)(1+\eta_y^2)+\eta_x^2\eta_y^2 & -2\,\eta_x\,\eta_y\,(1+\eta_x^2) & -\eta_x\eta_y^2+\eta_x(1+\eta_x^2) \\ \eta_y(1+\eta_y^2)-\eta_x^2\eta_y & -\eta_x\eta_y^2+\eta_x(1+\eta_x^2) & 2\,\eta_x\eta_y \end{bmatrix}$$

$$\boldsymbol{b}_N =$$

$$\frac{\eta_{yy}}{\Delta}\begin{bmatrix} \eta_x^2\eta_y^2 & -(1+\eta_x^2)\,\eta_x\,\eta_y & -\eta_x\eta_y^2 \\ -\eta_x\eta_y(1+\eta_x^2) & (1+\eta_x^2)^2 & \eta_y(1+\eta_x^2) \\ -\eta_x\eta_y^2 & (1+\eta_x^2)\eta_y & \eta_y^2 \end{bmatrix}$$

Here $\Delta = (1+\eta_x^2+\eta_y^2)^{5/2}$

$\boldsymbol{b} - 2H\boldsymbol{I}_s =$

$$\frac{1}{(1+\eta_x^2+\eta_y^2)^{(3/2)}}\begin{bmatrix} -\eta_{yy} & \eta_{xy} & \eta_y\eta_{xy}-\eta_x\eta_{yy} \\ \eta_{xy} & -\eta_{xx} & \eta_x\eta_{xy}-\eta_y\eta_{xx} \\ \eta_y\eta_{xy}-\eta_x\eta_{yy} & \eta_x\eta_{xy}-\eta_y\eta_{xx} & 2\,\eta_x\eta_y\eta_{xy}-\eta_{yy}\eta_x^2-\eta_{xx}\eta_y^2 \end{bmatrix}$$

$$\nabla_s\sigma = \frac{1}{1+\eta_x^2+\eta_y^2}\begin{bmatrix} (1+\eta_y^2)\sigma_x-\eta_x\eta_y\sigma_y \\ (1+\eta_x^2)\sigma_y-\eta_x\eta_y\sigma_x \\ \eta_x\sigma_x+\eta_y\sigma_y \end{bmatrix}$$

$$\nabla_s\boldsymbol{v}^{\,0} = \frac{1}{1+\eta_x^2+\eta_y^2}\begin{bmatrix} (1+\eta_y^2)\frac{\partial}{\partial x}-\eta_x\eta_y\frac{\partial}{\partial y}+\eta_x\frac{\partial}{\partial z} \\ -\eta_x\eta_y\frac{\partial}{\partial x}+(1+\eta_x^2)\frac{\partial}{\partial y}+\eta_y\frac{\partial}{\partial z} \\ \eta_x\frac{\partial}{\partial x}+\eta_y\frac{\partial}{\partial y}+\left(\eta_x^2+\eta_y^2\right)\frac{\partial}{\partial z} \end{bmatrix}(u,v,w)$$

$$\nabla_s\cdot\boldsymbol{v}^{\,o} = \nabla\cdot\boldsymbol{v}^{\,o} - \boldsymbol{n}\cdot\frac{d\boldsymbol{v}^{\,o}}{dn}$$

$$\boldsymbol{n}\cdot(\nabla\times\boldsymbol{v}^{\,o}) = \boldsymbol{n}\cdot(\nabla_s\times\boldsymbol{v}^{\,o})$$

Fully nonlinear expressions

- Normal stress boundary condition($z=\eta$) :

$$\begin{aligned} &-P+\frac{2\mu}{\mathcal{N}^2}[\eta_x^2u_x+\eta_y^2v_y+w_z+\eta_x\eta_y(v_x+u_y)-\eta_x(u_z+w_x)-\eta_y(w_y+v_z)] \\ &=\frac{(1+\eta_y^2)\eta_{xx}+(1+\eta_x^2)\eta_{yy}-2\eta_x\eta_y\eta_{xy}}{\mathcal{N}^3}\sigma+\frac{\mu^s}{\mathcal{N}^3} \\ &\quad[-\eta_{yy}u_x+\eta_{xy}u_y+(\eta_y\eta_{xy}-\eta_x\eta_{yy})u_z+\eta_{xy}v_x-\eta_{xx}v_y+(\eta_x\eta_{xy}-\eta_y\eta_{xx})v_z \\ &\quad+(\eta_y\eta_{xy}-\eta_x\eta_{yy})w_x+(\eta_x\eta_{xy}-\eta_y\eta_{xx})w_y+(2\eta_x\,\eta_y\eta_{xy}-\eta_{yy}\eta_x^2-\eta_{xx}\eta_y^2)w_z] \\ &\quad+\frac{(1+\eta_y^2)\eta_{xx}+(1+\eta_x^2)\eta_{yy}-2\eta_x\,\eta_y\eta_{xy}}{\mathcal{N}^5}(\kappa^s+\mu^s)[(1+\eta_y^2)u_x-\eta_x\,\eta_yu_y \\ &\quad+\eta_xu_z+\eta_yv_z-\eta_x\,\eta_yv_x+(1+\eta_x^2)v_y+\eta_xw_x+\eta_yw_y+(\eta_x^2+\eta_y^2)w_z] \end{aligned} \tag{A.4}$$

- Tangential stress boundary condition:

(1) on $x-z$ plane($z=\eta$):

$$\begin{aligned}
&\frac{\mu}{\mathcal{N}}[-2\eta_x(u_x-w_z)+(1-\eta_x^2)(w_x+u_z)-\eta_y(v_x+u_y)-\eta_x\ \eta_y(v_z+w_y)] \\
&=\sigma_x+(\kappa^s+\mu^s)[\frac{1}{\mathcal{N}^2}(\varphi_x+\eta_x\varphi_z)-\frac{\varphi}{\mathcal{N}^4}(2\eta_x\eta_{xx}+2\eta_y\eta_{xy})] \\
&\quad+\frac{2\mu^s}{\mathcal{N}^4}(-\eta_x D_1u-\eta_y D_1v+D_1w-\eta_x^2 D_3u-\eta_x\ \eta_y D_3v+\eta_x D_3w) \\
&\quad+\mu^s[\frac{1}{\mathcal{N}^2}\Phi-\frac{\Pi\Omega}{\mathcal{N}^4}]
\end{aligned} \tag{A.5}$$

(2) on $y-z$ plane(z=η):

$$\begin{aligned}
&\frac{\mu}{\mathcal{N}}[-2\eta_y(v_y-w_z)+(1-\eta_y^2)(w_y+v_z)-\eta_x(v_x+u_y)-\eta_x\ \eta_y(u_z+w_x)] \\
&=\sigma_y+(\kappa^s+\mu^s)[\frac{1}{\mathcal{N}^2}(\varphi_y+\eta_y\varphi_z)-\frac{\varphi}{\mathcal{N}^4}(2\eta_x\eta_{xy}+2\eta_y\eta_{yy})] \\
&\quad+\frac{2\mu^s}{\mathcal{N}^4}(-\eta_x D_2u-\eta_y D_2v+D_2w-\eta_y^2 D_3v-\eta_x\ \eta_y D_3u+\eta_y D_3w) \\
&\quad+\mu^s[\frac{1}{\mathcal{N}^2}\Theta-\frac{\Pi\mathcal{R}}{\mathcal{N}^4}]
\end{aligned} \tag{A.6}$$